STRESS AND FRACTURE PREDICTION USING GEOMECHANICAL RESERVOIR MODELS – A CASE STUDY FROM THE LOWER MAGDALENA VALLEY BASIN, COLOMBIA

Dissertation

Vom Fachbereich Material- und Geowissenschaften

der Technische Universität Darmstadt

zur Erlangung des akademischen Grades

Doktor Ingenieur (Dr. Ing)

genehmigte Dissertation

TECHNISCHE UNIVERSITÄT DARMSTADT

Von

M.Sc. Clairet Guerra

geboren am 26. April 1989 in Barcelona, Anzoategui / Venezuela

Referent: Prof. Dr. Andreas Henk

Korreferent: Prof. Dr. Eva Schill

Tag der Einreichung: Mai 9. 2019

Tag der Disputation: Juli. 10.2019

Darmstadt, May 2019

Vorsitzender der Prüfung:	Prof. Dr. Oliver Clemens
Berichter:	Prof. Dr. Andreas Henk
Mitberichter:	Prof. Dr. Eva Schill
Prüfer:	Prof. Dr. Christoph Schüth
Prüfer:	Prof. Dr. Hauke Zachert

Year of publication of dissertation in TUprints: 2019

URI: https://tuprints.ulb.tu-darmstadt.de/id/eprint/9029

URN: urn:nbn:de:tuda-tuprints-90296

Acknowledgements

First and foremost, I would like to thank my advisor, Prof. Henk, for letting me develop my doctoral studies in his group. He let me experience with the research process, discover, and find the blockages on my own, encouraged me to seek advice, showcase my work and gave me the space to learn and grow, as a scientist and as a person; this will always be a strong reminder that choosing kindness is always the right choice.

As part of my project, I had the opportunity to work with Schlumberger Inc. in Germany and the United Kingdom. From the Basin and petroleum systems technology group, I would like to recognise the assistance provided by the following specialists: Andy McGregor, Cassie Warren, Carlos, Adeline Parent, Daniel Palmowski, Thomas Hantschel, and Juan Carlos Hidalgo, who became more than an instructor, a mentor and a friend. From the Geomechanics centre of excellence in London, I would like to extend this message to the team I worked with, mainly Dr. Nick Koutsabeloulis, James Minton, Chad Karbinsky, Juliane Heiland, Qin Lai, Monzurul, Assef Muhammad, Xavier Garcia-Teijeiro, and especially to Adrian Rodriguez-Herrera and Karsten Fischer who shared their knowledge in the best way possible, with kindness and patience. They all did not only teach me about geomechanics but also about friendship and endurance. The lessons I learned here will never be forgotten.

I dearly appreciate the company of the entire staff of the Institute of Applied Geosciences at TU Darmstadt. To my group: Karsten, Tobias, Torben, Zain, Reimund, Dominique and Constantin. Special thanks to Steffi, who became my female support along these years. To my long-time friends, Claudia, Natalia, Ale, Stephany, Carito, Eduardo, Isabel and Max and my extended academic family in Colombia, for keeping an eye on me during my doctoral studies.

Thanks to all the new friends I made in Darmstadt, Russia and the United Kingdom, Valerie, Pablo Javi, Sina, Luis, Dimitris, Marwan and my roommates Anna, Kathrin and Jhonatan. You have all made this time an extraordinary adventure. Danke für die Hilfe, die Liebe und die Freundschaft. Ich bin sehr dankbar, dass ich diese Erfahrung unter euch allen erlebt habe.

Finally, I would like to thank my family for the endless support of the pursuit of my dreams. To my wonderful mom, who also became my advisor; my father and my sister who were the most influential moral and scientific support, and to my dear love, I am forever grateful for your patience, strength and willingness to see me shine. This work and all my personal success are dedicated to you for the constant support and love. I am extremely proud to be part of such a fantastic team.

A special dedication goes to every person in the world who cannot access any form of education, especially the younger generation of my country, Venezuela.

With all my love, Clairet

Nothing in life is to be feared; it is only to be understood. Now is the time to understand more, so that we may fear less. Marie Curie

Abstract

Proper characterisation of the mechanical and stress state of a hydrocarbon or geothermal reservoirs is crucial for optimal exploration and exploitation. The increasing complexity of discoveries push the boundaries of conventional methodologies, which often rely on local laboratory measurements or well-derived properties that may not represent the actual spatial distribution of relevant characteristics of the area. The early and accurate knowledge of pore pressure, mechanical properties and *in-situ* stress represent critical information to promote reservoir exploration, well placement and enhanced recovery techniques as well as avoidance of risky locations. Numerical modelling approaches serve as the solving tool as they can honour the heterogeneous and geometrical complexity of reservoir and associated structures.

This study evaluates the potential and pertinence of geomechanical modelling techniques for stress and fracture prediction. The methodologies performed in this research are applied to a tight sand gas reservoir located in the Lower Magdalena Valley Basin in northern Colombia. The target reservoir is an Oligocene to Miocene sequence known as Porquero formation which is composed of low-permeability sandstones and shale layers. The area has been explored for more than 30 years but, due to its difficulty to be adequately characterised, has only become of economic interest in the last decade, thanks to the implementation of seismic methodologies and advanced petrophysical studies. The exploitation of the Porquero formation will require non-vertical drilling paths and hydraulic fracturing for economic production. Therefore, an accurate understanding of reservoir mechanics and stresses is of critical importance.

In this study, different methodologies are proposed to study the general geomechanical behaviour of the stratigraphic column covered in the study area, as well as the inference of the natural fracturing behaviour along the reservoirs conforming the Porquero formation. Each methodology was developed around the data available, highlighting the integration between basin and petroleum systems modelling technique and geomechanical analysis as a pivotal approach to determine the mechanical state of a reservoir.

The first modelling phase presents the performance of a complete geomechanical assessment using log-derived properties. This section includes the analysis of log and core data, as well as hydraulic fracturing tests leading to detailed 1D mechanical earth models (MEM) for each of the wells available in the study area.

Subsequently, a 3D mechanical earth model was set up using two different property population methods that were tested and compared in terms of stresses. One method used a geostatistical approach based on well data mechanical models for property inter-/extrapolation, whereas the other, additionally used seismic inversion techniques to account for the vertical and lateral differences in mechanical rock properties. The combination of these methodologies serves as a base model of the present-day stress state of the area and is set to be the reference for potential predictive simulations.

The second modelling phase introduces basin and petroleum systems modelling (BPSM) technology for geomechanical purposes. The method takes advantage of a robust model construction intended to assess hydrocarbon generation, migration and accumulation. It ensures that the temporal basin evolution and spatial properties variations are consistent and assumed under adequate reasoning. Pore pressure model was derived from porosity-dependent compaction laws that answer to subsidence and

sedimentary registers of the basin. *In-situ* stresses were estimated through a poro-elastic approach. The definition of *process-based* mechanical properties, physics-driven pore pressure models and therefore enhanced resulting *in-situ* stresses, is presented as an alternative methodology to conventional modelling approaches, to perform a pre-drilling geomechanical assessment.

The modelling results provide a spatial mechanical characterisation, pore pressure models and the complete stress tensor, not only for the reservoir but for each point in the model domain. The simulation shows that the ruling stress regime in the study area is a normal faulting regime with a governing orientation of S_{Hmax} in a WNW-ESE direction. At reservoir depth, vertical stress gradient (S_v) has a mean value of 23.29 MPa/km, and S_{Hmax} is on average 1.2*S_{hmin}.

The final stage of the modelling work includes the study of the potential of the developed geomechanical models to infer natural fracture networks. Such fracture models are crucial in enhancing field development and promoting efficient well placement to maximise hydrocarbon production. Two methods were tested. The first method corresponds to a stochastic simulation enhanced by the definition of geomechanical constraints and well-log derived fracture metrics. Paleo-stress selection is performed through a stress-inversion approach. The second model showcases the potential of forward modelling of BPSM-derived properties. The critical difference, in this case, is that the dynamic setup allows the step-wise definition of maximum stress orientation correspondent to defined geological stages. The overall analysis is made in terms of fracture orientation metrics (Dip angle and dip azimuth), fracture intensity and the potential of the models to reproduce observed data.

The stochastically generated fracture network is based in a boundary element method, which is beneficial because of the computational speed. However, a concept of this method is the definition of homogeneous mechanical properties which may lead to oversimplified results when dealing with complex lithological distributions. On the other hand, the forward model approach, using the BPSM technology, displays great pertinence in gathering most of the evolutionary traits in the area. Moreover, the recognition of heterogeneous lithological distribution represents an enhancement and consequently leads to more reliable results. As a disadvantage, the construction endeavour of such models is of high complexity, as well as demanding in the necessity of the integration and cooperation of several disciplines to achieve a consistent result. Considering the mentioned generalities, the stochastic approach is advised for low-deformation regions, while the forward model approach may display its maximum capacity in areas with strong deformation.

The significant contributions of this research are fully customized geomechanical reservoir models that can reproduce the reported mechanical behaviour of the area but, moreover, are able to provide critical insights in the inter-well and undrilled regions of the model domain. The models are populated with actual field and laboratory data and are set to be the fundamental scenarios in any predictive simulation. The methods presented in this work are replicable and deployable in any other geographical and tectonic setting

Zusammenfassung

Die richtige Charakterisierung des mechanischen Spannungszustandes von Kohlenwasserstoff- oder geothermischen Speichern ist entscheidend, um deren Untersuchung und Abbau optimal zu gestalten. Die zunehmende Komplexität der Funde, lassen herkömmliche Methoden an ihre Grenzen stoßen, die sich oft auf lokale Labormessungen oder von Bohrlöchern abgeleitete Eigenschaften stützen, die möglicherweise nicht die tatsächliche räumliche Verteilung relevanter Merkmale des Gebietes darstellen. Die frühzeitige und genaue Kenntnis von Porendruck, mechanischen Eigenschaften und In-situ-Spannungen ist entscheidend, um die Erkundung von Lagerstätten, die Platzierung von Bohrlöchern und verbesserte Gewinnungstechniken sowie die Vermeidung von riskanten Standorten zu fördern. Numerische Modellierungsansätze dienen als Lösungsinstrument, da sie die heterogene und geometrische Komplexität von Reservoirs und zugehörigen Strukturen berücksichtigen können.

Diese Studie bewertet das Potenzial und die Relevanz geomechanischer Modellierungstechniken für die Vorhersage von Spannungen und Brüchen. Die in dieser Forschungsarbeit genutzten Methoden werden auf ein dichtes Sandstein-Gas-Reservoir im unteren Magdalena-Talbecken im Norden Kolumbiens angewendet. Das Zielreservoir ist eine Oligozän-Miozän-Sequenz, die als Porquero-Formation bekannt ist und aus schwach durchlässigen Sandsteinen und Schieferschichten besteht. Das Gebiet wird seit mehr als 30 Jahren erforscht, ist aber aufgrund von Schwierigkeiten, angemessen charakterisiert zu werden, erst in den letzten zehn Jahren dank der Anwendung fortschrittlicher gesteinsmechanischer und seismischer Methoden von wirtschaftlichem Interesse geworden. Die Nutzung der Porquero-Formation erfordert nicht-vertikale Bohrpfade und hydraulisches Aufbrechen für eine wirtschaftliche Produktion. Daher ist ein genaues Verständnis der Reservoirmechanik und spannungen von entscheidender Bedeutung.

Die erste Modellierungsphase stellt die Durchführung einer vollständigen geomechanischen Bewertung unter Verwendung von abgeleiteten Eigenschaften aus Bohrlochmessungen (Logs) dar. Dieser Abschnitt beinhaltet die Analyse von Log und Probendaten, sowie hydraulische Frakturierungstests, die zu detaillierten mechanischen 1D-Erdmodellen (1D Mechanical Earth Models, MEM) für jede der verfügbaren Bohrungen im Untersuchungsgebiet führen.

Anschließend wurde ein mechanisches 3D-Erdmodell (3D MEM) mit zwei verschiedenen Eigenschaftspopulationsmethoden erstellt, die getestet und in Bezug auf Spannungen verglichen wurden. Eine Methode verwendete einen geostatistischen Ansatz, der auf mechanischen Modellen aus Bohrlochmessdaten für die Inter-/Extrapolation von Eigenschaften basiert, während die andere zusätzlich seismische Inversionstechniken einsetzte, um die vertikalen und lateralen Unterschiede in den mechanischen Gesteinseigenschaften zu berücksichtigen. Die Kombination dieser Methoden dient als Basismodell für den gegenwärtigen Stand des Gebietes und soll als Referenz für potenzielle prädiktive Simulationen dienen.

In der zweiten Modellierungsphase wird die für geomechanische Zwecke genutzte Modellierungstechnik, BDSM (Basin and petroleum systems modelling) eingeführt. Das Verfahren nutzt die Vorteile einer robusten Modellkonstruktion zur Beurteilung der Kohlenwasserstoffbildung, migration und akkumulation. Es stellt sicher, dass die zeitliche Entwicklung des Beckens und die Veränderungen der räumlichen Eigenschaften konsistent sind und unter angemessener Argumentation angenommen werden. Das Porendruckmodell wurde aus einem porositätsabhängigen

Kompaktionsgesetz abgeleitet, das auf Bodensenkungs- und Sedimentregister des Beckens reagiert. Die In-situ-Spannungen wurden durch einen poroelastischen Ansatz geschätzt. Die Definition prozessbasierter mechanischer Eigenschaften, physikalisch-basierte (physics-driven) Porendruckmodelle und damit erhöhter resultierender in-situ Spannungen wird als alternative Methodik zu herkömmlichen Modellierungsansätzen vorgestellt, um eine geomechanische Vorbohrbeurteilung durchzuführen.

Die wichtigsten Modellierungsergebnisse liefern eine räumliche mechanische Charakterisierung, Porendruckmodelle und den kompletten Spannungstensor, nicht nur für das Reservoir, sondern für jeden Punkt in der Modelldomäne. Die Simulation zeigt, dass das herrschende Spannungsregime im Untersuchungsgebiet eine normale Verwerfung mit einer vorherrschenden Ausrichtung von S_{Hmax} in einer WNW-ESE-Richtung ist. In der Speichertiefe hat der vertikale Spannungsgradient (S_v) einen Mittelwert von 23,29 MPa/km und S_{Hmax} beträgt durchschnittlich $1{,}2*S_{hmin}$.

Die letzte Phase der Modellierungsarbeiten beinhaltet die Untersuchung des Potenzials der entwickelten geomechanischen Modelle zur Ableitung natürlicher Bruchnetze. Solche Bruchmodelle sind entscheidend für die Verbesserung der Feldentwicklung und die Förderung einer effizienten Bohrlochplatzierung zur Maximierung der Kohlenwasserstoffproduktion. Zwei Methoden wurden getestet. Die erste Methode entspricht einer stochastischen Simulation, die durch die Definition von geomechanischen Randbedingungen und Bruchmetriken aus Bohrlochmessungen (Logs) ergänzt wird. Die Auswahl der Paläospannung erfolgt über einen Ansatz der Spannungsinversion. Das zweite Modell zeigt das Potenzial der Vorwärtsmodellierung oder der von BPSM abgeleiteten Eigenschaften. Der entscheidende Unterschied besteht in diesem Fall darin, dass der dynamische Aufbau die schrittweise Definition der maximalen Spannungsorientierung entsprechend den definierten geologischen Phasen ermöglicht. Die Gesamtanalyse erfolgt in Bezug auf die Kennzahlen zur Bruchorientierung (Neigungswinkel und Azimut), die Bruchintensität und das Potenzial der Modelle zur Reproduktion der beobachteten Daten.

Die wesentlichen Beiträge dieser Forschungsarbeit sind vollständig angepasste geomechanische Reservoir-Modelle, die in der Lage sind, das berichtete mechanische Verhalten des Gebietes zu reproduzieren, aber darüber hinaus auch entscheidende Einblicke in die ungebohrten Regionen und Regionen zwischen Bohrlöchern der Modelldomäne liefern können. Die Modelle sind mit aktuellen Feld und Labordaten gefüllt und stellen zu Grunde liegende Szenarien in jeder prädiktiven Simulation. Die in dieser Arbeit vorgestellten Methoden sind reproduzierbar und in jedem anderen geografischen Umfeld einsetzbar.

Content

List of Figures

List of Tables

List of symbols and abbreviations

φ	Angle of internal friction
α	Biot coefficient
P_b	Breakdown pressure
K	Bulk modulus
C_b	Bulk Compressibility
BPSM	Basin and petroleum system model/modelling
μ	Coefficient of friction (faults)
μ_i	Coefficient of internal friction (intact rock)
C	Cohesion
V_p	Compressional wave velocity
Δtp	Compressional wave travel time - slowness
cos	Cosines
ρ	Density
Z	Depth
d	Diameter
K_b	Drained bulk modulus
DST	Drill stem test
σ'_{n}	Effective normal stress
σ'	Effective stress
σ'_V	Effective vertical stress
FIT	Formation integrity test
FFP	Final flow pressure
FSIP	Final shut-in pressure
Fcp	Fracture closure pressure
K_g	Grains bulk modulus
ρ_{gr}	Grains density
g	Gravitational acceleration
λ	Hardening parameter
ϕ_0	Initial porosity
I	Invariants
ISIP	Instantaneous shut-in pressure
IFP	Initial flow pressure

δ_{ij}	Kronecker's delta
l	Length
LOT	Leak-off test
LOP	Leak-off pressure
LMVB	Lower Magdalena Valley Basin
NCT	Normal compaction trend
Δtn	Normal compaction travel time
OBG	Overburden gradient
k	Permeability
εij	Plastic strain
v	Poisson Ratio
P_p	Pore pressure
ϕ	Porosity
P	Pressure
ε_1, ε_2, ε_3	Principal strains
σ_1, σ_2, σ_3	Principal stresses
σr	Radial stress
G	Shear modulus
Vp	Shear wave velocity
Δts	Shear wave travel time - slowness
sin	Sine
ε	Strain
ζ	Strain parameter
tan	Tangent
T_0	Tensile strength
S_{HMax}	Total maximum horizontal stress
S_{mean}	Total mean stress
S_{hmin}	Total minimum horizontal stress
S_V	Total vertical stress
UCS	Unconfined compressive strength
vol	Volume/volumetric
ρ_w	Water density
E	Young's modulus

Chapter 1 Introduction

1.1 Motivation and objectives

Geomechanical modelling has a dominant role in pre-drilling, completion and production stages in the hydrocarbon industry, as it intends to predict how rocks will sustain deformation after stress, pressure, temperature changes and other environmental variations. Planning a mud density program that ensures wellbore stability during drilling, intervention in hydraulic fracturing programs and the determination of stress transient variations are some of the relevant applications of a geomechanical study that derive in an optimal production of a reservoir. The heterogeneous nature of rocks in the subsurface is a matter of primary concern in the development of efficient production procedures. The accurate prediction regarding the mechanical variability at pre-drilling stage represents the difference between a successful or a failed attempt in resource exploitation.

Every kind of raw data that may provide insights of the subsurface (e.g., well logs, core samples, laboratory tests, geological evolution, geophysical surveys, etc.) should be integrated to create high-quality input data for simulations that deliver outputs in agreement with the geological and tectonic setting. Originally, at an exploratory stage, little to no measured data is available, so the best option becomes a layer-cake type model that roughly represents the structures and heterogeneous nature of rocks. As further data is collected certain numerical methodologies (i.e. log-based and seismic-driven models) are routinely performed in industry depending on the data availability and allow an explicit description of the heterogeneous conditions of the subsurface vertically and horizontally. These techniques are often successful and promote a good characterization of an area. Nevertheless, these methods focus on the present-day state of the area and ignore evolutionary treats that certainly impact the present-day and future states of a reservoir.

The work developed in this study intends to tackle the urgent necessity of methodologies that represent the increasing complexity of the *in-situ* conditions of subsurface formations and processes interrelations as accurate as possible. Alongside conventionally implemented methodologies, the presented research seeks to highlight the potential benefits that basin and petroleum systems modelling technology (BPSM) may represent towards integrated geomechanical assessment.

A basin and petroleum system modelling approach (BPSM) is a traditional concept to assess hydrocarbon generation, migration, and accumulation (Fig. 1). This modelling methodology integrates a series of geological, thermal, mechanical and geochemical temporally-related variables that makes up for a repository of data that can be of great relevance for reservoir evaluations in terms of rock stresses, pore pressure and potential failure. The concept of BPSM implies a great endeavour in terms of data integration, requiring often a multidisciplinary approach and it represents the technique that gathers the most complete set of variables to assess a reservoir mechanically. Moreover, this approach can take advantage of routinely performed methodologies (i.e., log and seismic-driven models) to fine-tune and calibrate its results. This modelling concept can be implemented from early exploratory stages and be constantly updated as new information is gathered throughout the reservoir-life cycle.

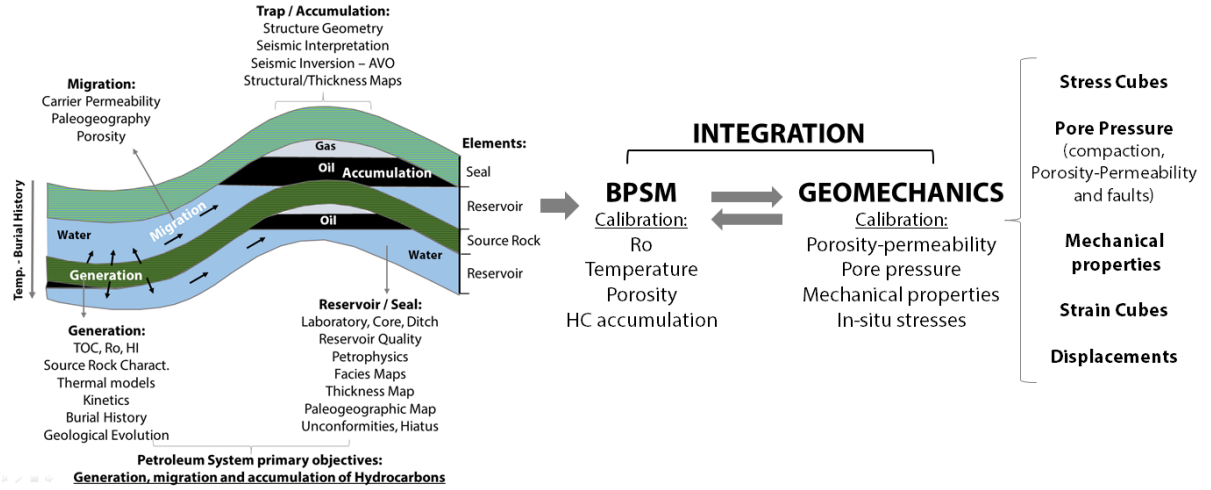

Fig. 1 Basin and petroleum system modelling primary objectives and its interrelation towards geomechanical assessment. Petroleum system diagram modified after Feijó (2010).

To take advantage of widely used geomodelling techniques, three methodologies were applied for the characterization of the geomechanical state of an Oligocene-Miocene tight gas sand reservoir of the Porquero formation in the study area: Block A, in Northern Colombia. The proposed geomechanical workflow targets *in-situ* stresses and natural fracture prediction through the implementation of log-based, seismic driven and basin and petroleum systems-derived models. An emphasis is given to BPSM approach, as a method that promotes geologically-consistent mechanical earth models. The estimation of natural fracture networks, a pertinent study for well placement and field development, was performed as means to assess the potential of the models to capture present-day conditions. This research aspire to provide means to diminish the uncertainty associated with reservoir characterization and prediction of the geomechanical behaviour, as well as promoting the integration between datasets, methods and disciplines to achieve the most consistent results.

Considering the data provided, the fundamental objectives for this study are two:

- Evaluation of the *in-situ* stress state and natural fracture network predictive potential of geomechanical models.

- Evaluation of the potential of basin and petroleum system modelling technology for geomechanical characterization

The following specific objectives were defined to address the general objectives:

- Audit and analyse seismic, wells and laboratory data.

- Audit and analyse the tectonostratigraphic evolution of the area.

- Perform a 3D integrated geomechanical finite element models with high resolution using well logs and seismic-driven data.

- Perform a 3D integrated geomechanical finite element models with high resolution using log, seismic data, and regional geological interpretations following the basin and petroleum systems approach.

- Perform discrete fracture prediction through stress inversion and iterative boundary element method.

- Perform natural fracture prediction through forward modelling, derived from basin and petroleum system modelling.

The accomplishment of these objectives will ensure a full geomechanical description of the case study area. The evidence of the potential of basin and petroleum systems modelling approach towards enhanced geomechanical characterization will provide means, alongside conventional methodologies, to obtain the best mechanical description of an area. Additionally, the practical application of natural fracture prediction will become valuable for field development stages and fluid-flow simulations. The generated models will serve as base case for the testing of future predictive scenarios.

This work was developed under the name *"Stress and fracture prediction using geomechanical models – A case Study from a tight gas reservoir in the Lower Magdalena Valley Basin, Colombia"*. It was performed from 2015 until 2019, with a dataset provided by Pacific Rubiales Inc. as the industrial partner, in combination with the Technische Universität Darmstadt as an academic partner. The proposed methodologies and modelling simulations were conducted independently at the Technische Universität Darmstadt. Specific data and figures were anonymised and coded well names were used to comply with confidential rules.

1.2 Study outline

This thesis begins with a description of the reservoir geomechanics state of the art, addressing the main approaches existing to assess the mechanical behaviour of a reservoir and the emerging techniques currently under development in industry (Chapter 1). The fundamental theories in which the applied reservoir geomechanics methods are founded are presented in Chapter 2. Main topics cover rock mechanics, pore pressure, numerical methods and fundamentals of basin and petroleum systems modelling fundamentals.

In Chapter 3, the reader is introduced to the case study where the numerical simulations took place. A general description of the Lower Magdalena Valley Basin is presented, the main stages of its geological evolution and a local context describing the area where the dataset is available. In Chapter 4 the reader can find a description of the dataset available for the pilot project. Chapter 5 describes the main methodologies and assumptions considered to develop and run the geomechanical models.

Chapter 6 presents a description of the resulting mechanical properties, pore pressure and stress state through the implemented methodologies. Chapter 7 presents a summary and discussion of significant modelling results and offers clearance on the benefits of implemented geomechanical models. Discussion targets the three major topics addressed, as are: the mechanical properties, the pore pressure model and in-situ stress state.

Implications of results cover the generation of a mechanical model for a pseudo-well and the estimation of a safe mud weight window for drilling purposes to display the predictive potential of the proposed methodologies. Concluding remarks on this works and takeaway messages and be found in Chapter 8. Finally, step-by-step guides on how to build 1D and 3D geomechanical models using primary datasets are added in Appendix A and Appendix B, respectively. Fig. 2 displays the organisation of this work.

Fig. 2 Research outline.

1.3 Relevance of basin modelling approach for geomechanics

Knowledge of the pre-production stress state and its changes on a hydrocarbon or geothermal reservoir is of vital importance throughout the reservoir life-cycle. Wellbore stability issues, stress-dependent permeability changes, reservoir compaction and subsidence as well as hydraulic fracturing, are just a few examples which require a careful *in-situ* stress state assessment in advance of the operation (Geertsma, 1973; Herwanger & Koutsabeloulis, 2011; Zoback et al., 1985). A thorough understanding of the mechanical rock properties and a robust quantitative prediction of the pore pressure and stress state are therefore crucial for safe and optimal reservoir development.

Having a set of *in-situ* parameters like mechanical properties, pore pressure and stress state, estimated before the drilling of exploratory and advanced wells, fracturing and other activities, will allow optimizing time, money and getting a better exploitation plan of a reservoir. A safe initial condition at the start of the subsurface operations is the primary motive for continuous working towards decreasing the uncertainty in geomechanical reservoir models. A great deal of research has focused on three principal targets addressed through mechanical earth models, namely: pore pressure, elastic mechanical properties, and in-situ stresses. To study these targets, existing geomechanical approaches are diverse and range from speculative or empirical approaches (Bowers, 1995; Eaton, 1975; Terzaghi, 1943; Traugott & Heppard, 1994) , as in well-scale mechanical models, to robust physical-geological compendium of processes (as is basin and petroleum systems modelling technology) (Hantschel & Kauerauf, 2009). The predictive potential of any implemented model is strongly conditioned by the amount and quality of the data available. This, plus an accurate geological interpretation can lower a model's uncertainty and help to achieve reasonable results.

Geomechanical modelling has proven to be a critical methodology for reservoir stress characterization as it integrates information on the subsurface structure, the mechanical properties of rocks and faults, the regional stress field and the basin tectonic history (Bernal-Olaya et al., 2014; Fernández & Alvarellos, 2011; Fischer & Henk, 2013; Frischbutter & Henk, 2010).

A one-dimensional mechanical earth model (1D MEM), helps in the assessment of mechanical properties for a selected depth of interest. 1D MEM's also serves to understand the vertical distribution of stress and pore pressure, while core, field and laboratory data helps to calibrate the model. Local calibration data is relevant as it is representative of small defined reservoir intervals or areas, but for a 3D setting, uncertainty increases away from the measurement points. Nevertheless, 1D MEM's can provide early warning of potential overpressured areas which can decrease non-productive times (NPT), among other applications. As a downside, fundamental geological evolutionary processes do not take part in the model construction. Some applications that can be addressed with a one-dimensional mechanical model are wellbore stability, hydraulic fracturing operations, among others (Afsari, Amani, Razmgir, Karimi, & Yousefi, 2010; Archer & Rasouli, 2012; Fattahpour, Pirayehgar, Dusseault, & Mehrgini, 2012; Legarth, Huenges, & Zimmermann, 2005; Zoback et al., 2003)

3D mechanical earth models (3D MEM's) are ideal when the site to be analysed covers a considerable extension. These are great tools to understand better the horizontal distribution or anisotropies of lithological and mechanical properties. These 3D MEM's are populated with a combination of datasets including logs, seismic data and core analysis (Herwanger & Koutsabeloulis, 2011; Koutsabeloulis & Zhang, 2009). This approach can provide more accurate information in the inter-well and undrilled areas. As presented, these methodologies describe the present state, but do not incorporate the geological processes leading to the present-day situation.

Basin and petroleum system modelling (BPSM) is a methodology where the primary objective is to simulate expulsion, migration pathways and accumulation of hydrocarbons (Hantschel & Kauerauf, 2009; Parent, 2012; Tissot & Welte, 1984). Advancement in computational tools made it possible to couple these processes with rock mechanical analysis becoming a powerful methodology to create stress-consistent models, considering the geological evolution at basin and reservoir scale (Hantschel et al., 2011; Maerten, 2010). BPSM is generally used in exploratory stages when most of the input data is derived from regional geological interpretations and heavy dataset integration to generate a logical model, with the possibility of being updated as new information is gathered throughout the reservoir life-cycle. It considers temporal variations by numerically solving coupled partial differential equations with suitable boundary conditions on discretised temporal and spatial grids (Hantschel & Kauerauf, 2009; Madatov & Sereda, 2005). Furthermore, the mechanical behaviour is tied to a detailed regional lithological description rather than answering empirical correlations or well extrapolation. The BPSM dynamic-model nature allows the complete characterisation of *in-situ* stress state through a poro-plastic and poro-elastic approach, increasing the potential application of the results. The geomechanical predictive potential of such models will enable process-based outputs with strong physical assumptions, towards the generation of low-uncertainty geomechanical models at early exploratory stages.

The implementation of well-grounded physical and chemical laws and assumptions, in addition to calibration data, ensures that this approach gathers most of the critical variables that alongside conventional methodologies promote geologically reliable and consistent geomechanical models (Madatov & Sereda, 2005). Overall, BPSM comprises data from the origin of the basin and uses as input data most the evolutionary treats and driving mechanism that the basin suffered until present-day. Considering these premises, it becomes relevant to highlight the potential benefits that represent using a robust process-based simulation approach towards the better constraints of mechanical behaviour of a reservoir.

This work displays a series of methodologies that take advantage of a high-quality dataset to implement a customized mechanical earth model through the basin and petroleum system modelling (BPSM) approach. The method presented in this work allows for a cross-comparison of properties between BPSM and standard modelling workflows.

1.4 State of research: Geomechanical reservoir modelling

Reservoir geomechanics is a discipline defined as the connecting point between petroleum engineering, rock mechanics, geotechnical engineering, geophysics, rock physics, structural geology and statistics (Aki & Richards, 2002; Fjaer et al. 2008; Jaeger et al. 2007; Lowrie, 2007; Mavko et al., 2009; Ragan, 2009). Geomechanical assessments currently play a crucial role in better exploration and maximising the production of oil, gas, CO2 storage site evaluation, geothermal reservoirs analysis, and repositories for high-level radioactive waste (Heidbach et al.,2015; Zhao et al., 2015).

The primary goals of a geomechanical study are to assess the performance and response of a rock mass, with economical relevance, under anthropological and natural disturbances (Brady & Brown, 2005; Fjaer et al., 2008). In the oil and gas industry, a primary goal, for example, is to estimate a safe mechanical and hydraulic operational window that allows efficient hydrocarbon extraction. The consequence of this may lead to a radical decrease of non-productive times (NPT) and savings of millions of dollars (Soroush 2013). The interaction of reservoir properties under common extraction methodologies derives in drilling-induced issues that compromise the mechanical integrity of rock formations altering the predicted planning and leading to potential tragic scenarios. Numerical

modelling has enabled great breakthroughs towards the characterisation of the regional and local distribution of stresses, pore pressure effects on a wellbore and the consequent impact in production processes (Jing & Hudson, 2002). Therefore, correct numerical abstractions become of paramount relevance and can have a high impact on the estimated budget as well as in the efficiency of model implementation (Hoedeman, 2015; Sayers & Schutjens, 2007).

Datasets are of high importance in numerical modelling, but the usual situation is that these are scarce and very limited considering the complexity of acquiring them. Numerical modelling takes into consideration how representative a dataset (data-driven models) or empirical assumption is, the homogenization and upscaling of properties, and whether the back-analysis or inverse solution is required (Jing & Hudson, 2002).

The most common methods associated with geomechanics (addressing applications in diverse fields) are continuum methods (Finite difference (FDM), finite element (FEM) and boundary element methods (BEM)), discrete methods (discrete element method (DEM), discrete fracture network (DFN)) and hybrid continuum/discrete methods (Jing, 2003; Jing & Hudson, 2002; O'Sullivan, 2011). The selection of the best modelling concept strongly depends on the type of problem analysed and mainly on the working-scale. Continuum methods (FEM-FDM-BEM) are the most widely used methods across disciplines. Rock mechanics has benefited widely from advances in FEM techniques as it was the first model to include non-homogeneous materials, non-linear deformation, complex boundary conditions, in situ stresses and gravity loads (Henk, 2008; Jing, 2003; Jing & Hudson, 2002).

FE models are a vital tool to assess the *in-situ* stress field. Reiter & Heidbach (2014) developed a regional scale geomechanical model in the Alberta Basin (Canada). Such models, as robustly calibrated as in this case, serve for better constraint of smaller models within, boundary conditions transfer and potential well-placement assessment. On the reservoir scale, numerical models help in the identification of stress rotations in the vicinity of faults or distinct structures and identification of overpressured units which may lead to changes in wellbore completion duties (Fischer & Henk, 2013; Fredrich et al., 1997). Further applications include the evaluation of seal integrity for CO2 storage (Aruffo, 2014; Ouellet et al., 2011) The problems addressed through numerical earth models are manifold but, independent of the final application, mostly address three specific properties that are pore pressure, mechanical properties and *in-situ* stress state.

Integrated modelling approaches are used to generate mechanical earth models (MEM's) as numerical abstractions that aim to characterize the reservoir in its present-day state and can be used to predict its mechanical response through the reservoir's life cycle (Giroldi et al., 2014; Orlic et al., 2013; Słota-valim et al., 2016). Throughout the detailed understanding of local mechanical properties, pore pressure and stress magnitudes and their variations, one can compute a safe mud window to ease the issues associated with wellbore stability (Afsari et al., 2010; Pašić, Gaurina-Međimurec, & Matanović, 2007). A safe mud weight window intends to avoid the generation of breakouts, washouts, unexpected induced fractures among other phenomena, and incur in non- productive times (NPT). Stress changes throughout extraction, generated from hydraulic fracturing or stress rearrangement, may trigger fault and fracture reactivation. This effect is highly relevant for geothermal reservoir confinement or nuclear waste repositories management (Evans et al., 2012; Schrefler, 2001). The corresponding assessment is performed under a detailed description of heterogeneities, often achieved through seismic data, and effective stress tracking on the productive stage (Garcia-teijeiro & Rodriguez-herrera, 2014; Moeck et al., 2009; Rutqvist et al., 2013).

Through these models one can efficiently address a variety of topics like the stability of horizontal wells (Hamid et al., 2016; Qiu et al., 2008), multistage hydraulic fracturing (Bhinde & Todman, 2016; Fox et al., 2013; Williams et al., 2016), identification of high sanding potential intervals (Franquet, Stewart, Bolle, & Ong, 2005) and fault reactivation (Rutqvist et al., 2013). Production-related methods may lead to sub-surface deformation and long-term affections to public properties. Integrated workflows allow the characterisation of an area targeting subsidence/compaction relationship and related seismic events (i.e. production induced seismicity) (Fredrich et al., 1997; Geertsma, 1973; Orlic et al., 2001).

In the oil and gas industry, a way to characterise subsurface sedimentary rocks came through the mainstreaming of well logging analysis around the 1920s. Acoustic and electric logging guarantees a continuous record of data where key parameters can be derived through empirical models (Asquith et al.,2004; Bassiouni, 1994). Log-based mechanical earth model is performed to assess the efficiency of a wellbore when subjected to drilling processes (Plumb et al., 2000). It utilises well log data to derive mechanical properties, pore pressure and subsequent stress profiles. Alongside discrete data, like the one obtained from rock mechanical laboratory test (i.e., triaxial test, unconfined compressive strength, ultrasonic test) it is possible to have reliable present-state mechanical profiles.

Early pore pressure models are defined through empirical models (Eaton 1975; Traugott & Heppard 1994; Bowers 1995; Gardner et al. 1974). Successful applications present a synergy between logs-derive pore pressure and field measurements for calibration. Robust petrophysical analysis helps in low uncertainty models and identification mineralogy and lithology effects on the register (Azadpour & Manaman, 2015; Ouadfeul & Aliouane, 2015; Zhang, 2011).

Upscaling and geostatistical extrapolation of 1D MEM's for each of the wells available at this stage can already provide first insights into the stress state on 3D models (Berard et al. 2015). Log-based MEMs work efficiently if wells are available and are important for the early detection of high-risk or instability-prone areas. However, the resulting properties have a restricted influence area, and extrapolation may lead to high uncertainty in areas far from wells or calibration points (Saikia et al. 2017)

A more sophisticated modelling approach involves considering the advantages that represent having a 3D seismic volume to derive mechanical earth models. Seismic data allows for the interpretation of existing structures like faults and horizons (Bacon et al., 2012). Significant advances have been developed to use the seismic data to extract pressure information (Dutta, 2002; Narciso et al., 2014; Sayers et al., 2002; Soleymani & Riahi, 2012). Gray et al. (2012) calculated principal stresses and elastic moduli from wide-angle, wide azimuth seismic data. Even though the calculations serve as a good first approximation and a general overview of small areas further calibration is required. A critical gap that rises from populating a model using only log-derived properties is the inaccuracy and uncertainty that may exist in the inter-well areas. The seismic-driven approach in combination with log-based models can then be used to plan well paths and optimise hydraulic fracture programs, decreasing the uncertainty that already exists.

3D seismic surveys combined with seismic inversion and amplitude vs offset (AVO) analysis techniques (Filippova et al., 2011; Meyer & Payne, 2017), can fill the gap as they provide not only detailed 3D information on the geometry of the subsurface structure, but also on the vertical and lateral distribution of rock mechanical properties (Barclay et al., 2007; Lowrie, 2007; Russell, 2012). These are methodologies that take on the reflection data and convert it to a rock property referred to as impedance (acoustic and shear), which is equal to the sonic velocity multiplied by the density (Di

Luca et al., 2014; Filippova et al., 2011). Resulting property cubes can be used to set up and populate 3D MEM's which ultimately provide the full 3D stress tensor throughout the entire model domain and allow for robust stress predictions in the inter-well space and in undrilled parts of the reservoir, respectively (Bosch et al., 2010; Gray et al., 2012; Sengupta et al., 2011). Limitations of this approach are commonly related to the resolution and coverage of the seismic survey.

Structures in a field strongly condition the stress (Finkbeiner et al., 1997). Faults act as bounding structures, compartment sealers while fractures, depending on their orientation may become preferred drainage conduits for hydrocarbons, therefore the relevance of its characterisation. To accurately represent the development of such structures the modelling approach requires a temporal study of paleo-stress under plastic constitutive modelling (Henk & Nemčok, 2008; Lefranc et al., 2014). These types of approaches are time-consuming and require dense datasets to describe present-day configurations and paleo-settings. The general approach requires 2D or 3D structure backstripping or restoration, depending on the deformation history (Maerten & Maerten, 2006) and a consequent forward model to simulate the temporal mechanical variation of a basin from its sedimentation until present-day state. For several case-studies extensive documentation exists but, this is a distinctive approach given the lack of suitable datasets (Mohamad et al., 2015; Noufal et al., 2015; Smart et al., 2012).

An approach that gathers almost every relevant variable to reproduce a basin evolution is known as basin and petroleum systems modelling (BPSM) (Hantschel & Kauerauf, 2009). BPSM primary goal is to assess petroleum generation, migration, and accumulation over a specified area. This is a simulation that requires strong physical considerations, present-day and paleo-structural constraints and detailed lithology description, in addition to regional geological characterisation and geochemistry assessment (Al-Hajeri et al., 2009; Hantschel & Kauerauf, 2009; Peters et al., 2012).

To take such elements as an advantage towards better geomechanical simulations an alternative sequence combines conventional BPSM building approach but contrary to the standard outputs (i.e.: pressure-temperature model, petroleum generation, migration, and accumulation), makes a strong focus in reservoir geomechanics: specifically, stress, strain, pore pressure and mechanical rock properties. Hantschel et al. (2011) presented an engine for basin-scale geomechanics that worked with poro-elastic and poro-plastic stress formulations. The modelling approach combined the dynamic model over a geological time scale, the coupling of stress calculations with a basin-scale fluid simulator, the consideration of plastic constitutive models and failure effects and suitable boundary conditions (Fadipe et al., 2016; Hantschel et al., 2011; Mosca et al., 2018).

The primary goal of this type of simulation is to monitor the development of properties through the defined geological ages to better understand the present-day configuration, understand key elements that contributed to this configuration and serve as a base model to accurately simulate predictive scenarios (Hantschel & Kauerauf, 2009). Two main questions raised from these statements: (1) what is the predictive potential and practicality of such a modelling endeavour? and (2) in which cases is this the best alternative possible?

Published applications of this modelling approach are few and often focus on one specific property which is pore pressure (Mosca et al., 2018; Satti, Ghosh, & Yusoff, 2015). Application cases are scarce due to the data density required to construct and calibrate such models. Satti et al. (2015) generated a pre-drill pore pressure model in a field of the Malay basin. The results showed a good match with field measurements after an extensive calibration process. This kind of studies is beneficial if wells are not adequately distributed across a field or basin (Saikia et al.,2017). In the later

study, full thermal-mechanical integration is performed. Nevertheless, the Terzaghi effective stress model is implemented, pore pressure is mainly due to disequilibrium compaction process. Additional stresses and pressure generating mechanism are neglected.

Mosca et al. 2018 presented a case study for the Gulf of Mexico (GoM). The three-dimensional earth model served as a proxy for "while-drilling" updates of the pore pressure model. Thus, it was possible to identify pressure-generating mechanisms through the geological time and direct causes for present day setting. Another valuable case study was developed in onshore Abu Dhabi using BPSM for full geomechanical characterization. Mechanical properties were directly derived from lithological mixtures. Calibration was performed using log and rock mechanics derived data (Fadipe et al., 2015). Main limitations of this modelling approach are related to computational muscle that is required to integrate the many variables involved and to the lack of extensive calibration points. Late advances in the basin modelling approach involve an integration known as geophysical basin models (GBM) (Prisco et al., 2015; Szydlik et al., 2015)

An apex in numerical modelling applications is the fracture network modelling. Fracture network assessment is critical for optimized hydrocarbon production and strategic well placement in tight sands reservoir, as they dominate and control the geomechanical and hydrological behaviour of a reservoir (Lei et al., 2017). Fracture analysis is complex considering the high variability in natural configurations and the variables that control the occurrence and propagations of them (Nelson, 2001).

Fracture formation is dependent on the *in-situ* stress, pore pressure and mechanical properties of the rock. According to Lei et al. (2017), one of the central conflicts when modelling fracture networks relate to the geometrical representation of three-dimensional discontinuity systems. Fracture data is often recovered from local, punctual sources as borehole logging or outcrops (Golf-Racht, 1982; Iverson, 1992), so the final distribution across a defined unit relies on geostatistical extrapolations. Fine details, particularly at reservoir or wellbore scale, are often neglected and may have a massive impact on budget-related matters. Considering the previous description, geomechanical models greatly benefit the fracture model and vice-versa.

The usage of mechanical earth models means that fracture locations will be constrained by strict geomechanical boundary conditions. Such conditions can be obtained stochastically (Legrand et al., 2013; Maerten et al., 2016) or through a step-wise imposition in a forward model. The latter is an approach that focus on the reproduction of rock geological deformation through time (Noufal et al., 2015). Under a plastic approach, it is possible to capture the accumulated strain and identify potential fracture location which derives in a key concept for well placement enhancement (Henk & Nemčok, 2008; Lefranc et al., 2014).

Chapter 2 Theoretical background

2.1 Rock mechanics

Rocks mechanics holds the following definition: " Rock mechanics is the theoretical and applied science of the mechanical behaviour of rocks; it is that branch of mechanics concerned with response of rocks to the force fields of its physical environment"- After Judd (1964) in (Brady & Brown, 2005; Jaeger et al., 2007). The fundamental target is the study of properties and behaviour of accessible rock masses whose stress state will be directly affected and modified by artificial disturbances. It deeply correlates with structural geology to assess potential behaviour of inaccessible rock bodies and as such enhances the performance of methods concerning mining activities or drilling (Jaeger et al., 2007). The topic is analogous and parallel to geotechnical engineering, depending on the specific engineering applications.

In the evolution of rock mechanics as a field of engineering science, there has been a tendency to regard the field as a derivative of soil mechanics (Brady & Brown, 2005). The critical distinction between rock and soil mechanics is that failure processes in intact rock involve fracture mechanisms such as crack generation and growth in a pseudo-continuum. In soils, failure is commonly associated with dilation, particle rotation and alignment and often it does not imply a lowering in the mechanical integrity of the medium (Brady & Brown, 2005). The fundamental concepts of geomaterials mechanics implemented in this work are described in the following section.

2.1.1 Stress

Stress is defined as the force acting on a point or over the area of a body (Fjaer et al., 2008). It is a designation restricted to rocks and materials with shear resistance. Stress knowledge is relevant in practice as rocks in its natural context are stressed from the overburden load and previous tectonic events. Furthermore, stress can change dramatically when anthropological disturbances occur (Hudson & Harrison, 1997).

Stress on a plane is described as a vector (first-order tensor) represented as the relation between a force (F) and the area (A) on which the force acts (Eq. 1). Contrary to engineering, in geoscience compressive stress is assumed to be positive and tensional stress is negative (Zoback, 2007). Conventional unit is Pascal [1 Pa = 1 N/m^2] or Psi [1 Pa = 0.000145 Psi]

$$\sigma = \frac{F}{A} \qquad \text{Eq. 1}$$

Stress on deformable bodies such as rocks or geo-materials are often non-homogenous as the nature of them is given by the synergy of different properties tied to geological evolution. Considering the variation of stress with orientation, it is normally represented through a numerical entity known as the stress tensor (Fossen, 2010; Jaeger et al., 2007).

2.1.2 The stress tensor

A tensor is a mathematical entity with magnitude, direction, and a plane under consideration, as there are different orientation-related correlations. Some familiar tensors are stress, strain, permeability and moment (Hudson & Harrison, 1997). The stress tensor provides a full description of the stress sate at a given point through nine components in three orthogonal directions, related to a defined coordinate axis (Fjaer et al., 2008; Hudson & Harrison, 1997). In total, this stands for three normal stresses and six shear stress vectors.

$$\begin{bmatrix} \sigma_{11} & \sigma_{12} & \sigma_{13} \\ \sigma_{21} & \sigma_{22} & \sigma_{23} \\ \sigma_{31} & \sigma_{32} & \sigma_{33} \end{bmatrix} \quad \text{Eq. 2}$$

Normal stresses occupy the diagonal σ_{11}, σ_{22} and σ_{33}. The rest of the components comprise the shear stresses. Assuming a stress state where opposite forces are of equal magnitude, this cancel each other leaving six independent components (Fossen, 2010; Hudson & Harrison, 1997). Considering this, in the stable situation where forces are balanced:

$$\sigma_{xy} = -\sigma_{yx}, \sigma_{yz} = -\sigma_{zy}, and\ \sigma_{xz} = -\sigma_{zx} \quad \text{Eq. 3}$$

Being a symmetric matrix implies that changing the rows to columns will not change the matrix but will change according to the coordinate system rotation and orientation. If the rotation happens until the shear stresses are zero, then normal stresses are left with non-zero values. These are called the principal stresses (Fig. 3). The Earth's surface is a principal stress plane since it is in contact with fluids and the atmosphere which cannot withstand shear stresses (Zoback 2007)

$$\begin{bmatrix} \sigma_{11} & 0 & 0 \\ 0 & \sigma_{22} & 0 \\ 0 & 0 & \sigma_{33} \end{bmatrix} = \begin{bmatrix} \sigma_1 & 0 & 0 \\ 0 & \sigma_2 & 0 \\ 0 & 0 & \sigma_3 \end{bmatrix} \quad \text{Eq. 4}$$

In other cases when the principal stress tensor is not in the principal stress axis, one can calculate the eigenvector and eigenvalues of the matrix, that correspond to the principal stress vectors and magnitudes respectively. These values remain the same over different coordinate systems (Zoback 2007; Fossen 2010).

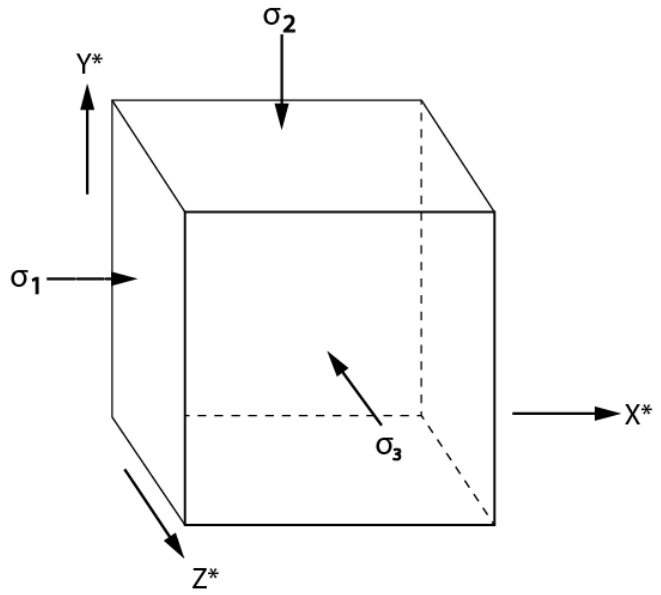

Fig. 3 Principal stresses as defined in a coordinate system in which shear stresses vanish. After (Zoback 2007)

2.1.2.1 Normal and shear stress

If the acting force is not perpendicular to the surface, it can be decomposed. A normal stress is that which acts perpendicular to a surface, whereas a shear stress is a tangential component which acts parallel to such surface (Fig. 4) (Fossen, 2010). Solids on the contrary to liquids and gases, can sustain such forces (Hudson & Harrison, 1997). For this case, each of the components of the stress tensor will have a defined magnitude.

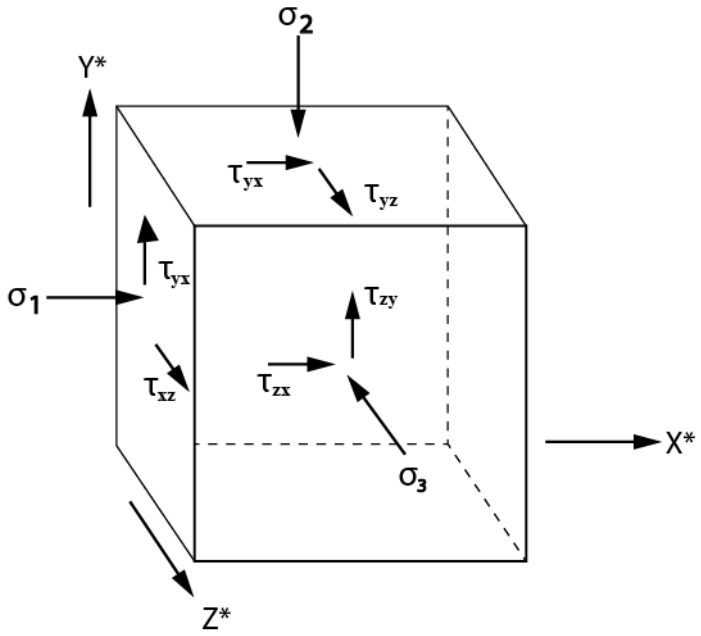

Fig. 4 Decomposition of stress acting on a surface in normal and shear components. After (Zoback 2007).

2.1.3 Deviatoric and mean stress

The deviatoric and mean stress calculation is a useful decomposition of the stress tensor that can account for the isotropic and anisotropic components of stress (Eq. 5). The mean stress σ_m corresponds to the arithmetic mean of the three principal stresses. The mean stress is also known as the hydrostatic pressure or hydrostatic stress and in the lithosphere is closely related to the lithostatic stress, which is controlled mostly by the burial depth and the density of the overlaying sediments (Fossen, 2010). The effects of the isotropic stress are inflation or deflation, also referred as dilation.

The deviatoric stress corresponds to the difference between the mean stress σ_m and deviatoric stress. Deviatoric stress is smaller than the isotropic is responsible for the generation of strain (Fjaer et al., 2008; Fossen, 2010). In contrast with the mean stress is magnitude is not equal in all directions, therefore is an anisotropic component (Jaeger et al., 2007)

$$\begin{bmatrix}\sigma_{11} & \sigma_{12} & \sigma_{13}\\ \sigma_{21} & \sigma_{22} & \sigma_{23}\\ \sigma_{31} & \sigma_{32} & \sigma_{33}\end{bmatrix}=\begin{bmatrix}\sigma_m & 0 & 0\\ 0 & \sigma_m & 0\\ 0 & 0 & \sigma_m\end{bmatrix}+\begin{bmatrix}\sigma_{11}-\sigma_m & \sigma_{12} & \sigma_{13}\\ \sigma_{21} & \sigma_{22}-\sigma_m & \sigma_{23}\\ \sigma_{31} & \sigma_{32} & \sigma_{33}-\sigma_m\end{bmatrix} \quad \text{Eq. 5}$$

Total stress tensor = isotropic component + anisotropic component

2.1.4 Stress invariants

Stress invariants (Eq. 6-Eq. 8) are stress combinations that are independent of the coordinate axes and have the same value in all coordinate systems, since the three principal stresses, which are functions only of these three invariants, and which have a clear physical meaning that is independent of the choice of coordinate system, must themselves be invariant (Fjaer et al., 2008; Jaeger et al., 2007).

$$I_1 = \sigma_1 + \sigma_2 + \sigma_3 \quad \text{Eq. 6}$$

$$I_2 = -(\sigma_1\sigma_2 + \sigma_2\sigma_3 + \sigma_1\sigma_3) \quad \text{Eq. 7}$$

$$I_3 = (\sigma_1\sigma_2\sigma_3) \quad \text{Eq. 8}$$

2.1.5 In-situ Stress

In-situ stress refers to the stress description at an arbitrary point of the material. There are two fundamental targets of *in-situ* stress determination (Hudson & Harrison, 1997):

- To understand the principal stresses acting direction and magnitude and which potential effect may derive from its disturbance.
- To have specific formal knowledge of the boundary conditions for stress analysis conducted in engineering design.

Normally the stress tensor can be defined through six parameters. In geosciences, the in-situ stress state in the subsurface can be often represented in a more practical way, through a simplification of the stress tensor as analysed in a principal coordinate system (as presented in section 2.1.2). In this case, shear stresses disappear and the definition changes from six components, to the magnitudes of

the three normal acting stresses, known as principal stresses, in addition to an orientation. The surface of the Earth is a principal plane, therefore it is a fundamental assumption that one of the stresses is vertical to the horizontal plane (Zoback, 2007).

This assumption is commonly accepted for subsurface depth of approximately >100 m and have been successfully proven in many occasions. However, it may not be 100% accurate for every geological setting. Stress state can vary when it interacts with different variables at surface levels, as are temperature variations, topographical irregularities, among others. Another case of this assumption differing from reality has been observed around salt structures. Salt creeps and is a weak material which cannot support shear stresses. The interface between rock an salt is an irregular free surface that become a new principal plane and therefore reorients stresses normal to the surfaces (Zoback, 2007; Zoback et al., 2003)

There are different ways to obtain the magnitudes that will fill in the stress tensor components. The International Society of Rock Mechanics (ISRM) specifies four direct measurement methods: (1) the flat-jack test, (2) the hydraulic fracturing test, (3) the United States Bureau of Mines (USBM) over coring torpedo and (4) the Commonwealth Scientific and Industrial Research Organization (CSIRO) overcoming gauge (Christiansson & Hudson, 2003; Haimson & Cornet, 2003; Hudson, Cornet, & Christiansson, 2003; Hudson & Harrison, 1997). These methodologies hold the lowest uncertainty. Each of these methods may define one or more components of the stress tensor with one application orientation. A full tensor description will require different application directions, which is not always possible (Fig. 5). While all these methods are widely used in civil and mining engineering, hydraulic fracturing is a preferred method to constrain two main parameters in the subsurface for hydrocarbon reservoirs: the *breakdown pressure* (σ_1), and the *shut-in pressure* (σ_3). In addition, some indirect methods useful for geomechanical characterization in the subsurface include: borehole breakouts, fault plane back-analysis, acoustic emission, differential strain, geometry of stress-induced core fracturing (Hudson & Harrison, 1997).

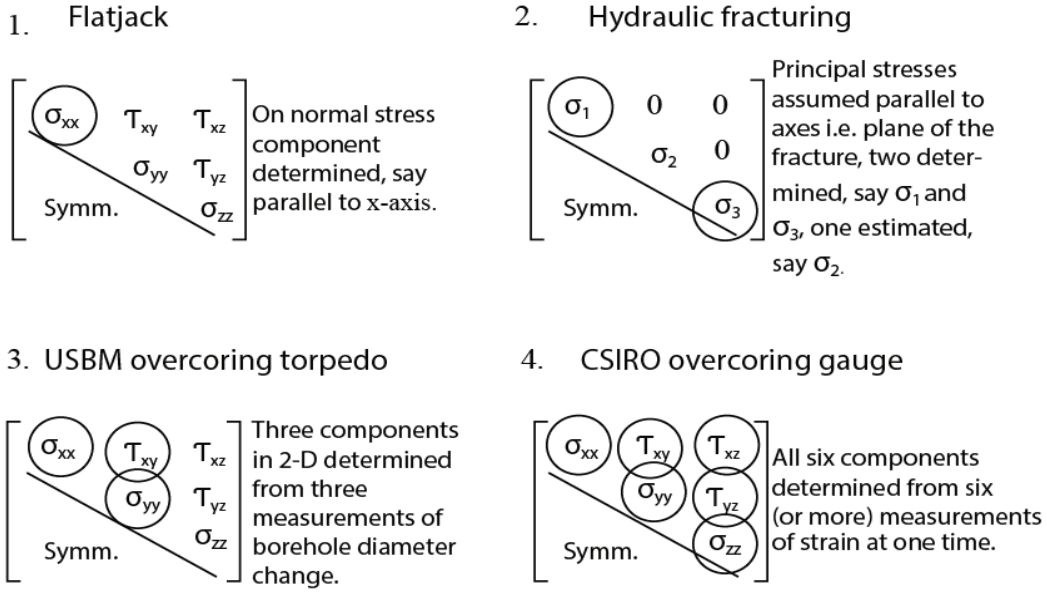

Fig. 5 The four ISRM suggested methods for rocks stress determination and their ability to determine the components of the stress tensor with one application of the method. After (Hudson & Harrison, 1997)

2.1.6 Deformation and constitutive models

Rock responds to stress differently depending on the pressure, temperature and mineralogical composition of the rock (Fossen, 2010). The change in the relative configuration of points within a solid is known as *strain,* represented in the same way as stresses, with a strain tensor (Hudson & Harrison, 1997). A constitutive law correlates two physical quantities, and in this case, a rock constitutive model describes the deformation of a rock in response to an applied stress (Zoback 2007).

Deformation of a rock can be reversible or elastic, to permanent (non-reversible) or plastic before reaching failure. The stress-strain curve, as the one presented in Fig. 6, is a graphical aid derived from laboratory tests and it is different for different materials. As an external load is applied, a curvature may generate due to micro-fracture closing. From this point there is a linear elastic behaviour. This behaviour continues until the applied stress becomes large enough for the rock to sustain it and deformations become plastic or irreversible. The threshold point between the elastic and plastic behaviour is known as yield strength (onset of inelastic behaviour). Whether a material is in one or the other region, design and resulting parameters will be different.

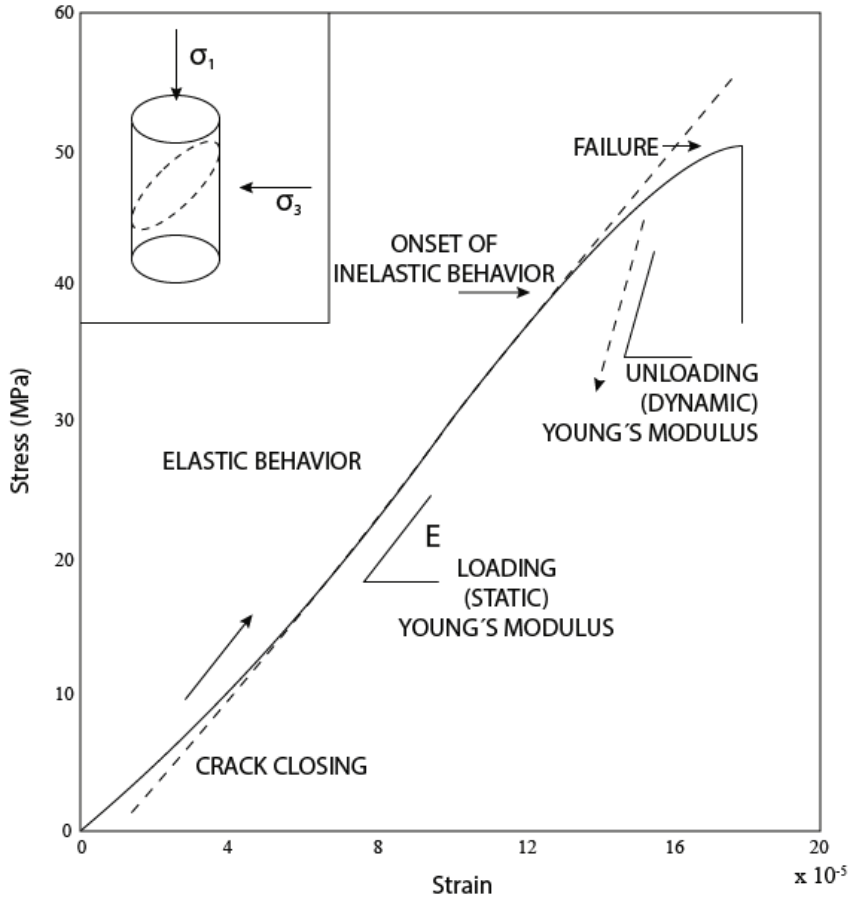

Fig. 6 Stress-strain curve for a well cemented rock being deformed uniaxially. The curve is a graphical representation of the existing relation between applied stress and resulting strain as related by a factor known as the Young's modulus. Commonly represents the elastic and plastic regions and key points along the curve. Different materials have different curves. Modified after (Zoback, 2007)

2.1.6.1 Linear elasticity

A linear elastic behaviour refers to the possibility of a rock to return to its original state after the stress action is over. It relates linearly stress and strain and is the most widely used relationship in practice. Nevertheless, rocks naturally behave following non-linear trends, considering its heterogeneous nature. The linear simplification is assumed to be accurate for small incremental stress changes (Fjaer et al. 2008; Jaeger et al. 2007). If the stress could be reversed, the rock would return to its original shape since they are proportional (Zoback 2007). Additionally, in this case, the material is treated as homogeneous, solid material (Fjaer et al., 2008). Considering an isotropic material (i.e., whose response to external forces is independent to the orientation of such force), the linear relation can be described using Eq. 9, which is known as the Hooke's law (Fjaer et al., 2008; Fossen, 2010). Coefficient E is known as Young's modulus, which is a measure of the stiffness of a rock sample. The greater the Young's modulus, the higher are the stresses the material can stand (Fischer, 2013; Fjaer et al., 2008).

$$\varepsilon_x = \frac{1}{E} \cdot \sigma_x \qquad \text{Eq. 9}$$

ε_x=one-dimensional strain; E=Young's modulus; σ_x=Stress in x-direction

In two and three dimensions, an additional deformation of the sample occurs as a lateral expansion relative to longitudinal contraction, known as the Poisson effect, represented by the negative ratio between transverse strain and axial strain. For rocks, Poisson's ratio is typically 0.15–0.25. For weak, porous rocks *v* may approach zero or even become negative (Fjaer et al., 2008).

$$\upsilon = -\frac{\varepsilon_y}{\varepsilon_x} \qquad \text{Eq. 10}$$

ε_x=strain in x-axis; ε_y=strain in y-axis; υ=resulting Poisson's ratio

Young's modulus (E) and Poisson's ratio (υ) are part of a group of coefficients known as the *elastic moduli* intending to represent the sample resistance or compliance to an imposed load. Among these coefficients, there are the Lame's parameters λ (Eq. 11) and μ (Eq. 12), also known as the shear modulus. When two of the moduli are defined, the rest can be easily estimated through coefficient correlations (Fjaer et al., 2008).

$$\lambda = \frac{2G\upsilon}{1-2\upsilon} = K - \frac{2G}{3} = \frac{E\upsilon}{(1+\upsilon)(1-2\upsilon)} \qquad \text{Eq. 11}$$

$$\mu = G = \frac{E}{2(1+\upsilon)} = \frac{3K(1-2\upsilon)}{2(1+\upsilon)} \qquad \text{Eq. 12}$$

υ=Poisson's ratio, E=Young's modulus

The stress-strain relations can be expressed in a compact manner using the index notation as in (Eq. 13) (Cheng, 2016; Fjaer et al., 2008):

$$\sigma_{ij} = \lambda\varepsilon_{vol}\delta_{ij} + 2(\frac{E}{2+2\upsilon})\varepsilon_{ij} \quad \text{Eq. 13}$$

i, j=x, y, z; σ_{ij} = stress tensor; ε_{ij} = strain tensor; E = Young's modulus; ν = Poisson's ratio; ε_{vol} = volumetric strain, δ_{ij}=Kronecker symbol

2.1.6.2 Poro-elasticity and effective stress

Natural materials like rocks, such as rocks or biological tissue and some artificial ones like paper or concrete are composite materials, inhomogeneous and have a porous structure. Specifically for geomaterials, the irregular accommodation of grains resulting from random and complex geological processes will leave voids within any volume of rock, which can be penetrated by fluids, affecting its response to external alterations (Cheng, 2016; Fjaer et al., 2008). The poroelastic theory describes the hydro-mechanical interaction between fluids and solids deformation within the porous media and is based on the Biot's theory (Detournay & Cheng, 1993).

The void fraction of a rock volume contributes to the resistance against applied stress, alongside the fluid fraction and the solid fraction, but in minor proportion. When an external load is applied, the fluid-filled pores experience a change in pressure under this mechanical stress, which, in turn, leads to fluid motion (Comsol, 2014). By assigning an apparent strength to the pore space, the composite nature of the rock volume is taken into account (Cheng, 2016). As a reaction to this change in pore volume, the solid material shifts and deforms elastically.

The formulation for an isotropic, porous and permeable material is similar to Eq. 13, but in this case, there is an extra kinematic variable added so that the total stress tensor is not dependent only on the total strain tensor but also on the variation of fluid content (Eq. 14) (Fjaer et al., 2008). This formulation is independent of the load history (deformation or stress path).

$$\sigma_{ij} = \lambda\varepsilon_{vol}\delta_{ij} + 2\mu\varepsilon_{ij} - C\zeta\delta_{ij} \quad \text{Eq. 14}$$

C=Additional elastic modulus to describe two-phase medium; ζ=strain parameter

The additional strain parameter ζ (Eq. 15) describes the volumetric deformation of the fluid relative to the deformation of the solid and can be derived from the change in pore volume (because of the change in external stresses) and the compression/decompression of the fluid. ζ is positive when the amount of fluid in the volume element is decreasing (Fischer, 2013; Fjaer et al., 2008)

$$\zeta = -\phi(\frac{\Delta V_p}{V_p} + \frac{P_f}{K_f}) \quad \text{Eq. 15}$$

ϕ= porosity; Vp=Pore volume; Kf=Bulk modulus of the pore fluid and Pf= pore pressure

The additional elastic modulus C , is necessary to describe a two-phase medium and can be described through relations among the elastic modulus of the rock constituents (Fjaer et al., 2008). This equation is derived from the known Biot-Gassmann equation (Fischer, 2013; Fjaer et al., 2008).

Effective stress concept

When the external loads are applied on a time-stepped manner and, conditioned by the permeability of the sample, the fluid cannot escape out of the rock volume, leaving a condition known as an *undrained* sample. The entire load is sustained in part between the solid fraction of the rock volume (σ'_{ij}) and the remaining fraction by αP_f. The concept is based on Terzaghi (1923) and his empirical work on soil mechanics. The so-called "simple" or Terzaghi definition of effective stress is described by (Eq. 16) (Zoback 2007)**.**

$$\sigma'_{ij} = \sigma_{ij} - \delta_{ij}\alpha P_f \qquad \text{Eq. 16}$$

Where the parameter δ_{ij} is the Kronecker symbol and alpha (α) is known as the Biot coefficient (Eq. 17) (Biot & Willis, 1957; Nur & Byerlee, 1971). For soils, $\alpha = 1$ is a reasonable assumption, while for rocks, the deviation of α from 1 should be considered.

$$\alpha = 1 - \frac{K_{fr}}{K_s} \qquad \text{Eq. 17}$$

Where K_{fr} correspond to the elastic modulus of the framework and K_s correspond to the bulk modulus of the solid. This general concept implies that the effective stress, rather than the total stress is determining whether the rock fails or not when exerted an external load (Fjaer et al., 2008).

2.1.6.3 Plastic deformation and failure analysis

Plastic deformation refers to a type of deformation which effect may not be reversed once the external force stops acting upon a rock volume. The inelastic behaviour is known as plasticity, when it does not depend on the deformation rate or viscoelasticity when is explicitly time-dependent (Jaeger et al., 2007). The threshold, in which the deformation turns irreversible, is known as yield point or yield strength (Fig. 6). Depending on the rock's ability to withstand stresses beyond the yield point, behaviour can be ductile or brittle.

Four major concepts are the basis for the plasticity theory (Fjaer et al., 2008): (1) Plastic strain associated with a stress increment that yields to plastic deformation (Eq. 18). The total strain consists of an elastic fraction, which disappears as the stress is released and a plastic fraction that implies a non-recoverable deformation (Eq. 18). (2) A yield criterion that defines the surface in stress space where plasticity is initiated. (3) A flow rule that describes the development of plastic strain for a given load. (4) A hardening rule that describes how the rock can sustain increasing load after the initial plastic failure, which is interpreted as a change of the yield surface in principal stress space.

$$d\varepsilon_{ij} = d\varepsilon^e{}_{ij} + d\varepsilon^p{}_{ij} \qquad \text{Eq. 18}$$

The behaviour of a sample is called ductile or brittle, depending on whether the rock sample deforms by bending and flowing or breaking into pieces and will correspond to larger or smaller elastoplastic region, respectively. The curve in the elastoplastic region of the same sample strongly depends on temperature and the speed of deformation (Hantschel & Kauerauf, 2009).

Plastic flow

Plastic flow occurs from the onset of yielding until the critical state is reached while critical state indicates damage and the inability of the specimen to support stresses (Hantschel & Kauerauf, 2009). A plastic flow rule describes the development of the plastic strain increments and considers the plastic fraction of the total strain.

$$d\varepsilon^{p}{}_{ij} = d\lambda \frac{\partial f}{\partial \sigma_{ij}} \qquad \text{Eq. 19}$$

λ=hardening parameter

When the plastic flow is derived from the yield criterion is called an associated flow rule, whereas when it is derived from the general plastic potential is known as a non-associated flow rule (Fjaer et al., 2008; Jaeger et al., 2007).

2.1.6.4 Brittle behaviour

Shear failure

Shear failure occurs when the shear stress along some plane in the sample is sufficiently high. The threshold that needs to be exceeded is known as shear stress (τ_{max}) and is dependent on the stress (σ) acting on the failure plane, as stated in the Mohr's hypo thesis (Fischer, 2013; Fjaer et al., 2008). The displacements of one plane with respect to another makes shear failure the defining mechanism of fault zones.

$$|\tau_{max}| = f(\sigma) \qquad \text{Eq. 20}$$

Eq. 20 defines the limit between a safe and an unsafe zone of failure, and it represents the failure surface or failure envelope, in the τ- σ plane. As the maximum and minimum principal stresses vary, as it would if the sample can drain, they may get further or closer to the failure envelope (Fig. 7).

The relation between the normal and shear stress combination that cause the shear failure is given by Eq. 21. The constant *C* corresponds to *the inherent shear strength*, or cohesion. The resulting criterion is called the Tresca criterion. It states that yielding will begin when the maximum shear stress at a point is equal to the stress at yield when subjected to uniaxial tension or compression (Fjaer et al., 2008). No circle can exceed the failure line in size since this would represent a state of stress the rock cannot sustain (Fjaer et al., 2008)

$$\tau_{max} = \frac{1}{2}(\sigma_1 - \sigma_3) = C \qquad \text{Eq. 21}$$

Derived from these premises, is the Mohr-Coulomb failure criterion, also known as the generalised Tresca criterion or the Navier-Coulomb criterion (Eq. 22). The parameter μ corresponds to the internal friction coefficient which is related to the angle of internal friction by $tan\,\varphi = \mu$.

$$\tau_{max} = C + \mu\sigma \qquad \text{Eq. 22}$$

This criterion represents an inclined failure line in the τ – σ plot, whose slope is defined by angle of internal friction and that intercepts the τ – axis at C (Fjaer et al., 2008). If one of the points of the Mohr's circle is in contact with the envelope, then the material is said to have failed. The state of failure is conditioned by the minimum and maximum principal stress, and the intermediate principal stress does not affect the shear behaviour as it is between the range of $\{\sigma_1 - \sigma_3\}$ and $\sigma_2 = 0$ (Jaeger et al., 2007). The point of tangency of the envelope to the Mohr circle at failure gives a clue to the determination of the inclination of the failure plane (2ß). The orientation of the failure plane can be finally determined by the pole method (Goodman, 1989).

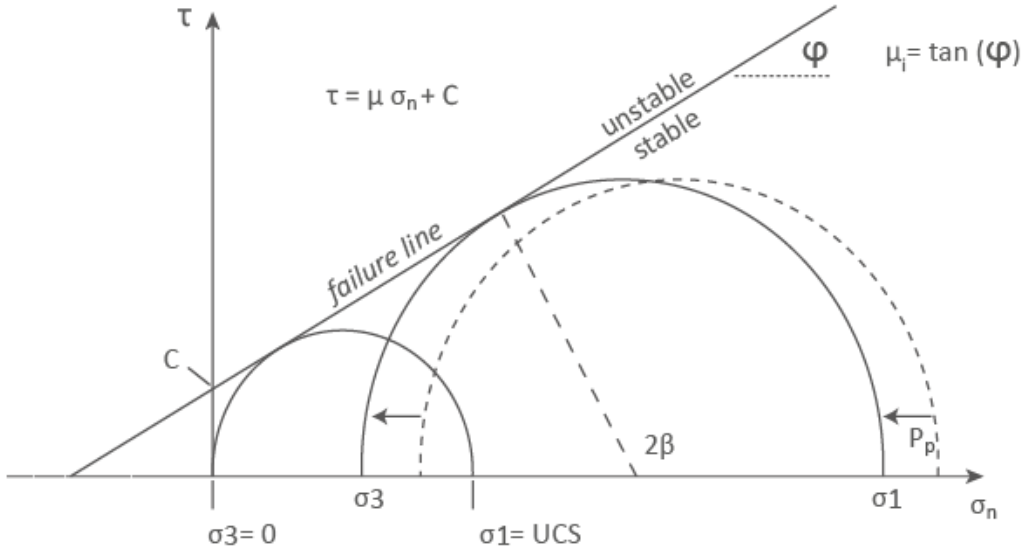

Fig. 7 Mohr–Coulomb criterion in τ–σ space. Slope of the line is driven by the coefficient of internal friction. Effect of decreasing pore pressure causes a shift of the Mohr circle closer to the failure boundary. After (Fjaer et al., 2008).

It has been tested experimentally that for 3D shear conditions, the intermediate principal stress does have an effect on the material failure, even though this is often minor with respect to other principal stresses (Fjaer et al., 2008). Nevertheless, some valid models were developed before the concept was clear. When considering a three-dimensional case, it is necessary to address the dependency on the intermediate principal stress.

Considering the advances in the knowledge of the intermediate stress effect, new models were proposed. One of these models is the Von Mises criterion (Eq. 23). The constant C is related to material cohesion. In the principal stress, plane is represented by a cylinder centered on the hydrostatic axis. The von Mises criterion is commonly used to describe yield in metals, and its application on geomaterials is somewhat limited (Fjaer et al., 2008).

$$(\sigma_1 - \sigma_2)^2 + (\sigma_1 - \sigma_3)^2 + (\sigma_2 - \sigma_3)^2 = C^2 \qquad \text{Eq. 23}$$

Another proposal is the generalization of the Mohr-Coulomb criteria, known as the Drucker-Prager criterion (Eq. 24). C_1 and C_2 are coefficients related to the cohesion and internal friction of the material. In the principal stress plane, the Drucker-Prager criterion surface corresponds to a cone (Fig. 8). The Drucker-Prager model (sometimes addressed as the extension of the Von Mises model) modifies the Mohr-Coulomb fluency function to avoid singularities associated with the corners.

$$(\sigma_1 - \sigma_2)^2 + (\sigma_1 - \sigma_3)^2 + (\sigma_2 - \sigma_3)^2 = C_1(\sigma_1 + \sigma_2 + \sigma_3 + C_2)^2 \qquad \text{Eq. 24}$$

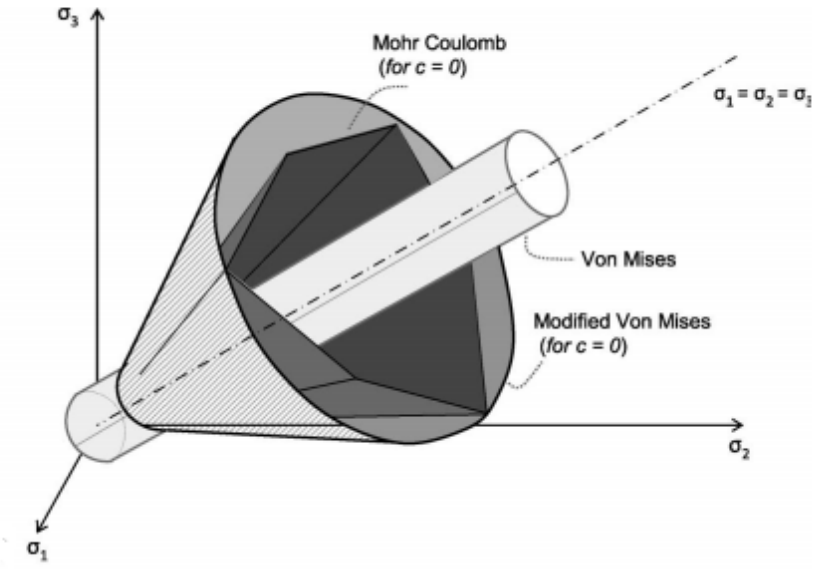

Fig. 8 The Von-Mises criterion, the Mohr-Coulomb and the modified Von-Mises criterion or Drucker-Prager model. After (Anastasopoulos et al., 2011).

Tensile failure

Tensile failure occurs when the effective tensile stress across some plane in the sample exceeds a critical limit called the tensile strength (T_o). It is common for geomaterials to have low tensile strength, which is why is often negligible (Fjaer et al., 2008). However, its characterization is becoming increasingly relevant for hydraulic fracturing purposes in unconventional resources. Tensile failure commonly occurs along pre-existing micro-cracks planes and is a localized event. The tensile strength of rocks obtained from hydraulic fracture experiments in solid rocks is commonly from 0.5 to 6 MPa, with a maximum value of about 9 MPa (Gudmundsson, 2011). The failure criterion is defined by Eq. 25. In Isotropic rocks it is conditioned by the minimum principal stress.

$$\sigma'_3 = -T_o \qquad \text{Eq. 25}$$

2.1.7 Discontinuities

Brittle deformation occurs when the ultimate strength of a rock is exceeded causing the material to fracture. Some physical evidences of such behaviour are fractures and faults. A fracture is commonly defined as any separation in a geologic formation, such as a joint or a fault that divides the rock into two or more pieces. On a small scale, when there is shear small displacement, the term used is fractures, whereas for large scale or massive displacement the term used is fault. Fractures act as preferred drainage conduits for hydrocarbon extraction as there is a permeability enhancement given the connectivity of pores. For this reason, is common that fractures are induced artificially to promote permeability enhancement in tight target units (Li et al., 2015). Common fracture occurrence models are based on the Griffith theory, which is an extension of failure models to address failure in compressive regime (Gudmundsson, 2011). The behaviour of a fractured rock depends both on the

properties of the fractures and on the properties of the intact rock. Generally, fractured rocks will be much weaker than the corresponding intact rock, as the resistance against shear failure is considerably less for an already existing fracture (Fjaer et al., 2008).

2.1.7.1 Fractures

As stated in Fossen (2010), "a fracture is any planar or sub-planar discontinuity that is very narrow in one dimension compared to the other two and forms as a result of external (e.g. tectonic) or internal (thermal or residual) stress". Fractures can be addressed as shear fractures (slip surfaces), opening fractures (joints), fissures and veins or compaction fractures (stylolite). Joints are those that have little to none extensional displacement and can be filled with gas, fluids, magma, or minerals. Strength of the rock depends on confining pressure or burial depth (Fossen, 2010) but the overall strain response to external forces will be conditioned by the discontinuities of the rock mass. The mathematical description of the threshold of fracture generation and propagation are further explained in (Gudmundsson, 2011; Hoek & Martin, 2014; Nelson, 2001).

Depending on the failure kinematics (that is, the relative movement of the two surfaces of the crack), three fracture modes are often distinguishable: (1) Mode I: cracks or opening cracks- tensile mode; (2) Mode II: slip surfaces parallel to the edge of the crack and (3) Mode III: slip is parallel to the edge of the crack. Fractures in nature are a result of a combination of fracture modes. These ideal displacement models apply to pure extension and pure shear fractures (Fig. 9). However fractures in nature interact with different environmental conditions and the movement may behave in hybrid or mixed-modes (Gudmundsson, 2011; Hudson & Harrison, 1997).

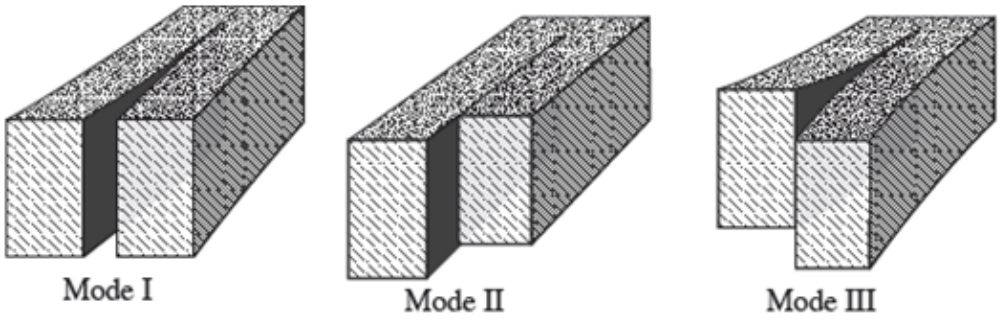

Fig. 9 Fracture opening modes I, II and III. (Fossen, 2010)

Fracture initiation requires a differential stress ($\sigma_1 - \sigma_3$) that exceeds the strength of the rock. If there is no differential stress, then the state of stress is lithostatic and there is no force pulling or pushing a rock volume in any direction. The physical stress conditions under which these three types of fractures develop are illustrated by the Mohr diagram in Fig. 10. Likewise, the Coulomb envelope, the Mohr's failure envelope illustrates the limit states of stresses over a range of differential stresses but regardless of whether they obey the Coulomb criterion. The envelope is individual for each rock type and is obtained through experimental rock fracturing. In some cases, the Coulomb fracture criterion is a reasonably good approximation for a certain stress interval, and in other cases the envelope is clearly nonlinear. It is common for the envelope to flatten as the ductile regime is approached. In fact, the ductile regime can be approximated by a constant shear stress criterion (horizontal envelope), known as the von Mises criterion (Fossen, 2010). The tensile regime is well described by the Griffith's theory of fracture (Fossen, 2010; Hoek & Martin, 2014)

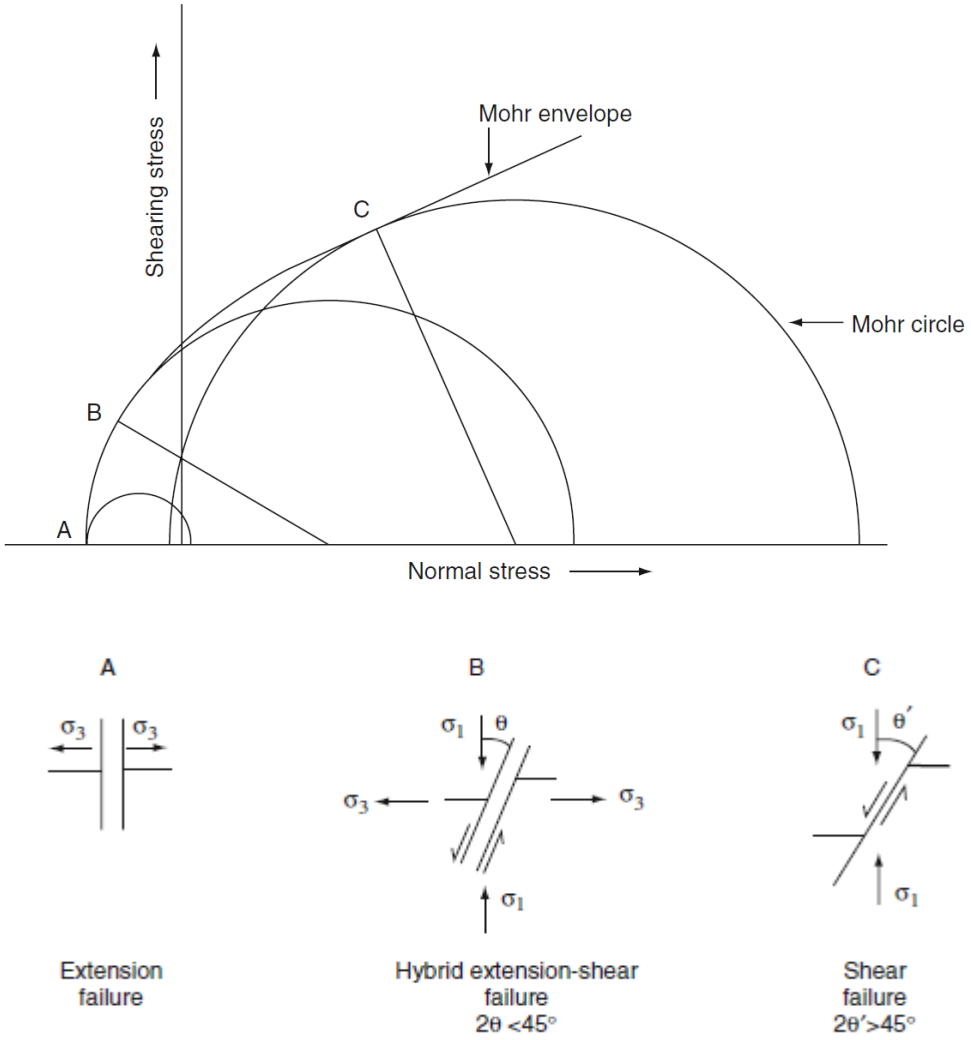

Fig. 10 Mohr diagram indicating the stress conditions for tensile and shear rock failure. After (Singhal & Gupta, 1999). The curve ABC is a Mohr envelope. The stress circles touching the Mohr envelope at A, B and C points indicate different failure conditions of the rock.

Shear fractures

A shear fracture refers to a fracture whose relative movement is parallel to the fracture. These type of fractures are generated in acute angles (>0° and <90°) with respect to the maximum stress (σ_1) and in obtuse angles (>90° and <180°) with respect to the minimum stress (σ_3) within a rock mass (Fig. 11). Shear fracture generate under compressive stress action. The acute angle between two shear fractures planes if known as conjugated angle and is mostly conditioned by (1) mechanical properties of the rock mass, (2) the absolute magnitude of the minimum stress (σ_3) the relative magnitude of the intermediate stress (σ_2) with respect to σ_1 and σ_3 (Nelson, 2001).

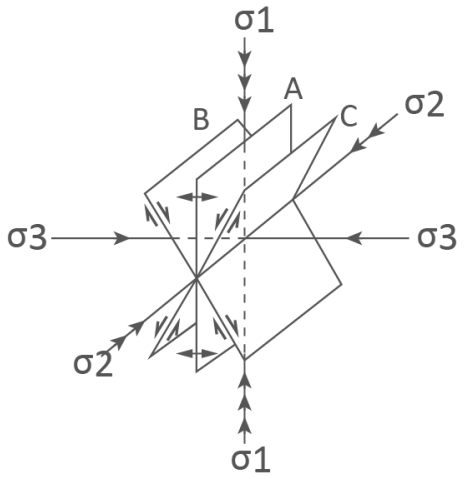

Fig. 11 Fracture planes development after compressive tests in laboratory. After (Nelson, 2001)

Tensile fractures

Tensile fractures are generated parallel to the maximum and intermediate stresses (σ1, σ2). One of the principal stresses must be negative, which normally is σ3. There is a clear distinction between *extension* and *tensile* fractures event though their name suggests the same behaviour. Extension fractures occur normally when the three principal stresses are compressive, whereas tensile behaviour explicitly points a negative principal stress.

Hybrid fractures

Hybrid fractures exhibit features of both shear and dilatational origin. They may occur in conjugate sets, they are open, may be partly filled with veins, and may also exhibit some shear displacement (Singhal & Gupta, 1999). These types of fractures are best modelled as mixed-mode cracks. However, even for mixed-mode fractures, one mode may be dominant (Gudmundsson, 2011)

Tectonic fractures

Fractures can be associated with two main deformation events (among other mechanisms), fault generation and folding. A fault-related fracture system refers to shear or tensile fractures in the vicinity of a fault surface. Experimentally, such fractures develop under the same stress field causing the fault. Because of this correlation, it is possible to determine the orientation of principal stresses at the time of a fracture formation. However, the generation of fractures is influenced by the lithology, the distance with respect to the fault plane, strain state, depth of burial and the type of fault. The governing variable inducing fractures is specific for each geological setting. On the other hand, fold-related fractures are those associated with the shearing and flexural mechanisms that deform a rock layer (Kolo et al., 2015). Fracture intensity is often higher at the vicinity of the fold axis and decrease towards the flanks. To accurately assess stress orientation at the time of fracture formation, tectonic history modelling methods have been implemented (Grover et al., 2016; Lefranc et al., 2014) .

2.1.7.2 Faults

A fault is a conventionally large-scale, approximately planar fracture on which a relative displacement has occurred (Jaeger et al., 2007). The dynamic movement relation of faults can be classified as

normal, reverse, transform and strike–slip faults, although most of the faults are mixed mode faults (Hantschel & Kauerauf, 2009). In areas with large structural deformation faults may severely impact production performance. Reservoir characterization of faults can be done at field scale or well scale and will depend on the development stage. Mechanical characteristic of fault formation and reactivation provide key insights of the stress state of an area. Faults can be of critical importance for specific production cases and its effects can be amplified on low-permeability or overpressured formations. Also, faults can act as reservoir seals, and contrary to the mentioned enhancements, hinder the production performance. Displacement reactivation associated with production can lead to major compaction and subsidence of the subsurface. Currently, the general public concern relates to the generation of man-induced earthquakes (Rutqvist et al. 2013; Dahm et al. 2010).

2.1.7.3 Tectonic stress regimes

The "*Andersonian"* classification of faults stands under the assumption that given the interaction of rocks with fluids and gas, and the fact the in the later shear stresses cannot occur. Therefore, one of the principal stresses can be assumed as vertical and the other two as horizontal. According to this theory, fracture takes place in one or both of a pair of conjugate planes that pass through the direction of the intermediate principal stress and are equally inclined at an angle less than 45° from the direction of the maximum principal stress (Jaeger et al., 2007).

The theory classifies an area as being characterised by normal, strike-slip or reverse faulting based on whether (i) the crust is extending and steeply dipping normal faults accommodate movement of the *hanging wall,* (ii) blocks of crust are sliding horizontally past one another along nearly vertical strike-slip faults or (iii) the crust is in compression and relatively shallow-dipping reverse faults are associated with the hanging wall block moving upward with respect to the footwall block (Zoback 2007) (Fig. 12).

The vertical stress, S_v, is the maximum principal stress (S_1) in normal faulting regimes, the intermediate principal stress (S_2) in strike-slip regimes and the least principal stress (S_3) in reverse faulting regimes (Fossen, 2010; Zoback, 2007). The definition of which stress is greater is defined by specific geological settings (Zoback 2007).

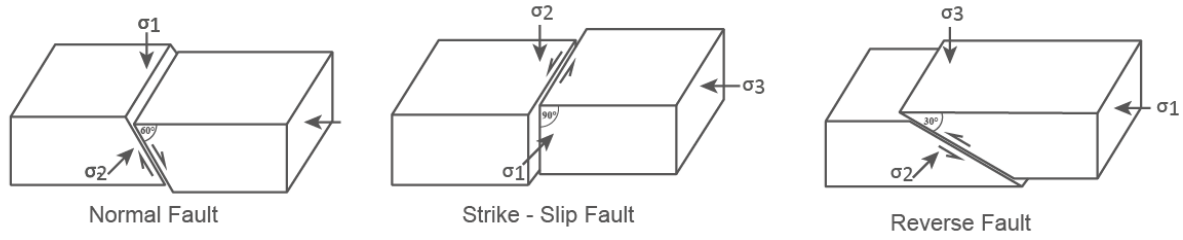

Fig. 12 Diagram of three of the main tectonic regimes as proposed by Anderson (1905).

2.2 Pore pressure

Pore pressure evaluation intends to identify in each depth interval, the behaviour of the stresses exerted by fluids in the rock. Pore pressure is one of the key variables of this study. Its interaction with rock stress and intricate phenomena controls the compaction behaviour of a formation.

The normal pressure resulting exerted by a column of water at a specific depth is known as the *hydrostatic pressure* (Pp-hydro) (Eq. 26). Hydrostatic pressure depends on the fluid density, which in turn depends on the concentration of dissolved solids, for salt is the most essential solid. Formation

water salinity depends on a number of factors including connate water history[1], temperature, diagenesis, salt proximity and osmosis (Fertl, 1976, Zoback 2007).

$$P_p^{hydro} = \int_0^z \rho_w(z) g dz \approx \rho_w g Z_w \qquad \text{Eq. 26}$$

P_p^{hydro}= pressure, ρ_w= average water density, g= gravity value; Z_w = height of water column.

Often, variations with respect to the hydrostatic pressure can be caused by a combination of factors and given this non-unique behaviour is an analysis that requires high detail. Most of the drilling design is based on a pore pressure prediction magnitude. A wrong prediction can lead to hazardous situations and incur in non-productive times (NPT). Considering its magnitude pore pressure can be classified like: normal, abnormal, and subnormal, depending upon whether the pore pressure is equal to, greater than or less than the hydrostatic pressure at the given depth (Fertl, 1976; Kesarwani et al., 2013).

Pore pressure at a specific depth represents the average scalar value of that acting within an interconnected pore space and is normally used to address pressures that are not compliant with the hydrostatic pore pressure. Conceptually, the upper bound for pore pressure is the *overburden pressure* (overburden stress), which is the stress excerpted by the overlying rocks at a specific depth by rocks and fluids. Because of the minimum tensile strength of rocks, pore pressure will always be less than the least principal stress, and may sometimes be limited by leakage along faults (Baker Hughes 1993; Zoback 2007).

Abnormally pressured rocks are those that have pore pressures significantly higher than hydrostatic (overpressured), or less than hydrostatic (underpressured). If the fluid cannot escape the pore, pore pressure begins to increase at a *faster-than-normal* rate, causing the abnormal trend (Fertl, 1976). Hydrostatic pressures, pressures in equilibrium with the free water level near the surface, are approximately 10Kpa/Km or 0.43psi/ft (Fertl, 1976). Reservoir engineers are interested in fluid gradients. Water has a fluid gradient of 0.43-0.54psi/ft (1.00sg). Oil and gas are lighter and have much steeper pressure gradients, particularly gas.

Burial records alongside thermal history are relevant tools in the analysis of the potential of a basin to generate oil and gas, as well as useful towards the estimation of porosities and permeabilities and consequent inference of overpressure generating mechanisms (Allen & Allen, 2013). Over the years more than a dozen mechanisms have been proposed (Fertl, 1976; Gluyas & Swarbrick, 2004; Hantschel & Kauerauf, 2009; Zhang, 2011). Burial or tectonic stress is a primary overpressure-generating mechanism, particularly in rapidly subsiding basins and active tectonic areas. Vertically, the governing process would be mechanical compaction, whereas horizontally would imply tectonic stresses (Hantschel & Kauerauf, 2009; Swarbrick, Osborne, & Yardley, 2002). Progressive burial of sediment by overlying layers during basin evolution causes several physical and chemical changes to the basin-fill. Thermal and diagenetic changes can generate overpressure in-situ when thermal and

[1] *Connate water*: Water trapped in the pores of a rock during formation of the rock.

chemical conditions allow. Some mechanisms may include Burial metamorphism, kerogen conversion and hydrocarbon generation (Dutta, 2016).

Once generated, overpressure wants to equilibrate back to hydrostatic condition. In this way, fluid redistribution in permeable zones can locally alter the overpressures (Doornhof et al., 2006) . Some mechanisms may include: Lateral transfer of fluids, hydrocarbon buoyancy, hydraulic head (e.g., uplift/erosion; elevation related to datum), aqua-thermal pressuring (Dutta 2016). One of the most significant problems in pore pressure prediction is to define which mechanisms apply where. Not only are there several different possible over- or under-pressuring mechanisms possible. It is also possible, and indeed common, to have more than one mechanism in the same basin or well.

The analysis of pore pressure is an important activity in the planning and design of well drilling. A correct pore pressure gradient is of paramount importance for drilling operations throughout the reservoir life-cycle since abrupt changes may cause costly problems (Traugott & Heppard, 1994). During drilling operations, pore pressure changes are associated with two causes (Fjaer et al., 2008): (1) Changes due to the invasion of drilling fluids (drilling mud) and (2) generation of volumetric strains due formation stresses redistribution. The accurate assessment of pressure allows establishing with low uncertainty some key parameters process, such as: a window of appropriate mud weight, the chemical composition of the mud, an optimal trajectory of the well, among others to avoid potential problems. The adequate study and prediction of pore pressure reduces the risk of problems such as loss of circulation, influx, or blowout and well instability among other problems, making well drilling a cost-efficient and safe process.

2.2.1 Compaction of porous sediments

Compaction is the expulsion of fluids in a porous media in response to mean stress. This is usually predominantly due to burial stress but could be associated to tectonics (Swarbrick et al., 2002). Compaction and porosity loss are affected by three sets of interrelated processes: (1) Mechanical compaction, which is the mechanical rearrangement and compression of grains in response to loading. This is usually predominantly due to burial stress but could be tectonic (Baker Hughes, 1993); (2) Physic-chemical compaction due to processes such as pressure solution, which is particularly crucial in carbonates and (3) Cementation, which involves the filling of pore space by chemical precipitation, which is related to temperature rather than to loading (Allen & Allen, 2013). Initially, when deposited on the seabed, sediments are highly porous. Porosity loss due to compaction is rapid at first but takes much higher stresses to reduce porosity at higher stresses or depths (Chilingarian, Serebryakov, & Robertson, 2002).

Undercompaction, sometimes called disequilibrium compaction, occurs when burial stress is added to the rock and dewatering is inhibited. This can happen due to the rapid deposition not giving enough time for the fluids to drain or due to the formation of seals and barriers to fluid flow. As burial continues, the pore fluids start to support part of the weight of overlying sediments, instead of the grain-to-grain contacts, and the fluid becomes overpressured. As rocks are buried, and fluids are expelled in response to burial stress, rocks will compact. If fluids are retained, either due to rapid burial or the formation of a seal, then porosities are preserved. The fluids start to take up part of the weight of the overburden and overpressure develops (Chilingarian et al., 2002; Fertl, 1976; Hantschel & Kauerauf, 2009).

Several factors affect the porosity-depth relationship. Some of them are: (i) gross lithology, shales compacting quickly compared to sandstones; (ii) depositional facies, which controls grain size, sorting

and clay content and therefore initial (surface) porosity; (iii) composition of framework grains: for example, pure quartz arenites differ from lithic arenites containing ductile fragments; (iv) temperature strongly affects chemical diagenesis, such as quartz cementation, clay mineral growth and pressure solution; and (v) time: porosity loss may require sufficiently long periods of time (Allen & Allen, 2013).

Estimation of porosity from borehole logs (e.g. density, neutron, sonic etc.), for a wide range of different lithologies, suggest that customarily pressured sediments exhibit an exponential reduction of porosity with depth. There are several different formulations of this exponential relationship, with different pre-exponential factors and exponents. Substantial deviations from the expected porosity-depth curve are found in overpressured units (Allen & Allen, 2013). The most straightforward trend recognized between porosity and depth is a linear trend of the form (Eq. 27)

$$\phi = \phi_o - az \qquad \text{Eq. 27}$$

$\emptyset$ and $\emptyset_0$ = porosity and initial porosity at depth Z

A more widely used porosity-depth relation, therefore, has the form of a negative exponential which produces an asymptotic low porosity with increasing depth (Allen & Allen, 2013). This relation is known as the *Athy's law* (Athy, 1930) (Fig. 13) (Eq. 28). On a depth versus log porosity graph, the value of k is the inverse of the rate of change of porosity with depth. The coefficient k can, therefore, be estimated if a number of porosity measurements can be made, for example from a sonic log from a representative borehole in the basin (Allen & Allen, 2013; Zoback, 2007).

$$\phi(y) = \phi_o \exp(-kz_e) \qquad \text{Eq. 28}$$

ϕ and ϕ_o = porosity at depth Z and initial porosity; K= compaction coefficient, z_e = equivalent depth.

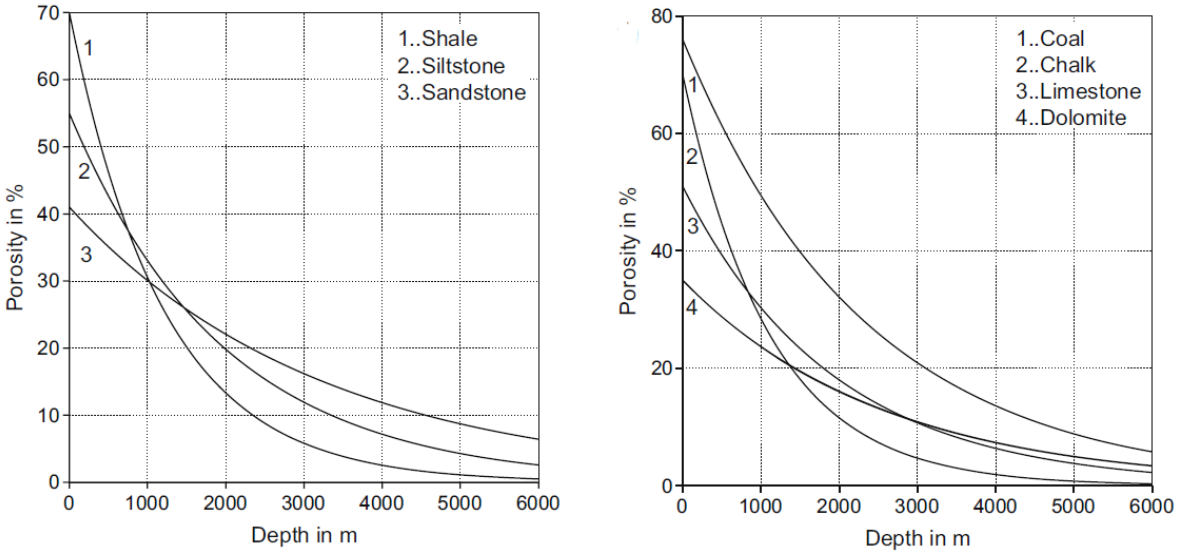

Fig. 13 Porosity vs hydrostatic depth using Athy's depth law for different lithologies. After (Hantschel & Kauerauf, 2009)

2.2.1.1 Porosity-permeability relationships

Permeability consists of two factors that are the intrinsic (k) and the relative permeability. k is affected by the pore structure and therefore, can be estimated as a function of porosity (Hantschel & Kauerauf, 2009). The porosity-permeability relationship was studied by Chilingarian & Wolf (1975), and they found that the permeability of isotropic sediments is controlled by their porosity and grain-size distribution. However, the rate of porosity loss reduces with increasing pressure (Fadipe et al., 2016). The most commonly used permeability relationship is the *Kozeny–Carman* relation. A derivation can be drafted from *Hagen–Poiseuille's law* for fluid flow through a porous structure (Hantschel & Kauerauf, 2009) (Fig. 14).

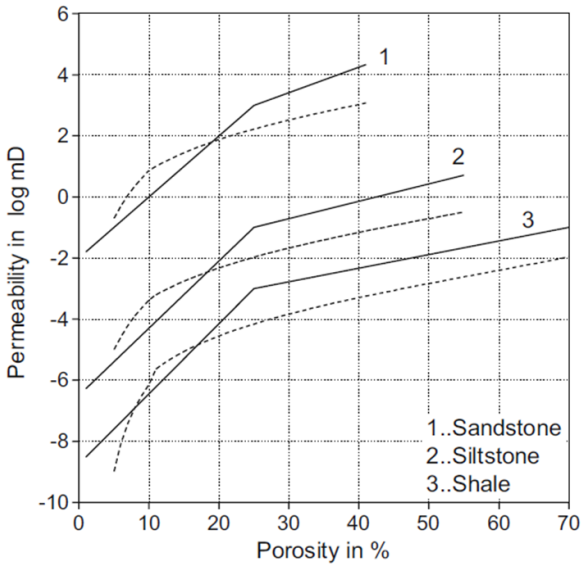

Fig. 14 Permeability curves for various lithologies with piecewise linear (solid) and Kozeny–Carman (dashed) relationships. After (Hantschel & Kauerauf, 2009).

2.2.2 Pore pressure numerical solutions

The numerical expression of pore pressure is a one phase fluid flow equation that correlates driving forces with flow rates. To model fluid flow phenomenon, mass conservation is also needed, implying that compensating mechanisms are involved to derive the equation (Eq. 29).

As described by Darcy's law, there exists a correlation between the discharge velocity of fluid and the pressure difference along the porous medium (Hantschel & Kauerauf, 2009; Mavko et al., 2009). This law is related by a mobility factor, which is a function of the rock permeability and fluid viscosity (k/v). The resulting pressure of a system is a consequence of multidimensional conditions that span along and across a rock formation involving mechanical, chemical and thermal processes. Mechanical compaction, which is associated with porosity reduction (ϕ), is addressed through the Terzaghi's compaction law. Aqua-thermal pressuring, mineral transformation or petroleum occurrence, may lead to important local changes in fluid densities (ρ) and cementation, are addressed as chemical compaction and pore fluid expansion (Chilingarian et al., 2002; Fertl, 1976). The bulk compressibility (C_b) describes the ability of the rock framework to compact and it also controls how overburden influences pore pressure (Hantschel & Kauerauf, 2009; Jaeger et al., 2007). When using these concepts, suitable boundary conditions must be defined for consistent modelling of in- and outflow of fluids.

$$div\frac{k}{v}grad\ u - C_b\frac{\partial u}{\partial \mathrm{t}} = -C_b\frac{\partial u^a}{\partial t} + \frac{1}{\phi}\frac{\partial \phi^c}{\partial t} + \frac{1}{\rho}\frac{\partial \rho^c}{\partial t} \quad \text{Eq. 29}$$

Despite the consideration that pore pressure generation strongly depends on horizontal permeability variations, main mechanisms and processes relating overpressure generation and compaction may be described with a 1D approach. A 1D simplified formulation of the general pressure equation is Eq. 30 (Hantschel & Kauerauf, 2009).

$$C_b\frac{\partial u}{\partial t} - \frac{k}{v}\frac{\partial u}{\partial z} = C_b\frac{\partial u_l}{\partial t} \quad \text{Eq. 30}$$

Where C_b represents the bulk compressibility, t refers to time, z corresponds to depth and ul corresponds to a lithostatic potential (lithostatic pressure minus hydrostatic pressure). Further explanation on the derivation of the equations can be found in (Cheng, 2016; Hantschel & Kauerauf, 2009)

2.3 Numerical methods in rock mechanics

Numerical methods are the preferred way to perform computer assisted analysis of complex multi-physics problems in the engineering field. Rock engineering has benefited greatly from the developments in computational technology and the mainstream usage of numerical modelling software. The broad catalogue of methods allows representing and analysing the discontinuous nature of earth-materials through abstractions for different circumstances and purposes.

The overall modelling and design of rock engineering covers an extensive list of methodologies that can work towards close-to-reality reproduction of field conditions or may be methodologies that are not to an exact scale, but derive properties and require iterative cycles to produce meaningful product (Jing & Hudson, 2002). Numerical methods make part of the first group and aim to use explicit relations and parameters. Nevertheless, it is often the case that the recommended solution promotes an integrated approach which combines different data sets, estimated trends and field measurements to come up with better solutions.

The commonly implemented methodologies to assess earth-material numerical modelling can be classified as (1) Continuum methods (Finite element, finite differences and boundary element models), (2) Discrete methods (discrete element method and discrete fracture network) and (3) Hybrid methods (continuum/discrete methods). The selection of the preferred method will depend on the specific case and complexity of the problem. The geomechanical models developed in this research include as main methodologies the finite element method (FEM), the boundary element method (BEM) and the discrete fracture network (DFN) approaches. Further insights on other relevant methods are available in (Jing, 2003; Jing & Stephansson, 1995; O'Sullivan, 2011)

2.3.1 Finite element method (FEM)

The finite element method is one of the most popular for mechanics-related disciplines, considering its versatility regarding material heterogeneity, non-linear capabilities, complex boundary condition implementation among other variables (Jing & Hudson, 2002). An approximation of a field quantity is obtained through the convenient discretization of a continuum model domain in smaller fractions to obtain an approximation of the real solution. In stress analysis, the target parameters may be

displacement field or stress field. FEM is a method better suited for complex geometrical constructs, where a convenient exact formula is hard to obtain or calculate (Cook, 1995).

The FEM divides the solution domain into simply shaped regions, or "elements". An approximate solution for the partial differential equations (PDE) can be developed for each of these elements. The total solution is then generated by linking together, or "assembling," the individual solutions taking care to ensure continuity at the inter-element boundaries. Thus, the PDE is satisfied in a piecewise fashion by as many polynomial expressions as there are elements (Chapra & Canale, 2015; Cook, 1995). The use of elements, rather than a continuum grid, provides a much better approximation for irregularly shaped systems. Further, values of the unknown can be generated continuously across the entire solution domain rather than at isolated points.

Pre-processing and post processing

Finite element analysis is an integral part of computer-aided engineering. Commercial software is now capable of handling complex numerical modelling setups. As a standard, the user normally handles pre and post processing stages. Pre-processing may include the description of loads, overall description of materials and the resolution and type of mesh. Post processing step includes classification of the outputs, listing and plotting. These capabilities may be found in a single software or as stand-alone packages, providing FE users a broad range of tools to adjust to specific problems (Cook, 1995). To apply the finite element method, a typical description of the problem includes: scalar parameters (number of nodes, number of elements), material properties, coordinates of nodes, connectivity array for finite elements, description of boundary conditions, and description of surface and concentrated loads, among other parameters (Nikishov, 2007).

Discretization

Finite elements resemble fragments of a structure (Cook, 1995). The description of finite element mesh or grid generally consists of nodal coordinates and element connectivities. Finite elements refer to elements of finite size. The geometry of the elements and the resolution of the mesh will depend on the model geometry and the target areas. Normally, target areas will require a finer mesh. Areas away from the target zones, or accessory features of the model, may have coarser meshes.

Mathematical model

To solve mechanics problems governed by a set of partial differential equations, the problem domain is first discretised into small elements. In each of these elements, the profile of the displacements is assumed in simple forms to obtain element equations. The equations obtained for each element are then assembled together with adjoining elements to form the global finite element equation for the whole problem domain. Equations thus created for the global problem domain can be solved easily for the entire displacement field (Quek & Liu, 2003). The selection of the interpolation functions comprises the definition of the equations to approximate the solution for each element. Interpolation functions are used to interpolate the field variables over the element. Polynomial functions are selected as interpolation functions considering they are easy to manipulate mathematically (Chapra & Canale, 2015). In the finite element approach, the nodal values of the field variable are treated as unknown coefficients which make up the unknown values to be determined. The interpolation functions are predetermined functions of the independent variables, also known as *shape functions*;

and these functions describe the field variable distribution within the finite element (Chapra & Canale, 2015; Quek & Liu, 2003).

After the individual element equations are derived, they must be linked together using continuity or compatibility equations, to characterize the unified behaviour of the entire system. By connecting elements together, the field quantity becomes interpolated over the entire structure in a piecewise fashion. The best fit value of the field quantity at nodes, are those that minimize some function such a total energy (Cook, 1995). The minimization process is known as the energy principle which creates a weak form of the system equations. This process generates a set of simultaneous algebraic equations for values of the field quantity at nodes. The entire system is expresses in matrix form as:

$$[k]\{u\} = \{F\} \qquad \text{Eq. 31}$$

Where $[k]$ = the element property or stiffness matrix, $\{u\}$ a column of unknown's coefficients at the nodes and $\{F\}$ a column vectors for external applied forces. The primary characteristics of a FE are embodied in the element stiffness matrix. For a structural finite element, the stiffness matrix contains the geometric and material behaviour information that indicates the ability of the material to withstand deformation under an applied load (Chapra & Canale, 2015).

Boundary conditions are required to solve the system. There are two types of boundary conditions, namely: displacement or essential and force or natural (Quek & Liu, 2003). The terms 'essential' and 'natural' come from the use of the so-called *weak form* formulation (such as the weighted residual method) for deriving system equations. In such a formulation process, the displacement condition must be satisfied first before derivation starts, or the process will fail. Therefore, the displacement condition is *essential*. If the essential (displacement) condition is satisfied, the process will lead to the equilibrium equations as well as the force boundary conditions. This means that the force boundary condition is *naturally* derived from the process, and it is therefore called the natural boundary condition (Quek & Liu, 2003).

Common methods to solve the global FE equation assembly include Gauss elimination and LU decomposition for small systems and iterative methods for large systems. Once the results are available, these can be catalogued as lists or visualize as graphics.

Property of material or medium

Many engineering systems consist of heterogeneous materials. Property of materials can be defined either for a group of elements or each individual element, if needed. For different phenomena to be simulated, different sets of material properties are required (Quek & Liu, 2003). The heterogeneity of earth mechanical models implies a complexity increase in the property definition of finite element models. For applications like reservoir geomechanics, material property definition are often the result of different data sets integrated to the model.

Transient response

A transient response is a highly dynamic, time-dependent force exerted on the solid or structure, such as earthquake, impact and shocks (Quek & Liu, 2003). There are two types of direct integration methods, required to solve the problems in question: implicit and explicit. Implicit methods are

generally more efficient for a relatively slow phenomenon, and explicit methods are more efficient for a very fast phenomenon, such as impact and explosion (Quek & Liu, 2003).

2.3.2 Boundary Element Method (BEM)

The boundary element method (BEM) is a powerful alternative to FE modelling (Crouch & Starfield, 1983). Contrary to the finite element method (or the finite difference method) the methodology of formulating boundary value problems as boundary integral equations describes problems only by equations with known and unknown boundary states. Hence, it only requires discretization of the surface rather than the volume, i.e., the dimension of problems is reduced by one (Antes, 2010). Consequently, the necessary discretization effort is mostly much smaller and, moreover, meshes can easily be generated and design changes do not require a complete remeshing. BEM works with less elements and nodes than FEM and needs less boundary divisions. Therefore, time consumption using BEM is reduced considerably in terms of model construction and in computer requirements (Antes, 2010).

On the other hand, BEM is not as efficient as the FEM in dealing with material heterogeneity, because it cannot have as many sub-domains as elements in the FEM. In small scale models, as the cases presented in this research, materials modelled through BEM are homogenous in its entire extension. The BEM is also not as efficient as the FEM in simulating non-linear material behaviour, such as plasticity and damage evolution processes, because domain integrals makes part of the method. The BEM is more suitable for solving problems of fracturing in homogeneous and linearly elastic bodies (Jing, 2003; Jing & Hudson, 2002). There are direct and indirect formulations for BEM. The typical indirect approach is the displacement discontinuity method or DDM (Crouch, 1976) which is the approach implemented in fault and fracture mechanical analysis. The method involves complicated and lengthy integrations even for simple geometrical figures (Maerten et al., 2014).

2.3.3 Discrete fracture network model (DFN)

Fractured reservoirs induce special problems in static and dynamic modelling. Calculation of the contribution of fractures to the total porosity, as well as their spatial distribution and density are essential for production forecasting, and for correct simulation of the field performance in terms of stored hydrocarbon volume, fluid dynamics and matrix/fracture exchange (Balzarini et al., 2001; Jing & Stephansson, 1995). Moreover, the density and orientation of fracture networks will control the mechanical behaviour of a rock mass, making it a critical aspect throughout extraction processes (Golf-Racht, 1982). The DFN methodology is a special discrete modelling approach that integrates fluid flow and transport phenomena in fractured rock masses. This is an attractive concept as it allows representing the hydro-mechanical behaviour of fractured systems and honouring the discontinuous nature of earth materials (Jing, 2003).

With respect to computer models, a DFN models parts with the discretization of a surface as volumetric cells, where each cell hold information regarding the mechanical properties of the rock. A 3D models works with the fracture intensity metric P32 (m^2/m^3) (Dershowitz & Herda, 1992). A mechanical advantage is the possibility of generating stress-consistent models, where DFN are derived from a selected stress or strain field. The stress field can be defined in present-day conditions, in young formations, or, in more sophisticated studies, a paleo-stress can be estimated that fits with the conditions of fracture generation (Dershowitz, Pointe, & Doe, 2004).

The DFN model is established on the representation of the two factors: fracture system geometry and aperture/transmissivity of individual fractures (Jing & Stephansson, 1995). The former is based on stochastic simulations of fracture systems, using probabilistic density functions of the geometric parameters of the fractures (density, orientation, size, aperture, or transmissivity) formulated according to field mapping results, in addition to the assumption about fracture shape (circular, elliptical or generally polygonal). Direct mapping can only be conducted at surface exposures of limited size, boreholes of limited diameter/ length/depth and on the walls of underground excavations (tunnels, caverns, shafts, etc.) of more limited measurement space and with cut-off limits for mapping.

The reliability of fracture network information depends on the quality of mapping and sampling, and hence its adequacy and reliability is difficult to be evaluated. Equally difficult also is the determination of the aperture/transmissivity of the fracture population, due to the fact that in situ and laboratory tests can only be performed with a limited number of fracture samples from restricted locations, and the effect of sample size is difficult to determine (Jing & Stephansson, 1995).

Stochastic simulation of fracture networks

Stochastic simulation of fracture systems is the geometric basis of the DFN approach and plays a crucial role in the performance and reliability of DFN models, in the same way as for the DEM. The key process is to create probabilistic density functions (PDFs) of geometric parameters of fracture sets relating to the densities, locations, orientations and sizes, based on field mapping results using borehole logging, surface mapping, window mapping or geophysical techniques (Dershowitz & Herda, 1992; Jing & Stephansson, 1995)

- Fracture intensity definition

The form in which fracture intensity is known is with the designation P, for persistence, and the addition of subscripts that indicate the dimension of the sampling region and the dimension of the fracture feature (Dershowitz & Herda, 1992). In industry, P_{32} (Area of fractures per unit volume of rock), is the preferred measurement of fracture intensity as it is not dependent on the fracture size, orientation, and wellbore trajectory. Also, it is not dependant of the scale of the analysed region. Often, corrections are made as the fracture count per dimension is made from well interpretation and well deviation affects the result. Further intensity measurements will depend on the data availability and integrated intensity models should be the goal for numerical modelling.

- Fracture plane orientation

Fracture orientations are normally derived from the Fisher distribution (Fisher, 1953). It has been validated that this distribution is able to represent the orientation of a fracture set based on statistical measures. Extensive description on the Fisher distribution and further models can be examined in (Gutierrez & Youn, 2015).

2.4 Basin and petroleum systems modelling overview

The concept of basin and petroleum system modelling (BPSM) is an integrative modelling approach that is driven towards the study of oil and gas accumulations, promotes the accuracy in plays and prospects proposals and guides exploration programs towards oil discoveries in the petroleum industry. Its principal objective is to study petroleum occurrence, migration and accumulation (Hantschel & Kauerauf, 2009; Tissot & Welte, 1984). It represents two different coupled concepts: the sedimentary basin analysis covers the studies of the basin generation and evolution through

geological time (Allen & Allen, 2013; Dembicki, 2016; Hantschel & Kauerauf, 2009), whereas the petroleum system concept (PSC) focus on the petroleum occurrence, migration and accumulation in an area given specific basin physical, chemical, and thermal conditions (Magoon & Dow, 1994; Magoon & Beaumont, 1999; Perrodon, 1992). The latter is a unifying concept based on an orderly sequence of geological phenomena, starting with the genesis of oil or gas, followed by its migration and end with its entrapment. It can significantly increase the possibilities when dealing with oil and gas potential and exploration- associated risks. Extensive description of all the building blocks of petroleum systems can be found in (Gluyas & Swarbrick, 2004; Hantschel & Kauerauf, 2009; Magoon & Beaumont, 1999; Perrodon, 1992; Tissot & Welte, 1984).

In basin modelling, numerical solution of differential equations is a fundamental requirement and the most challenging, complex and costly process to accomplish. In most of the scenarios, temperature and pressure are modelled with parabolic diffusion equations. Multi-dimensional differential equations with complicated geometries are usually solved with the finite element method, whereas finite differences are often used in individual cases of approximately one-dimensional problems, such as simplified crustal layer models (Hantschel & Kauerauf, 2009; Saikia et al., 2017) .

The structure and physics-driven assumptions of the BPSM approach represent an outstanding advantage for geomechanical modelling. Some of these advantages include: (A) modelling through geological time, (B) porosity-permeability-fault and compaction-derived pore pressure assessment, (C) mechanical and stress-dependent fracture orientations estimation, (D) detailed fault properties definition and numerical representation, (F) paleo-geometries for temporal constraint and (G) Facies-derived properties: Porosities, permeabilities, elastic mechanical properties (Young's modulus and Poisson's ratio). From these features, all the necessary variables for a full mechanical analysis can be gathered, setting the foundations for improved petroleum systems modelling or migration analysis.

2.4.1 Numerical modelling

Basin and petroleum system modelling comprise the simulation of geological processes that occur in sedimentary basins across geological time spans. The model starts with the oldest sedimented layers until the present-day condition is reached. General processes analysed using this approach are deposition, compaction, heat flow model, generation, expulsion, phase dissolution, migration and accumulation. Modelling basin and petroleum systems requires an extensive dataset that covers present day model data with depth horizons, facies maps, fault planes, the age assignment table for the geological event definition, additional data for the description of paleo–geometries, thermal and mechanical boundary conditions through geologic time, the property values for lithologies, fluids, and chemical kinetics (Hantschel & Kauerauf, 2009). A recommended data list can be found in (Peters et al., 2017).

The input dataset considered for the model construction is derived from a synergy between geophysical, stratigraphic, sedimentological and geochemical models. Each model goes through an extensive analysis, under a multidisciplinary scope and is matched to the evolution history of the basin and present-day stratigraphic-physical properties. In general, key elements and processes can be summarized as follows:

1. General well data (coordinates, stratigraphic well tops, formation thickness, porosity estimated from petrophysics, temperature measurements and corrected-temperature interpretation, source rock metrics (%Ro and %TOC).
2. Kinetics analysis to estimate the generation potential of the source rock.

3. A master table or age assignment chart generation. Each stratigraphical unit is linked to a structural map, facies maps, thickness of sedimentary units, and sedimentary events like erosion, deposition or hiatus. Moreover, a connection is generated between the sedimentary units and the boundary conditions i.e. paleo water depth maps, sediment-water interface temperature (SWIT) and the thermal model.

Current software simulates the burial history, pressure changes considering several variables and a thermal model that lead to formation maturity and consequent hydrocarbon occurrence, migration and accumulation. The dynamic modelling through geological time tracks the structural changes, sedimentation of new layers, and compaction of former layers and hydrocarbon behaviour.

2.4.2 1D and 3D simulations

1D basin models recreate the geological history in one single point, which is commonly a well location. Nevertheless, they become useful in the exploration of the extent of oil and gas generation. On the contrary, it may be of very high uncertainty to generate pseudo-3D models out of 1D as the lateral temperature, and pressure gradients cannot be considered. 3D models gather the most variables to represent a basin and petroleum system, being the most important the representation of the structures that form traps and representation of carrier beds for migration simulation. The principal disadvantages of 3D models are an important consideration when deciding on a 1-D, 2-D, or 3-D modelling study. Although appealing, realistic 3-D models generally require more data and time to construct than 1-D or 2-D models, and necessary computer processing time may impede the progress of other studies having deadlines (Peters et al., 2017).

2.4.3 Decompaction and backstripping for paleo-stress assessment

Backstripping of present-day configuration, is a methodology that considers decompaction of sediments, erosive events and certain paleo-constraints to deliver an acceptable approximation of the paleo-geometries in low-deformation areas (Hantschel & Kauerauf, 2009). The decompaction of a layer is performed according to Eq. 32.

$$d_0(1-\phi_0) = d_p(1-\phi_p) \qquad \text{Eq. 32}$$

With present day and depositional porosities ϕ_p and ϕ_0, respectively.

Resulting porosity of a layer at present day, is assumed to be conditioned by a series of depositional and erosion events and is affected directly by pore pressure development. The first simulation is performed using the hydrostatic pressure for reference. When the forward model is performed, then the engine will estimate the present-day conditions based on pore pressure-controlled compaction (Fig. 15). Modelling of erosion requires the definition of the eroded thicknesses and the erosion ages. The eroded thickness and the compaction history of the layer before erosion has to be taken into account in the optimization procedure (Hantschel & Kauerauf, 2009).

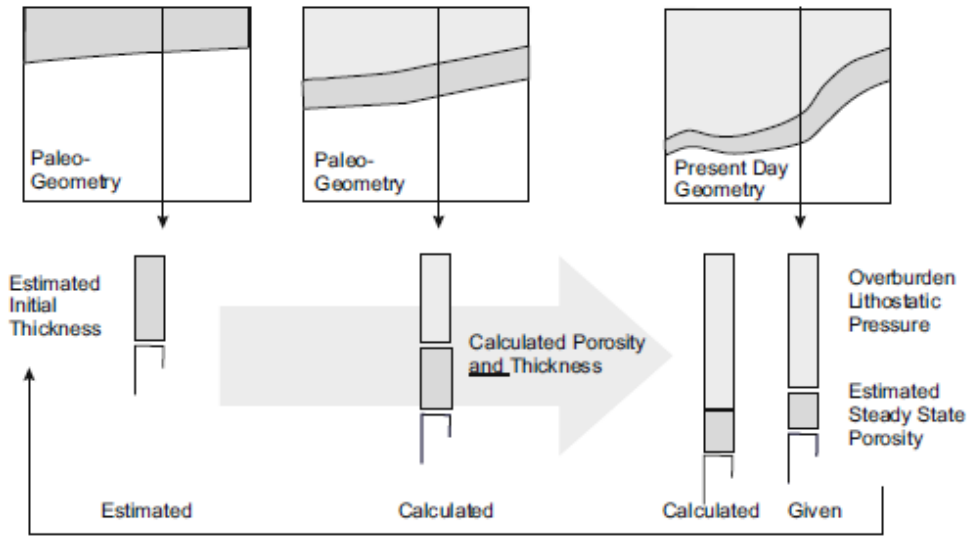

Fig. 15 Backstripping with decompaction is based on estimated present-day porosities. The calculated porosities of the forward simulation usually improve backstripping in the next run. After (Hantschel & Kauerauf, 2009)

Complete paleo–geometries are alternatively used as input for the simulation. The estimation of water depth for a given stratigraphic horizon is complex, yet it is essential in order to accurately constrain subsidence history. Information on paleo bathymetry comes from several sources, main of which are benthic microfossils, other faunal and floral assemblages, sedimentary facies and distinctive geochemical signatures. Biostratigraphy plays a key role in constraining paleo bathymetry (Allen & Allen, 2013).

The simulator then jumps from predefined paleo–geometry to paleo–geometry in the analysis. It must identify the new location of each single facies and must consider facies movements and deformations. A meshing algorithm based on pre-defined grid-points and sublayers can yield new volumetric cells which are no longer related to the same rock of the previous time step. The effect this causes is that all bulk rock properties have to be transferred according to the new location (Hantschel & Kauerauf, 2009).

When the compaction has already been predefined via paleo–geometries, both the pressure and the compaction equations can be solved in the usual way. The change in the overburden load of each layer is calculated from one paleo–geometry to the next. The time-dependent modelling for overpressure can then be solved with the transformed cell values of the previous time step. The results are a change in the overpressure as well as a reduction in the porosity. The difference from the usual procedure is that the porosity change is not converted into the new layer thicknesses, since they are already predefined with given paleo–geometries (Fig. 16). Hence, porosity reduction and compaction are decoupled processes here and it is accepted that the volume rock matrix is no longer conserved (Hantschel & Kauerauf, 2009).

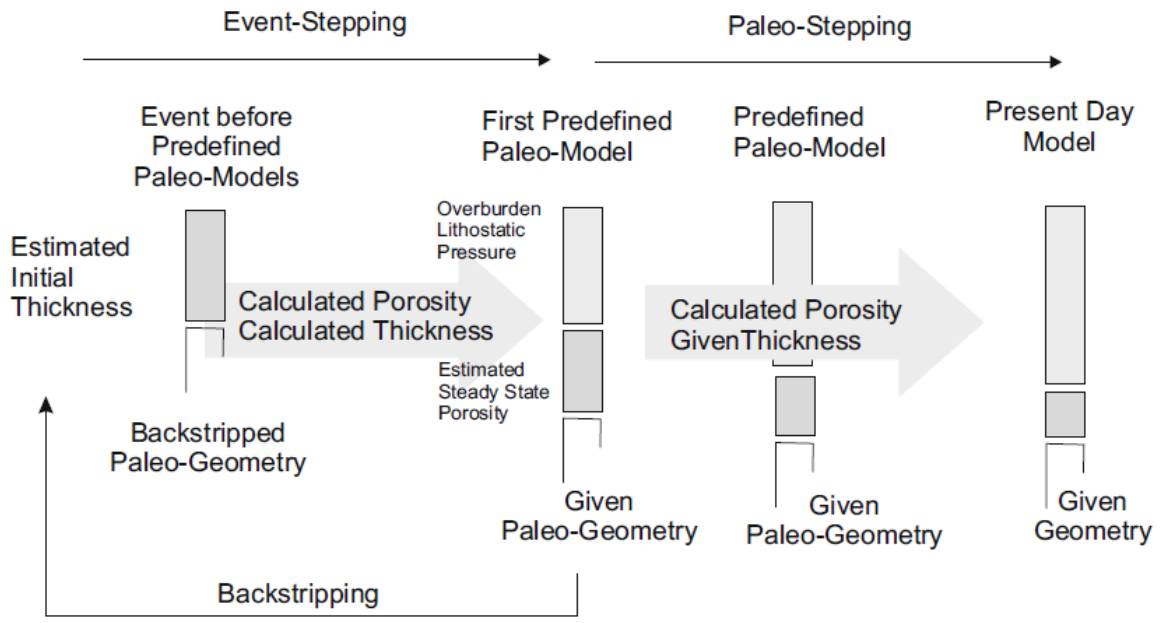

Fig. 16 Decoupling of compaction and porosity calculation during paleo–stepping. After (Hantschel & Kauerauf, 2009).

2.5 Field and laboratory data sources

2.5.1 Formation well logging

2.5.1.1 Sonic and density logs

Sonic log measures the formation transit travel time, a value that represents the potential of the formation to transmit sonic waves. The acoustic logging tool works emitting sonic waves from one or two transmitters and is later received by one or two receptors at a known distance. The emitted wave goes through fluid and refracts on the well wall and then reflects in the receptors. If the lithology and the type of fluids are known, the porosity can be estimated empirically (Bassiouni, 1994; Rodriguez-herrera et al., 2006; Tixier et al., 1959).

The results are presented as the inverse of velocity, known as slowness, in μseg/ft units. The slowness is equal to the inverse of velocity, and corresponds to the transit time given by the conventional sonic tools (Ávila-carrera et al., 2011). There are three different wave types that can be obtained from the acoustic log: compressional (P), shear (S) and Stoneley. Compressional and shear components are fundamental in the determination of dynamic elastic properties.

On the other hand, density log is one of the most porosity−sensitive measurements of a formation, and from it an apparent formation density is obtained, which is a total density of the rock including the solid matrix, the pore spaces between grain and fluids. Density logs are often used to derive indirect porosity and to identify specific minerals (Bassiouni, 1994). The functioning principle of the density logging tool consist in emitting medium to low-energy gamma rays to the target formation and measuring the attenuation between the source and receptors. The log unit is g/cm^3 and is typically presented in an interval of 1.65 to 2.65 g/cm^3.

Density, P and S waves are fundamentals to the geomechanical analysis, since they allow the estimation of dynamic moduli of the rock like Shear modulus, Poisson's ratio, Lamé constant, Young's modulus and compressibility.

2.5.1.2 Image logs for borehole breakouts and drilling induced tensile fracture detection

Image logging tools are conducted down an open well. It measures physical properties in the wellbore wall such as electric conductivity or the sonic travel time plus acoustic reflectance. Its difference with respect to other logs relies on the 360° coverage of the wellbore. Image logs take several measurements on the wellbore wall that after computer-processing, a full image of the wellbore is generated. It has a very high vertical resolution, compared to other logs. Images can be acoustic or resistive. Acoustic image tools send and receive ultrasonic pulses towards and from the wellbore wall, creating an image that covers the entire circumference and can be used with any type of drilling fluid (Cheung et al., 1994; Tingay, Reinecker, & Müller, 2008).

Regarding structures, image logs provide accurate interpretation of bedding dips, natural and induced fractures, wellbore breakouts and washouts. Borehole breakouts and drilling induced fractures (DIF) provide the strongest stress orientation indicators in petroleum and geothermal systems (Tingay et al., 2008; Zoback et al., 2003). Borehole breakouts can be defined as a pronounced enlargement with respect to the standard hole diameter or bit size. Frequently, the enlargement happens in one clear direction and is directly related to the compressive stresses (Fig. 17). If the enlargement happens in the whole bit size diameter is called a *washout*. Borehole breakouts are caused by the loss of integrity caused by the drill bit, drilling fluids among other causes. The longer axis of a borehole breakout is parallel to the orientation of the minimum horizontal stress (Reinecker et al.,2003).

When a wellbore is drilled *in-situ* stresses rearrange to get back to equilibrium. This rearrangement promotes stress concentration around the wellbore that may exceed the tensile strength of the rock. This fracturing of the rock under known conditions is referred to as drilling induced fractures (DIF). The stress concentration around a vertical borehole is at a minimum in the S_{HMax} direction. Hence, DIFs develop approximately parallel to the S_{HMax} orientation (Tingay et al., 2008). Both borehole breakouts and DIFs' have a quality ranking criteria proposed by (Tingay et al., 2008). The ranking is based on distinct measurements and counts of events along a well interval.

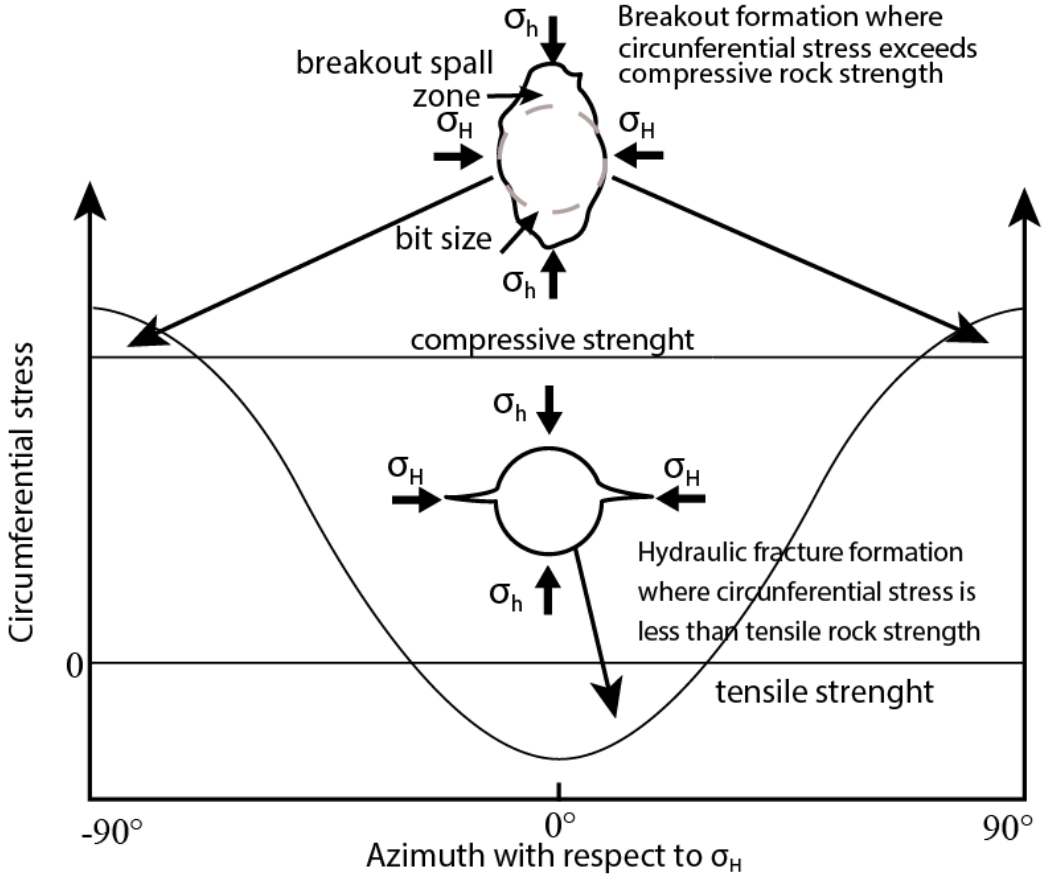

Fig. 17 Relation between stress concentration and orientation constrained by the rock compressive and tensile strength. Borehole breakouts generate when the stress exceed the compressive stress of the rock. Drilling induced fractures form when the stress concentration exceeds the rock tensile strength. Modified after (Tingay et al., 2008)

2.5.2 Rock fracturing field testing for stress constrain

Hubbert and Willis (1957) presented a compelling physical argument that hydraulic fractures in the earth will always propagate perpendicular to the orientation of the least principal stress, σ_3 (Zoback, 2007). Because of the work done to open a Mode I fracture, a given amount is proportional to the product of the stress acting perpendicular to the fracture plane times the amount of opening (*i.e.* work is equal to force times distance), hydraulic fractures will always propagate perpendicular to the least principal stress because it is the least energy configuration (Zoback, 2007).

A leak-off test (LOT) is the name given to a controlled hydraulic fracture procedure in a unit of interest. Even though it is a suitable indicator, there is inherent uncertainty given operational limitations of the test itself (Zhang et al., 2017). For a driller, the primary objective of the LOT is to test the integrity of the casing cement job near the casing shoe and determine the maximum mud weight (MW) that can be withstood by the formation before initiating a hydraulic fracture. On the other hand, for a geomechanical engineer, it is relevant to create a small hydraulically induced fracture in the rock to estimate the *in-situ* stress.

The LOT pressurizes a selected section up to a point where there is a rapid decrease in the pressure, known as the formation breakdown pressure. A variation of the LOT is known as the XLOT or mini-

frac and has the same principle as the LOT, but the pumping continues after formation breakdown to propagate the fracture (Fig. 18). If the LOP is not reached, a limit test, or formation integrity test (LT, or FIT) (Zoback, 2007).

A formation integrity test or FIT (Fig. 18) is conducted in a similar manner as an LOT, except the formation usually is not fractured or broken down (unless accidentally because the fracturing pressure is less than anticipated) (Baker Hughes, 1996). The test objective is to test the integrity of the cement and fracture pressure of the formation below the shoe to a pre-determined amount.

Relevant pressure points to take from hydraulic fracture tests are the following: (1) *Leak-off pressure* (LOP): point where the slope of the curve starts to decrease, deviating from the best fit straight line at the beginning of the test. This represents the point at which micro-fractures are forming near the wellbore, (2) *Breakdown pressure (P_b):* the highest pressure achieved during the test, corresponding to the formation of a major fracture and massive fluid losses; (3) *Instantaneous shut.in pressure (ISIP):* first point after the pumps are stopped. Any pressure associated with friction due to viscous pressure losses disappears. (4) *Closure stress (F_{cp}):* first point after the slope of the curve starts to decrease just beyond the short linear behaviour observed after ISIP (Baker Hughes, 1996).

Mini-Frac is a special kind of pump-in/decline test designed to measure the closure stress and estimate the leak-off coefficient in a thin interval just prior to a hydraulic fracturing job (Baker Hughes, 1996). Step-rate test or *SRT* is performed in preparation for a hydraulic fracturing treatment. It is developed when an injection fluid is injected for a defined period in a series of increasing pump rates (Schlumberger- Oilfield Glossary).

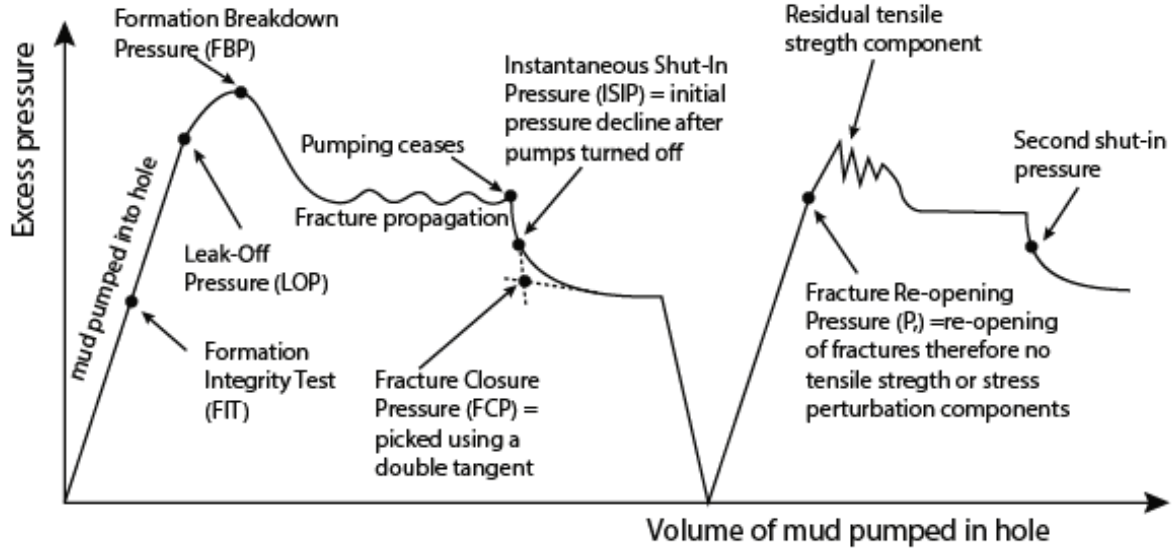

Fig. 18 A schematic mini-frac or extended leak-off test showing pressure as a function of volume, or equivalently time (if the flow rate is constant). After (Zoback 2007)

2.5.3 Pore pressure *in-situ* measurements

Methods to determine pore pressure are different, depending if they are being measured in a pre-drilling stage or post drilling. It is recommended to use all the data sources available, both primary and secondary since one data source, alone, gives inaccurate pressure prediction.

2.5.3.1 Pre-drilling estimations: Geophysical well logging techniques

Pore pressure estimation before further drilling activities can be performed using seismic methods or seismic velocities, which are very helpful in identifying overpressure zones or trends different from the hydrostatic pressure. Performing predictive workflows require a sound knowledge of seismic data processing and rock physics (Avseth et al., 2005; Mavko et al., 2009; Rana & Dvorkin, 2011). The fundamental datasets require compressional and shear waves (Vp and Vs) (Sayers et al., 2002)

- ***Trend-line methods***

Trend-line methods refer to methods which directly relate the amount of pore pressure divergence from its normal trend-line to the pore pressure gradient at a given depth. This trend-line represents the "normal compaction trend" (NCT) as a function of burial depth, and fluid pressure exhibited within this normal trend is hydrostatic (Kumar et al., 2012). One problem is that normally pressured intervals are required to establish the trend, and this may not always be present. In deep-water, in particular, overpressure may begin very shallow and before there is little to non-existent data to establish a trend (Baker Hughes, 1996).

Overall, it is their very flexibility that makes this type of methods appealing. They allow to quickly get an answer, matching RFT's (Repeated formation testing is a tool to measure pressure), kicks, hole problems, gas, mud density or any other indicator available. This also creates a risk, particularly in real-time operations, where the operator can easily customize the trend to get the answer the customer is expecting (Baker Hughes, 1996).

- ***Pore pressure prediction from interval velocity and travel time***

This category comprises the methods that use compressional travel time and interval velocity obtained from logs to derive the pore pressure gradients. The most commonly used empirical models are Eaton's method (Eaton 1975) (Eq. 33) and Bower's method (Kumar et al., 2012; Zhang, 2011).

  - Eaton method

The Eaton method is applicable in some petroleum basins, but it does not consider unloading effects. This means that a decrease of effective stress caused, for example, by fluid expansion is no considered. This limits its application in geologically complicated areas, such as formations with uplifts. To apply this method, one needs to determine the normal trend or transit time (Δtn) (Fig. 19) (Zhang, 2011). Eaton established exponents for the Gulf of Mexico (GOM) shelf as 1.2 for resistivity and 3.0 for sonic. These values may need altering for other basins and generally need adjusting down to account for overpressure mechanisms other than undercompaction (Baker Hughes, 1996).

$$P_{pg} = OBG - OBG - P_{ng}(\frac{\Delta t_n}{\Delta t})^3 \qquad \text{Eq. 33}$$

Ppg=Pore pressure gradient; OBG= Overburden gradient; Δtn = normal compaction trend; Δt=compressional wave travel time.

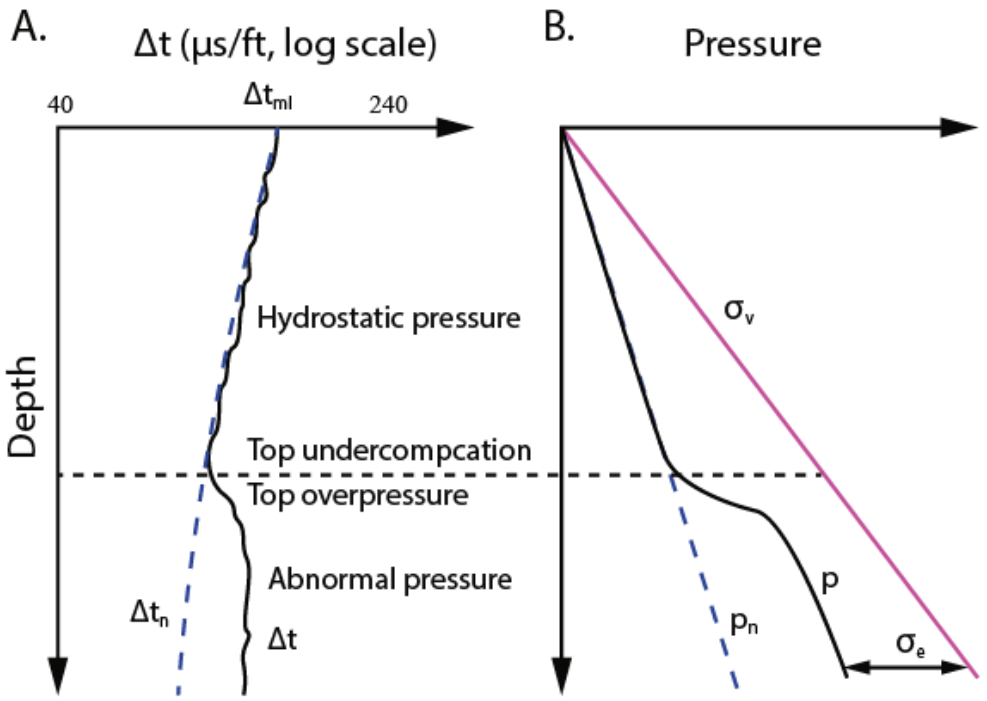

Fig. 19 Schematic plot showing sonic travel time measured in shale. Modified after (Zhang, 2011).

- Bowers method

This method uses the sonic velocity and empirically determined parameters to determine the vertical effective stress, which is then subtracted from the overburden stress to determine the pore pressure. This method is recommended for pore pressure prediction when governing mechanisms are compaction disequilibrium or due to some source mechanism (Kumar et al., 2012).

Some advantages of the pore pressure derivation using acoustic measurements include: Ability to calculate bulk density and porosity from which overburden and pore pressure is derived; low sensitivity to hole size, formation temperature and pore water salinity; small effect of measurement around salt; ability to calibrate with seismic-based predictions; generally, obtain good agreement with measured pore pressure data. Δ_{TS} shear data tends to show improved response in isolated pressured zones (Baker Hughes, 1996).

2.5.3.2 Post drilling estimations: Drilling data

After drilling is over, it is possible to collect pressure trend data using measured drilling parameters (ROP, WOB, RPM, flow rate)[2], registered drilling events, properties of frill cuttings from samples

[2] ROP= Rate of penetration; WOB=weight on bit; RPM =rotation per minute

collected at the shale shaker, measure gas levels from well, estimate a lithological column while drilling (Kesarwani et al., 2013).

- ***Drill Stem Test data (DST)***

A drill stem test is a temporary completion where a section of the wellbore is isolated and relieved of the mud column pressure through the drill pipe (drill stem) (Baker Hughes, 1996). The data from a drill stem test consists of all the qualitative, quantitative, and procedural information recorded at the surface and the pressure charts retrieved from the bottom-hole test assembly. All these data sets are necessary for complete and proper interpretation of the test results. A qualitative inspection of the pressure chart should be made to ensure that the sequence of events is understood and that no irregularities or tool failures occurred (Fig. 20). The pressures listed below are computed by measuring the deflection above the base line and obtaining a corresponding pressure from a calibration curve for the recorder (Baker Hughes, 1996). These pressures include: (1) Initial hydrostatic pressure (IHP), extended by the column; (2) Initial shut-in pressure (ISIP); (3) Initial flow pressure (IFP). The pressure just before the tool is closed; (4) Final Flow Pressure (FFP), the pressure just before the tool is closed; (4) Final Shut-In Pressure (FSIP) and (5) Final Hydrostatic Pressure (FHP).

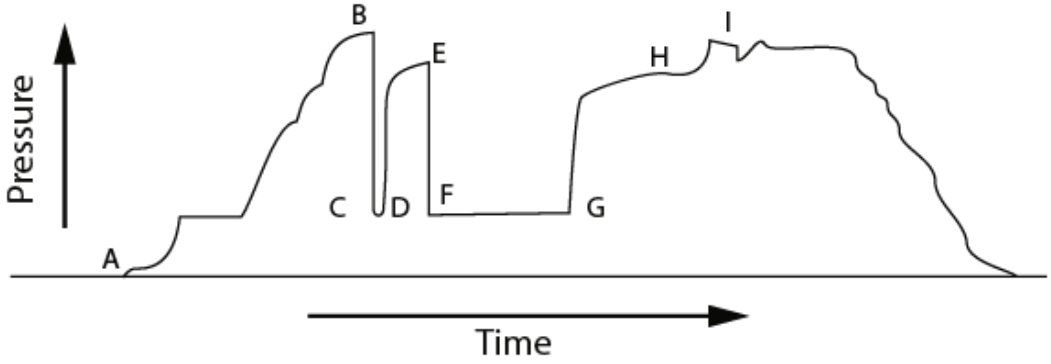

Fig. 20 Sketch of a typical DST chart. AB - Increasing Hydrostatic Pressure as tool is run to depth, B - Initial Hydrostatic Pressure, BC - After Packers are set, tool is opened, CD - Initial Flow Period, DE - Initial Shut-In Pressure, EF - Tool is opened a second time, FG - Final Flow Pressure Curve, HI - Mud column is allowed into test interval and packers are unseated, I - Final Hydrostatic Pressure. After (Baker Hughes, 1996).

2.5.4 Rock mechanical laboratory tests

2.5.4.1 Triaxial test

A triaxial test is a versatile method to measure the mechanical behaviour of soils and rocks. It is widely used as it allows the determination of the shear strength and stiffness of a sample (Rees, 2013). This test is rigorously described as a cylindrical compression or extension test. The sample is loaded by applying an axial stress (σ_a) and a radial stress (σ_r).

The sample height usually is 2:1 height-to-diameter ratio and is encased in a rubber membrane. Its advantage relies on the possibility of controlling the sample's drainage and the ability to measure the pore pressure. Main results of this test are the angle of shearing resistance ϕ, cohesion C and undrained shear strength C_u. Additional parameters that can be estimated include shear stiffness G,

compression index and permeability (Lancellotta, 2009; Rees, 2013). The stages followed are sample saturation, consolidation, and shearing. To assess soil response there are three triaxial test variations: (1) Unconsolidated undrained test (UU), (2) Consolidated undrained test (CU) and (3) Consolidated drained test (CD). The latter is applicable to describing long-term loading response, providing strength parameters determined under effective stress control (i.e. ϕ' *and* C) (Rees, 2013).

The stresses acting on the rock sample are the confining pressure ($\sigma_c = \sigma_r$) which is equal to the minimum principal stress σ_3. The deviator stress (q) is generated by applying an axial strain to the sample ($\mathcal{E}_a$). The deviator stress acts in addition to the confining stress in the axial direction, with these combined stresses equal to the axial stress (σ_a), or major principal stress σ_1 (Rees, 2013).

2.5.4.2 Brinell hardness test

The Brinell Test is an indentation hardness test consisting of two steps. First, the indenter is brought in contact with the test's specimen perpendicular to the surface, and the specified test force is applied. The test force held for the specified time and then withdrawn. Afterwards, the diameter of the indentation is measured in at least two directions perpendicular to each other (ASTM International, 2012).

2.5.4.3 Ultrasonic test

Dynamic elastic mechanical properties can be obtained in laboratory through ultrasonic pulse velocity test. Ultrasonic velocity testing offers a non-destructive way to characterize geological core sample properties subjected to high temperatures and pressures in a triaxial cell. The main advantage of the test is the ability to deliver essential data about specimen elastic properties, rock structure, deformational stress and other attributes. A review of theoretical aspects of ultrasonic wave propagation and attenuation in solids can be found in (ASTM International, 2000; Basu & Aydin, 2006).

Chapter 3 Lower Magdalena Valley Basin

3.1 Lower Magdalena Basin regional framework

The Lower Magdalena Valley Basin (LMVB) is located in the north-western part of Colombia. The basin is constrained to the west by the San Jacinto Fold Belt (SJFB), to the north and northeast by the Santa Marta –Bucaramanga fault system (SMBFS), to the southeast by the San Lucas mountain range and to the south, by the Central Cordillera foothills. This basin has a length of 355 km along its north-south axis and a width from west to east of 240 km (Fig. 21) (Arminio et al., 2016). The main operational features to the east of SJFB are two sub-basins called: Plato (PSB) and San Jorge (SJSB), which are divided by the Magangué High (also known as Cicuco High) (Arminio et al., 2016; Bernal-Olaya et al., 2015; Mata, 2014; Reyes Harker et al., 2004).

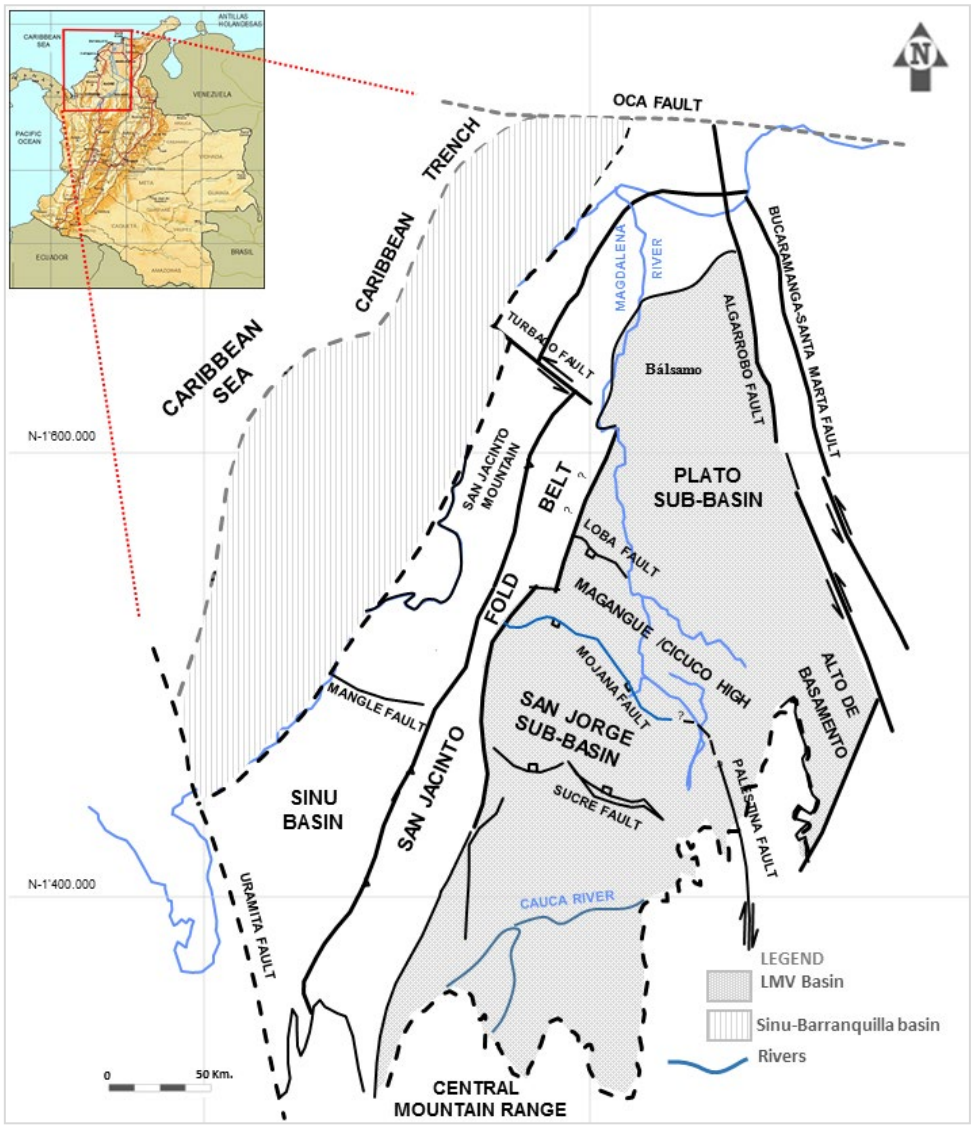

Fig. 21 Geographical location of the Lower Magdalena Valley Basin. Main depocenters and bounding faults are highlighted. Modified from (Reyes Harker et al., 2004)

The LMVB was formed in north-western Colombia due to the collision, displacement and subduction of the Caribbean Plate with respect to South America. Although sedimentation in the LMVB basin began during the Oligocene, the tectonic processes occurring in north-western Colombia should be taken into account from the Cretaceous period to explain its origin (Arminio et al., 2011; Bernal-Olaya et al., 2015; Reyes Harker et al., 2004; Villamil, 1999). The evolution of the Caribbean region includes the spatial relationships of the plates through time, derived from an initial reconstruction and the subsequent relative motion of the North American, African, South America and Farallon plates. Theses plate boundary zones are broadly dominated by strike-slip motion, from central Guatemala to the Puerto Rico Trench in the north, and from Colombia to Trinidad in the south (Caro & Spratt, 2003; Pindell & Barrett, 1990).

The Caribbean plate was formed during the Late Cretaceous and migrated eastwards relative to North and South America plates to its present position (Paul Mann & Escalona, 2011) (Fig. 22). The Caribbean plate is moving eastward accommodated by right-lateral strike-slip faults along the South American plate boundary and left-lateral strike-slip faults along the North American plate boundary (Caro & Spratt, 2003; Mann, 1999). This eastward plate migration is responsible for the oblique subduction that is interpreted to have affected the northern edge of the South America. During Oligocene to Miocene period the Caribbean slab was subducting at an angle greater than 30° and less than 8° during the late Miocene interpreted as the entry of thicker Caribbean oceanic plate crust beneath South America (Bernal-Olaya et al. 2015). In general, the authors agree that the stratigraphic and structural variations of the geological provinces in northern Colombia were determined by diachronic eastward displacement of the Caribbean plate with respect to the South American plate.

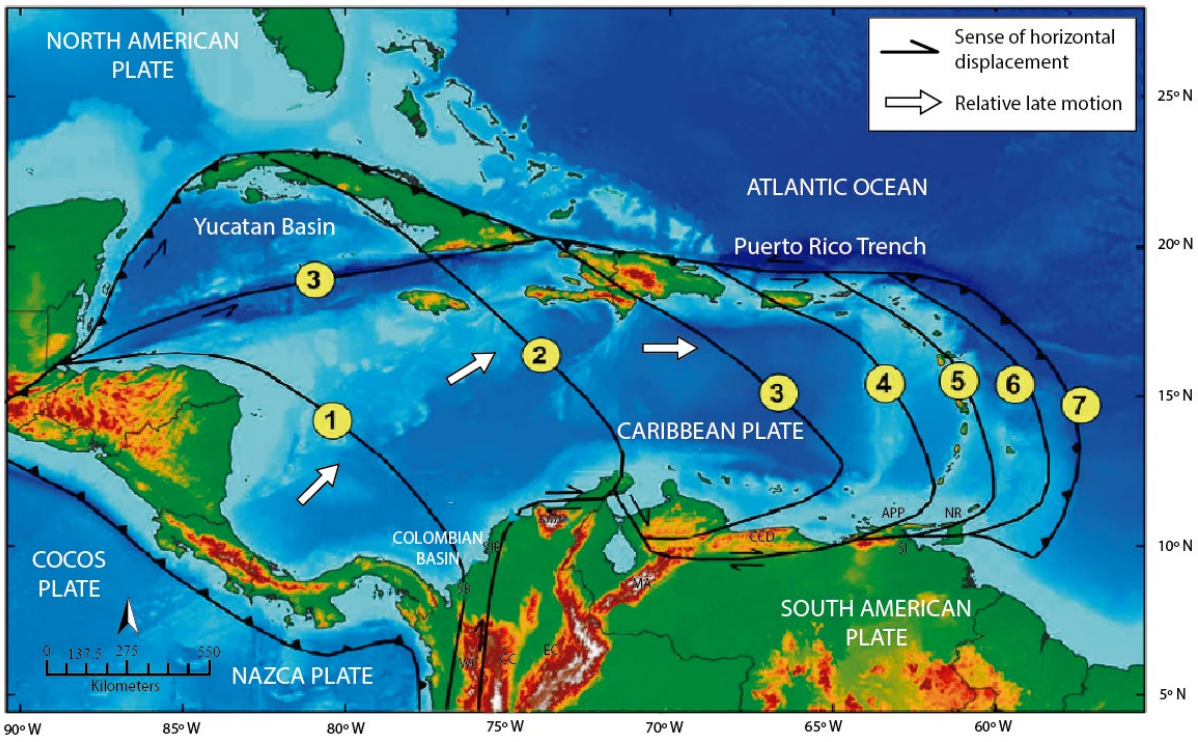

Fig. 22 Diachronous eastward displacement of the Caribbean plate relative to the North and South American plates with numbered, solid black lines representing the inferred locations of the leading edge of the Caribbean plate at the following times. (1) Late Cretaceous (≈80 Ma); (2) Middle Paleocene (≈60 Ma); (3) Middle Eocene (≈44 Ma); (4) Middle Oligocene (≈30 Ma); (5) Middle Miocene (≈14 Ma); (6) Pliocene (≈5 Ma); and (7) Recent. Modified from Escalona and Mann, 2011) in (Mata, 2014).

The geological position of the San Jacinto Fold Belt (SJFB) is vital to understand the tectonic evolution of the Caribbean area (regional plate kinematics) given its location at the junction of four tectonic plates, the Caribbean, Cocos, Nazca and South American plates. On a regional scale, the sedimentation and tectonic evolution of the LMVB was controlled by five main features, the Romeral fault, the Sinú lineament, the Bucaramanga – Santa Marta fault (BSMF), and the Oca fault (Caro & Spratt, 2003). The Romeral Fault forms the eastern border of the SJFB separating oceanic crust to the west from continental crust to the east. This structure limited the sedimentation to the west until Oligocene, when sedimentation started in the San Jorge and Plato Sub-basins with the Ciénaga de Oro formation. From Upper Cretaceous to Early Eocene, the Romeral Fault acted as a mega-shear with left lateral movement (Caro & Spratt, 2003). The Bucaramanga - Santa Marta Fault is a left-lateral strike-slip fault, with a maximum rate of displacement during the Miocene (Gulf, 1983). Campbell (1968) estimated 110 km of post-Miocene displacement. In the Early Miocene, the Santa Martha Massif was uplifted as a horst along the BSMF and Oca fault.

Three periods of tectonostratigraphic evolution are recognized in the LMVB: the first one goes from the Oligocene to Early Miocene, characterised by tilted blocks bounded by normal faults with continental sedimentation at the east and shallow marine towards the west. The second period is from Early Miocene to Late Miocene, characterised by high subsidence rates due to the isostatic accommodation due to the rising of Santander and Santa Marta Massifs. The third period corresponds to the Andean orogenic (Late Miocene-Pliocene), with intense folding and uplift in the Romeral fault vicinity (Arminio et al., 2011; Bernal-Olaya et al., 2015; Caro & Spratt, 2003; Reyes Harker et al., 2004; Villamil, 1999). These tectonic processes made possible the formation of several zones with different structural and stratigraphic behaviour, defined by the authors as tectono-stratigraphic regions with their respective hydrocarbon potential.

The Guama field located in Plato sub-basin is a stratigraphic accumulation of gas condensate in the LMVB and probably the first commercial field in deep marine sands of the basin. The main reservoir, named Porquero formation, is composed by low permeabilities sandstones from basin floor laminar facies, interlaminated with shales. These reservoir characteristics led to the development of a high-detailed stratigraphic, petrophysical studies and specialized geophysical analysis (Betancourt et al., 2016). It has become apparent the necessity of a very detailed analysis of petroleum system modelling and geomechanical integration to decrease the uncertainty in the hydrocarbon exploitation plans for the area. The study area (Block A) is located within the Guama field. The study area was selected because of its hydrocarbon potential and the extensive data acquisition campaign that was performed, including seismic surveys in 2D and 3D, sophisticated geophysical techniques, core recovery and lab testing, providing a good dataset available for simulation processes and calibration.

3.2 Present-day tectonic and stratigraphic setting

3.2.1 Structural style

Different tectonic elements, influenced by geologic events such as extension, compression and strike-slip movements, defined the main structural styles in LMVB. From southwest to northeast three structural highs are present: *Montelíbano – Cintura*, *Cicuco* high (also known as Magangué arch) and *El Difícil* high. From northwest to southeast, may be identified: The San Jacinto Fold Belt (SJFB), at the western edge of the basin, Apure high and Chimichagua platform delineates the eastern side (Flinch, 2003; Reyes Harker et al., 2004).

Two major depocenters correspond to the San Jorge sub-basin (SJSB) in the south and Plato sub-basin in the north (PSB). Two additional depocenters have also been defined: Tirón depocenter (Td), to the west of San Jorge sub-basin, associated with Tirón fault; and the Bálsamo depocenter (Bd) in the north of Plato sub-basin. All the faults are identified as steeply-dipping normal faults with almost no horizontal component. The normal faults with almost vertical displacement bounded the structural highs, most of which were active until Early – Middle Miocene, when the sedimentation of Porquero formation buried them. The Mojana and Violo faults delineate the Cicuco high extents in its western and eastern flank respectively, and the Alejandría fault constitutes the southern edge of the El Difícil high. The Algarrobo fault (AF), is a left lateral strike-slip system that is part of the Santa Marta – Bucaramanga fault system (SMBFS). Transcurrency has also been defined within the basin; the most prominent strike slip features are located along the Santa Marta – Bucaramanga Fault zone in the east (Arminio et al., 2011). Fig. 23 and Fig. 24 show respectively the geographical location of the main structures of LMVB and a cross section that covers the SJSB and PSB. The last one indicate the basement configuration and the lateral thickness variations in the sedimentary sequences (Arminio et al., 2011; Mata, 2014).

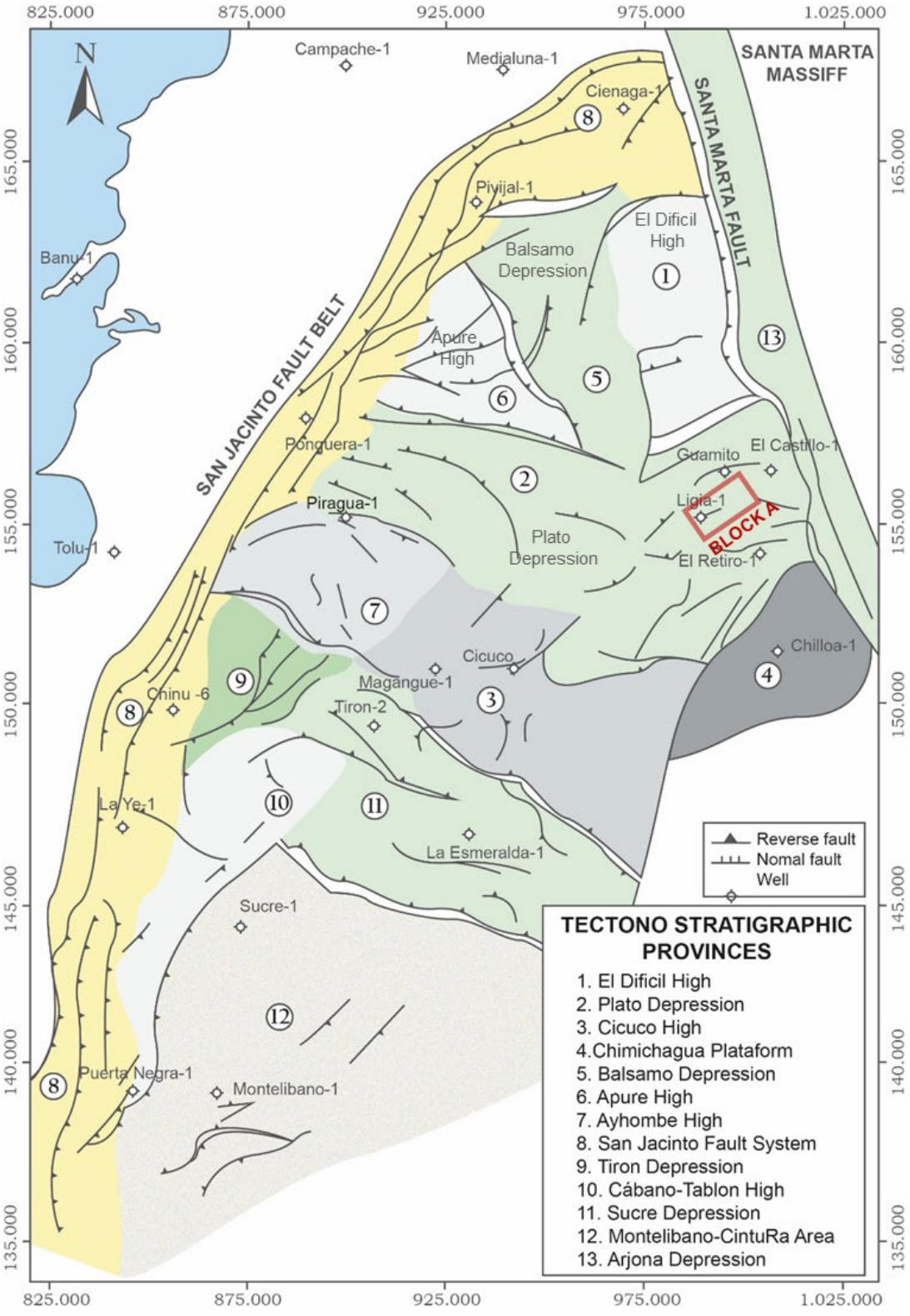

Fig. 23 Present-day structural style of LMVB. Location of major faults. Block A is added for reference. Modified after (Arminio et al., 2011)

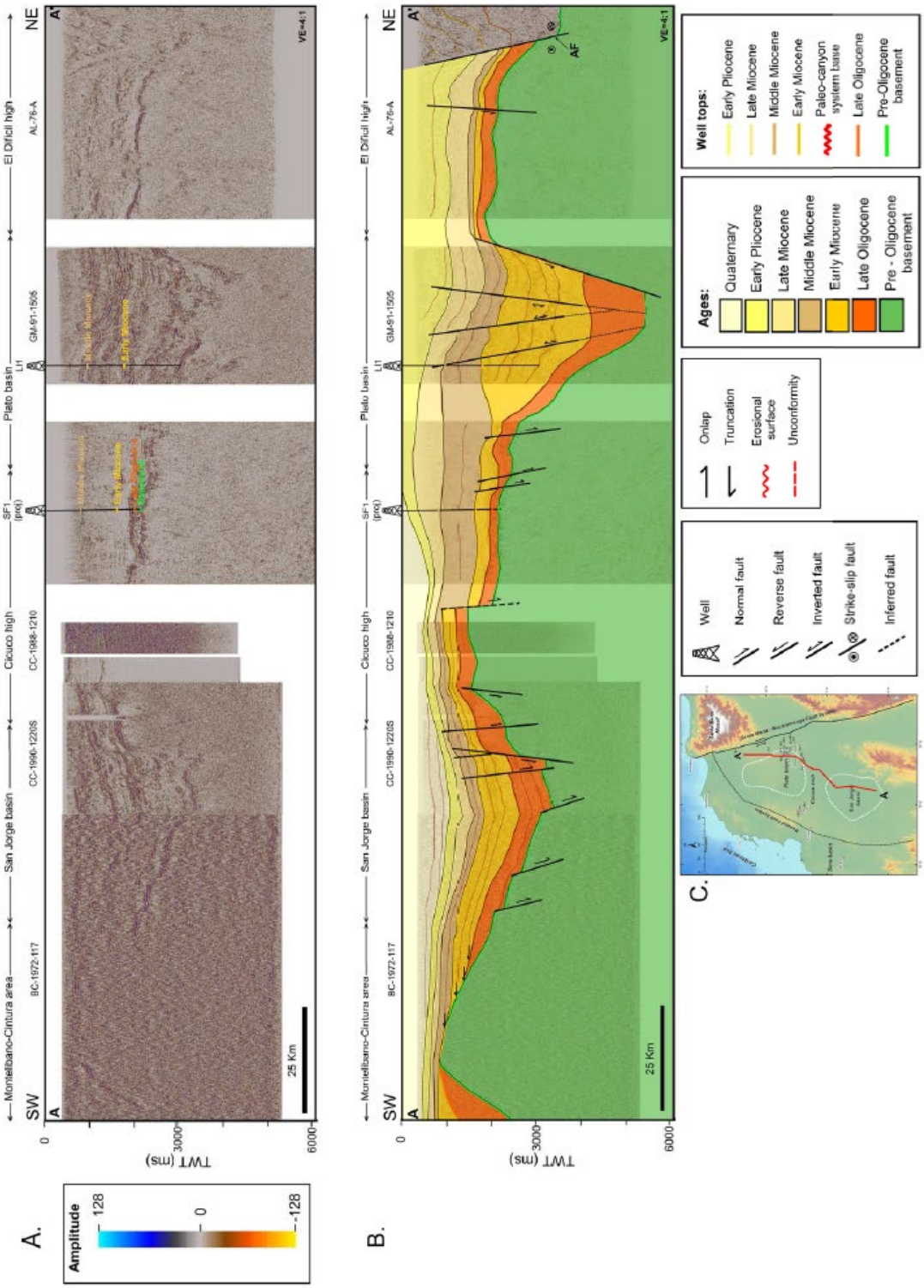

Fig. 24 (A) Raw regional seismic transect going from San Jorge sub-basin (SJSB) in the southwest to *El Difícil* high (Edh) in the northeast. (B) Interpreted regional seismic showing the basement configuration and the lateral thickness variations in the sediment sequences. (C) Base map of the Lower Magdalena Basin (LMB) showing the location of the regional seismic transect (bold red line). Abbreviation: AF = Algarrobo fault. After (Mata, 2014).

3.2.2 Regional stratigraphy

The constant and varied interrelation of the tectonic plates over time in the continental margin of the Colombian Caribbean made possible the formation of diverse zones with structural and stratigraphic behaviours that differentiate the tectonostratigraphic units and its respective exploratory potential. The stratigraphic variation by evolutionary phases is condensed in Fig. 25 and explained below.

During Oligocene – Early Miocene an extensional regime is registered as well as opening of the basin, with accommodation space and steep normal faults bounding the main depocenters. During this time Ciénaga de Oro formation (CDO), was deposited from a fluvio-deltaic to a deep marine environment, represented by calcareous shales and sandstones. The clastic fill of this formation includes: (1) sandstones interbedded with shales deposited in a fluvio-deltaic environment in the eastern PSB, (2) shoreface sandstones deposited in the western and (3) turbiditic sandstones and conglomerates interbedded with shales deposited in the northern PSB. The Oligocene deposits record shallow marine units east of the San Jorge Sub-basin and bathyal marine units to the west. Diachronically, above some of the paleo highs, isolated carbonate banks formed as later equivalent of this Late Oligocene-Early Miocene flooding event (Duque-Caro, 1979; Flinch et al., 2003; Reyes Harker, Montenegro, & Gomez, 2000; Reyes Harker et al., 2004). The Late Oligocene Ciénaga de Oro (CDO) formation is the most important hydrocarbon producer in north-western Colombia.

In Early-Middle Miocene age, as normal faulting continued, subsidence accelerated, causing the regional flooding marked by the early Miocene transgression that also caused isolated carbonate platforms to develop above paleo-highs. In most of the basin, the carbonates have an Early Miocene age, e.g. El Difícil and Cicuco limestone formations (Arminio et al., 2011). The entering of the water is interpreted through corridors located in the north and south sections of the Apure high (Reyes et al., 2004). In PSB and SJSB an Early Miocene and Middle Miocene unit, corresponding to the Porquero formation marks the end of the Early Miocene transgressive event. In the PSB sediments are interpreted as turbidites deposited in a marine environment with facies described from internal neritic to bathyal. Clastic fill includes predominantly shales, lithic sandstone, conglomerate, and turbidites that represent the deepest marine depositional environments. The formation thickness is over the 1200 m. Early Miocene sequence reached its thickest value in the Plato basin, where a shale and turbidites were deposited during this time (Reyes et al., 2004).

In Middle – Late Miocene, main tectonic subsidence time occurred, the sedimentation is mainly controlled by the isostasy processes that equilibrate the orogenic pulses of the Sierra Nevada de Santa Marta, Perijá and the Central and Eastern mountain ranges (Reyes et al., 2004). This uplifting in the east, may have also caused the Middle Miocene carving of the deep shelf canyons in the Plato depression (Arminio et al., 2011). The upper part of Porquero formation was sedimented during this time.

In Late Miocene – Recent, the convergent dynamic movements between the Caribbean and South American plates are reactivated, subsidence slowed and the shallowing-up Tubará formation were laid down. During early Pliocene the final pulse of the Andean Orogeny caused a regional unconformity and started tilting the basin towards the south-west. Fluvial deposits of Corpa formation overlie basal marine shales interbedded with sandstones of Tubará formation (Gomez Tapias et al., 2007). This unconformity represents the highest pulse of the Andean Orogeny registered in the basin (Arminio et al., 2011).

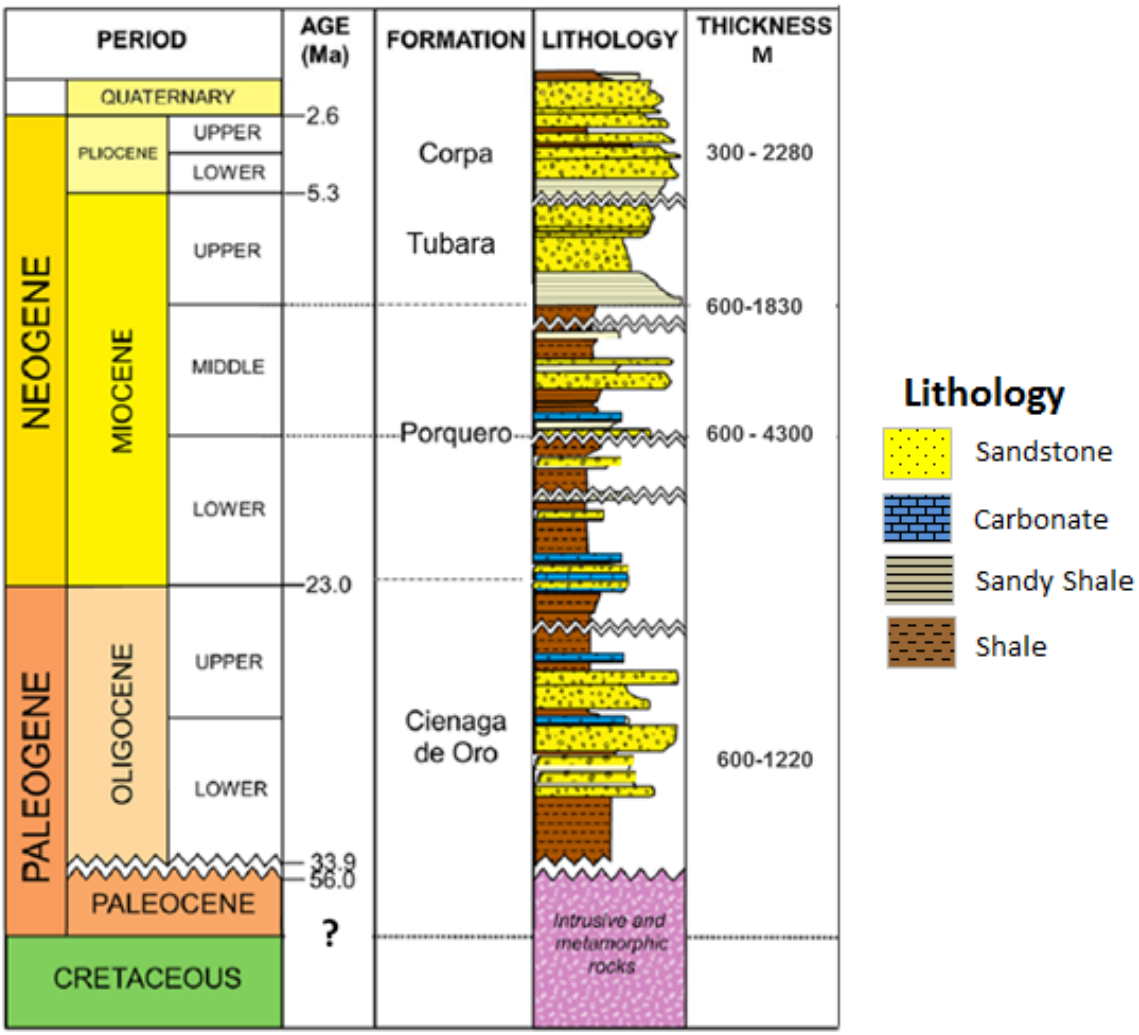

Fig. 25 Idealized chrono- and lithostratigraphic chart for the filling of the LMVB. Total thickness of the Porquero formation is ~3000 m consisting of mainly shales; silty shales and limestones with intercalated low-permeability sandstones (Arminio et al. 2016).

3.2.3 Petroleum systems

Two petroleum systems were proposed in the LMVB based on geological, geochemical, and modelling information. There are evidences of migration and accumulation of hydrocarbons from the Ciénaga de Oro and Porquero source rocks. The following petroleum systems are proposed: Ciénaga de Oro [!][3] and Porquero-Ciénaga de Oro [!] (Arminio et al. 2011). In Arminio 2016 a new petroleum system is proposed in the Guama field, the hydrocarbons found were contributed by a Porquero – Porquero – Porquero [!] mixed petroleum system, with an *in-situ* bacterial gas charge (biogenic petroleum system) from Porquero shales into adjacent Porquero sand reservoirs (Arminio et al., 2016).

[3] The symbol [!] represents a known or confirmed petroleum system (Magoon & Beaumont, 1999).

During the maximum burial processes (Late Miocene) high percentages of organic matter in shallow marine to bathyal sequences, increases the hydrocarbon potential generation in Ciénaga de Oro and Porquero formations. The geochemical evaluation of crude oils, extracts, and rocks, and the integration with structural and stratigraphic information allowed to identify the elements and processes necessary to support the presence of petroleum systems in the basin (Arminio et al., 2011).

Fig. 26 is an event chart of the regional synthesis of subsidence history for the Lower Magdalena Valley Basin, in a simulation based on a pseudo-well located to the NW where the basin is deeper. In this location the hydrocarbon generation came from the Ciénaga de Oro and Porquero formations, from a stratigraphic section deposited during Oligocene-Early Miocene. The expulsion processes occurred mainly since the late Miocene with the critical moment occurring in the Pleistocene (Arminio et al., 2011).

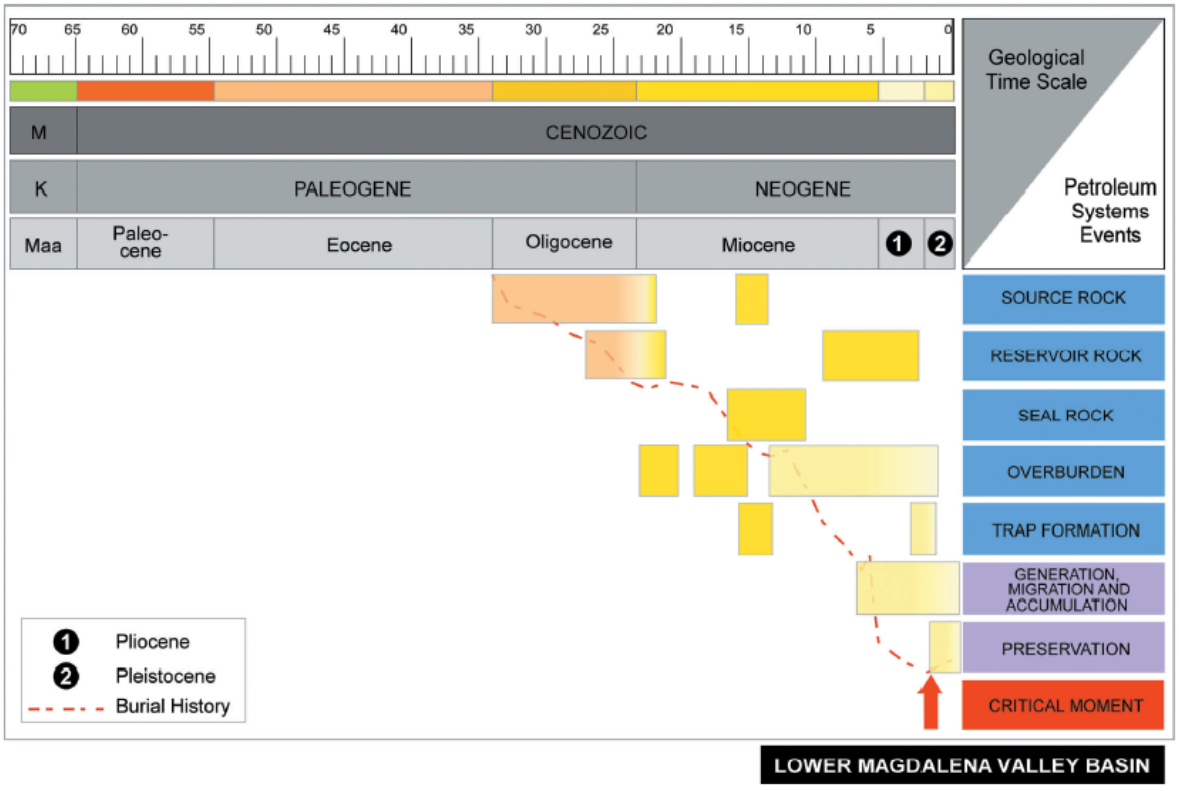

Fig. 26 Event chart of the petroleum systems found in Lower Magdalena Valley basin. Modified after (Arminio et al., 2011).

Fig. 27 displays the estimate burial depth for the basin and associated temperatures. In this simulation the lower Oligocene sequence reached a maximum depth of burial of 6250 m (20500 feet) during the Late Pliocene, and maximum temperatures of 168.33 °C (335°F). The stratigraphic intervals simulated covered Ciénaga de Oro and the Porquero formation. Results of the simulation suggest that these intervals reached maturation levels in the late stage of the oil generation window, i.e. %Ro = 0.9 -1.2, with expulsion processes during the Pliocene (5 to 3 Ma) as stated in (Arminio et al., 2011).

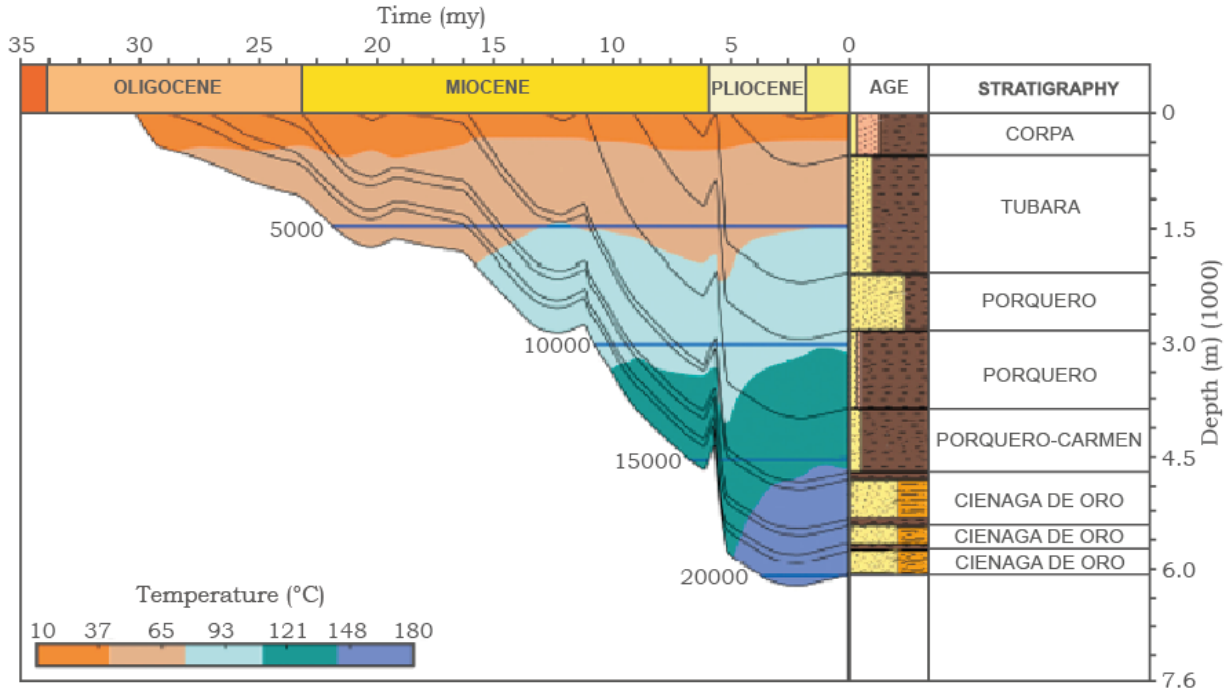

Fig. 27 Burial depth curves for the stratigraphic succession of the LMVB. Modified after (Arminio et al., 2011).

3.2.4 Current regional stress state

Lower Magdalena valley basin is located in the northern part of south America, in a seismo-tectonic region referred as the North-Andean block (NAB), which covers most of north-western South America and the Maracaibo block in Venezuela (Colmenares & Zoback, 2003). The area, from south to north, is characterised by a clockwise rotation of the maximum compression from an E-W orientation to a NW-SE. The maximum compression in the area varies with the dip orientation and depth of the Caribbean slab, which suggest that rotation of maximum compression is a consequence of dynamic events and density heterogeneities in the intraplate zone (Colmenares & Zoback, 2003; Fleitout & Froidevaux, 1982).

The arcuate nature of the subduction margin of north western South America has been emphasized by Colmenares and Zoback (2003) as fundamental tectonic control on its modern stress state and style of faulting. This eastward Caribbean plate migration is responsible for the oblique subduction that is interpreted to have affected the northern edge of the South America continent (Mann & Escalona, 2011) in (Bernal-Olaya et al., 2015).

In the study presented by Vargas and Duran (2005), stress inversion analysis was applied to 94 focal mechanism, satellite geodesy results from the CASA project (Mora-Páez et al., 2018; Trenkamp et al., 2002) were used to improve the analysis and finally shear wave splitting was analysed. Main results of this study suggest tendencies of NW-SE to W-E throughout the Colombian Pacific Coast, and the final stress inversion by means of deep seismicity (>130 Km) suggest a tendency of NW-SE (Perico & Perico, 2014). According to the World Stress Map (WSM) (Heidbach et al. 2016) selected data points out a regional maximum horizontal stress (S_{Hmax}) with an azimuth between 61° to 110°. Fig. 28 shows an excerpt of the current WSM. It shows that the present-day stress field in the LMVB area is characterised by a S_{Hmax} orientation striking between W-E and WNW-ESE (86°- 120°). This fits to the

regional stress pattern in north-western South America described by Colmenares & Zoback (2003) and Vargas and Duran (2005), indicating a clockwise rotation of the maximum horizontal stress axis from a W-E to a NW-SE orientation between Peru and northern Venezuela.

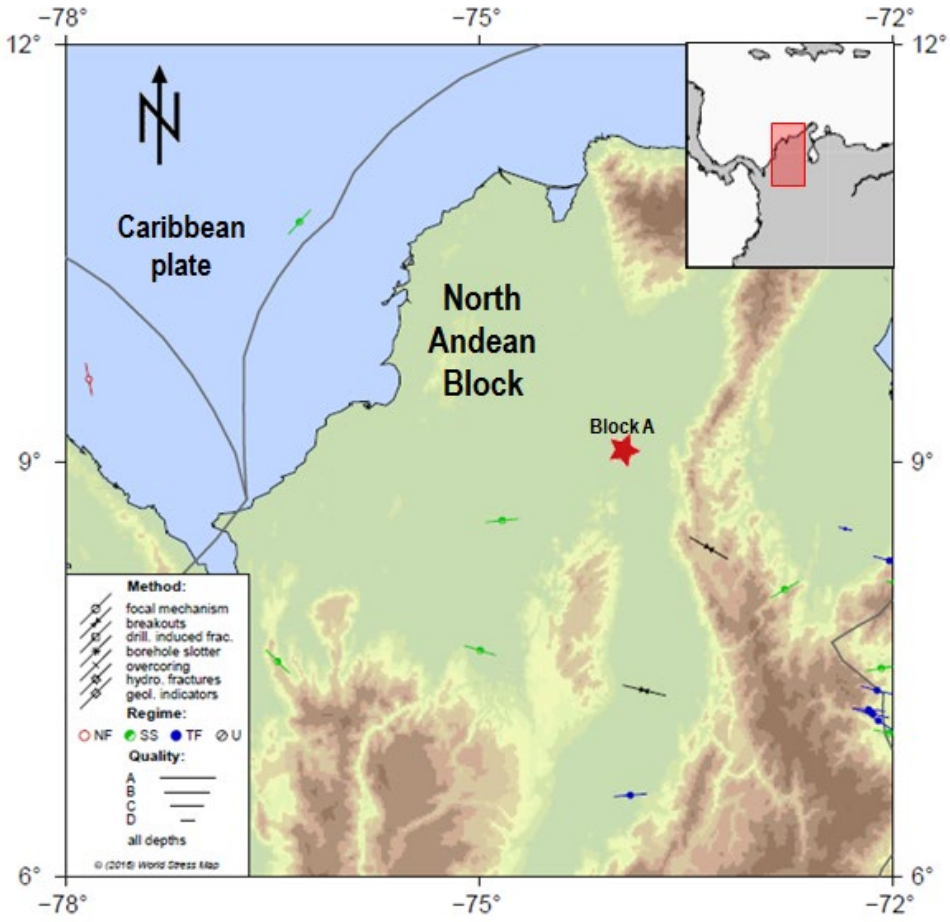

Fig. 28 Excerpt from the World Stress Map (Heidbach et al., 2016) showing the orientation of the maximum horizontal stress (S_{Hmax}) for northern Colombia and surrounding areas. Red star indicates location of study area in the north-eastern part of the LMVB.

3.3 Tectonic evolution of northern Colombia and the Lower Magdalena Valley Basin

During Cretaceous time (Fig. 29-A and Fig. 29-B) the Nazca plate underneath the South American plate generating a volcanic arc. During Paleocene the Caribbean Plate opened a space between the north and continental rocks of South American plate and simultaneously the folding process of the San Jacinto Folded Belt began. By this time, the block to the east of SJFB was exposed and represented by the Central mountain range together with the Santa Marta Massif to the north (Paul Mann & Escalona, 2006) in (Bernal-Olaya et al., 2015; Reyes Harker et al., 2004).

By Eocene time, a regional tectonic change occurred; the Caribbean plate collides changing the displacement direction eastwards, uplifting pulses of the Perijá mountain range, Santa Marta and Santander massifs (Reyes et al., 2004). The collisional belt migrated eastward to the north of South American plate generating a right-lateral strike-slip displacement (Bernal-Olaya et al., 2015; Kroehler et al., 2011; Mann & Escalona, 2006).

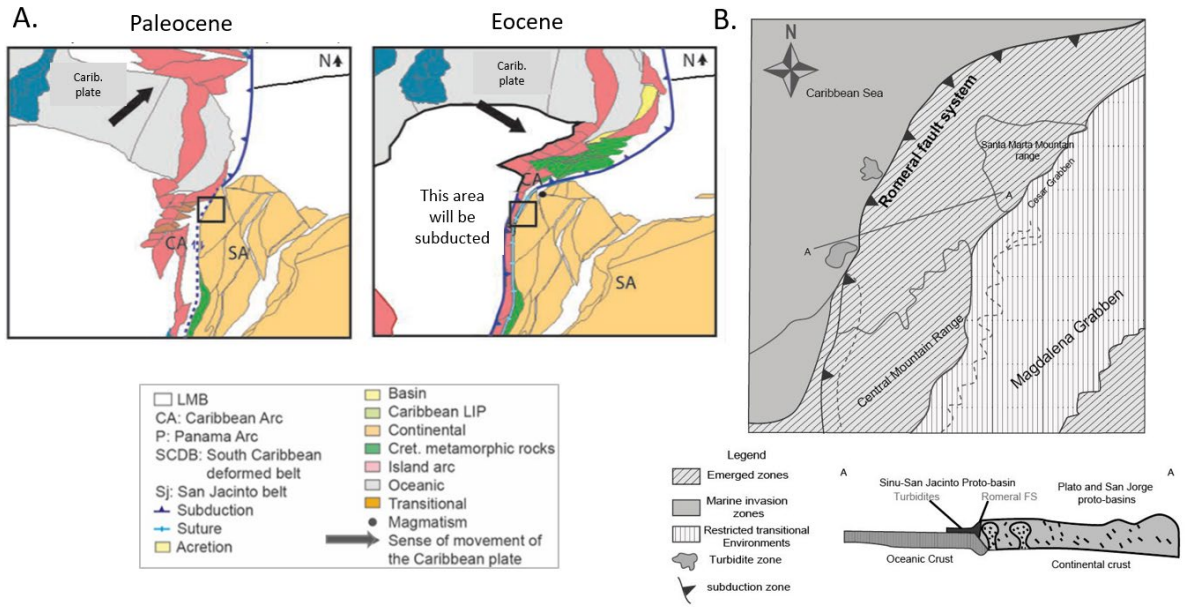

Fig. 29 (A) Paleocene-Eocene north-western margin tectonic setting. The arrows shows the Caribbean plate changing the displacement direction eastward. After (Reyes Harker et al., 2004). (B) The paleogeography of during Paleocene - Eocene period. The block to the east SJFB was exposed. Modified after (Bernal-Olaya et al., 2015).

Although the authors agree the stratigraphic and structural variations of the geological provinces in northern Colombia were determined by diachronic eastward displacement of the Caribbean plate, they have shown differences in the specific proposal that explains which elements and processes allowed the transformation of the PSB and SJSB. The following section describes the different points of view among the models, using as reference the proposal of (Bernal-Olaya et al., 2015; Mata, 2014; Reyes et al., 2004)

- Models for the LMVB origin involving subduction-related forearc basins: Bernal 2016, Caro 2002.
- Models for the LMVB origin involving large-scale rotation: Reyes et al., 2004.
- Tectonic collapse of the Central Cordillera: Villamil, 1999; Arminio et al., 2011.

Details of such proposals are addressed in (Arminio et al., 2011; Bernal-Olaya et al., 2015; Caro & Spratt, 2003; Mata, 2014; Mora et al., 2018; Reyes et al., 2004; Villamil, 1999). Deciding on a specific model of LMVB evolution does not correspond to the scope of this study. The section below explains in an illustrative and representative manner the tectonic events responsible for the LMVB origin in chronological phases from Oligocene to Recent, as a summary of the models presented in (Bernal-Olaya et al., 2015).

During Oligocene age, extension was greater to the north of the Plato Sub-basin (PSB), where short and discontinuous normal faults at right angles to the subduction direction (NW-SE) constrained the depocenters. Low sediment deposition characterised the Oligocene and Early Miocene underfilled period (Fig. 30-A to Fig. 30-C) (Bernal-Olaya et al., 2015) .

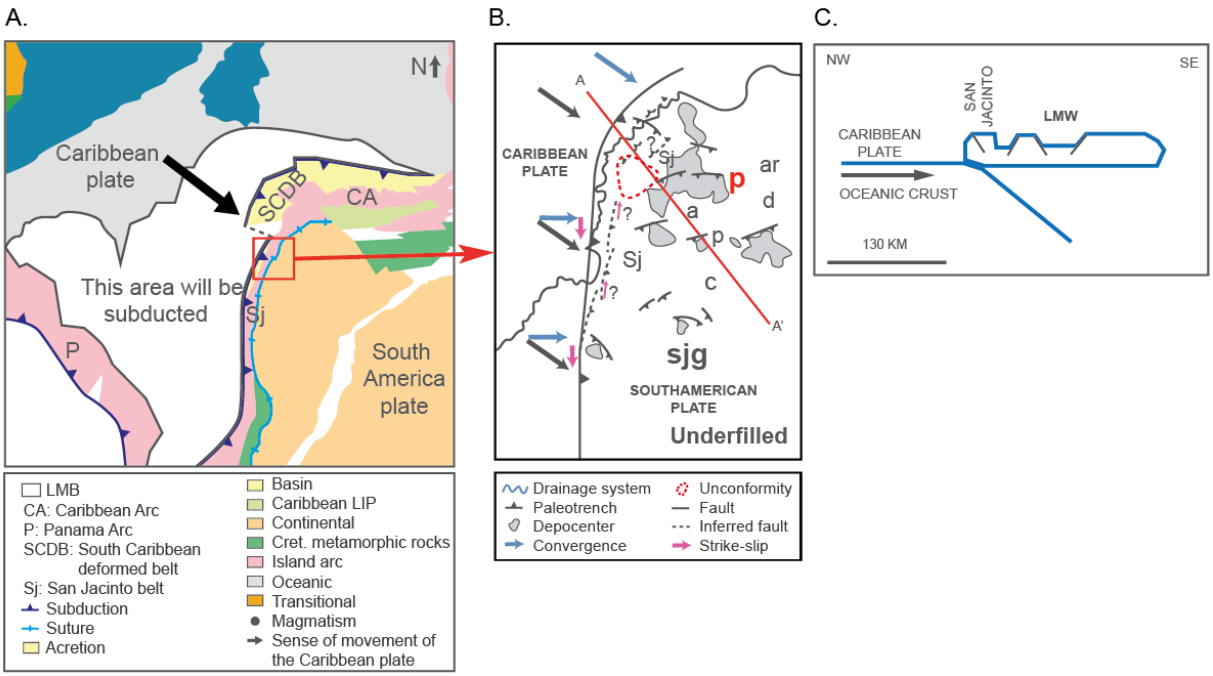

Fig. 30 (A) Reconstruction at 26 Ma (Chattian) showing continued subduction of the Caribbean plate beneath South America. White polygons identify areas to be subducted (B) Radial normal faults that are perpendicular to the margin and parallel to the convergence direction are active. (C) Cross-section A-A' showing underfilled depocenters. Modified after (Bernal-Olaya et al., 2015)

During Early Miocene age (Fig. 31), the geometry of the subducted slab at depth beneath the South American plate, may have promoted deepening of the forearc basin. Once the lows where infilled, sediment was dispersed along and across the basin infilling all available accommodation space. Neritic depositional environments were mainly developed and interconnected the earlier fault-controlled depocenters (Bernal-Olaya et al., 2015).

In the Middle Miocene (Fig. 32) regional east-west convergence began. There is a regional unconformity that marks the change of deep to shallow facies. This unconformity coincides with the age of the first pulses of the Andean Orogeny and probably involves uplifting on the San Jacinto Folded Belt. Sediment input increased rapidly, infilling the available space for deposition. The lower angle of Caribbean subduction (~4°) beneath the South American plate, may explain the prominent middle Miocene unconformity seen in the north-western San Jorge Sub-basin (Bernal-Olaya et al., 2015).

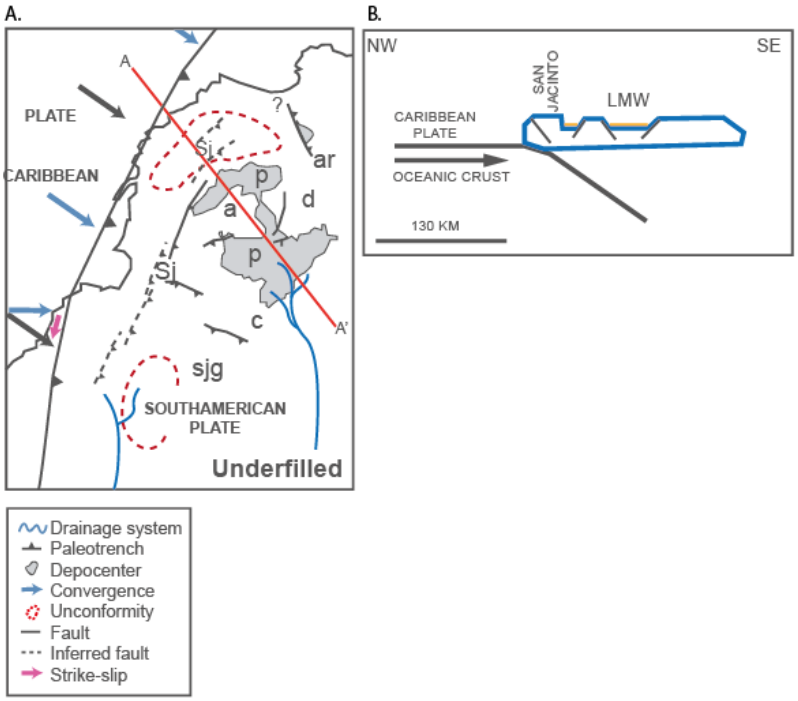

Fig. 31 Early Miocene tectonic setting. (A) Active deposition of terrigenous sediments. Radial normal faulting and definition of discrete, sub-circular and radial depocenters indicates that steep subduction remained active. (B) Cross-section A-A' displaying underfilled basin (Bernal-Olaya et al., 2015).

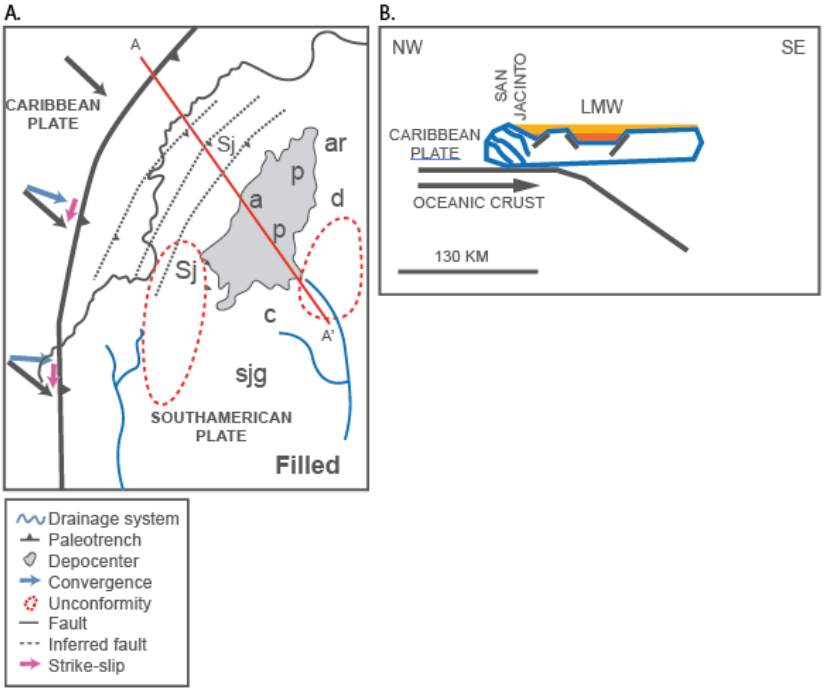

Fig. 32 (A) Middle Miocene: At this time the basin is filled to sea level and regional uplift occurs along the western edge of the main depocenter. (B) Cross-section A-A' displaying basin infill. Modified after (Bernal-Olaya et al., 2015)

By late Miocene to Pliocene time (Fig. 33), subduction of the Caribbean plate continues beneath both the LMVB in Colombia and Venezuela (Bernal-Olaya et al., 2015). This is a time of great instability and uplifting to the north-western side of Colombia as a result of the lateral compressional (northwest – southeast) stresses that produced continuously increasing processes of rifting, erosion and fracturing (Bernal-Olaya et al., 2015). The basin became overfilled and eventually shed sediments into the offshore Magdalena delta as submarine fan. During this time, eastward migration of the Caribbean plate has continued, and compressional deformation has increased significantly across de Caribbean. The Sinú belt continued emerging because of lateral compression. During this time an increment of continental sedimentation occurred in the Plato and San Jorge Basins. This event has been correlated with the Andean Orogeny climax (Pindell & Barrett, 1990).

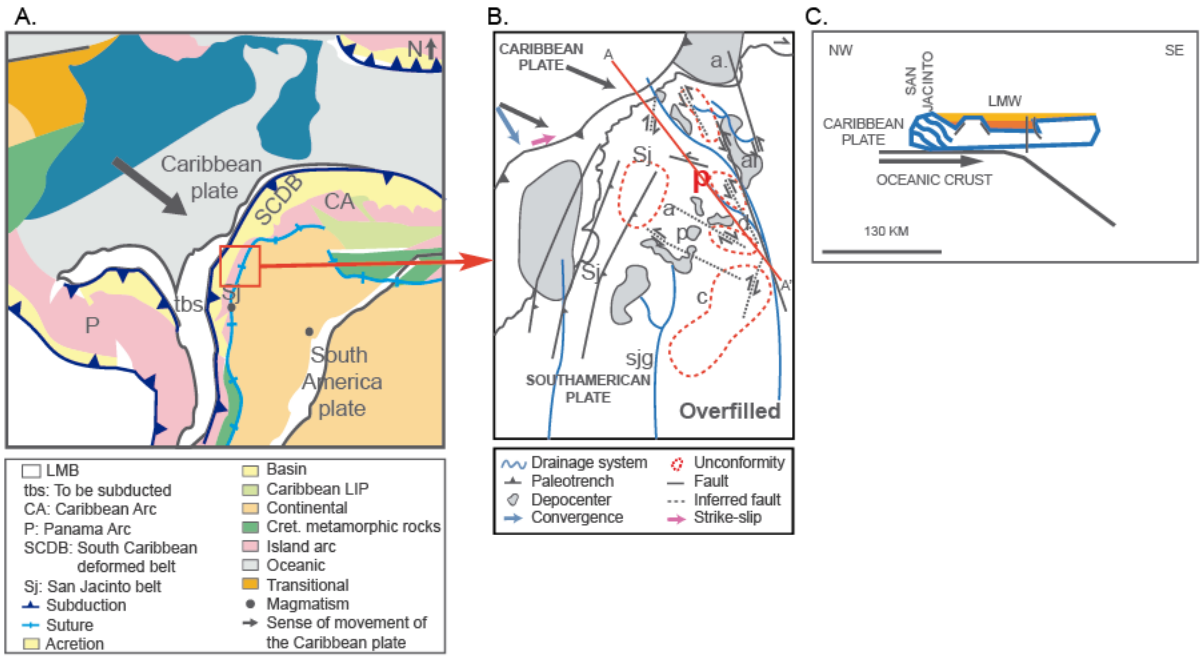

Fig. 33 Late Miocene to Pliocene. (A) Strongly arcuate Caribbean–South America plate boundary. Maximum subduction. (B) Structural features in the basin area (C) Cross-section A-A' shows the overfilled basin. Modified after (Bernal-Olaya et al., 2015).

3.4 Case study area: Block A

The Block A is a seismic survey area with an extent of 110 km², located in the Guama field, to the north-eastern part of the Plato sub-basin (PSB). Five wells have been drilled (wells A, B, C, D and E) which correspond to the last exploratory stage of LMVB (Fig. 34).

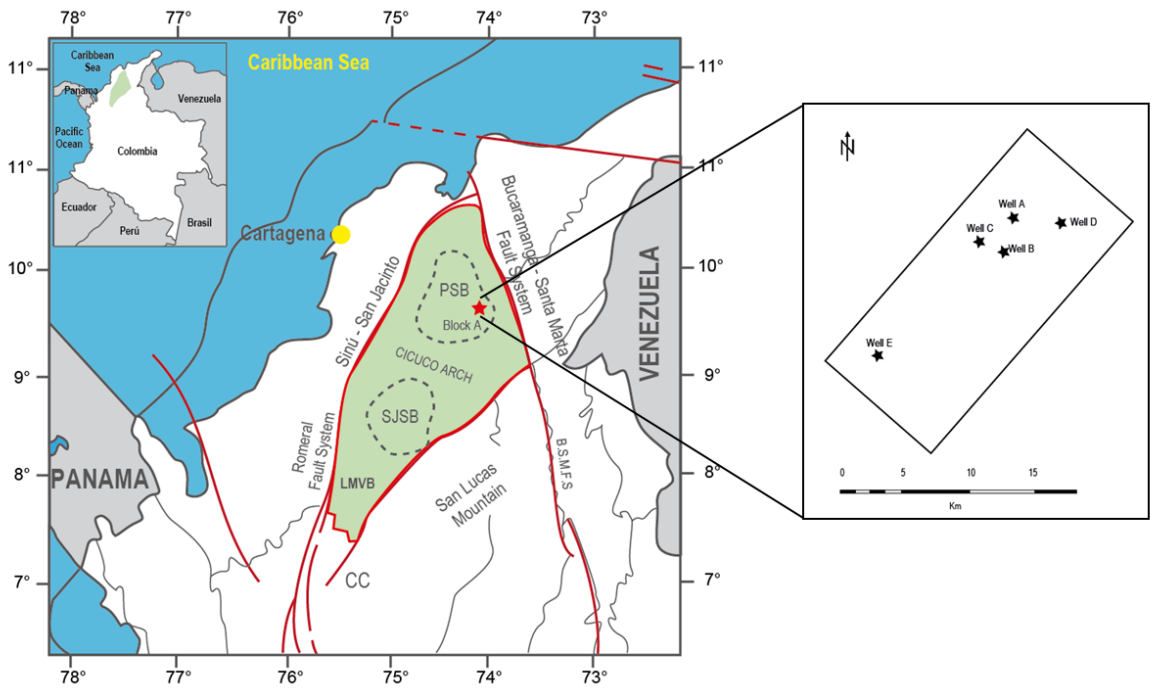

Fig. 34 Geographical location of the Lower Magdalena Valley Basin and an extraction displaying Block A and the wells available for the study.

3.4.1 Stratigraphy

In Guama field the depositional facies were described as turbidites taking into consideration vertical gamma ray log, cuttings, biostratigraphic evidence and descriptions of cores (Duque – Caro 1992 and Bolivar et al, 2013). Between these interpreted turbidites, the sub-facies are: submarine channels, levee - crevasse splay and matrix – supported conglomerates (Arminio et al. 2016).

The Block A is filled with a thick shale-prone marine sequence of Upper Oligocene to Late Miocene age, represented by the Ciénaga de Oro, Porquero and Tubará formations. This formations exceeds 3000 m of total thickness of massive shales and silty shales with subordinated laminated fine grain sandstone (Arminio et al., 2011; Di Luca et al., 2014). The sequence sedimented during the Oligocene known as Ciénaga de Oro formation, has not been drilled in Block A. Seismically, a sedimentary sequence interpreted below the last level reached by the wells in the area, could be equivalent to this formation.

For characterization purposes of the reservoir, Porquero formation was divided for practical applications, into further units known as Porquero F, E, D, C sedimented during Early Miocene; B, A and AA during Middle Miocene. These units were defined between unconformities interpreted on logs and 3D seismic as shown in Fig. 35-A and Fig. 35-B. The Plio-Recent molasses, known as Corpa formation is missing in Block A due to recent uplifting and erosion.

The oldest stratigraphic control drilled is the top of the Carmen Shale of early Miocene age in well E. Seismic geo-transects suggest that the undrilled section contains more than 2130 m of Carmen Shale and Oligocene Ciénaga de Oro formation, most probably sedimented in pro-delta and marine muds environments. Through 2D and 3D seismic was identified a basal unconformity of Early Miocene age, related to paleo-canyon erosive processes (Arminio et al., 2016; Reyes Harker et al., 2000; Suarez, 2009). Bernal and Mann (2015) dated this unconformity as Aquitanian 20-22 Ma. In well E, the top of

the unit F, is eroded by this unconformity. During early to middle Miocene period, a high sedimentary load was transported to the basin through submarine canyons (Plato paleo-canyon) and many unconformities were generated, due to the isostatic accommodation as a result of the rising of Santander and Santa Marta Massifs and Central and Oriental mountain range (Reyes Harker et al., 2004) (Fig. 36). The Middle Miocene lower contact is a regional unconformity that marks the change of deep to shallow facies, which indicate the effects of compressive regime in the study area.

During the drilling of well E, from approximately 2500 m, specifically in the sedimentary sequence represented by units E and F, operational problems increased. The drill rate decreased, the formation pressure exceeded the hydrostatic pressure exerted by the mud fluid column, the gas units, and the kick events in the well increased. The weight of the mud had to be adjusted abruptly from ~1400 to ~2200 Kg/m^3, to obtain a well drilling control (Internal reports). This process was also observed in the same sequence, in wells located in the vicinity of Block A. From there, it could be assumed that the normal gradient of formation pressure from unit D downwards was affected by the tectonic effects that occurred in the early stages of the evolution of the basin. Continuous and abrupt processes of subsidence and fillings of large sediment inputs could have created an imbalance in the normal compaction of the sediments, originating high regime overpressures in the sequences deposited in the Early Oligocene – Early Miocene period.

The Late Miocene to early Pliocene succession, known as Tubará formation, is mainly shale prone and shows a shallow - upward trend from bathyal to outer neritic according to biostratigraphic data. During Pliocene – Recent, molasse deposits known within the basin as Corpa formation, is considerably thick in the west of the basin, while in Block A is missing altogether due to recent uplifting and erosion (Suarez, 2009). Instead, a flat – lying Late Pliocene to Quaternary alluvium, not thicker than 300 m, covers the entire block in angular relation with the underlying shale section.

Mud diapirism

Through the interpretation of 2D and 3D seismic surveys, it was identified the presence of two mud diapires, towards the eastern side of the Block A. These have been dated as Miocene to Pliocene structures and do not show surface expression (Arminio et al., 2011; Vernette et al., 1992). The diapiric processes registered during this period may be a consequence of the large amount of material contribution during the recent orogeny to the Colombian Caribbean Basin on a relatively short period of time (Reyes et al., 2004). The presence of shale diapires in the region was proposed by Cáceres *et al*., 1981.

Diapires are cut off by the recent alluvium, reasons for which they are considered inactive at present. The diapires are vertical and cut through Late Miocene and Pliocene tilted beds, indicating that they mobilized in Early to Late Pliocene. The detachment is immediately above Porquero C, and the sand in Porquero C and D are continuous below the diapires. Pressure data from well D also indicates that the reservoir pressure regime continues below the diapires with a main overpressured compartment interpreted across the area (Arminio et al., 2016).

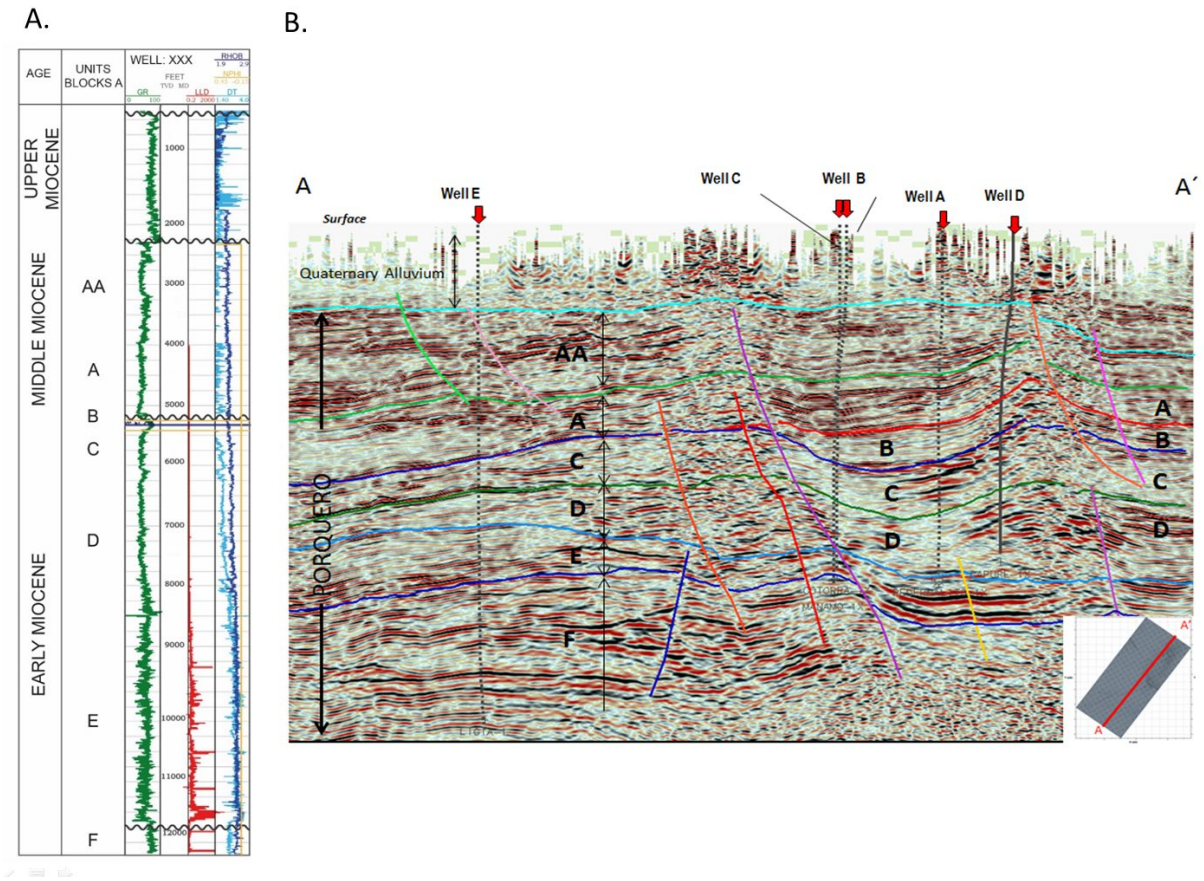

Fig. 35 (A) Borehole electric logging typical of the area showing the local division of stratigraphic units. (B) SW-NE oriented seismic section through Block A with structural and stratigraphic interpretation. Letters correspond to units of the Porquero formation. Red arrows show well locations (Modified after Di Luca et al. 2014).

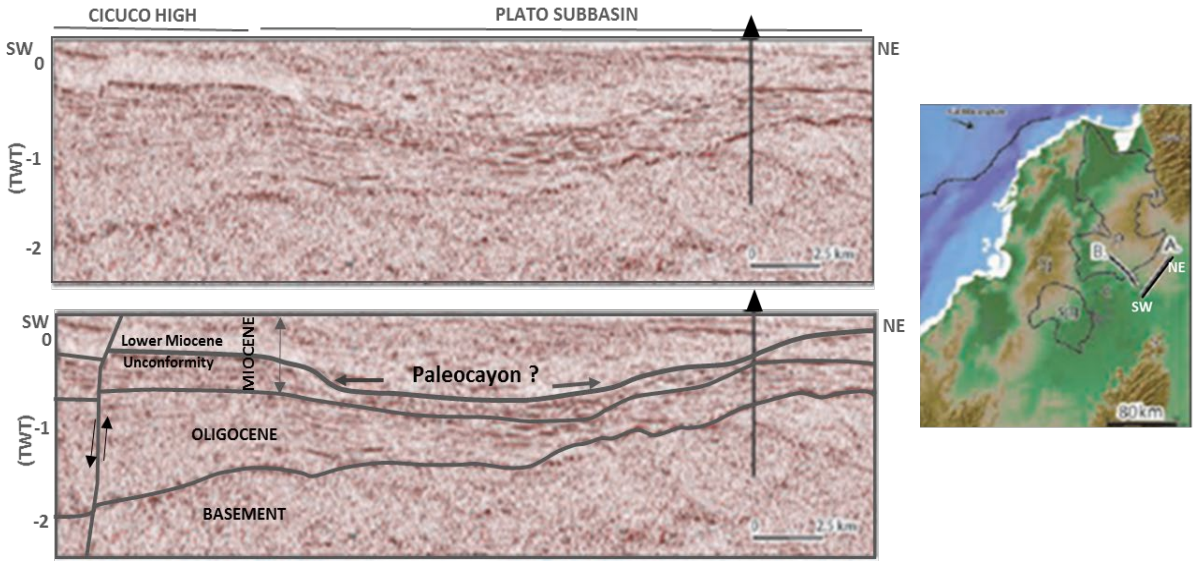

Fig. 36 SW-NE oriented seismic section through Block A, showing the Early – Middle Miocene paleo-canyon. Modified after (Bernal-Olaya et al., 2015).

3.4.2 Local paleogeography

The paleogeography in Block A was interpreted after a biostratigraphic and sedimentological analysis of core and drilling samples from wells located in the study area and surrounding, with the integration of the regional study for the LMVB basin described in (Bernal-Olaya et al., 2015)

During Oligocene extensive regime, the normal faults controlled the wedge of costal to shallow marine sedimentary deposits in the underfilled Plato sub basin. As the subsidence processes continued during Miocene period, the sea level increased generating important flooding surfaces (External neritic to Bathyal) that covered the Oligocene age sequence with silty / shale sediments and intercalations of fine-grained sandstones. The units E, D and C, sedimented during Early Miocene, are quartz rich and sub-lithic sandstone interbedded with shale and micritic limestone to the top of the sequence, defining a shallow−to−deep environment condition. Average thickness of Porquero D range from 300 m to 750 m. Porquero C has a predominant lithology of shales and laminated sandstones and reported thickness ranges from 240 m to 360 m

Unit B represents the deepest marine depositional environments in the basin during the Miocene age (approximately 15.6 Ma) (Mata, 2014). This unit was deposited in an external neritic to bathyal paleo-bathymetry and it is conformed by shales, pyrite traces and disseminated limestones and organic matter. In Block A, at the top of this unit an unconformity represents the end of the extensional regime and the first pulses of the Andean Orogeny. The stratigraphic units A and AA were deposited in similar but shallower environment (Fig. 37).

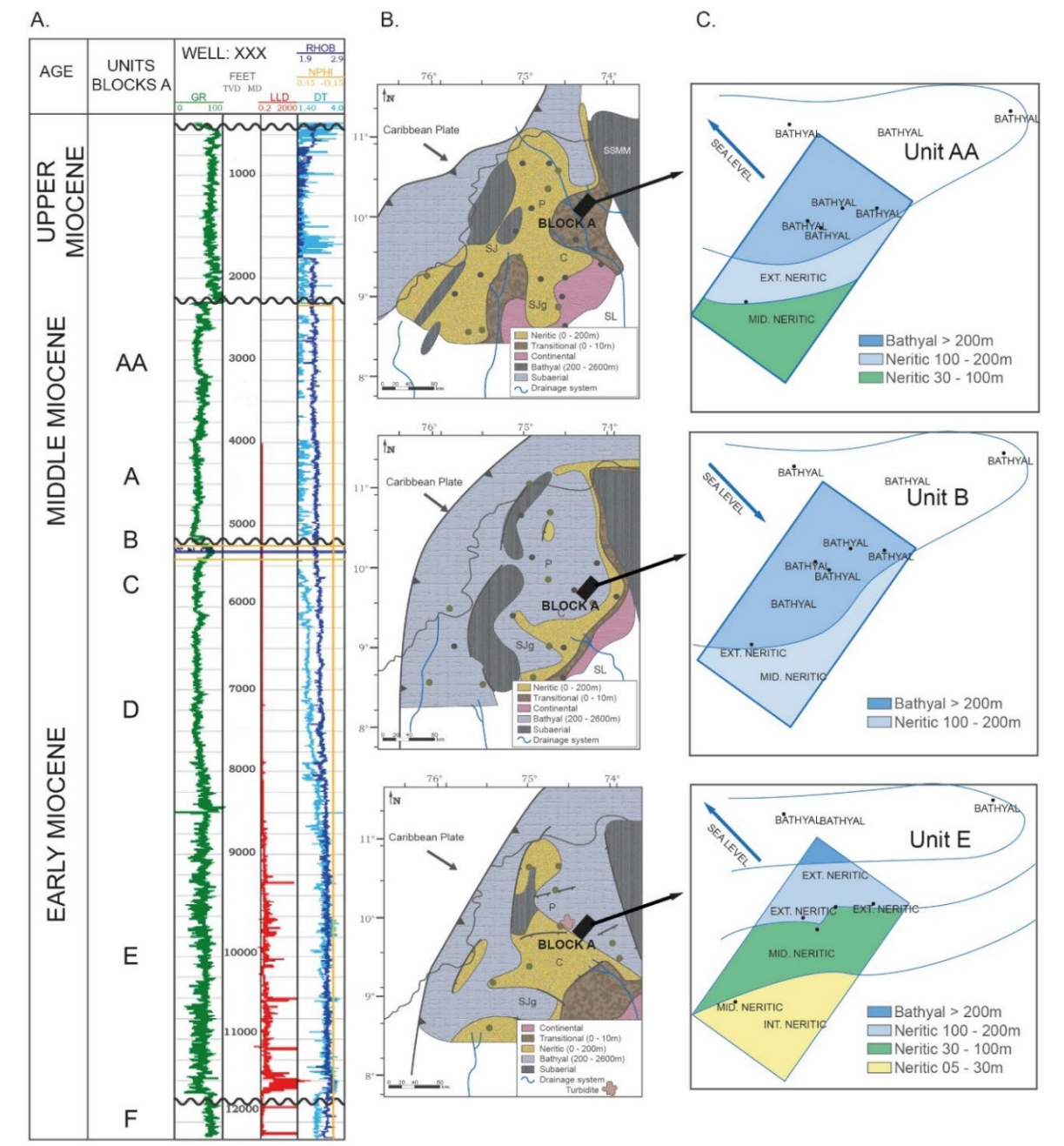

Fig. 37 (A) Reference well log for the area. (B) Paleogeography of the LMVB after Escalona and Norton (2010) in (Bernal-Olaya et al., 2015). (C)Paleo-water depth interpreted in the Block A area.

Chapter 4 Dataset of Block A

The reliability of a proper mechanical model, independent of its further application (e.g., wellbore stability, critical state faults analysis, geothermic or CO_2 storage), relies strongly on the accuracy of the description of the rock mechanical property along the wellbore. For this, is necessary to integrate several datasets and perform an adequate interpretation of the rock behaviour.

Well logs have become a primordial data source of subsurface properties, as they allow taking vertical records of different parameters through the register of the responds of an electric pulse - radioactive source into the formation or wellbore wall image records. It is possible to derive a handful of formation petrophysical and fluid properties from the registers, as well as extract elastic and strength parameters, given the relationships that exist between rock physical properties and the mechanical properties (Archer & Rasouli, 2012). The data recovered from logs serve for a wide range of purposes depending on the type of project (geometrical parameters, petrophysics, rock physics, formation damage, image logging, etc.).

Obtaining a core from a target of interest and performing the necessary laboratory procedures, can be a costly process. However, rock mechanical testing on cores help in the definition of the correlation between static and dynamic properties, which are required to build mechanical earth models (Herwanger & Koutsabeloulis, 2011). Core laboratory testing represents hard data and should be the ultimate reference points for calibration of the model. Rock mechanical tests results accuracy is subjected to laboratory procedures, and proper corrections and empirical correlations should be undertaken carefully.

Seismic interpretation, well log analysis, stratigraphy, sedimentology, biostratigraphy, core analysis, drilling data and dynamic behaviour of the reservoir are fundamental to know which methodology is more efficient and will reflect better the *in-situ* state of the reservoirs. The data base for Block A available for this study (Table 1) was provided by the industrial partner and consists of a 3D seismic survey and five wells, including comprehensive log data, cores for rock mechanical lab tests and various *in-situ* stress measurements.

For the basin and petroleum systems approach, specifically, regional trends and thickness maps with quantitative lithologies were generated, considering ditch and core samples, master logs, paleo-bathymetry maps and information from 10-12 additional wells, so that relevant information is available for each defined geological horizon. The whole dataset was provided by the industrial partner. Furthermore, charts with total organic carbon (TOC %), vitrinite reflectance (Ro), structural tops, Kelly bushing (KB) depths and coordinates were sorted. These datasets are used to set up and calibrate the geomechanical models outlined below.

In the following section, there is a general overview of the most relevant data alongside standard management methods to ensure its best quality. The theory behind certain methods is further explained in section 2.5.

Table 1: Data available for Block A

Well/Data	A	B	C	D	E	F
GR/RT	✓	✓	✓	✓	✓	✓
RHOB/NPHI	✓	✓	✓	✓	✓	✓
DTCO/DTSM	Dipole 8 1/4	12 1/4	✓	Dipole 12 1/4	DT	DT
Caliper	✓	✓	✓	Oriented	✓	✓
Form. Pressure	✓	✓	✓	x	x	x
OBMI/DLIS	x	✓	✓	✓	x	x
Lithology	✓	✓	✓	✓	x	x
Well tops	✓	x	✓	✓	x	x
VSP	Triaxial/Brinell	x	x	x	x	x
Drill. diaries	✓	✓	✓	✓	✓	x
survey	✓	✓	✓	✓	✓	✓
LOT/FIT	FIT	FIT	LOT	LOT	x	x
Mech. State	✓	✓	✓	✓	x	x
Mud log report	✓	✓	✓	✓	x	x
ECD (MD)	✓	✓	✓	✓	x	x
Hydro-frac data	✓	✓	✓	✓	x	x
3D seismic	Horizons, geo-bodies, faults, diapires.					

GR=Gamma Ray, RHOB= density log, NPHI= neutron log, DTCO= compressional slowness, DTSM= shear slowness, OBMI=oil-based image logs, LOT= Leak-off test, FIT= formation integrity test, ECD=equivalent circulation density.

4.1 Well logs

There are five wells (termed A, B, C, D and E) within the seismic survey area. Wells A to D comprise, among others, the gamma ray, density, and dipole sonic logs, that are fundamental for geomechanical modelling. Well E counts only with compressional slowness log. To fill in this data gap, a linear correlation was stablished between the compressional and shear velocities. The resulting regression was then applied to the well E profile and synthetic shear slowness was derived. Auxiliary wells are named wells Y and Z and are located surrounding the 3D seismic survey and are helpful for local correlations. These wells (Y-Z) have pressure data and act as further constrain for the pressure model.

An overview of the available sonic and density data for well A can be observed in Fig. 38. It is common that old wells, or those with a basic logging set, does not have dipole sonic but just register compressional slowness (Δ_T), as is the case of wells E, Y and Z. Well E, as the first well drilled in the area, has only a compressional slowness, but no shear slowness log. To fill this gap, a specific empirical correlation between shear and compressional wave velocities was established in wells A to D and subsequently applied to well E to generate a synthetic shear wave sonic log (Fig. 39).

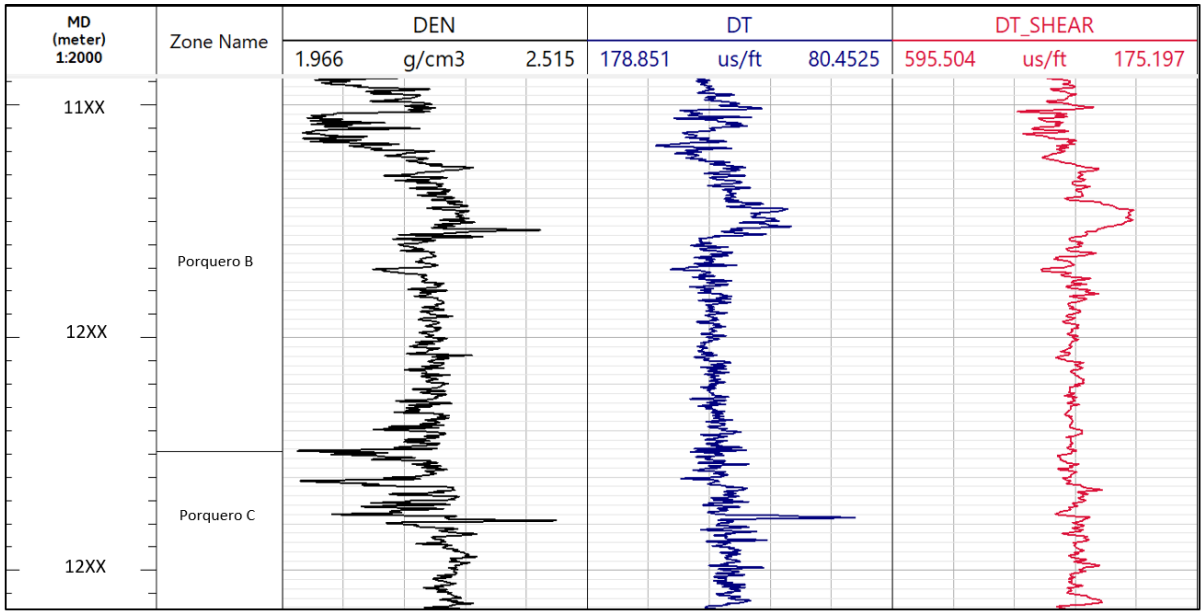

Fig. 38 Overview of density, compressional and shear slowness available for Porquero units.

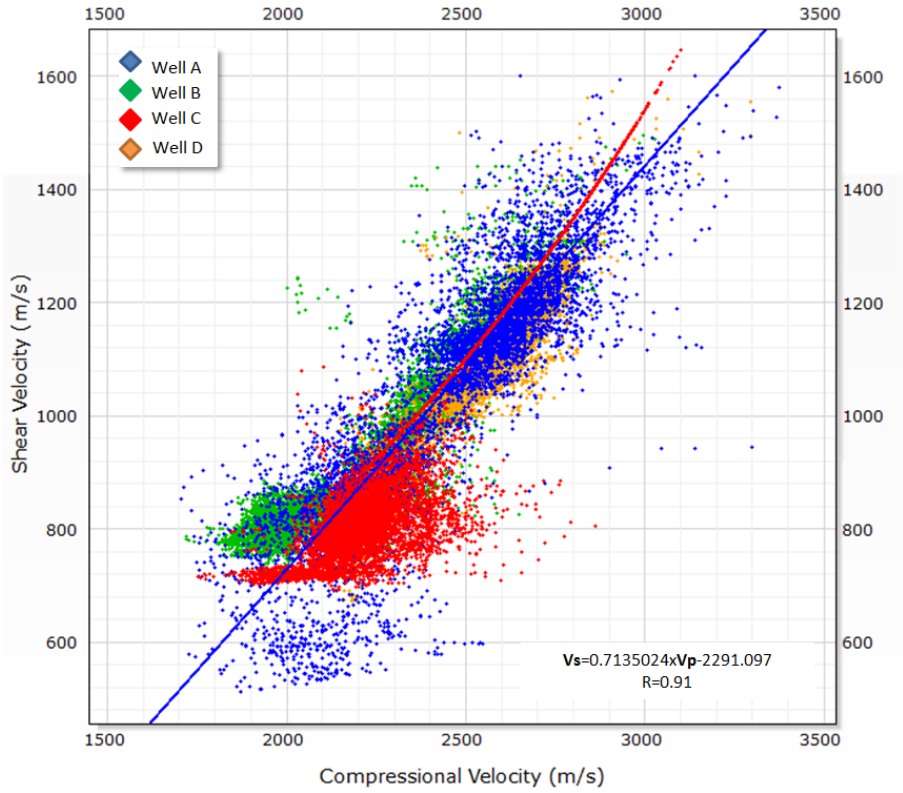

Fig. 39 Vp. vs Vs. linear regression for wells A-D. The correlation is later applied to fill in the data gaps in well E.

An example of the determination of induced fracture presence along a wellbore is observed in Fig. 40. For well B an interval >1000 m was evaluated. Likewise, for well C, an interval >800 m was analysed. These intervals correspond to the end of Porquero B to middle Porquero D units. The evaluation of these fractures resulted in an approximate striking orientation of WNW-ESE (~120°). With respect to the borehole breakout information, there is a standard agreement based on previous studies (internal reports) which conclude that the breakouts do not show a preferred orientation. Within Block A, image logs for analysis of borehole breakouts and drilling-induced fractures are available for wells B and C (Fig. 41-A and Fig. 41-B).

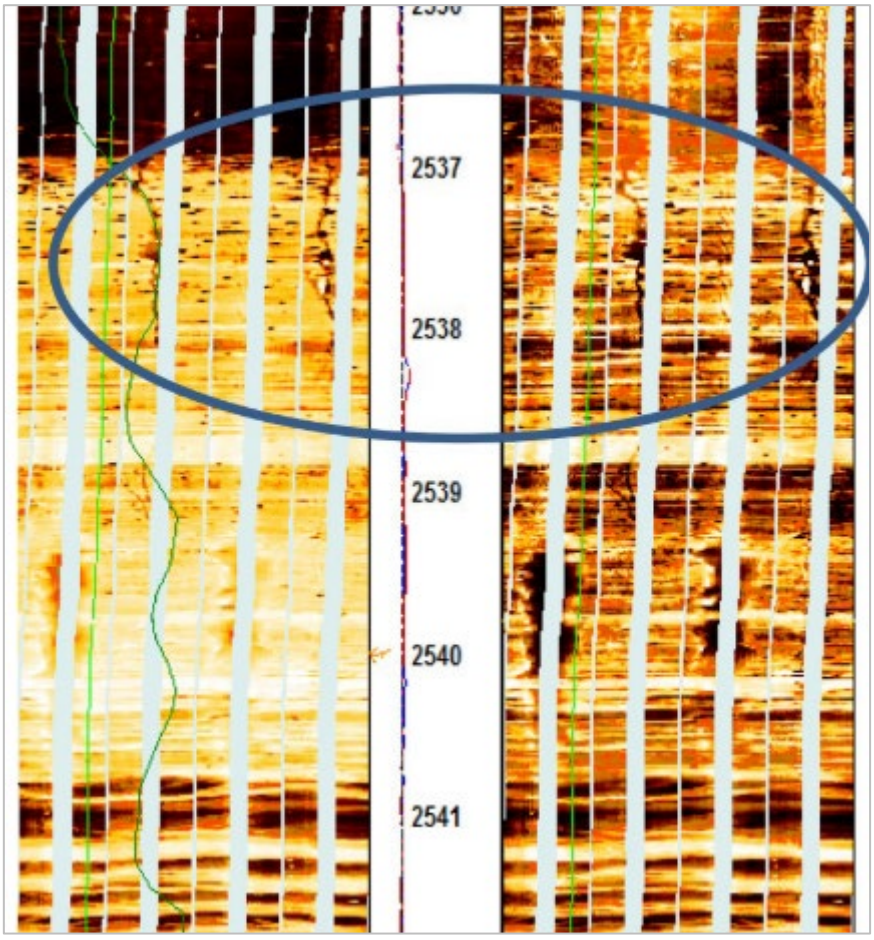

Fig. 40 Example of image log processing to assess drilling induced fracture presence. After (Tiwari, 2013).

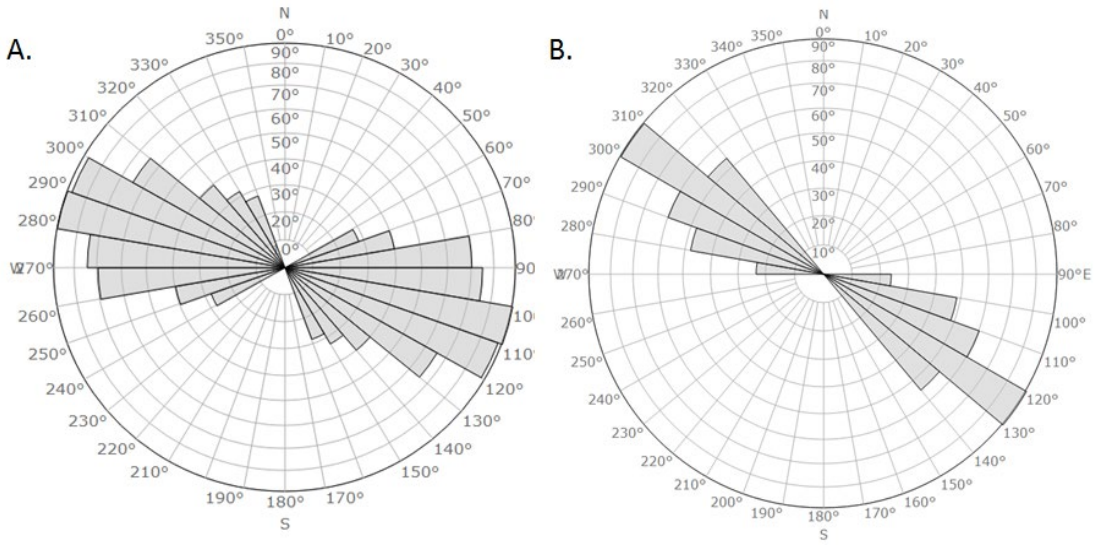

Fig. 41 Drilling induced fracture strikes in rose diagram for wells (A) Well B and (B) Wells C. The intervals covered for each dataset are 1463-2286 m for well B and 1478-2133 m for well C. The datasets were filtered to consider information pertinent to Porquero C and D units.

4.2 Pore pressure

Pore pressure data comes mainly from field tests for the five wells available within block A. Testing includes drill-stem tests and register of bottom hole pressure measurements displayed in Table 2. Additional indirect information to constrain the pore pressure models included abnormal events registered in the drilling diaries and the equivalent hydrostatic pressure as a function of the mud weight used to stabilize the wellbore walls. Wells Y and Z also account for records of formation pressure. These data will not be used in the property extrapolation but for trend calibration.

Table 2: Pore pressure data available per well available.

Well	Data type	Magnitude [MPa]	Depth [m]	Additional data
Well A	DST	18.89	1794	MW/Drilling events
Well C	Bottom hole pressure	32.64	1983	MW/Drilling events
Well E	DST	55.15	3343	MW/Drilling events
Well E	DST	65.57	3614	MW/Drilling events
Well E	DST	67.15	3473	MW/Drilling events
Well E	DST	65.20	3357	MW/Drilling events
Well Y	DST	38.16	2383	MW/Drilling events
Well Z	DST	63.35	3170	MW/Drilling events

Well Y and well Z are located outside the simulation volume and are used only for trend correspondence. DST =drill stem test, MW= mud weight.

4.3 Stress magnitude constraints

Mini-frac and step-rate tests (SRT) were performed in three wells targeting various intervals of the Porquero formation (Table 3). Fracture closure pressure (F_{cp}) was retrieved from these tests providing an estimate for the magnitude of the minimum horizontal stress (S_{hmin}) (Zoback 2007). For the wells available, F_{cp} values in the depth interval between 1789 m and 1908 m range between 35 MPa and 36.5 MPa. Leak-off tests (LOT) and formation integrity tests (FIT) are also available for wells C and D. However, they can only provide a lower bound for S_{hmin} magnitudes (Reynolds et al., 2006).

To constrain S_{Hmax} magnitudes the stress polygon approach (Zoback et al., 2003) was used. As an example, Fig. 42 shows all the conceivable S_{Hmax} magnitudes considering possible faulting regimes and wellbore failure constraints for a specific depth in Well A, based on the frictional faulting theory. Having knowledge of specific rock strength parameters, it is possible to define a range of stresses based on the wellbore failure analysis. Eq. 34 and Eq. 35 correspond to the estimation of S_{Hmax} magnitude that coincides with the generation of wellbore breakouts and tensile fractures respectively (Zoback 2007).

Wellbore breakouts

$$S_{Hmax} = \frac{(Ceff + 2Pp + \Delta Pp + \sigma^{\Delta t}) + S_{hmin}\,(1 + 2\cos 2\theta b)}{(1 + 2\cos 2\theta b)} \qquad \text{Eq. 34}$$

Tensile fractures

$$S_{Hmax} = 3S_{hmin} - 2Pp - \Delta Pp - T_0 - \sigma^{\Delta t} \qquad \text{Eq. 35}$$

Where S_{Hmax} and S_{hmin} correspond to the minimum and maximum horizontal stresses, $Ceff$ correspond to the effective compressive strength, Pp correspond to registered pore pressure and ΔPp is the difference between the fluid and formation pressure, $2\theta b = 180° - \text{breakout width}$, $\sigma^{\Delta t}$ correspond to cooling stresses and T_0 correspond to the tensile strength.

The mentioned parameters correspond to a depth of 1320 m, for which analysis of logging data (see below) indicates a vertical stress magnitude (S_v) of 28.4 MPa, a pore pressure of 19 MPa, a S_{hmin} of 26 MPa, and an UCS value 12.22 MPa. Assuming a coefficient of friction of 0.6, the resulting range for S_{Hmax} is 26.7 MPa to 28.21 MPa as lower and upper bounds, respectively. This considers the absence of borehole breakouts in the analysed image logs. Thus, higher S_{Hmax} magnitudes would cause the generation of borehole breakouts.

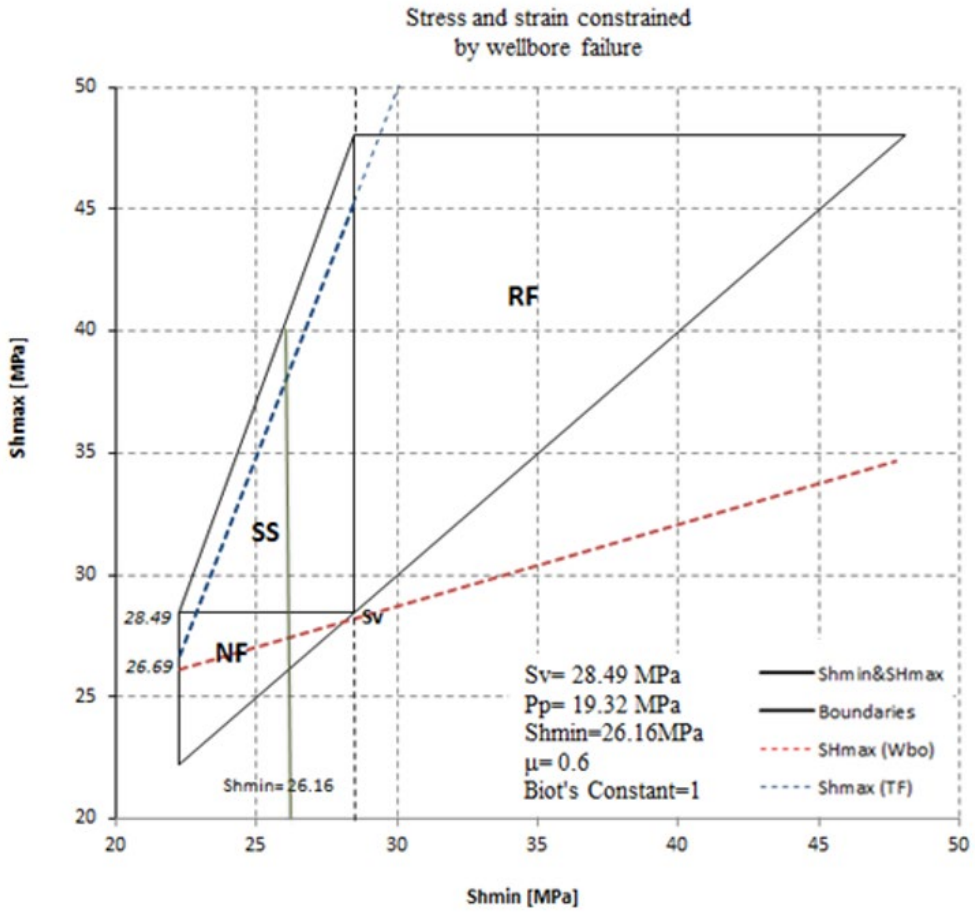

Fig. 42 Application of the stress polygon approach (Zoback et al., 2003) to constrain the magnitude of S_{Hmax} in well A at a depth of 1320 m. The analysis considers the absence of borehole breakouts.

Table 3: Stress magnitude data overview

Wells	Data source	Formation	Parameter	Magnitude [MPa]
Well A	Fracturing (SRT-DF)	Porquero C	Fcp	35.13
Well B	Fracturing (SRT-DF)	Porquero C	Fcp	35.53
Well B	Fracturing (SRT-DF)	Porquero C	Fcp	36.55
Well C	LOT	Porquero C	LOP	30.33
Well D	LOT	Porquero C	LOP	6.97
Well D	LOT	Porquero C	LOP	29.27

SRT=Step rate test, DF=Data frac, Fcp=Fracture closure pressure, LOT=Leak-off test, LOP= Leak-off pressure.

4.4 Rock mechanics laboratory data

Drill core samples are available for wells A, B, C and D. However, standard laboratory tests to define mechanical properties were only carried out for the samples of well A (Table 4). Three samples were taken at an interval which corresponds to the Porquero C unit. Triaxial tests were conducted at a confinement pressure equivalent to the sample depth, leading to the static Young's modulus (E_{stat}) and Poisson's ratio (υ_{stat}) at reservoir conditions. These tests provide average values of 2.06 GPa for E_{stat} and 0.23 for υ_{stat} for the Porquero C unit. Unconfined compressive strength (UCS) was inferred from Brinell hardness tests leading to an UCS of approximately 12.75 MPa. Rock mechanical laboratory tests results are used as calibration data to constrain the properties used in the models.

Table 4: Summary of static laboratory data for Well A

Sample	Depth [m]	Confining Pressure [MPa]	Bulk density [g/cm3]	Compressive Strength [MPa]	E [GPa]	υ	Brinell - UCS [MPa]
1	1517	5.10	2.21	24.06	24.82	0.24	13.84
2	1519	5.10	2.21	23.82	19.30	0.24	8.24
3	1522	5.10	2.20	29.42	17.92	0.21	16.16
Mean value	1520	5.10	2.21	25.77	20.68	0.23	12.75

4.5 3D reflection seismic surveys

In a recent exploration campaign, from 2008 until 2010, approx. 107 km^2 of 3D seismic survey were acquired. Reflection seismic data has been processed and depth-converted down to approximately 5 km depth. The interpretation of this seismic dataset was used to build a structural model for Block A comprising seven lithostratigraphic horizons and 22 faults. Fig. 43-A and Fig. 43-B show a representative seismic section with interpreted horizons and faults. Further studies also include a detailed seismic inversion and AVO (amplitude variation with offset) analysis that was used to generate the property distribution used in this study (Di Luca, 2016; Di Luca et al., 2014).

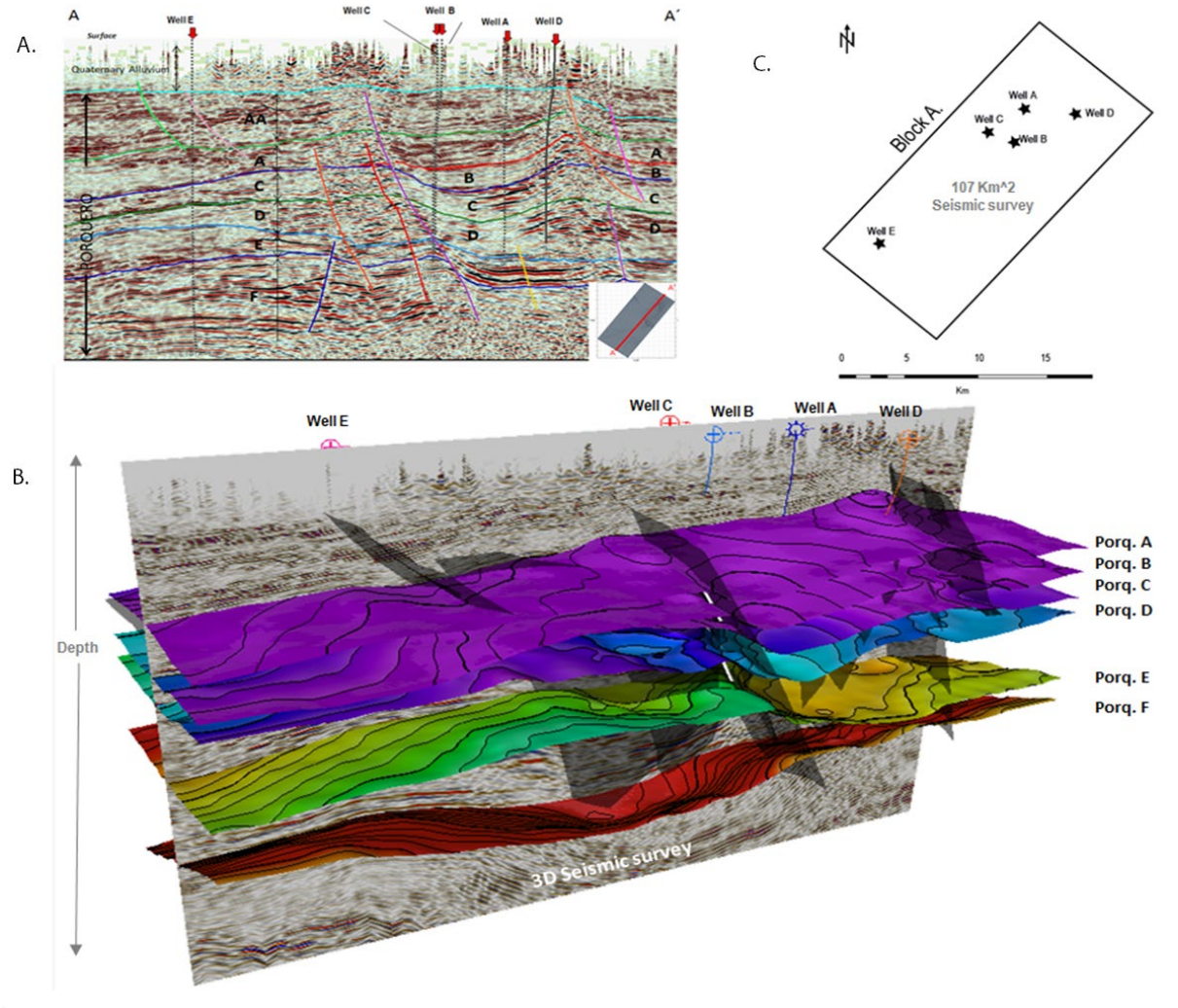

Fig. 43 (A) SW-NE oriented seismic section through Block A with structural and stratigraphic interpretation. Letters correspond to units of the Porquero formation. Red arrows show well locations (Modified after Di Luca et al. 2014). (B) Structural framework derived from seismic interpretation for Block A. Shown there are six main horizons and 22 faults covering the entire extension. Main wells can be seen. Inline and crossline from the 3D seismic survey in side view. (C) Location of the five wells within the Block A seismic survey area.

4.6 Facies maps for lithology input data

Lithological description has been estimated from wells lithological description integrated with paleogeographical changes. The trends were charted and assigned to a corresponding section within a map for each of the described units (Porquero AA, A, B, C, D, E, F) and tagged with an identification code. This code and its corresponding lithological description are referred to as “coded maps” and are used to add the lithological information for the facies modelling in the basin and petroleum system modelling approach in the software (Fig. 44).

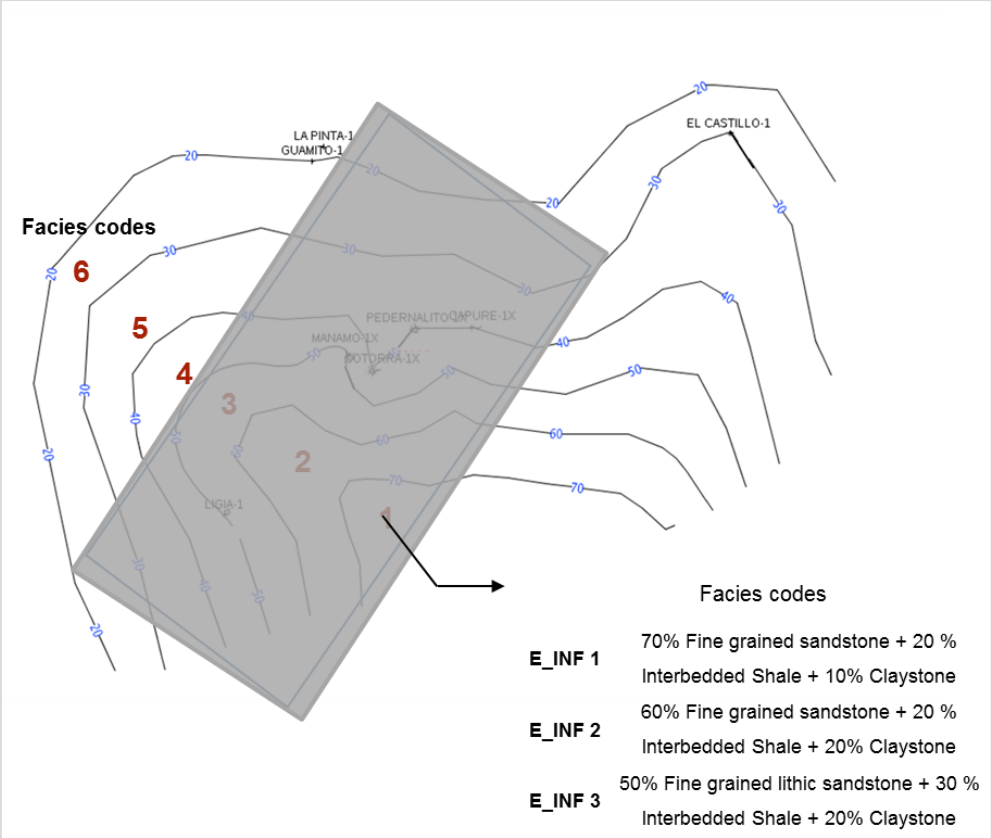

Fig. 44 Coded map example corresponding to unit Porquero E-INF. Each code corresponds to a specific lithological mixture that will assist in the facies definition for the BPSM model.

4.7 Geochemical and temperature data

Hydrocarbon generation potential is estimated per source rock at each of the facies maps where it corresponds. Source rock properties include kerogen type, TOC values, HI values, and kinetic models of the supposed source rocks. Studies sorting this data include Arminio (2011) and Castillo (2012) (Table 5).

Table 5: Summary of geochemical data for Block A

PSE	Facies unit	TOC %	HI [mgHC/TOC]	Kinetics model
Source Rock	Porquero D	0.72	160	Behar_et_al (1997) _TIII(Mahak)-cs
Source Rock	Porquero E	1.52	143	Behar_et_al (1997) _TIII(Mahak)-cs
Source Rock	Porquero F	1.47	176	Behar_et_al (1997) _TIII(Mahak)-cs

PSE=Petroleum system element, TOC%= Total organic carbon, HI= hydrogen index.

SWI-temperature

As described in (Hantschel & Kauerauf, 2009), the sediment-water-interface temperature (T_{swi}), can be determined with estimated paleo mean-surface temperature or air temperatures (Ts) and corrections for water depths. The model used in this work corresponds to the proposed by Wygrala (1989) (Fig. 45). In order to derive paleo surface temperatures, an understanding of paleo latitude

and paleo-water depth changes with geologic time is crucial (Hantschel & Kauerauf, 2009; Wygrala, 1989).

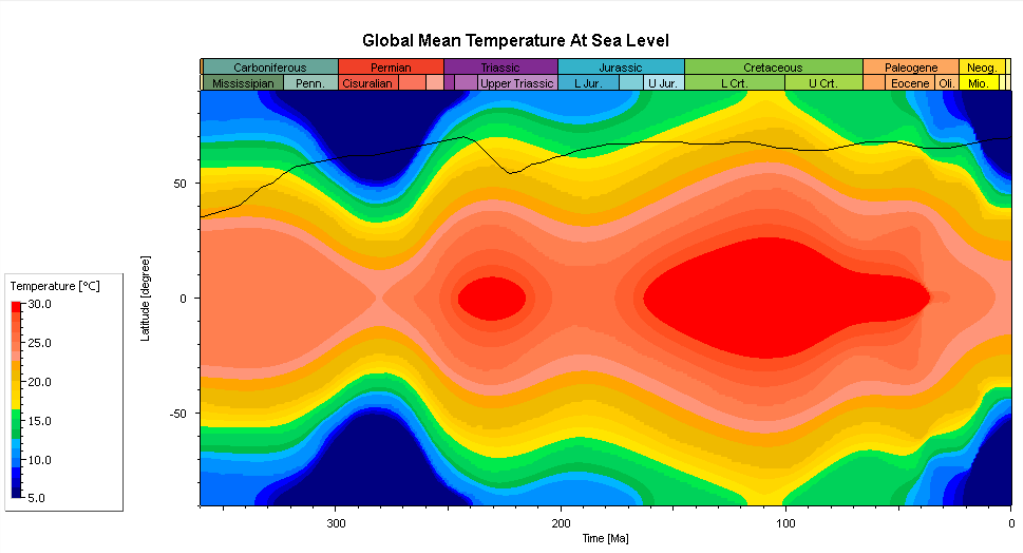

Fig. 45 Sediment-water interface temperatures. After (Wygrala, 1989). The image displays the annual surface temperature distribution history over the last 360 Million years on Earth. The black line represents the mean temperature across the geologic time. Y-axis corresponds to geographical latitude. X-Axis corresponds to geologic time.

Heat flow

The data sorted to stablish the heat flow model is based on the work presented in (Briceno, 2013). In this study the subsurface temperature was estimated for 108 wells distributed across the LMVB through linear regression (Table 6).

Table 6: Heat flow model (After (Briceno, 2013))

Age from [Ma]	Mode	Value [mW/m2]
0.00	Value	72.00
10.00	Value	35.00
15.00	Value	35.00
20.00	Value	30.00
30.00	Value	30.00
40.00	Value	30.00

Chapter 5 Methods

The following section describes the modelling approaches carried out for stress and fracture characterisation applied to Block A. The Fig. 46 describes the critical parameters necessary in each modelling step. The named data sources are used to extract information that will be used as input for the geomechanical models. Validation of the models is performed through a comparison of the modelled magnitudes versus laboratory and field measurements.

The aims of the proposed methods are to illustrate the advantages of different datasets. This specifically includes the construction of models using logs and seismic derived data, and to analyse the predictive geomechanical potential based on basin and petroleum system models. Three different datasets feed the corresponding geomechanical finite element models which are calibrated in different phases specifically for each approach. The information gathered in this modelling approaches serve to generate a first approximation of natural fractures networks in the target formations. The Fig. 47 shows the interrelations and outputs of each modelling approach as well as comparison points between the models.

The first approach is referred as a *log-based* mechanical earth model (MEM) and is performed using 1D calibrated mechanical earth models from five wells to populate the area corresponding to Block A, with elastic mechanical properties and pore pressure. The second method is known as a *seismic-driven* approach. This approach presents an enhancement in the definition of mechanical properties, as they are derived from a 3D seismic survey and seismic inversion considering the lateral heterogeneities of the formations. Pore pressure model used in this section correspond to the one derived from well logs.

The third approach resembles an early exploratory phase when most of the data is based on geological interpretations and, when available, pre-existing information on the area. Basin and petroleum system model (BPSM) works with seismic-derived structures, basin-scale geological survey, facies models for property population, and takes into account the present-day data to calibrate the model (wellbore data). Also, the results from the previous models can be used to cross-calibrate and fine-tune the resulting outputs of BPSM. Data sources and corresponding input data are used to populate a 3D finite element model representing Block A which is structurally constrained using horizons and faults from reflection-seismic interpretation. From each of the three models, three main properties were analysed: (1) *in-situ* stress state, (2) vertical and horizontal mechanical properties distribution and (3) pore pressure distribution.

Natural fracture prediction study was generated through two modelling approaches: the first one known as natural fracture prediction, a stochastic approach, where present-day structures were used, and a stress-inversion technique was implemented to select the paleo-stress model that most likely generated the fractures.

The second approach was the generation of a natural fracture network, through BPS models. An equivalent plastic strain concept was used as a historical deformation record extracted from a poro-plastic basin and petroleum system model. A correlation was used to establish fracture intensity where fractures were most likely formed. The results are two discrete fracture networks (DFN#1 and DFN#2). The metrics selected for analysis include fracture intensity and preferred orientation.

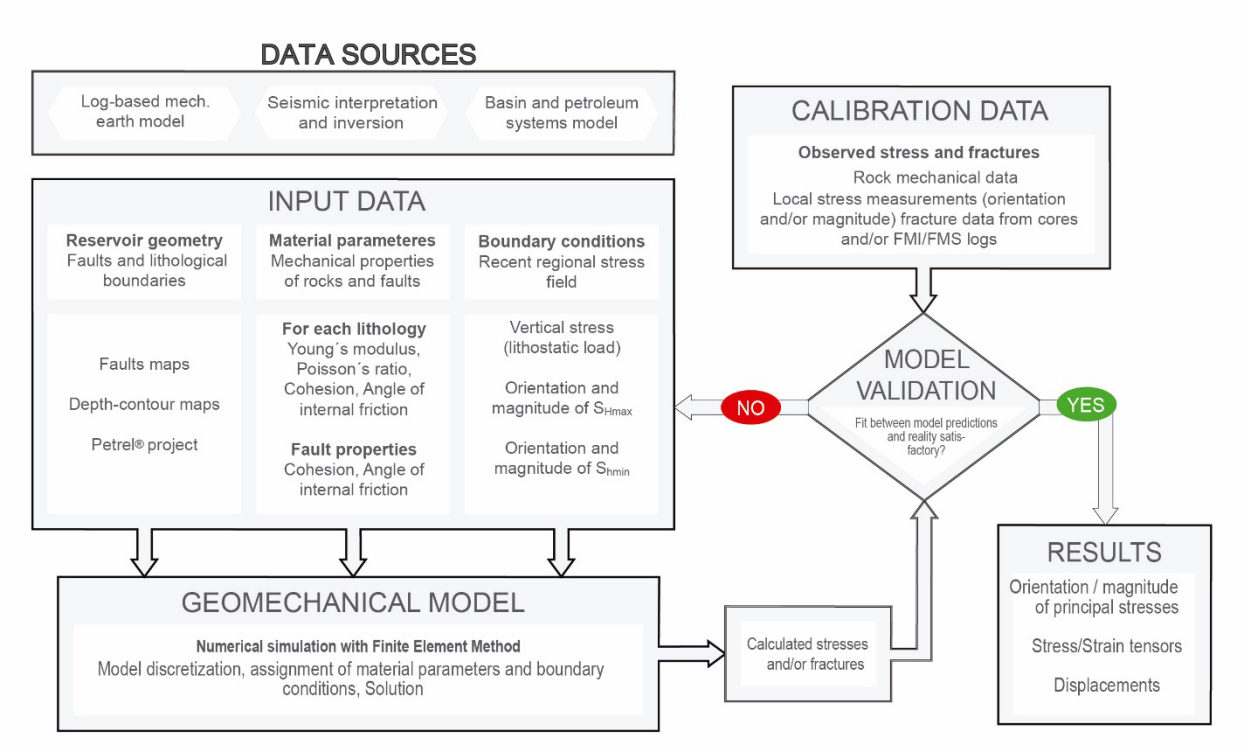

Fig. 46 Geomechanical modelling workflow. The research design workflow is describing the input data necessary in each step and critical components of the modelling sequence.

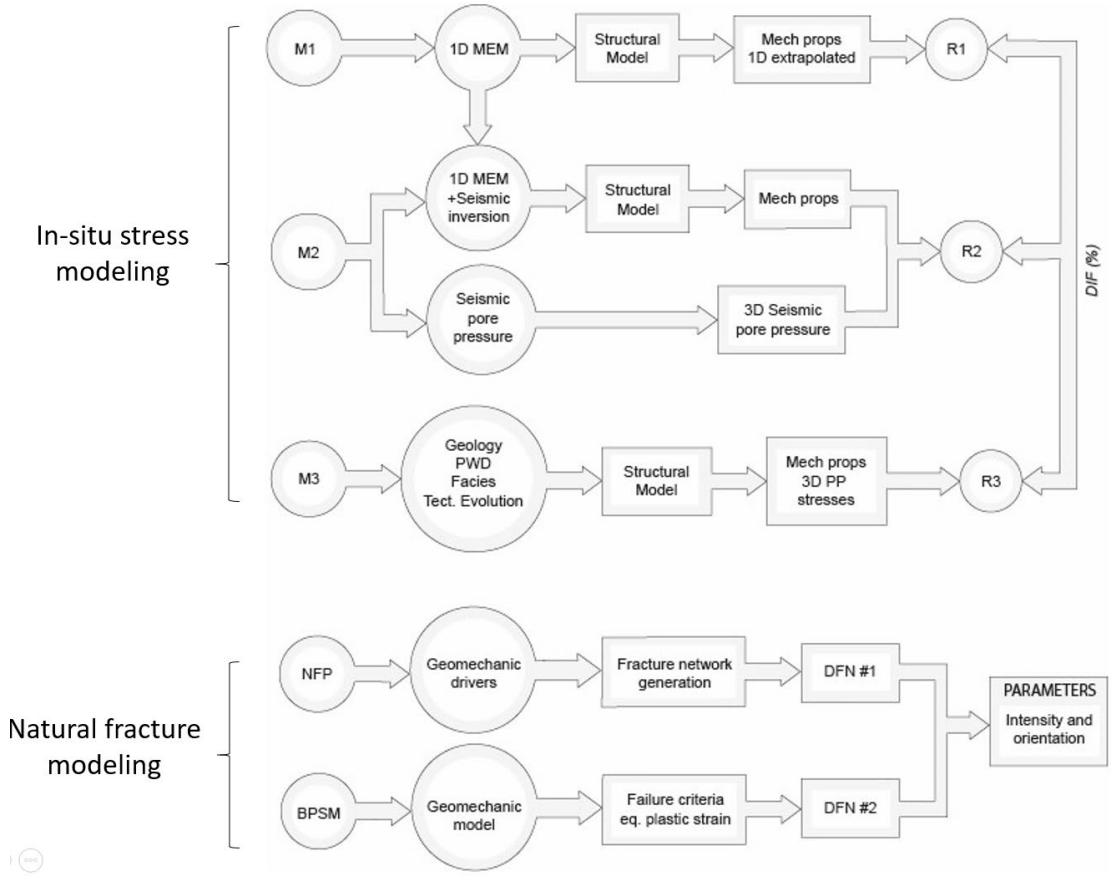

Fig. 47 Research sketch showing the interconnection between modelling approaches, outputs of each phase and specific comparison points and metrics.

5.1 Log-based mechanical earth model

The implemented workflow (Fig. 48) utilises a log-based methodology to estimate the elastic mechanical properties, pore pressure and in situ stress state for five wells within Block A. This 1D-data is afterwards used as input data for a 3D mechanical earth model (MEM).

Primary data necessary for the model construction (per well) include sonic logs (simple or dipole) and density logs. Moreover, a calibration dataset is necessary to validate the model assumptions, which may be made up by rock mechanical testing results, derived stress measurements (e.g. from hydraulic fracturing tests) and pressure measurements (e.g. from drilling stem tests (DST)).

The dynamic mechanical properties are estimated through empirical correlations, and subsequently, the static properties are calculated and validated with rock mechanical data. The overburden gradient and a pore pressure model can be calculated afterwards. Up to this point, all the variables necessary to estimate horizontal stresses (S_{Hmax} and S_{hmin}) through a poro-elastic approach have been gathered. Each property is calibrated against measurement and field data, and the model is adjusted until an acceptable error is achieved.

Once the 1D property profiles are estimated, the 3D structural model can be populated through property upscaling and extrapolation. The model geometry is discretised using finite element (FE) techniques, and displacements are applied to the lateral sides of the model to account for the tectonic strain. 3D MEM results comprise the full 3D stress tensor for each point of the model domain in

addition to the spatial distribution of the mechanical properties and the pore pressure. Well log analysis, stress calculations, as well as integration of rock mechanical and stress calibration data, are performed using the commercial software Techlog® geomechanics module[4].

Fig. 48 1D geomechanical modelling workflow considering independent datasets for input and calibration.

5.1.1 Mechanical properties from well logs

Well logs are a reliable source to chart the vertical variation of different properties as these can be derived through empirical correlations (Archer & Rasouli, 2012). Dynamic elastic properties can be directly estimated using compressional slowness, shear slowness and density, as in Eq. 36 and Eq. 37.

[4] Techlog is a trademark of Schlumberger

$$E_{dyn}(\Delta ts, \Delta tp) = \frac{\rho * (\left(\frac{3}{\Delta tp^2}\right) - (\frac{4}{\Delta ts^2}))}{\Delta ts^2 * (\left(\frac{1}{\Delta tp^2}\right) - (\frac{1}{\Delta ts^2}))} * 10^{-12} \quad \text{Eq. 36}$$

$$v_{dyn}(\Delta ts, \Delta tp) = \frac{\rho * (\left(\frac{3}{\Delta tp^2}\right) - (\frac{4}{\Delta ts^2}))}{\Delta ts^2 * (\left(\frac{1}{\Delta tp^2}\right) - (\frac{1}{\Delta ts^2}))} \quad \text{Eq. 37}$$

Static Young's modulus can be estimated through several standardised empirical correlations, namely Modified Morales, John Fuller, Morales and the Plumb Bradford correlation (Bradford et al.,1998; Morales & Marcinew, 1993). Detailed estimation for a section of Well A is shown in Fig. 49. The best fit among the correlations is selected by comparing the correlations available with calibration data extracted from rock mechanical laboratory tests. Common empirical approximations for mechanical properties are detailed in Table 7.

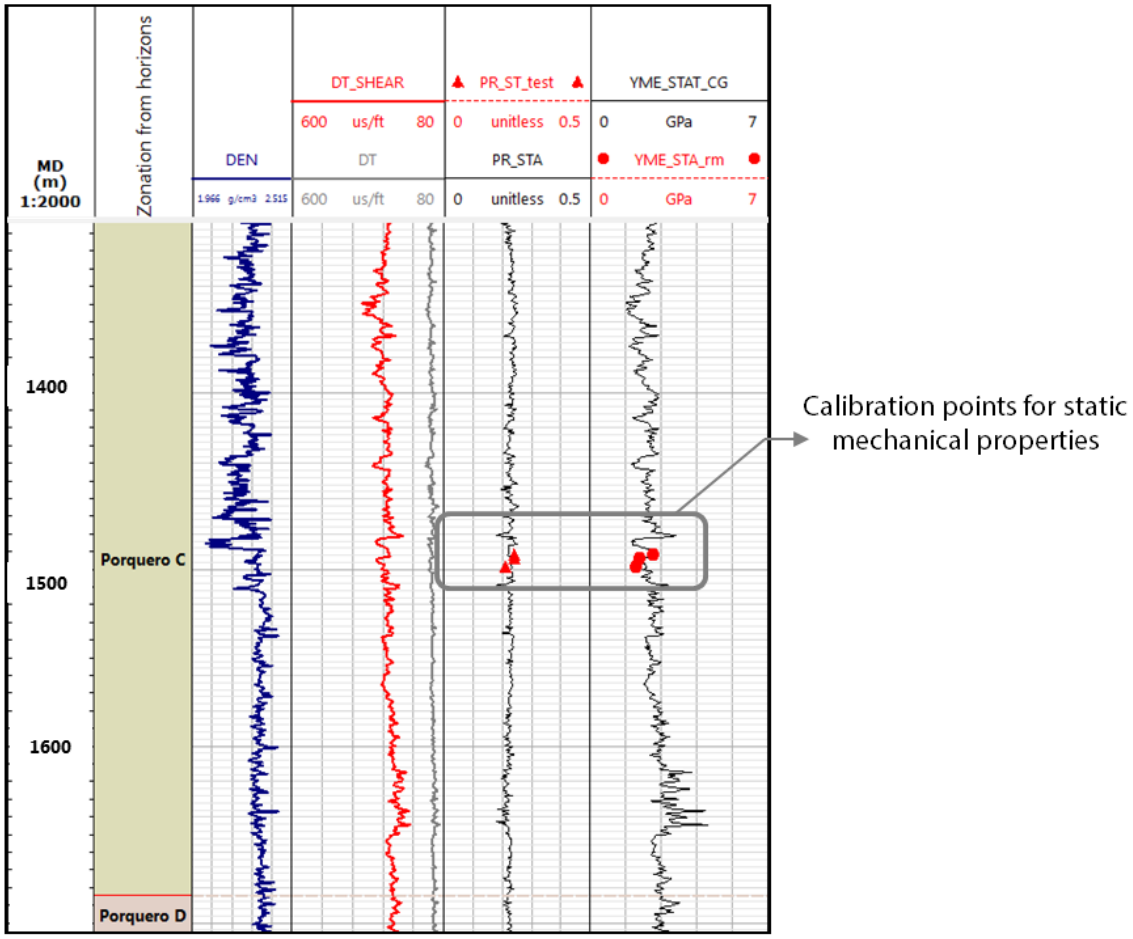

Fig. 49 Estimation of static Young's modulus and Poisson`s ratio through empirical correlations (i.e. John-Fuller correlation-YME_STAT_JFC) for a selected interval of well A. Red points correspond to calibration points. In order from left to right (1) Compressional slowness - Shear slowness, (2) density logs and (3) dynamic Young's modulus.

Table 7: Summary of equations

Property	Calculation
V_p - P- wave velocity (m/s)	$= \frac{10^6}{DTCO} \times 0.3048$
V_s – S-wave velocity (m/s)	$= \frac{10^6}{DTSM} \times 0.3048$
G - Shear Modulus (Pa)	$= RHOZ \times V_s^2$
K – Bulk Modulus (Pa)	$= RHOZ \times V_p^2 - \frac{4}{3}G$
Edyn – dynamic Young's Modulus (Pa)	$= \frac{9.0 \times G \times K}{G + 3.0 \times K}$
ν – dynamic Poisson Ratio	$= \frac{3.0 \times K - 2.0 \times G}{6.0 \times K + 2.0 \times G}$
E_stat – static Young's Modulus (GPa)	$= YME_{dyn} * C$
ν_static – Static Poisson Ratio	$=$ ν_dynamic $* C$

5.1.2 Vertical stress or overburden

Vertical stress (Sv) or overburden stress at a point in the Earth's crust is caused by the weight of the overlying rock column. Its magnitude at depth z can be derived based on density log data according to Eq. 38.

$$Sv = \int_0^z \rho(z) g dz \approx \bar{\rho} g z \qquad \text{Eq. 38}$$

Where $\rho(z)$ is density as a function of depth, g is the gravitational acceleration and $\bar{\rho}$ is the average density of the total overlying rock formation (Jaeger et al., 2007).

To perform this estimate it is required an extension of the density log to cover the entire depth of the well. To fill the data gaps along the wellbore, it is suggested to estimate a pseudo-density using empirical correlations. The extrapolation method used in this case (Fig. 50), works when at least a section of the log is available. The trend is extrapolated from the surface to the bottom using two control factors through the following equation:

$$\rho_{extrapolated} = \rho_{mudline} + A_0 \times (TVD - AirGap - WaterDepth)^a \qquad \text{Eq. 39}$$

Where $\rho_{mudline}$ is the density at the sea floor or ground level and A_0 and a are the fitting parameters. After the density is calculated, the overburden stress can be calculated using Eq. 38 as observed in Fig. 51.

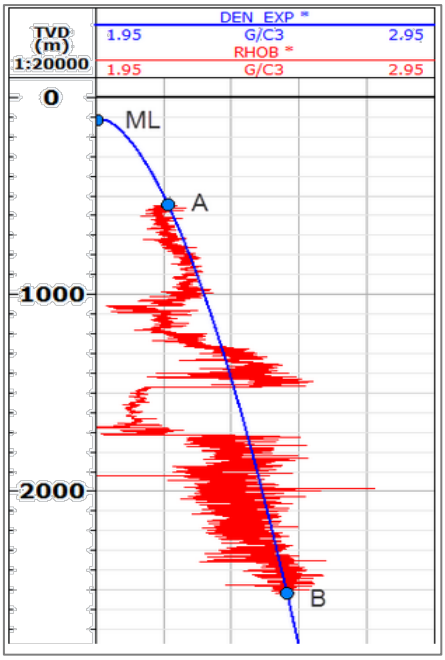

Fig. 50 Sketch showing the estimation of the synthetic density log from a section of raw density log and fitting the extrapolation model. Points A and B are graphical calibration points corresponding to shallow depth density (A) and bottom depth density (B). Extracted from Techlog® online help assistant.

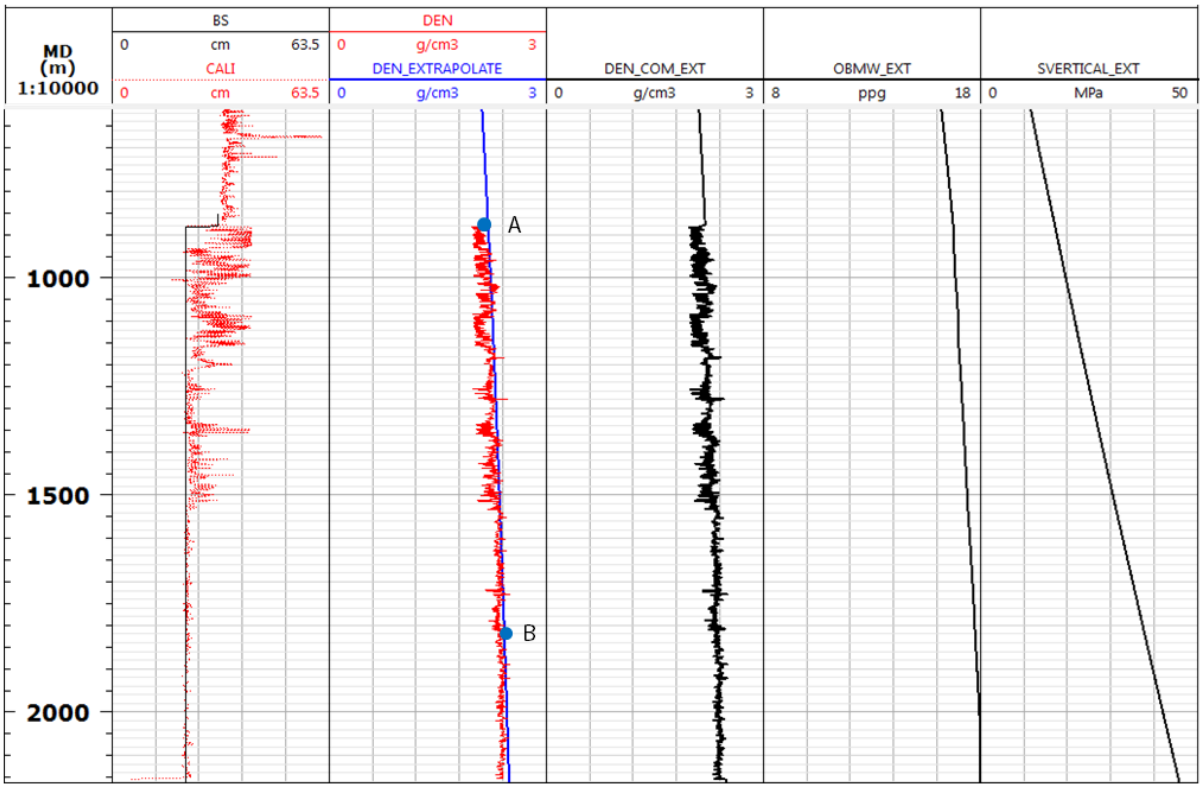

Fig. 51 Overburden stress calculation. Section extracted from well A. Considering the density data coverage it is necessary to extrapolate the existing piece of data all the way to the top of the well and extend it to the bottom. From the pseudo-density, the overburden stress can be calculated through density integration.

5.1.3 Pore pressure model

To estimate the pore pressure at well location, the implemented method was the *Eaton slowness method* (Fig. 52) (Eaton 1975; Zhang 2011) which is described with the following equation:

$$P_P = Sv - (Sv - P_{\text{hydro}}) * \alpha * (\frac{\Delta t_n}{\Delta t})^n \qquad \text{Eq. 40}$$

where P_P is the formation pore pressure, S_v is the overburden stress magnitude, P_{hydro} is the formation hydrostatic pore pressure, α and n are fitting parameters named Eaton factor and Eaton exponent respectively, Δt_n is the compressional transit time or slowness in shales at normal pressure, following the normal compaction trends (Sayers et al., 2002) and Δt is the compressional transit time or slowness taken from the sonic log. This method is suggested for sedimentary basins where the generation of geo-pressures are generally a consequence of compaction in response to the stress of the overburden (Eaton 1975). The model was chosen after adding calibration data and finding the best fit. Other suitable methods for pore pressure models estimation considered included the Traugott slowness (Traugott & Heppard, 1994) and the Bowers methods (Bowers, 1995).

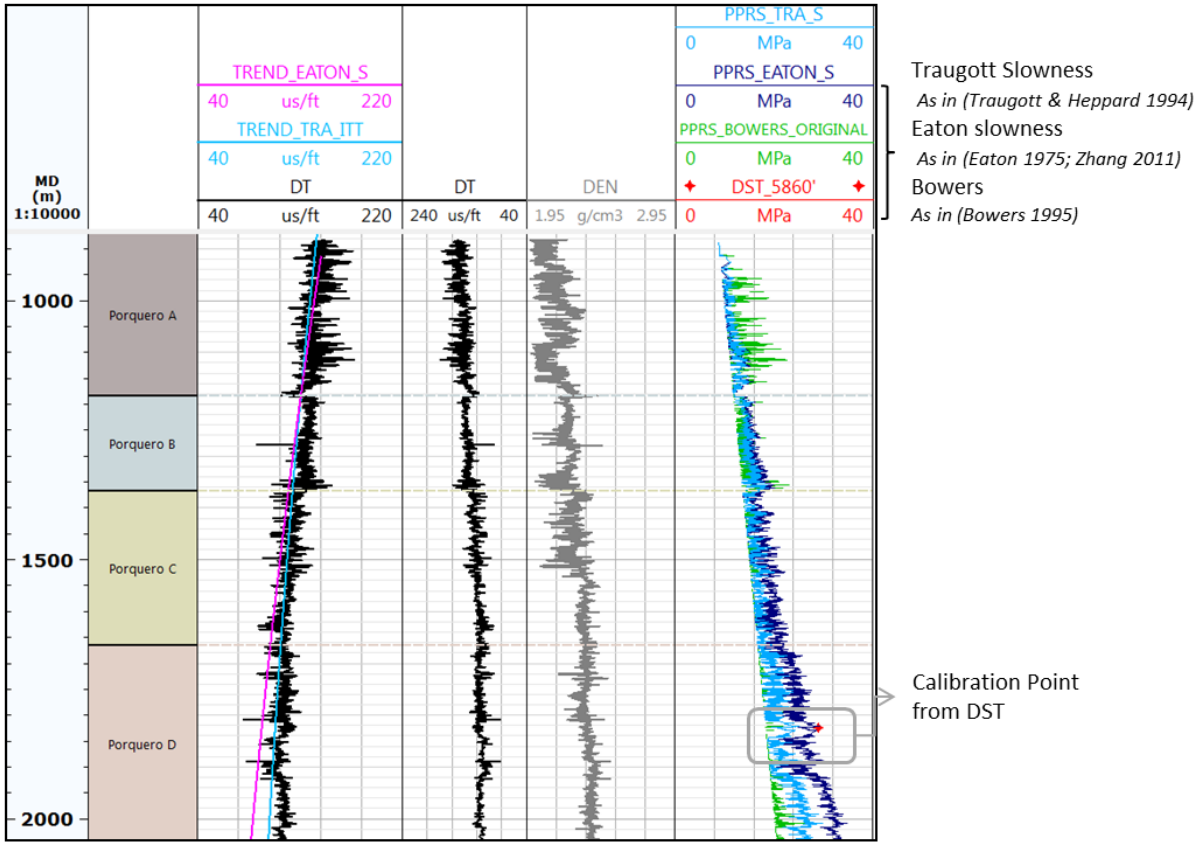

Fig. 52 Pore pressure calculation for well A at depth matching calibration data. Calibration data is used to select the best model fit for the well.

5.1.4 Horizontal stress magnitudes and orientation

Minimum and maximum horizontal stresses magnitudes are calculated through a poro-elastic approach using the properties outlined in the following equations:

$$S_{\mathrm{Hmax}} = \frac{\mathrm{v}}{1-\mathrm{v}}\mathrm{S_V} - \frac{\mathrm{v}}{1-\mathrm{v}}\alpha\mathrm{Pp} + \alpha\mathrm{Pp} + \frac{\mathrm{E}}{1-\mathrm{v}^2}\varepsilon_{\mathrm{H}} + \frac{\mathrm{vE}}{1-\mathrm{v}^2}\varepsilon_{\mathrm{h}} \quad \text{Eq. 41}$$

$$S_{hmin} = \frac{\mathrm{v}}{1-\mathrm{v}}\mathrm{S_V} - \frac{\mathrm{v}}{1-\mathrm{v}}\alpha\mathrm{Pp} + \alpha\mathrm{Pp} + \frac{\mathrm{E}}{1-\mathrm{v}^2}\varepsilon_{\mathrm{h}} + \frac{\mathrm{vE}}{1-\mathrm{v}^2}\varepsilon_{\mathrm{H}} \quad \text{Eq. 42}$$

Where S_{hmin} and S_{Hmax}, are the minimum and maximum horizontal stresses magnitudes respectively, α is the Biot-Willis coefficient, ε_h and ε_H are tectonic strains in minimum and maximum horizontal stresses directions, respectively (De Gennaro et al., 2014; Fjaer et al., 2008; Jaeger et al., 2007). The strain increments are added to the poro-elastic approach to reflect the impact of the regional stress field on the local horizontal stress magnitudes in addition to overburden load and pore pressure (Blanton & Olson, 1999). Orientation of horizontal stress was derived from hydraulic fracturing tests and borehole image analysis.

5.1.5 1D model calibration

The 1D calibration process is carried out sequentially for the pore pressure, the mechanical properties, and the local stress magnitudes at a well location. First, the calculated pore pressures are calibrated against measured data, i.e., Drill Stem Test (DST) results and with the pressure differential behaviour between the drilling mud equivalent hydrostatic pressure and pore pressure of the rock. Subsequently, modelled static mechanical properties are calibrated against their laboratory measurements counterparts.

Calculated stress magnitudes are compared to S_{Hmax} magnitudes derived from the stress polygon method and S_{hmin} magnitudes derived from the F_{cp} data. Horizontal stress calibration was performed by adjusting the strain increments (ε_H *and* ε_h) in Eq. 41 and Eq. 42 until a satisfactory fit between calculated and measured stresses was achieved. Final strain increments for ε_{h} and ε_{H} derived by this procedure are 0.001 and 0.003, respectively (Fig. 53).

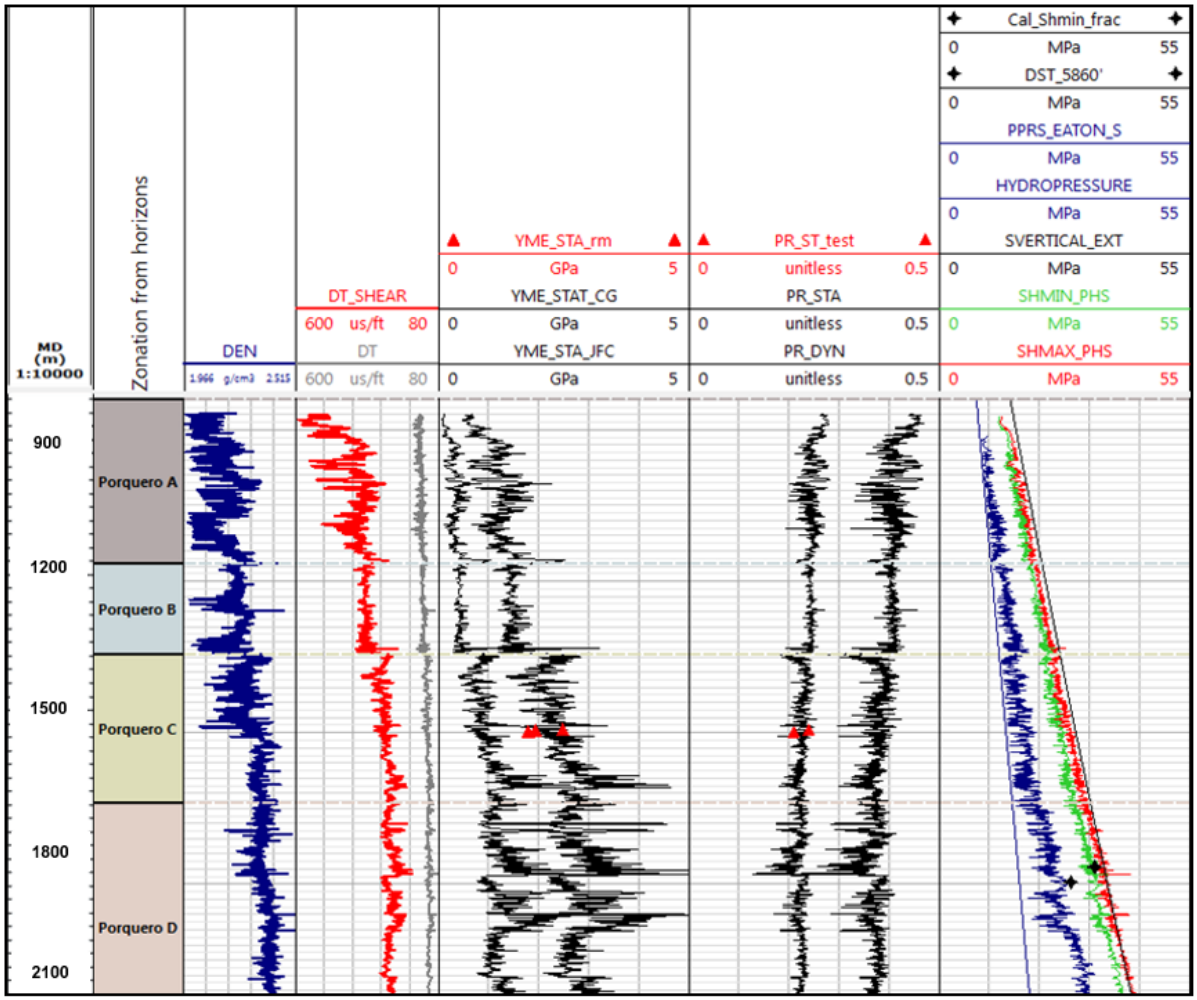

Fig. 53 1D MEM calibration using rock mechanical testing results and field measurements to constrain elastic mechanical properties, pressure and minimum horizontal stress (S_{hmin}). Red points correspond to laboratory derived static mechanical properties.

5.1.6 Log-based 3D Model construction and discretization

The principal structural elements of the area, i.e., faults and horizons, were defined using 3D reflection seismic interpretation and well tops from drilling records to match the horizon depth. Within Block A, six lithostratigraphic horizons were defined subdividing the Porquero formation into units A to F and reaching depths between 2.56 and 4 km. Elevation maps of the ground level were incorporated to define the top of the model. Based on regional considerations the top of the crystalline basement in the study area was assumed to be at 6 km depth, but neither the seismic survey nor the deepest well available reaches this level.

The structural model comprises a total of nine horizons including those derived from 3D seismic, topography, basement top and a flat model base. In addition, the seismic interpretation led to the detection of 22 main faults. Five of these faults intersect the prospective reservoir showing a high dip

angle, normal faulting pattern striking NW-SE (Arminio et al., 2016). The structural model and 3D geomechanical computations were done using the software Petrel E&P ®[5].

Following set-up of the model geometry comprising the horizons and faults derived from 3D seismic interpretation, a structured geomechanical grid is built for the reservoir and the surrounding formations through the finite element technique. Thereby, the model is aligned with the regional S_{Hmax} and S_{hmin} directions. The grid resolution is higher at the reservoir level (likewise near faults or complex structures), and lower in zones distant to the areas of interest. In this way, the final grid is achieved through a balance between the required precision and the computational demand.

The horizontal resolution of the grid at reservoir level is 50 m leading to 210,000 elements. Such elements are quadrilateral. This core area (Block A), is embedded into a larger grid with 866,868 cells in total (Fig. 54). This embedding ensures that no undesired boundary effects influence the simulation results. The final geomechanical grid covers an area of more than 900 km ^{2}.

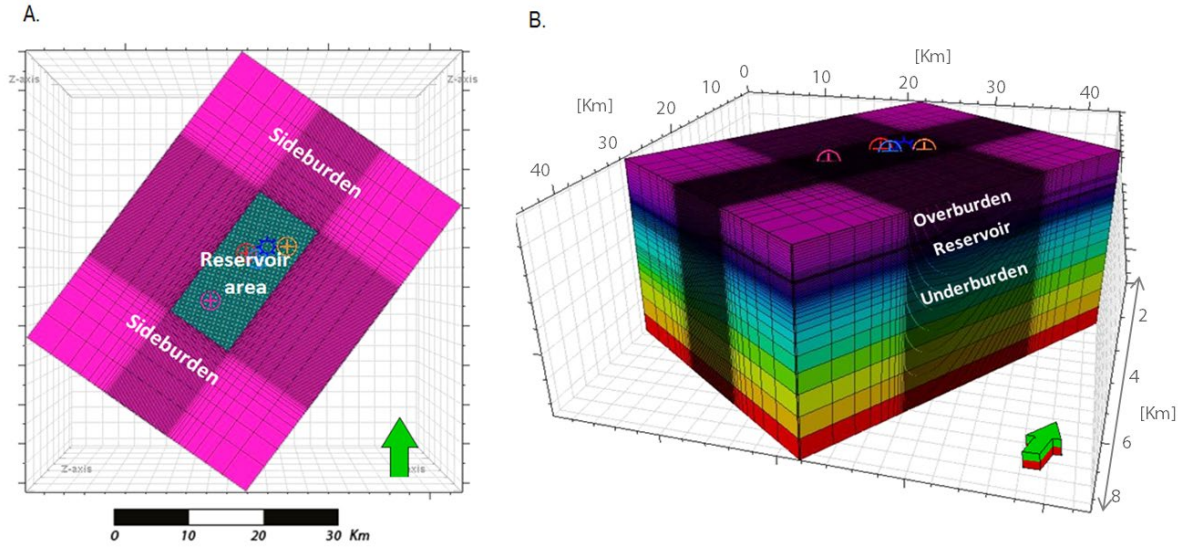

Fig. 54 Three-dimensional geomechanical grid comprising the actual Block A model (Blue rectangle in (A)) embedded in side, over and underburden volumes to avoid edge effects. (A) Top view and (B) Side view.

5.1.7 Property population

Well logs (including raw data and elastic mechanical properties) are upscaled to the geomechanical grid (Fig. 55). This means that each cell will coincide with the trajectory and depth of the well and will have a bulk property value derived from the log. Afterwards, properties are spatially distributed using the kriging method (Goovaerts, 1997), i.e. a geostatistical procedure that delivers a deterministic model which honours wells properties according to a defined variogram (spherical model was selected). In the case of pore pressure, this property is first upscaled and extrapolated as a gradient and afterward computed to pore pressure magnitudes. Undefined cells, corresponding to cells where no

[5] Petrel® is a trademark of Schlumberger

well data is available, are filled with depth-trends. These are property vs. depth linear correlations for the wells available.

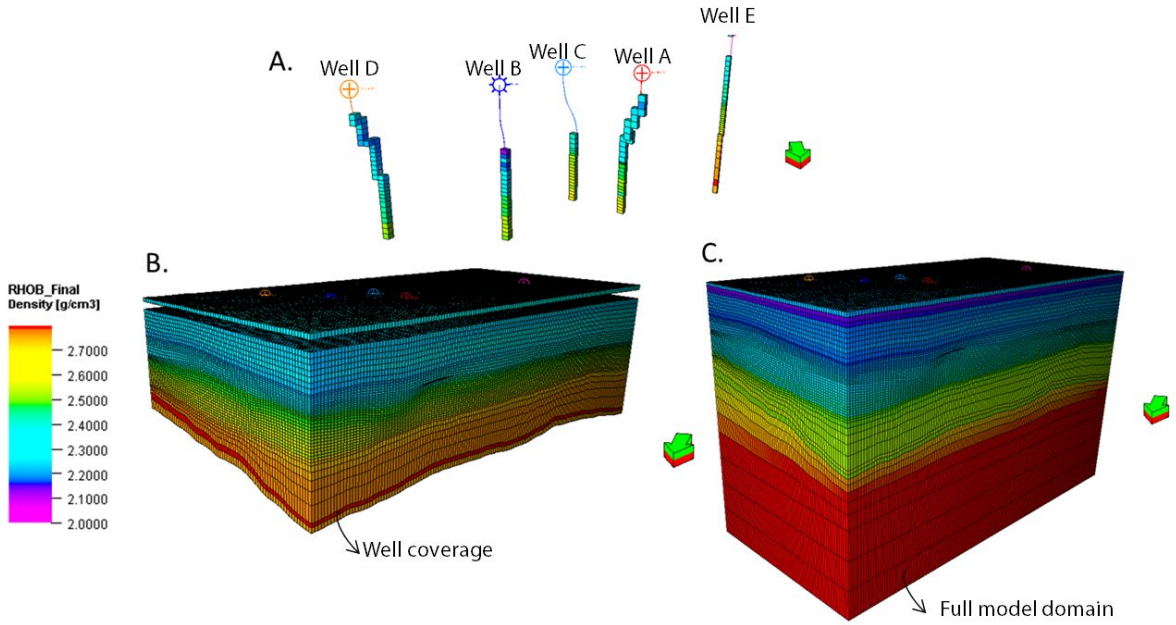

Fig. 55 Property population sequence for five well logs into the geomechanical model grid, corresponding to density property. (A) Upscaled density logs. (B) Property horizontal extrapolation up to the depth of wells available. (C) Incorporation of depth trends data for the remaining units and final configuration. The same process was carried out for mechanical properties and pore pressure. Arrow points to North.

5.1.8 3D Model calibration

The calibration process is carried out, for the pore pressure, the mechanical properties, and the local stress magnitudes at wellbore location, prior to the extrapolation. Initially, the calculated pore pressures are calibrated against measured data, like drill stem test (DST) results. Subsequently, modelled static mechanical properties are calibrated against their laboratory measurements counterparts. Finally, calculated stress magnitudes are compared to S_{Hmax} magnitudes derived from the stress polygon method and S_{hmin} magnitudes derived from the F_{cp} data. Horizontal stress calibration was performed by adjusting the strain increments (ε_H *and* ε_h), until a satisfactory fit between calculated and measured stresses was achieved. Final strain increments for ε_h and ε_H derived by this procedure are 0.001 and 0.003, respectively. This calibration ensures that the model is answering to the regional trends considering the data used in the approach and provides a good approximation of the properties.

5.2 Seismic driven mechanical earth model

A seismic-driven geomechanical models is a way to exploit the seismic data in order to capture horizontal heterogeneities that would be otherwise neglected by a more straightforward approach. Input data, used to build a seismic-driven mechanical earth model (MEM) of Block A, includes the geological interpretation of a 3D depth-converted seismic survey, elastic mechanical properties retrieved from the seismic inversion process, static elastic properties, and pore pressures from the log-based MEM (Fig. 56).

In addition, data for model calibration including core, laboratory, and field measurements are used. Seismic inversion results were used to infer the spatial distribution of the mechanical properties (Young's modulus and Poisson's ratio) which are required to populate the model.

The resulting parameters (mechanical properties, pore pressure and stresses) can be compared to and calibrated against observational well data (rock mechanical tests, drill stem test (DST), fracture closure pressure (Fcp), drilling induced fractures (DIFs) etc.) and trends obtained from the log-based MEM. Poorly constrained input parameters and boundary conditions are iteratively adjusted until a satisfactory fit between seismic-driven MEM extracted profiles, and the calibration data at well level, is achieved. The resulting best-fit model is considered as a validated model regarding the measured data presently available. Thus, it should be updated each time new well data is provided in course of the field development.

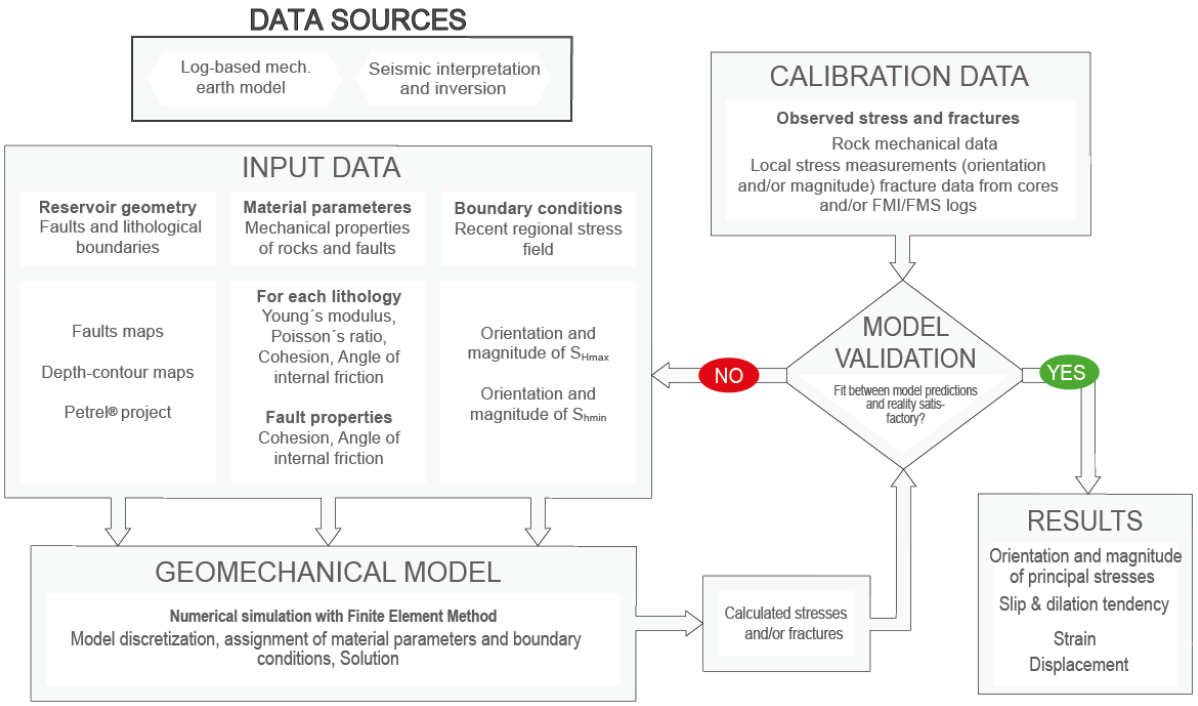

Fig. 56 Seismic- driven geomechanical modelling workflow includes different data sources for model set-up and calibration. Seismic data, besides being used for the structural interpretation, is used to add enhancements in the horizontal mechanical property's distribution through AVO inversion (modified after Fischer & Henk, 2013).

5.2.1 Mechanical properties from seismic inversion

Previous studies in the area include a complete pre-stack seismic inversion and amplitude versus offset (AVO) analysis using wells A, B, C and D (Di Luca, 2016). In general, the process aims on a detailed subsurface characterization, especially regarding the spatial distribution of mechanical properties (Mavko et al., 2009). Fig. 57 shows the corresponding seismic inversion workflow. The input includes seismic angle stacks, well logs (dipole sonic and density), check-shots and horizons derived from seismic interpretation. In addition, a low frequency model is used as further input data.

The results of this study included cubes of acoustic impedance, shear impedance, density and the derived elastic parameters like Poisson's ratio and P-wave impedance, which together with petrophysical evaluation allowed discriminating fluids and lithologies in the target interval

(Betancourt et al., 2016). The data input for the method includes: (a) seismic angle stacks, (b) well logs: dipole sonic, density and check-shots, and (c) seismic derived horizons.

A low frequency model is used as further input data. The goal of this external model is to contribute with the low frequency component that is not present in the surface seismic data and strengthen the initial acoustic and shear impedance and density volumes. The low frequency model was created by inserting the impedance profiles, calculated from wells, in the correct position within the seismic volume and interpolating to the entire geometry, using as guide seismic-derived horizons (Russell, 2014). This is necessary to obtain absolute impedance models (Barclay et al., 2007).

The following step was to perform the seismic inversion based on partial stacks, wavelets obtained for each partial stack and the low frequency model. This was a model-based pre-stack seismic inversion that used an initial impedance model disturbed until the observed seismic data and the synthetic seismic data generated through the model showed minimum error. As a result, a global solution was obtained, applying constraints provided by well logs information (Di Luca, 2016; Russell, 2014). For this case, the Fatti approximation (Fatti, 1994) was used, which is a variation of the Aki-Richards approximation (Aki & Richards, 2002). These approaches are established under the well-known Zoeppritz equations (Zoeppritz, 1919)

The results of Di Luca (2016), include various property cubes, i.e., cubes of absolute acoustic impedance, shear impedance and density. These resulting property cubes were used to calculate E_{dyn} and υ_{dyn} using relationships like Eq. 36 and Eq. 37. Subsequently, these parameters were transferred to their static counterparts using again the empirical relationships of Morales & Marcinew (Morales & Marcinew, 1993) and Bradford et al. (Bradford et al., 1998). The resulting E_{stat} and υ_{stat} property cubes (Fig. 58-A and Fig. 58-B) show substantial variations in both vertical and horizontal direction. These data sets provide the spatial distribution of the mechanical rock properties used for the 3D MEM.

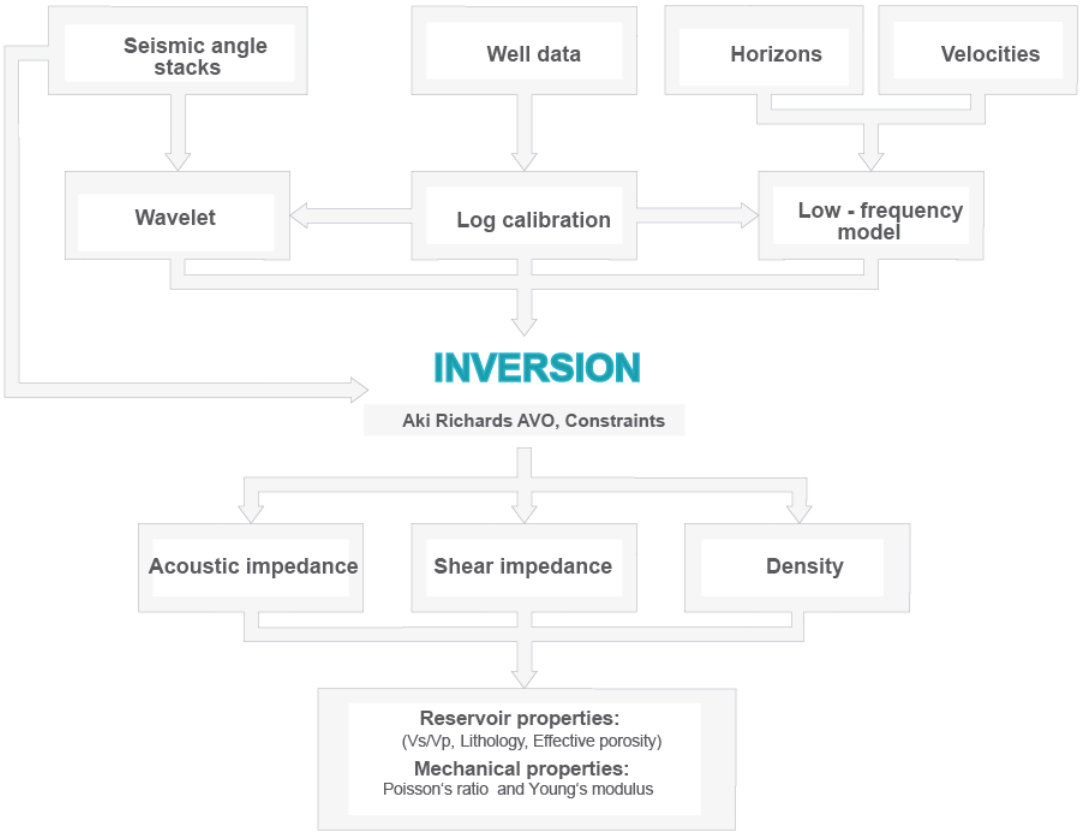

Fig. 57 Seismic inversion workflow and derivation of reservoir properties. Modified after (Di Luca et al., 2014)

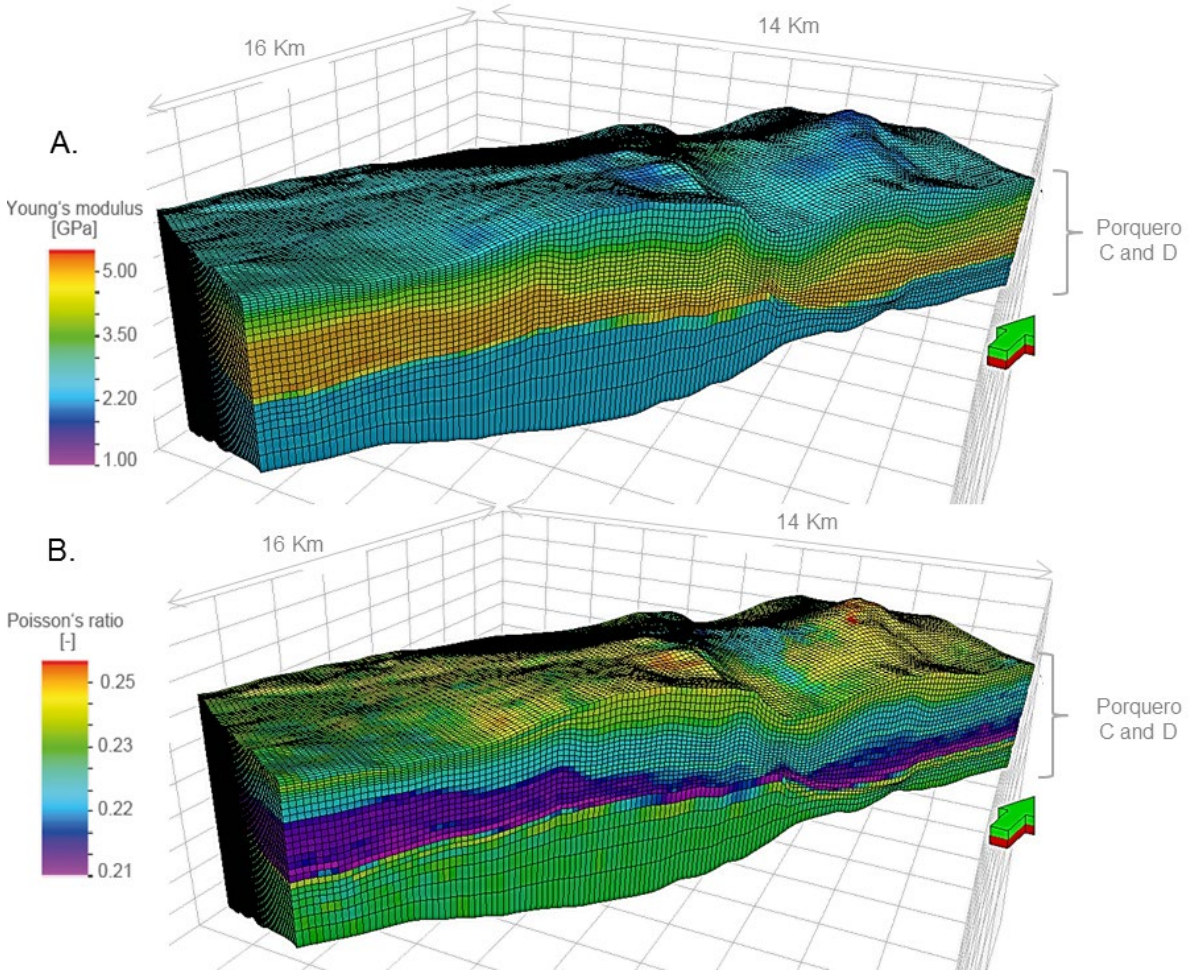

Fig. 58 Final mechanical property cubes after seismic inversion and transformation from dynamic to static material parameters. (A) Static Young's modulus. (B) Static Poisson's ratio. Note property variations both in vertical and horizontal directions.

5.2.2 Property population

This population method uses an integration of the static elastic property derived from the seismic inversion and AVO analysis described above, and the log-derived mechanical properties to achieve a model with lower uncertainty in the inter-well regions. The pore pressure volume used in this section corresponds to the extrapolated pressure gradient volume.

The log-derived property volumes are used as background properties. The seismic-derived data is resampled to the finite element grid and overrides the information in the corresponding cells. Given the coverage of each data type, the final configuration combines property population considering well log data in the overburden section, seismic inversion-derived properties within the reservoir level, and for the underburden depth-trends from well logs (Fig. 59). Pore pressure model remains as in the log-derived approach. The spatial distribution in mechanical properties resulting from this population method, is driven mainly by observed seismic velocity variations rather than inter-/extrapolation by geostatistical methods. The geometry implemented remains the same as in the previous section.

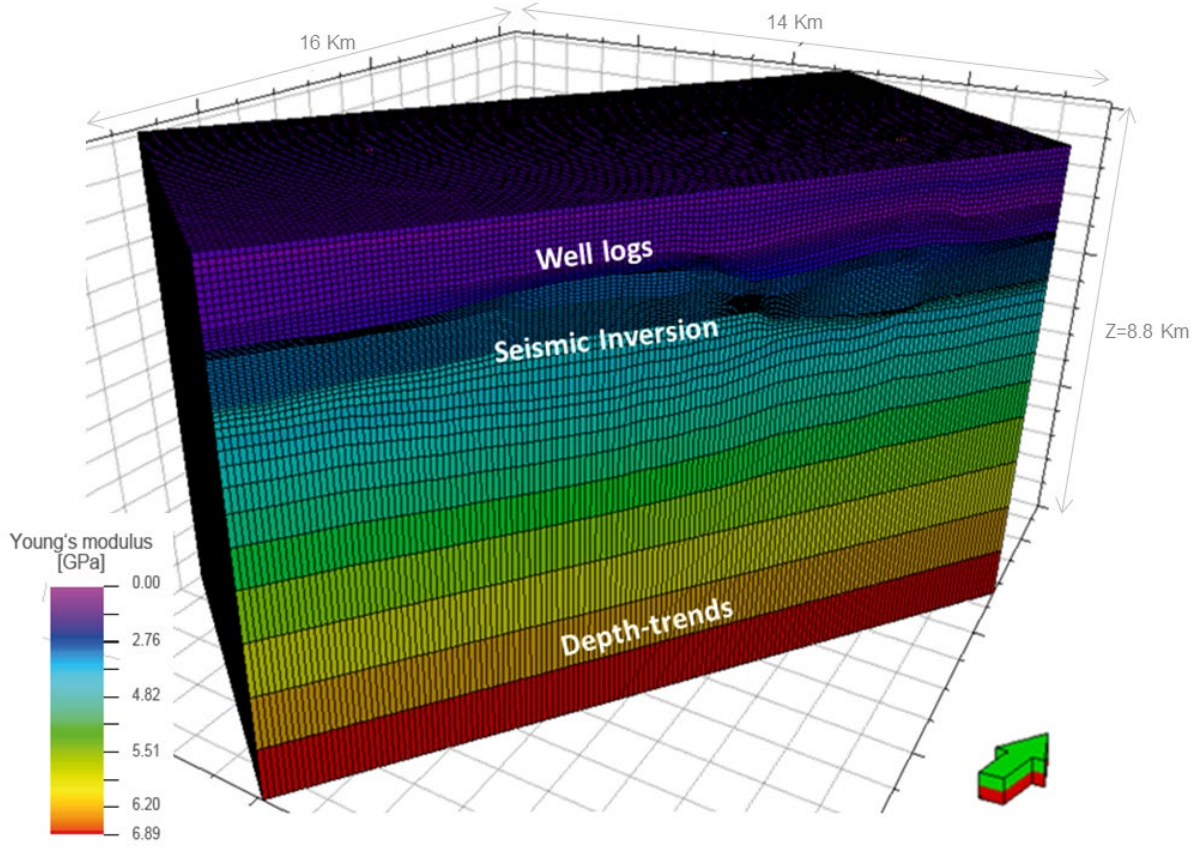

Fig. 59 Population of properties from seismic inversion resulting cubes. Shear impedance resulting from seismic inversion (acoustic-shear impedance and density) were used to derive Young's modulus and Poisson's ratio. The final population is an integration of well logs, seismic inversion data and depth trends.

5.2.3 Model calibration

Like the log-based mechanical earth model, the seismic-driven geomechanical models are also calibrated by comparing simulation results to data measured. Model parameters and boundary conditions are iteratively adjusted until an acceptable correspondence is achieved. In the present study, static elastic properties are calibrated using standard rock mechanical lab testing. Modelled pore pressures area constrained by DST measurements, pore pressure gradients reported in literature (internal reports by Pacific Inc.) and formation pressures from mini-frac tests, finding good correspondence among each other. S_{Hmax} magnitudes are constrained using the stress polygon approach (4.3), while S_{hmin} is calibrated using F_{cp} data (Table 3). After calibration, even for poorly constrained wells, like well E, simulated and measured pore pressures show a difference below 10 %. Concerning stress magnitudes, the calibrated 3D MEM shows a difference at well A of < 5%, while for well E it is between 8-10% (Fig. 60).

The difference between 1D profiles and 3D modelled property extraction of well E, is assumed to be a consequence of several events. First, well E drilled through a very complex formation from ~2500 m onwards, where numerous drilling accidents and events were reported. This supports the assumption that the logs could be affected by these events. The lack of mechanical data from cores makes it complex to restrict the dynamic-to-static correlations of mechanical properties. Furthermore, well E was not considered for calibration of the seismic inversion. The area of influence of well E is assumed to have low uncertainty up to the bottom of Porquero F unit. From this depth onwards, is assumed to

be under constrained. However, having a better understanding of the phenomena of the area, data from well E still represents a valuable source to feed the model.

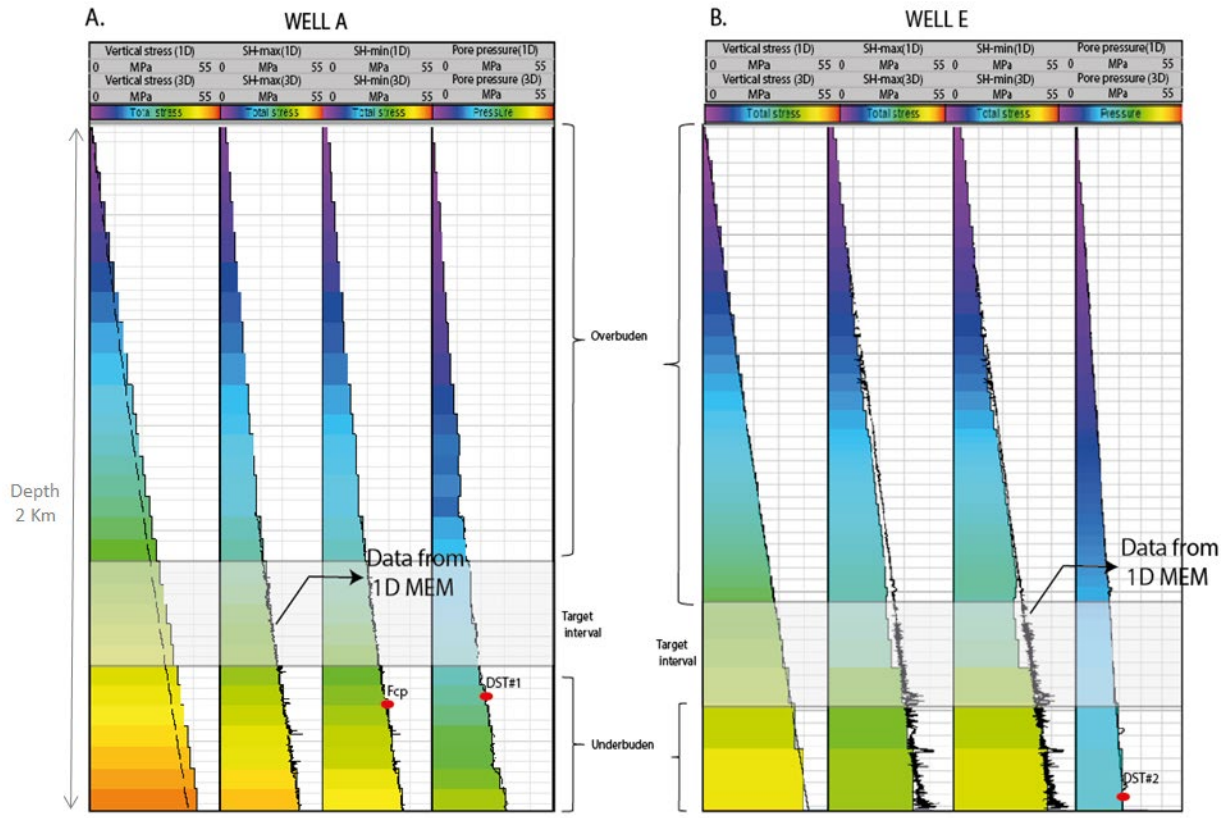

Fig. 60 Comparison of stresses and pore pressure obtained from 1D and 3D modelling. Black irregular line in the profiles represents data from the 1D MEM. (A) Well A, included in the seismic inversion process. (B) Well E was not used in the seismic inversion process. Red points represent the calibration data available for each case. (Fcp= Fracture closure pressure and DST= Drill stem test).

5.3 Basin and petroleum system modelling for geomechanics

Basin and petroleum system modelling technology (BPSM) is a methodology that gathers information since the origin of the basin until present-day conditions. This approach executes deterministic calculus to simulate a sedimentary basin geological history and the generation of associated fluids. Such calculus nowadays requires high computational capacity for numerical resolution, discretised models with detailed lithological descriptions, organic matter and fluid characterisation, as well as paleogeography and structural configurations. This allows the modelling approach to assess the temporal variation and basin's characteristics over the geological time.

Hydrocarbon migration and accumulation represents a key process of BPSM. Nevertheless, the main objective of the BSPM approach is to study the potential applications in the geomechanical field, specifically for the study of (1) pre-drilling pore pressure model and (2) *in-situ* rock stress state. The structure and physics-driven assumptions of the BPSM approach represent and outstanding advantage for geomechanical modelling. Some of these advantages include: (A) modelling through geological time, (B) porosity-permeability-fault and compaction-derived pore pressure assessment, (C) mechanical and stress-dependent fracture orientations estimation, (D) detailed fault properties definition and numerical representation, (F) paleo-geometries for temporal constraint, (G) lithology-

derived properties: porosities, permeabilities, elastic mechanical properties (Young's modulus and Poisson's ratio). From these features, all the necessary variables for a full mechanical analysis can be gathered, setting the foundations for improved petroleum systems modelling or hydrocarbon migration analysis.

The construction of a basin and petroleum system model (BPSM) includes the present-day subsurface geometry such as horizons and faults. Each horizon requires a corresponding age of origin, and phases of erosion or hiatus must be quantified. Additionally, the model is structurally constrained in time by paleogeographic maps. Following the geometrical build-up of the model, it is necessary to add the lithological information as derived from well log analysis and correlations. For each lithology, thermal, hydraulic, and mechanical parameter must be assigned. Mechanical properties are derived from facies maps which contain different combination of lithologies, often based in mixtures of the main rock components. The lithological mixtures are used to derive the compaction behaviour of the specific formation. Given this data-dense model construction it is possible to take advantage of the geomechanical properties evolution.

For this simulation, the general workflow (Fig. 61) is applied in the case study area of Block A. In order to track pore pressure generation mechanisms and stress-changing variables, simulations were performed by increasing the density of the information. Initially, a Terzaghi stress approach was performed considering disequilibrium compaction as the main pore pressure generation mechanism and based on an effective stress model. Following this step, a poro-elastic stress model was used, where extensional and compressional strains were considered.

Calibration is performed in stages through the model construction. The first calibration stage is that of temperature, vitrinite reflectance (Ro%), porosity and pore pressure; the second phase focus in the rock mechanical properties of the unit (Young's modulus and Poisson ratio) where the obtained parameters are matched with properties derived from rock mechanical tests. Afterwards, the model outputs are matched with field and laboratory measurements. Once the desired accuracy has been reached, analysis of pore pressure, rock mechanical properties and *in-situ* stresses, can be performed.

The accurate construction and controlled calibration ensure that this model may serve for further predictive applications. The basin and petroleum system model was performed using PetroMod®[6] software

[6] PetroMod®[6] is a Schlumberger trademark

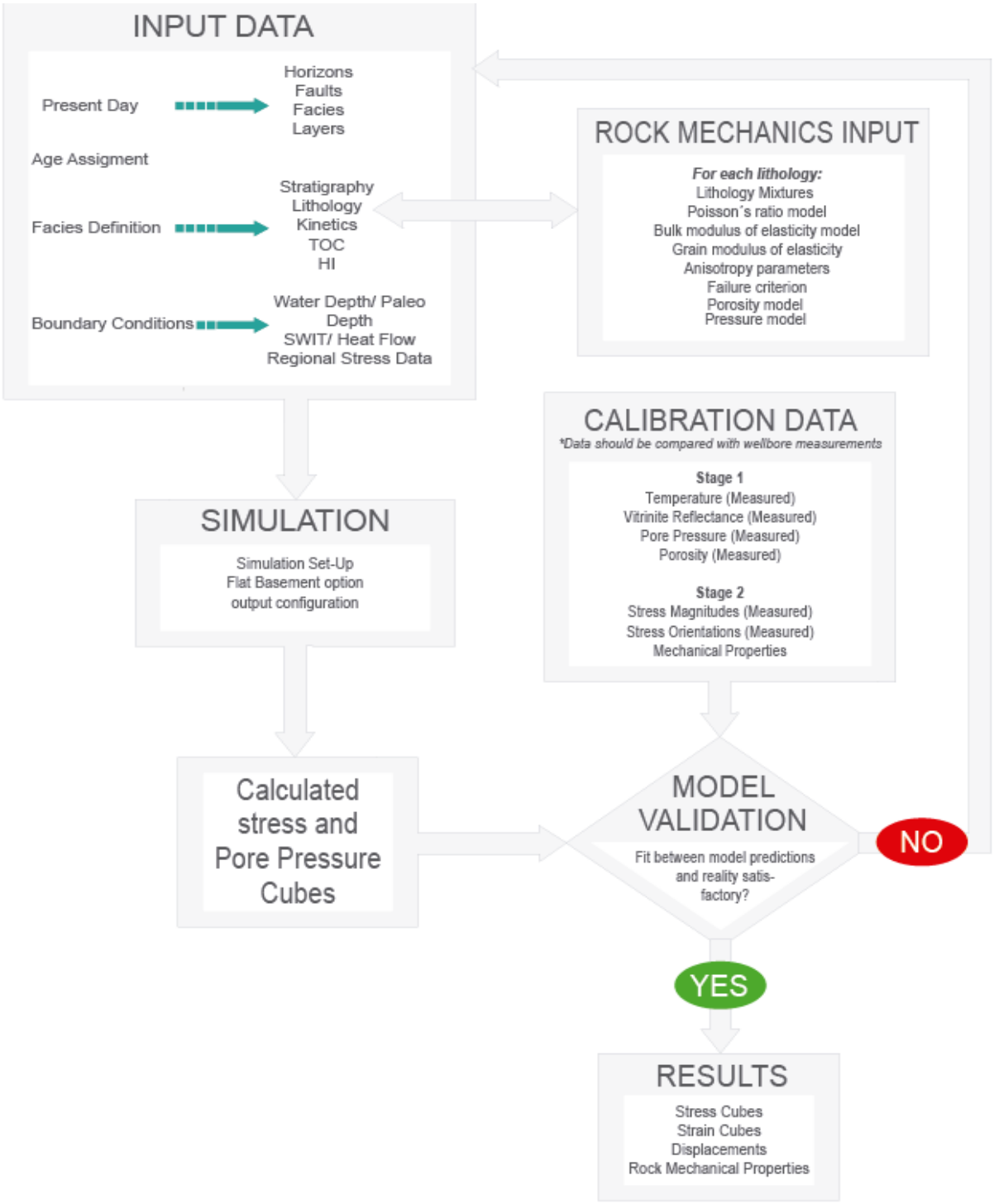

Fig. 61 Basin and petroleum system modelling with a geomechanical approach. There is focus in the geomechanical phases of the simulation

5.3.1 Horizons and fault surfaces

Present-day structural model uses the same elements as presented in 3.1.In summary, 14 horizons, including topography and a flat basement were defined, as well as 13 fault surfaces. Beside officially reported intervals, elevation map at surface level and a flat basement layer were added to increase geometrical homogeneity and avoid generation of shear stresses at the base of the model. Structural elements were derived from reflection seismic interpretation. Horizons and faults were imported in a depth format (Fig. 62-A and Fig. 62-B).

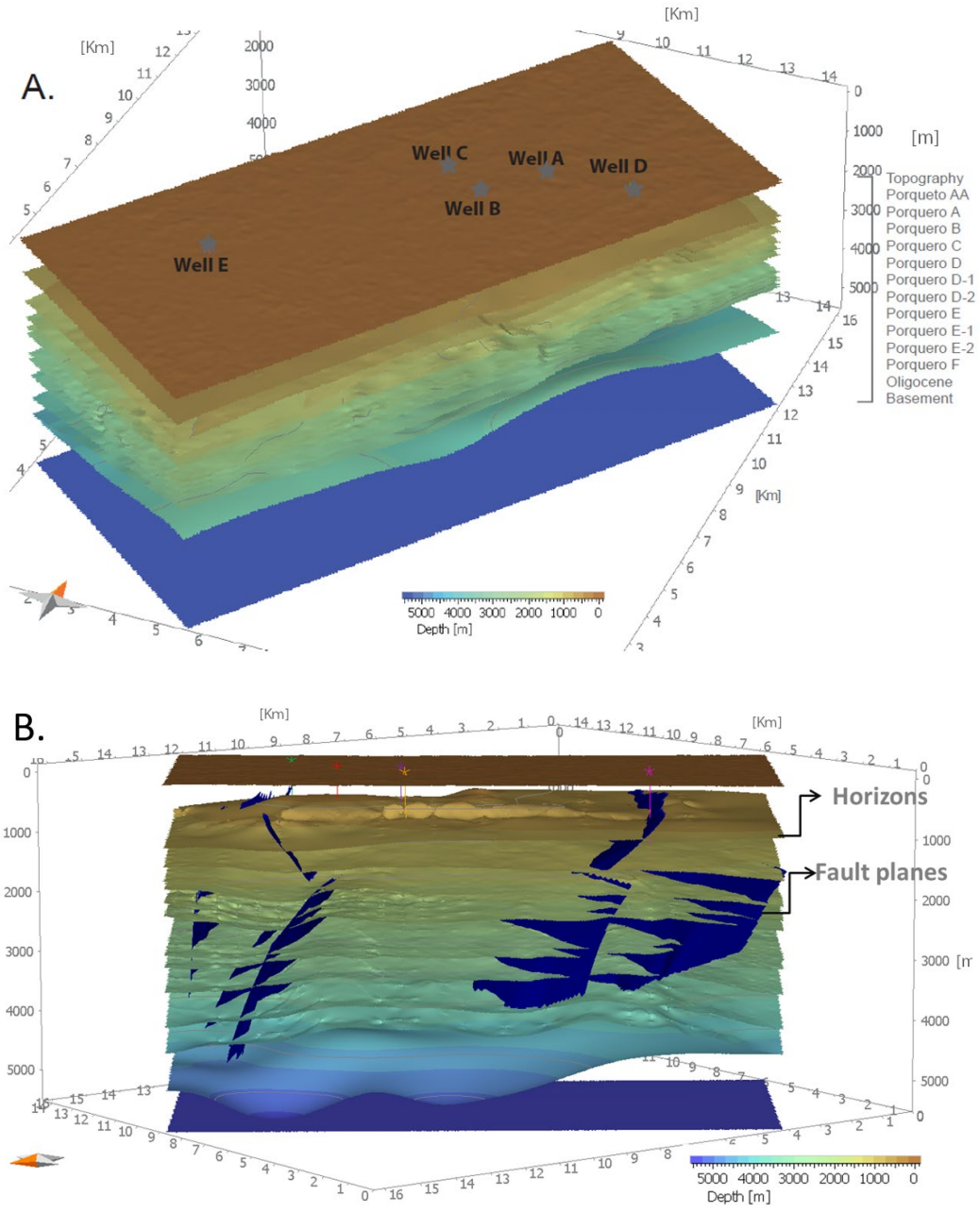

Fig. 62 (A) Imported structural depth maps that conform the model geometry. Topography and a flat basement have been included. (B) Distribution of faults on side view.

5.3.2 Paleo water depth maps

To assess the paleogeography concerning Block A, regional paleogeographic variation proposed in (Bernal-Olaya et al., 2015) was considered. To estimate the local trends, lithological changes were analysed, alongside, biostratigraphic studies and tectonic evolution models that affected locally the case study area (Block A) (Fig. 63).

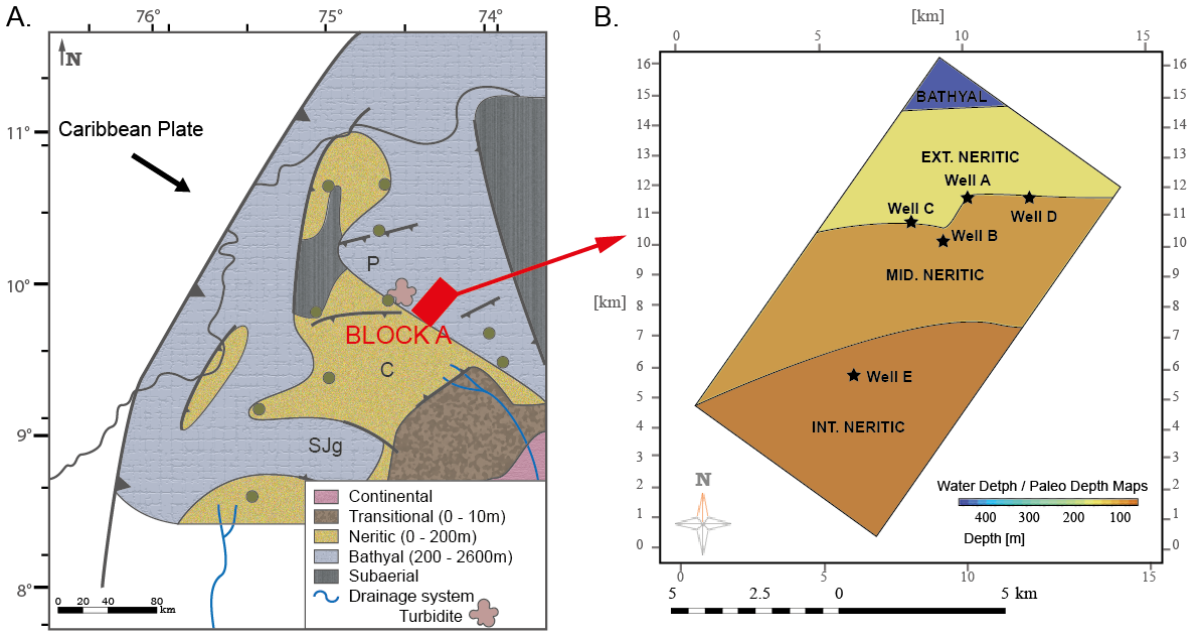

Fig. 63 (A) Regional paleogeography of the Lower Magdalena Valley Basin; modified after Escalona and Norton (2010). (B) Paleo-water depth maps extracted from well trends inside and surrounding the area.

5.3.3 Facies maps definition

Facies maps are a direct result of regional interpretation of geology which is tied with well data for confirmation of trends. Afterwards, the maps are imported as image files to the software and used as a template to draw a final item.

Lithology mixtures

Each sub-layer of each stratigraphic unit was detailed lithologically, considering ditch samples, core data and well logs. The results of such interpretation were integrated with paleogeographic map analysis for each geological age to generate facies maps. Each numbered stripe of the map represents a lithological variation defined through a lithology manager available in the software (Fig. 64). This is a tool that has an extensive catalogue of predetermined lithologies and minerals. These, alongside with percentage-based lithology composition information, were needed to generate custom lithological mixtures. For each code, a lithology mixture was created and afterwards assigned to the map.

Afterwards, for each mixture, parameters as mechanical compaction description, permeability-porosity relations, rock mechanical properties, among others, are set and tuned to resemble the geological context. Finally, the defined mixture is assigned to specific area of the map. Lithology definition in basin modelling comprises a large set of variables and parameters. The way the bulk value of a property is calculated is relevant, since from this definition the mechanical behaviour of the material is defined. Lithological mixtures used in each map are explained in Table 8.

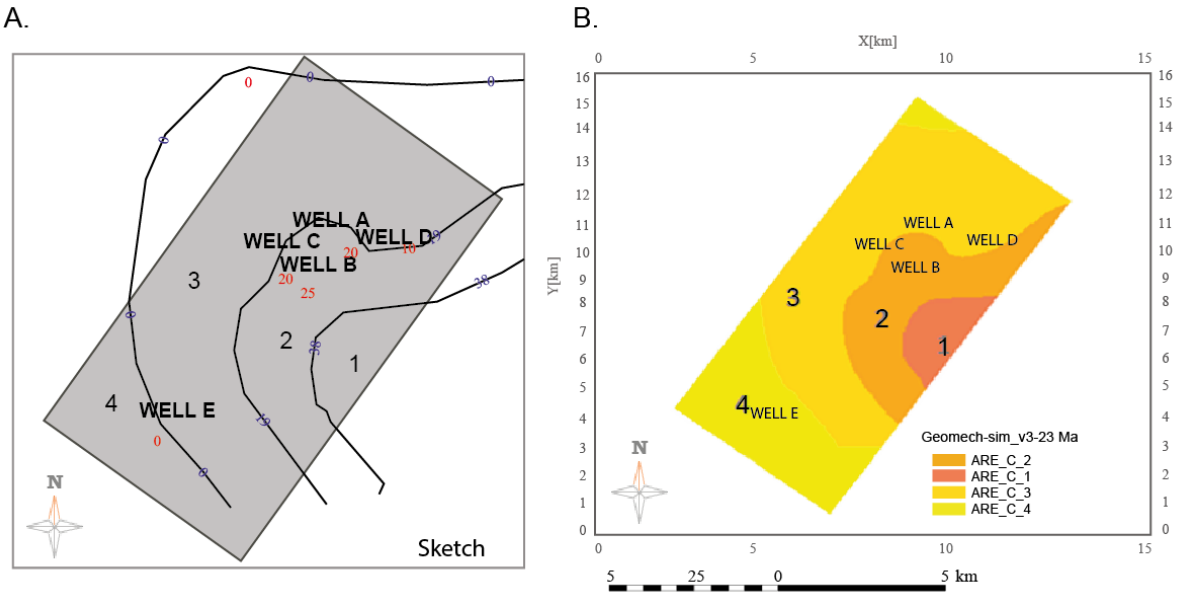

Fig. 64 Lithology assignment to a facies map. (A) Sketch of number-coded maps indicating the area with different lithology. (B) Final map with lithology assignment on top of Porquero C unit.

Table 8: Lithology mixtures. Example for sedimentary target units.

Group	Model layer Name	Facies map	Facies Section	Lithology Mixture Definition
Porquero formation	Porquero AA	FINO_INF_AA	FINO_INF_AA 1	40% Fine grained sandstone + 40 % Claystone + 20% Claystone
			FINO_INF_AA 2	20% Fine grained sandstone + 60 % Claystone + 20% Claystone
			FINO_INF_AA 3	80 % Claystones + 20% Limestone
			FINO_INF_AA 4	90 % Claystones + 10% Limestone
			FINO_INF_AA 5	100% Claystones
		FIN_SUP_AA	FIN_SUP_AA 1	30% Fine grained Sandstone + 70% Claystone
			FIN_SUP_AA 2	10% Fine grained Sandstone + 80% Claystone + 10% Limestone
			FIN_SUP_AA 3	80 % Claystones + 20% Limestone
			FIN_SUP_AA 4	100% Claystones
	Porquero A	ARE_A	ARE_A 1	40% Fine grained (Cemented) sandstone + 40% Claystone + 20% Limestone
			ARE_A 2	30% Fine grained sandstone + 60% Claystone +10% Limestone
			ARE_A 3	20% Fine grained sandstone + 60% Claystone +20% Limestone
			ARE_A 4	10% Fine grained sandstone + 40 % Interbedded Shale + 30% Claystone
			ARE_A 5	5% Fine grained sandstone + 80 % Interbedded Shale + 15% Claystone
			ARE_A 6	80% Shale (calcareous) + 20% Limestone
	Porquero B	LUT_B	LUT_B 1	80% Dark interbedded Shale + 20% Limestone
			LUT_B 2	70% Dark interbedded shale + 10% Claystone + 20% Limestone
			LUT_B 3	80% Dark interbedded shale + 10% Claystone + 10% Limestone
			LUT_B 4	100% Dark interbedded Shale
	Porquero C	ARE_C	ARE_C 1	40% Fine grained lithic sandstone + 50 % Interbedded Shale + 10% Limestone

			ARE_C 2	25% Fine grained lithic sandstone + 50 % Interbedded Shale + 25% Limestone
			ARE_C 3	10% Fine grained lithic sandstone + 70 % Claystone + 20% Limestone
			ARE_C 4	80% Fine grained lithic sandstone + 20% Limestone
	Porquero D	ARE_D	ARE_D 1	40% Fine grained lithic sandstone + 40 % Interbedded Shale + 20% Claystone
			ARE_D 2	30% Fine grained sandstone + 40 % Dark Interbedded Shale + 10% Claystone
			ARE_D 3	20% Fine grained lithic sandstone + 20 % Interbedded Shale + 50% Claystone + 10% Limestone
			ARE_D 4	15% Fine grained sandstone + 30 % Interbedded Shale + 30% Claystone +15 limestone
	Porquero E	E_INF	E_INF 1	70% Fine grained sandstone + 20 % Interbedded Shale + 10% Claystone
			E_INF 2	60% Fine grained sandstone + 20 % Interbedded Shale + 20% Claystone
			E_INF 3	50% Fine grained lithic sandstone + 30 % Interbedded Shale + 20% Claystone
			E_INF 4	40% Fine grained sandstone + 30 % Interbedded Shale + 30% Claystone
			E_INF 5	30% Fine grained sandstone + 40 % Shale+ 15 limestone + 15% Claystone
			E_INF 6	20% sandstone + 60 % Shale + 20% Claystone
		E_SUP	E_SUP 1	60% Fine grained sandstone + 40 % Dark Interbedded Shale
			E_SUP 2	50% Fine grained sandstone + 40 % Interbedded Shale + 10% Claystone
			E_SUP 3	40% Fine grained Lithic sandstone + 50 % Interbedded Shale + 10% Claystone
			E_SUP 4	30% Fine grained sandstone + 30 % Interbedded Shale + 30% Claystone
	Porquero F	F	F_1	50% Fine grained sandstone + 25 % Siltstone + 25% Shale
			F_2	30% Fine grained sandstone + 30 % Siltstone + 40% Shale

5.3.4 Age assignment table

The converging point of the whole model construction is a master table (Table 9). In this stratigraphic table, each stratigraphic unit is linked to a structural map, a specific age, geological event as deposition, erosion or a hiatus, and structural, facies and paleo water depth maps. Units that have considerable thickness can be divided through the generation of sub-layers. As data is included, recurrent updating of the chart is necessary to guaranty the link between datasets.

Table 9: Age assignment chart.

Age [Ma]	Horizon	Depth map	Layer	Event type	Facies Map	sublayers
0	Topography	Topography corrected	Topography	Deposition	Porquero SUP AA	3
5.50	Erosion	Ero_Depth1	Erosion	Erosion	-	
10.80	Porquero AA	Porquero AA	Porquero AA	Deposition	Porquero AA	3
11.50	Porquero A	Porquero A	Porquero A	Deposition	Porquero A	3
15.60	Porquero B	Porquero B	Porquero B	Deposition	Porquero B	1
16.40	Porquero C	Porquero C	Porquero C	Deposition	Porquero C	2
17.00	Porquero D	Porquero D	Porquero D	Deposition	Porquero D	1
17.61	Porquero D_1	Porquero D_1	Porquero D_1	Deposition	Porquero D_1	3
19.44	Porquero D_2	Porquero D_2	Porquero D_2	Deposition	Porquero D_2	1
20.00	Porquero E	Porquero E	Porquero E	Deposition	Porquero E	1
20.88	Porquero E_1	Porquero E_1	Porquero E_1	Deposition	Porquero E_1	1
22.10	Porquero E_2	Porquero E_2	Porquero E_2	Deposition	Porquero E_2	1
22.30	Erosion	Ero_Depth2	Erosion	Erosion	-	
23.00	Porquero F	Porquero F	Porquero F	Deposition	Porquero F	4
26.10	Oligocene-Early Miocene	C.de Oro/Porquero	C.de Oro/Porquero	Deposition	C.de Oro/Porquero	8
	Unconformity					
>40.00	Pre-Oligocene	Basement				

5.3.5 Porosity model

A compaction law or model relates porosity to effective stress ϕ (σ'), equivalent hydrostatic depth φ (Z), and bulk compressibility ϕ (C_b). Most reported porosity–effective stress relations show an inverse relation between the parameters (Fadipe et al., 2016; Hantschel & Kauerauf, 2009). The implemented approach, in this case, is that formulated with hydrostatic depth, considering non-zero minimum porosity, as presented in (Hantschel & Kauerauf, 2009).

$$\phi(z) = \phi_1 + (\phi_0 - \phi_1)\, exp(-\mathrm{kz}) \qquad \text{Eq. 43}$$

Where ϕ is the porosity, ϕ_0 is an initial porosity, ϕ_1 is a minimal porosity, k is compaction parameter (Athy's parameter), and Z_e is the equivalent hydrostatic depth. Calibration of porosity is performed using conventional core analysis results. Geological analysis is necessary to ensure the model follows previously charted trends. Fig. 65-A displays the compaction law for one specific lithology before and after calibration. The tuning of this parameter is performed per formation and for each well independently. The resulting porosity profile (Fig. 65-B) will correspond to a specific facies map stripe and will lead to a distribution as observed in Fig. 65-C. Porosity, depending on the type of sediment, affects greatly the drainage capacity of a formation and may lead to overpressure generation as fluids cannot flow easily.

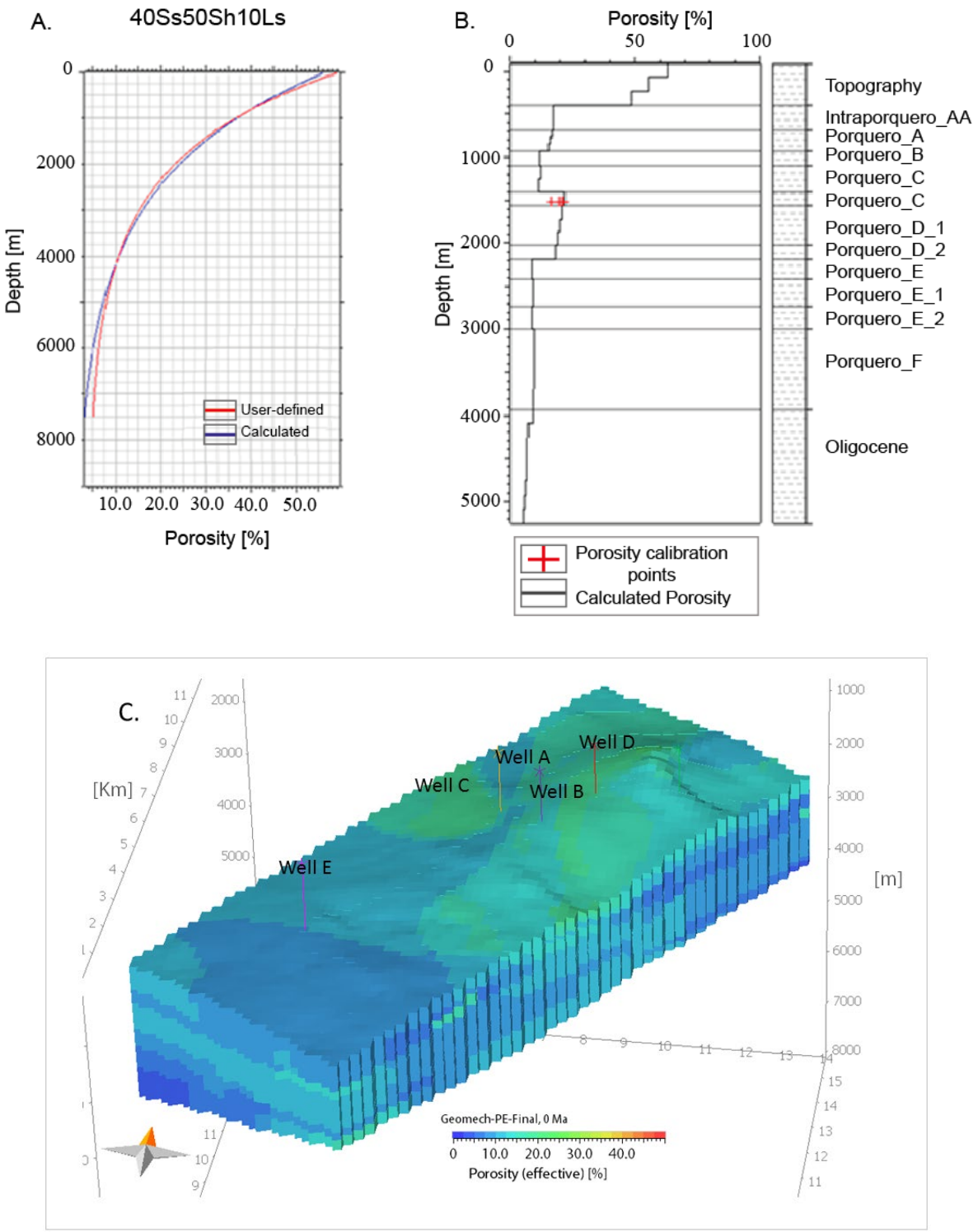

Fig. 65 (A) Porosity calibration for Well A by modification of compaction curve. (B) Porosity derived curve for well A and correspondence with calibration points. The calibration process was performed for the five wells available in the area. (C) 3D porosity model showing porosity variations across the block.

5.3.6 Pore pressure model

The pore pressure approach is studied in stages. In the first stage, the pore pressure formation is assumed to be mainly caused by overburden load, which condition the compaction rate and therefore fluid flow behaviour and drainage capabilities. The fundamental consideration is a porosity reduction in time assessment. The subsequent step considers a porosity-permeability interaction throughout the basin. The spatial permeability variations that affect the pressure field, is conditioned by the connectivity between sediments and the presence of faults.

Faults act as preferential conduits of fluids drainage, depending on the filling material or whether they are open or closed, and therefore determine pressure variations in certain areas. Mechanisms that can be studied from the basin modelling pore pressure approach go beyond the compaction and decompaction of sediments, and may cover diagenetic processes, hydrocarbon generation, among others (Hantschel & Kauerauf, 2009). Fig. 66-A shows the pore pressure calibration for well A using DST measurement and registered mud weight equivalent pressure. On Fig. 66-B, the pressure distribution across the model is observed.

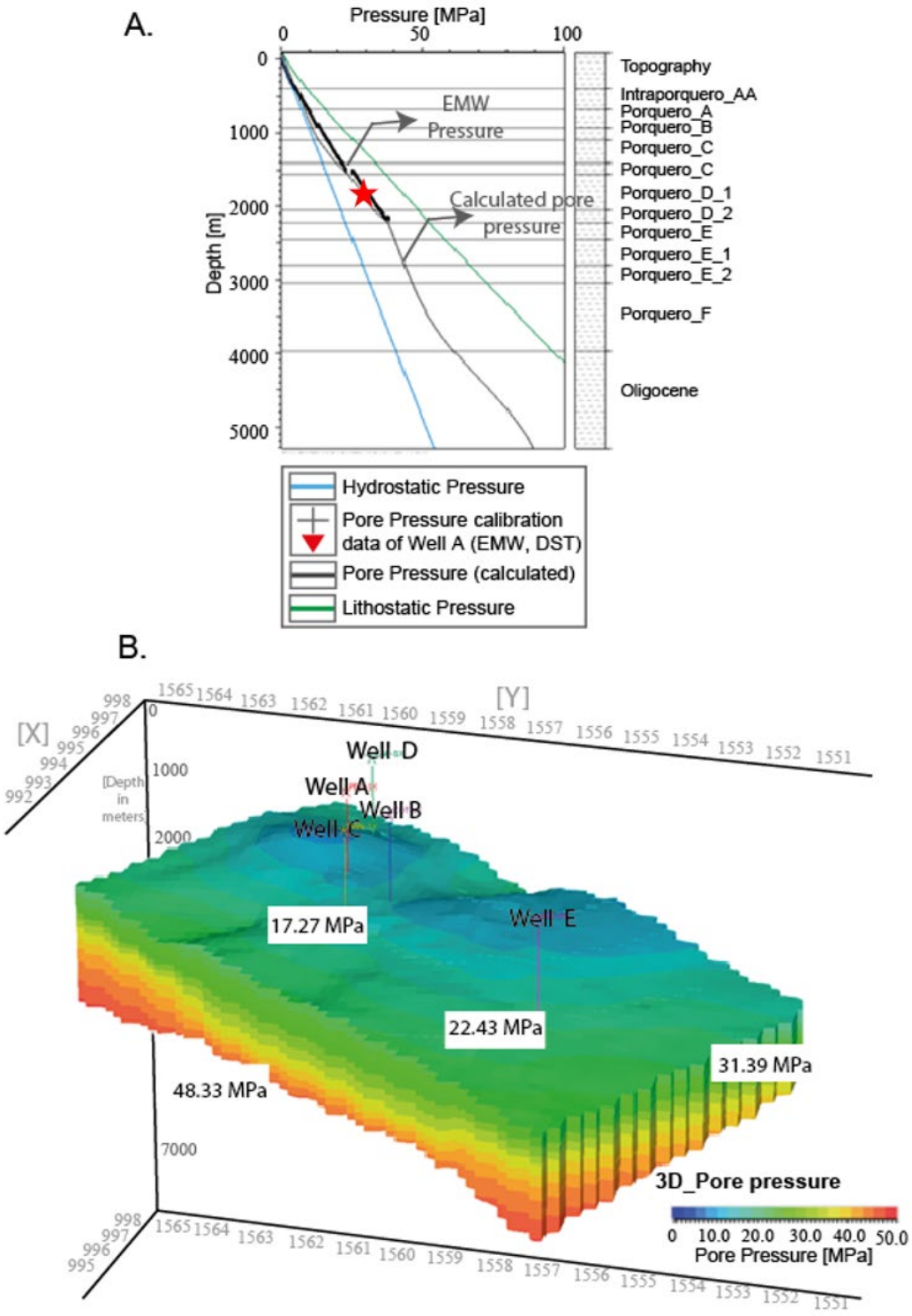

Fig. 66 (A) pore pressure at well location after calibration of porosity-permeability relationship and mud weight trends matching and (B) 3D pore pressure model across Block A.EMW = equivalent mud weight pressure. DST= Drill stem test.

5.3.7 Mechanical properties from facies modelling (Rock composition)

Mechanical properties are defined from facies maps and the lithological mixtures assigned to them. This means that the resulting mechanical property of a cell will be a direct result of the intrinsic properties of the lithologies encountered in that point as estimated from the averaging of its different constituents. The built-in constitutive models available in the simulator are four: *Isotropic poro-elastic, anisotropic poro-elastic, non-porous elastic, and isotropic poro-plastic*.

Depending on the selected model, either isotropic or anisotropic, it may be necessary to define additional parameters like anisotropy in horizontal and vertical directions. In addition, the resulting property volumes consider the subsidence and compaction history suffered by the basin throughout its evolution

5.3.7.1 Poisson's ratio and Young's modulus

The calculation of mechanical properties is described as function of the porosity curve for each lithology. The porosity is conditioned by the mineralogy of a rock, is sensitive to fluid presence, drainage and expansion and also is affected by the subsidence and compaction of sediments. In other words, is sensitive to pore pressure and applied stresses (Mavko et al., 2009). The selected approach for the estimation of Poisson's ratio is a relation "linear from porosity" using Eq. 44. This means that there is an interpolation of values between the initial and minimal porosity defined for each lithology mixture (PetroMod® online help assistant.)

$$\nu(\phi) = \frac{\nu_{\phi m} - \nu_{\phi i}}{\phi_m - \phi_i}(\phi - \phi_m) + \nu_{\phi m} \qquad \text{Eq. 44}$$

Where $\nu_{\phi m}$ corresponds to Poisson's ratio at minimum porosity, $\nu_{\phi i}$ corresponds to Poisson's ratio at initial porosity, ϕ_m equals to minimum porosity and ϕ_i to the initial porosity value. Likewise, the calculation of Bulk modulus of elasticity was performed with the same approach using Eq. 45.

$$E(\phi) = \frac{E_{\phi m} - E_{\phi i}}{\phi_m - \phi_i}(\phi - \phi_m) + E_{\phi m} \qquad \text{Eq. 45}$$

Where $E_{\phi m}$ and $E_{\phi i}$ corresponds to the Bulk moduli of elasticity at minimal and initial porosity, ϕ_m equals to minimum porosity and ϕ_i to the initial porosity value (PetroMod® online help assistant.)

5.3.8 Model discretization and boundary conditions

The model covers an area of 14.8 km of width and 6.81 Km of longitude. Total depth is of ~5.5 km. The structural framework and sedimentary units were discretised using finite element modelling. The master grid comprises 2,887,680 elements, 2,997,819 grid nodes and 32 vertical cells. This is a structured grid with quadrilateral elements. Given the computational *in-house* capacity, it is an advantage to work on a sample grid. For this case, the sampling led to a model of 721,920 elements, 754,446 grid nodes. Vertical divisions remain the same. Horizontal step size of the grid is of 50 m (Fig. 67).

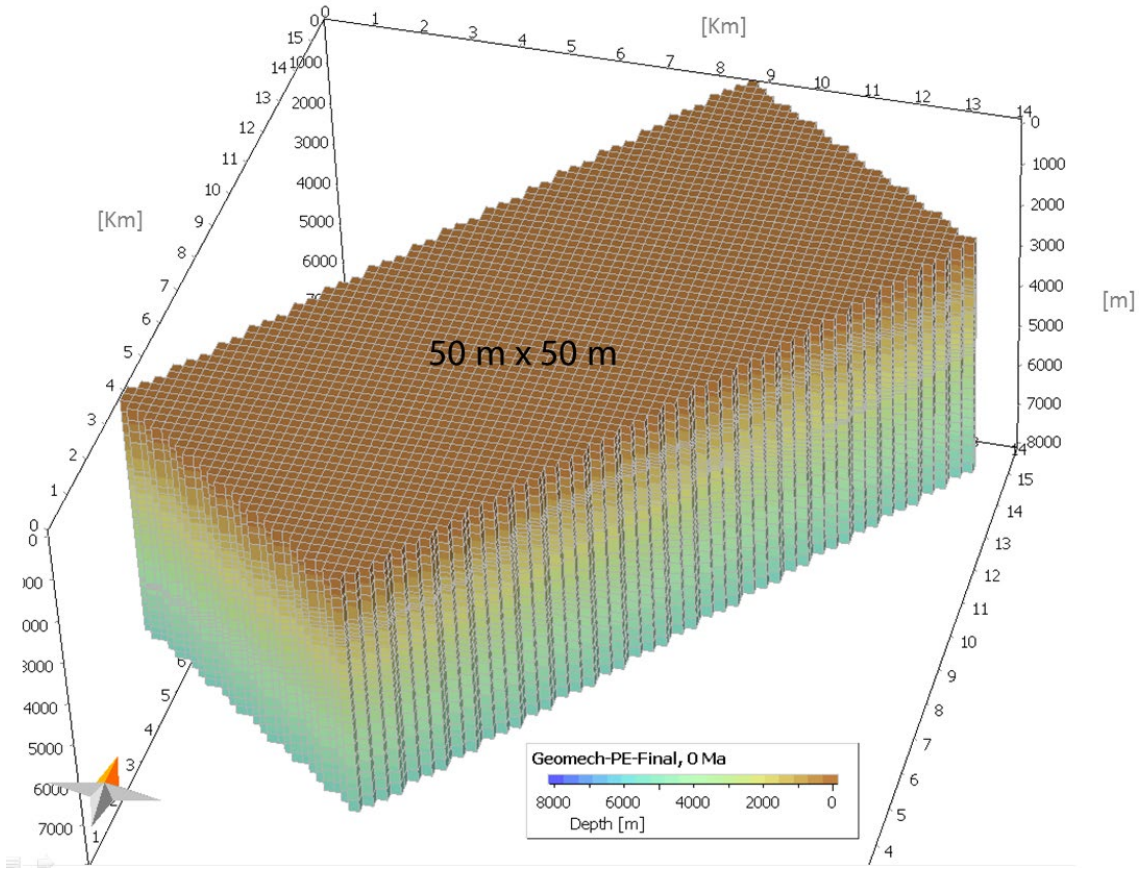

Fig. 67 Model discretization through finite element technique. Horizontal step is 50 m, whereas vertically the model is divided into 32 layers that makes up to 15 horizons.

5.3.9 Geomechanical boundary conditions

The usual boundary conditions are traction free surface, fixed walls on the side boundary (zero horizontal displacements) and a fixed basement (horizontal and vertical displacements are zero) (Hantschel et al., 2012). This model will consider the lateral variations of the materials in a similar way as in the log-driven and the seismic-driven approaches. Tectonic strains, contrary to the previously implemented, will now be considered as a fraction of the total horizontal stretching of the basin. Several sensibilities were tested, and final tectonic strains will be those resulting from the calibration with hydro-fracture data.

5.3.10 Paleo-stress models

Considering the defined tectonic stages extensively explained in 2.5.3, it was possible to estimate the approximate stress orientations for several geological ages corresponding to Block A. The definition of such paleo-stresses will enhance the overall description of fractures and faults generation and will constrain the dynamic model even further. The representation of evolutionary stages takes advantage of the model's present-day thickness of stratigraphic units, lithologies compaction curves, stratigraphic age and paleo-water depth maps for temporal constrain. Geomechanical constraints were added through the imposition of an approximate maximum stress azimuth and a default tectonic strain.

This exercise is generated using the software PetroMod®[5]. The engine recognizes the orientation of displacement which is provided as an azimuth (in degrees). The corresponding tectonic strain for ages different than present-day holds a higher uncertainty and will be considered seed values for further modelling tests.

The process of setting a previous sedimentary unit-thickness is referred as decompaction and backstripping (see section 2.4.3). This works with the defined porosity-permeability relationship assigned for each lithology served to stablish a paleo-geometry, constrained by paleo-bathymetry maps, which will be used again for the forward modelling.

The tectonic mechanisms in the northern part of South America address regional conditions that may be associated with the modelled area to provide a first approximation of the tectonic stresses that affected the Block A. Local tectonic stages were proposed to explain the geological evolution of the basin and the documented tectonic events. The estimated orientations are displayed in Fig. 68, alongside a sketch of the software abstraction. Parameter information includes an estimated orientation and approximated tectonic strains to indicate compressive (negative) or extensive (positive) movements. The stages are assigned to a specific age and are tied to a mechanical property description, derived from the facies definition.

The first tectonic stage imposed in the model corresponds to a representation of Oligocene to Early Miocene age (~26 to 20 Ma), where distension started western side of the area, in the continental platform, which promoted the normal fault generation (Caro & Spratt, 2003) (Fig. 68-A). For this age units Porquero E and F were already sedimented. The orientation of maximum displacement is set to be WNW-ESE (~130°). In Middle Miocene (~15 Ma), regionally, there was a registered cessation of extension, an initiation of convergence and great volumes of sediment filled the existing depression. The local setting is assumed to be compressive in a WNW-ESE (~125°) (Fig. 68-B). In Late Miocene to recent (~ 11-0 Ma) regional effects of the Andean orogeny increased showing northwest-south east shortening of the basin (Fig. 68-C). The stress orientation is derived from the registered collision and consequent compression between the Caribbean and South American plates. An estimated direction of WNW-ESE (~115°) was imposed.

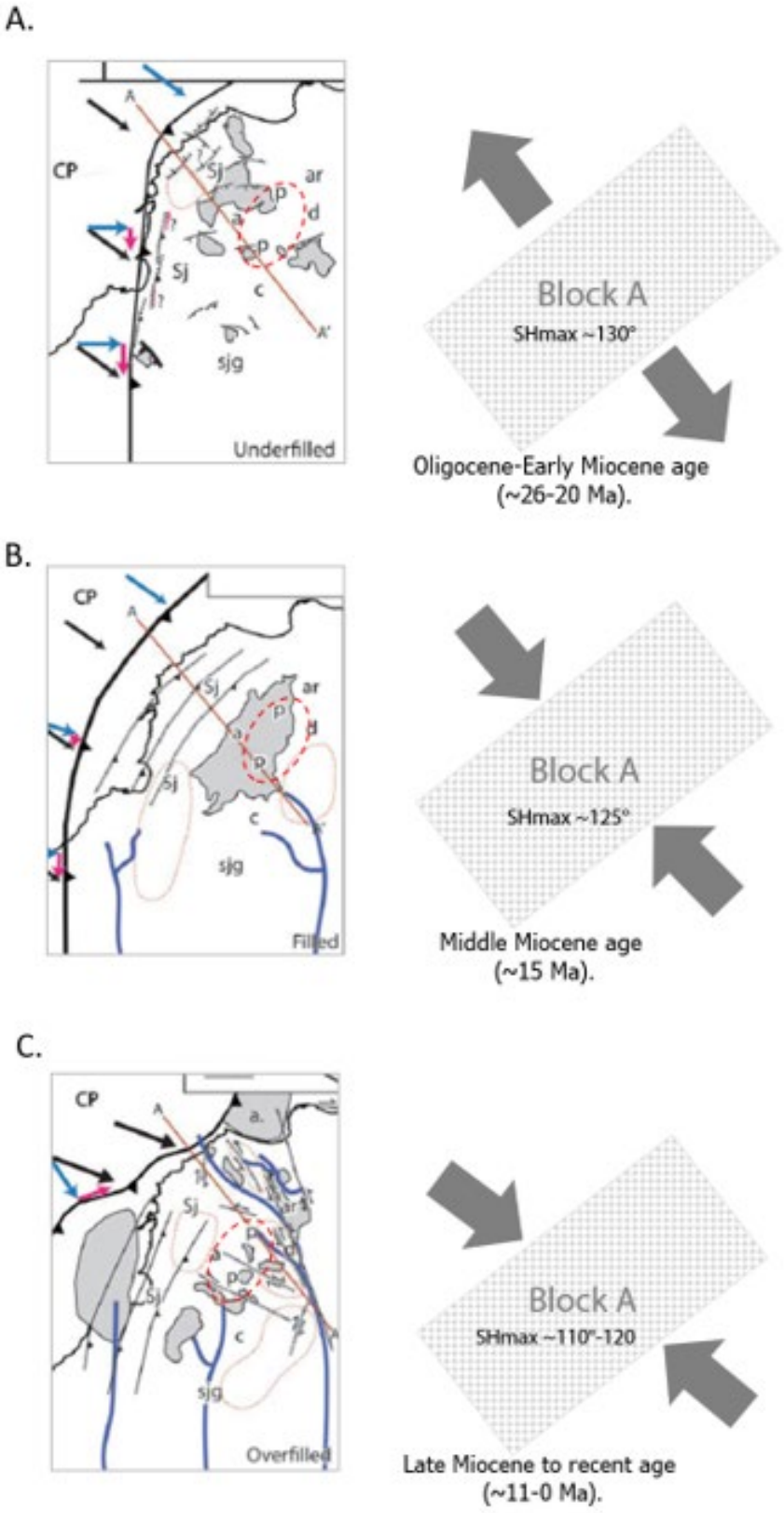

Fig. 68 Representation of paleo-tectonic stresses for the Plato sub-basin (A) Oligocene to Early Miocene (B) Middle Miocene (C) Late Miocene to recent. After (Bernal-Olaya et al., 2015). The area corresponding to the Plato sub-basin is within the red dashed-line circle.

5.3.11 Faults numerical description.

Definition of faults is crucial to obtain a representative pressure model. Each fault surface interpretation is transformed into a structured surface (a continuous plane) and afterwards added into the modelling software. Depending of the numerical and lithological modelling of faults and the sedimentation rates, these will act as a drainage or seal elements that will affect the resulting pore pressure of an area (Yu & Lerche, 1995). Faults can be defined in three ways: as boundary elements, as volumetric elements and as locally refined volumetric elements (LRVM) (Fig. 69). When considered volumetric elements all cells adjacent to the fault plane are defined as fault cells. The advantage of using volumetric elements over boundary elements is the ability to assign permeability values to the fault cells. The downside is the overestimation of fault zones, which can result in large errors in the pressure calculation (Hantschel & Kauerauf, 2009; Peters et al., 2017). When boundary elements are considered, faults act between two volumetric elements with zero volume.

Although capillary entry pressure[7] can be assigned, fault permeability is ignored because it is not possible to assign a value to elements without volume. Because the faults have no width and, therefore, no volume, they do not influence the pressure and impact only hydrocarbon migration (Hantschel & Kauerauf, 2009; Peters et al., 2017).

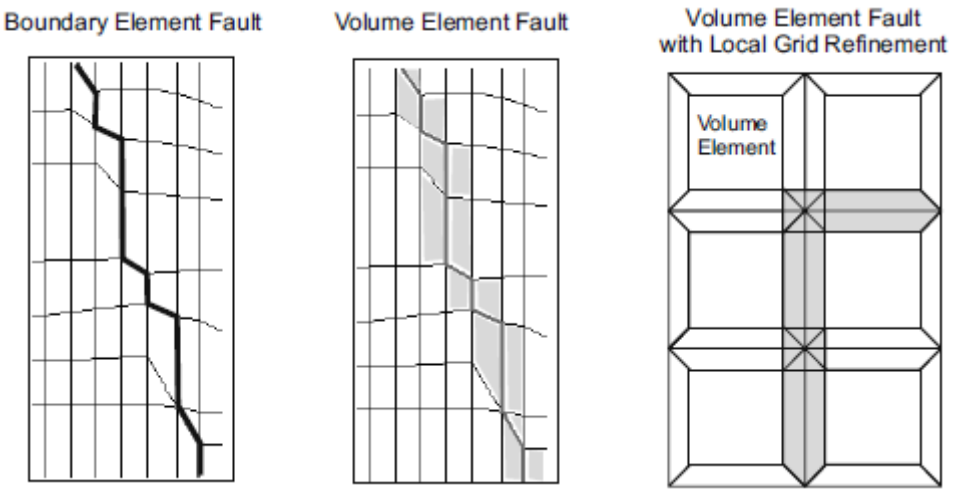

Fig. 69 Numerical representation of faults as boundary elements, volumetric elements of local grid refinement. After (Hantschel & Kauerauf, 2009)

Thirteen faults are included in the model. For these structural elements, an age of origin and whether they are open or closed at a specific geological age was defined. The numerical representation of faults conditions the permeability. When the fault is open permeability is conditioned by the cementation or a default value that is imposed (~1 mD). In the case of setting a fault to be closed or sealed, the minimum permeability is implemented (~0.025 mD) (Fig. 70-A and Fig. 70-B). This behaviour makes a fault to act as a bounding structure and may promote pressure generation or

[7] The minimum pressure you need to apply to force oil into a water-wet rock during primary drainage.

release. An extensive analysis of the characteristic of faults hydraulic properties is beyond the scope of this study but will greatly improve the pressure estimation.

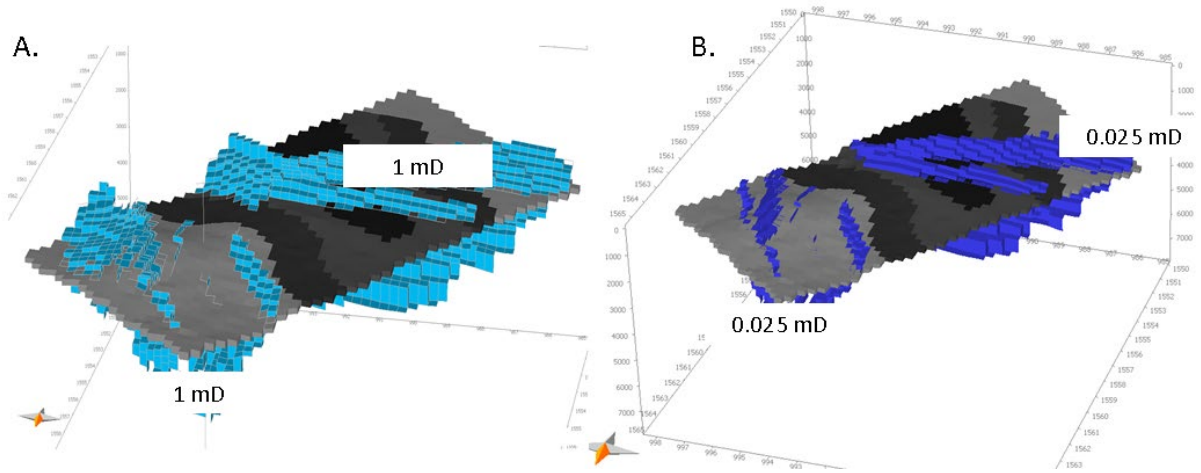

Fig. 70 Fault permeability variations for open and close faults. Fault permeability and accurate description lead to effect in the overall pore pressure generation. (A) All faults open and (B) all faults closed.

5.3.12 Model calibration

Subsequent model calibrations represent the most critical step in modelling basin and petroleum systems, due to the large number of variables considered. Considering the great benefit that represents having a BPS model for a geomechanical study, it is essential to confirm that relevant variables and process interactions are being captured by the software. Sanity check is performed to guaranty the model reproduction of the burial history and thermal model of the basin (Fig. 71-A and Fig. 71-B). The thermal model is considered valid by calibrating the vitrinite reflectance curve against field data, and temperature against reported wellbore temperatures.

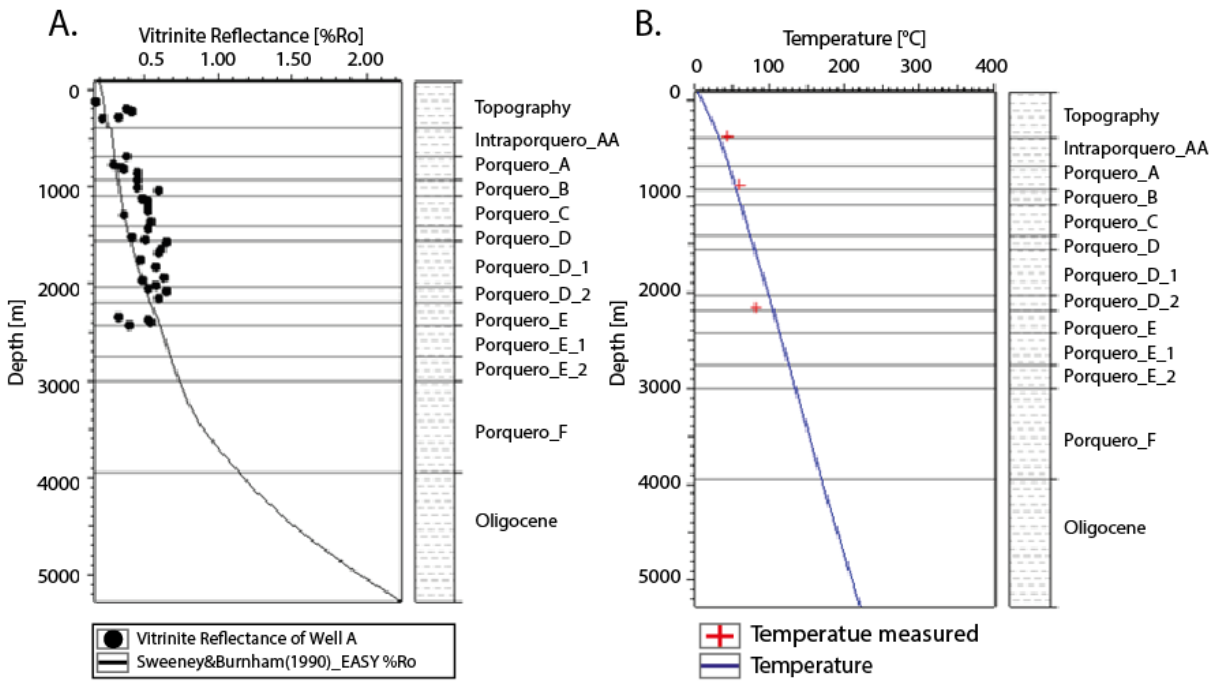

Fig. 71 (A)Vitrinite reflectance calibration. (B)Temperature calibrated against field measurements. Extraction from 3D model for well A.

Porosity trends from compaction curve and associated pressure profiles extracted from the 3D simulation will not necessarily match the calibration data accurately (Fig. 72-A and Fig. 72-B). The curves are therefore calibrated against conventional core data modifying the compaction law at each facies until a best fit is found along the profile (Fig. 73-A and Fig. 73-B).

Porosity is higher in the shallower units as these are loosely sedimented. The porosity trend shows a decrease in magnitudes associated to the compaction of sediments among other mechanisms (chemical compaction, mineral dissolution, etc.). Overall porosity behaviour is modified by shifting the Athy's factor in the compaction law of a specific facies map. There is an inverse relation between the Athy's factor and the resulting porosity.

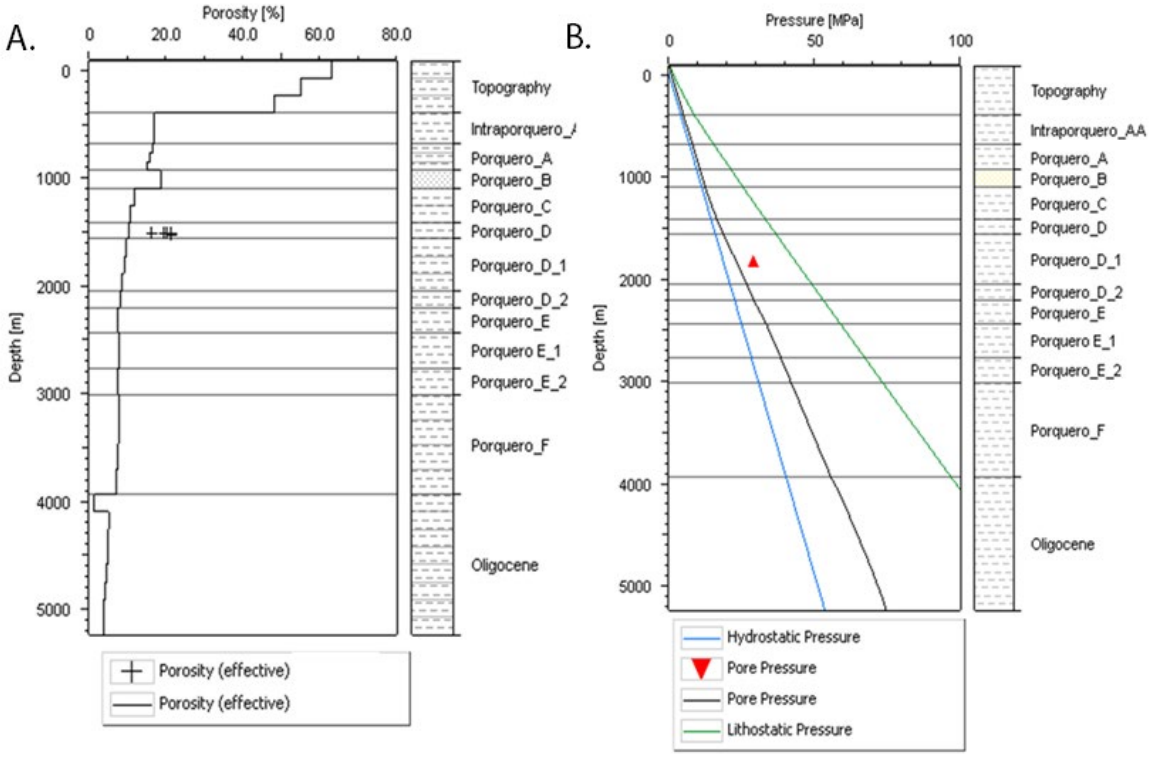

Fig. 72 (A) Porosity profile and (B) pore pressure profile before calibration. Extraction for well A.

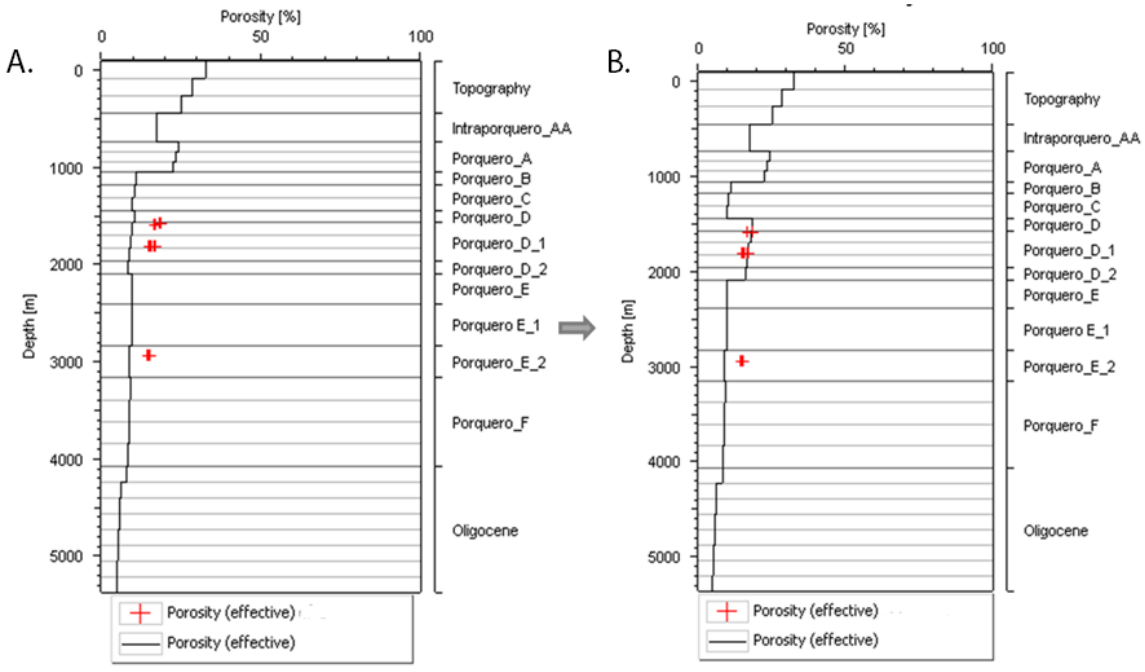

Fig. 73 (A) Porosity profile before calibration. (B) Porosity profile after calibration. Lithologies crossed by the well are modified either by tuning the Athy's factor or adding calibration points where these are available. The compaction curve shifts and adjusts to the calibration point to reproduce the porosity behaviour in the facies map. Extraction performed at well B.

The first attempt to calibrate the pressure model is done under the Terzaghi stress model approach, neglecting the horizontal compressive behaviour of the reservoir. It is performed using the information available at wells including DST results, reported pressures from drilling reports and equivalent mud weight pressure. Fig. 74-A and Fig. 74-B show the calibration process for Well A. The same process was used for the rest of wells available.

Porosity-permeability relation is modified to control the drainage potential of a unit. Mud equivalent pressure from wells and measured pressure points are used to validate the result and pore pressure trends. Mud weight equivalent pressure in drilling practices is used to sustain the formation pressure along the wellbore and represents the upper bound for pore pressure; therefore, pore pressure profile is expected to be below the mud weight equivalent pressure. The detachments in the equivalent pressure from mud weight are associated with increase in the weight of the mud to sustain the increase in formation pressure. This "kicks" and loss of mud circulation are used to fine-tune the changes in pore pressure across formations, for example: the change from unit A to a more-shaley unit B or the change between unit C and D.

Additionally, faults are considered as pressure generation elements, so different trials are performed to check the influence of faults on the final pressure model. Fully open fault setting assumed a permeability associated with the filling sediments of the fault or a default permeability that allows fluid flow. On the other hand, fully closed faults drop permeability to a minimum, obstructing the fluid flow and promoting the pressure build-up. In the case of well A (Fig. 75-A and Fig. 75-B), closed faults generate an abrupt increase in the region of units D and E. This rise in pressure generally matches the overpressure behaviour described for shallower units.

Mechanical properties and stresses calibration process takes place in the following stage. Mechanical properties are a result of the lithological description and are also associated with the compaction of sediments. The behaviour displays a decreasing trend of Poisson's ratio and an increasing trend from Young's modulus. These properties are calibrated against core and rock mechanical results data (Fig. 76-A). Given the scarce data available for calibration, well data from the log-based mechanical model was used (Fig. 76-B). The highest reliability is found in the region between Porquero B and D units.

Stress profiles, including vertical stress, minimum horizontal and maximum horizontal stresses, are obtained by coupling the rock stress model to the simulation. Stress profiles are calibrated against fracture closure pressure measurements (F_{cp}), while the magnitude calibration point for S_{Hmax} is derived from the stress polygon for a specific depth. Log-derived profiles were used to tune the general stress trend at target formations (Fig. 77-A and Fig. 77-B).

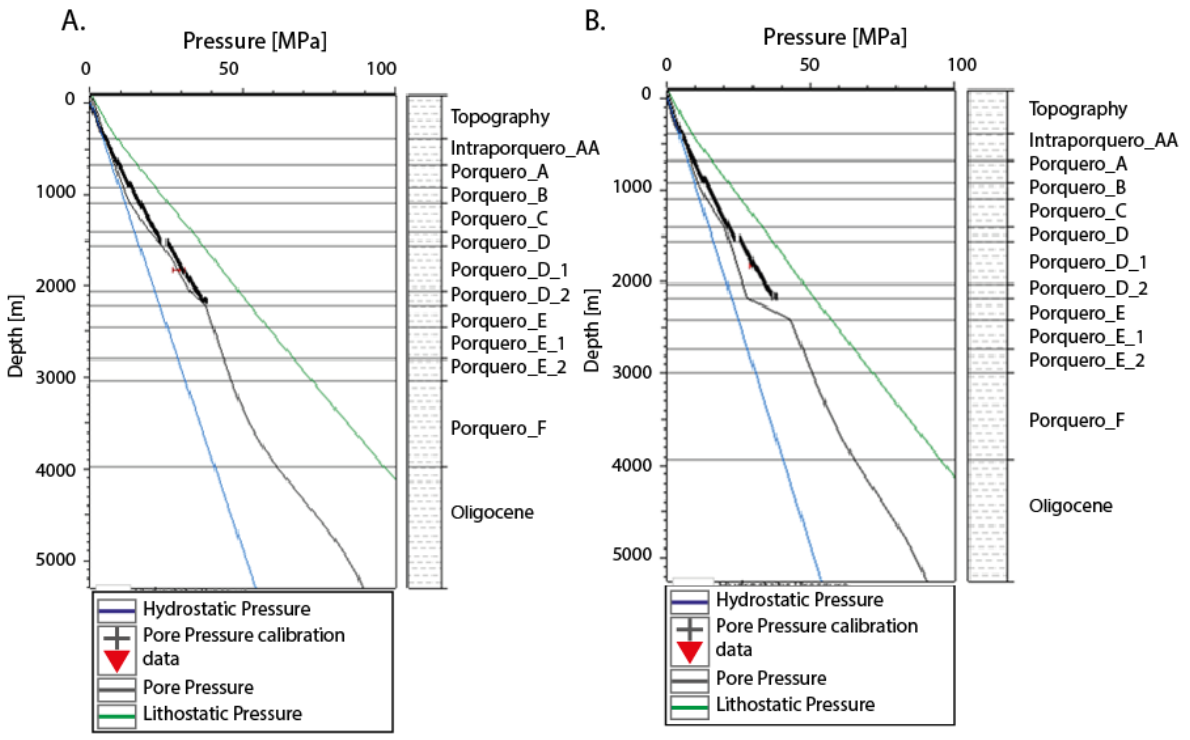

Fig. 74 Pore pressure behaviour on well A. (A) Before calibration and (B) After calibration, using porosity-permeability relations per facies map. An additional calibration of trend is performed using equivalent mud pressure.

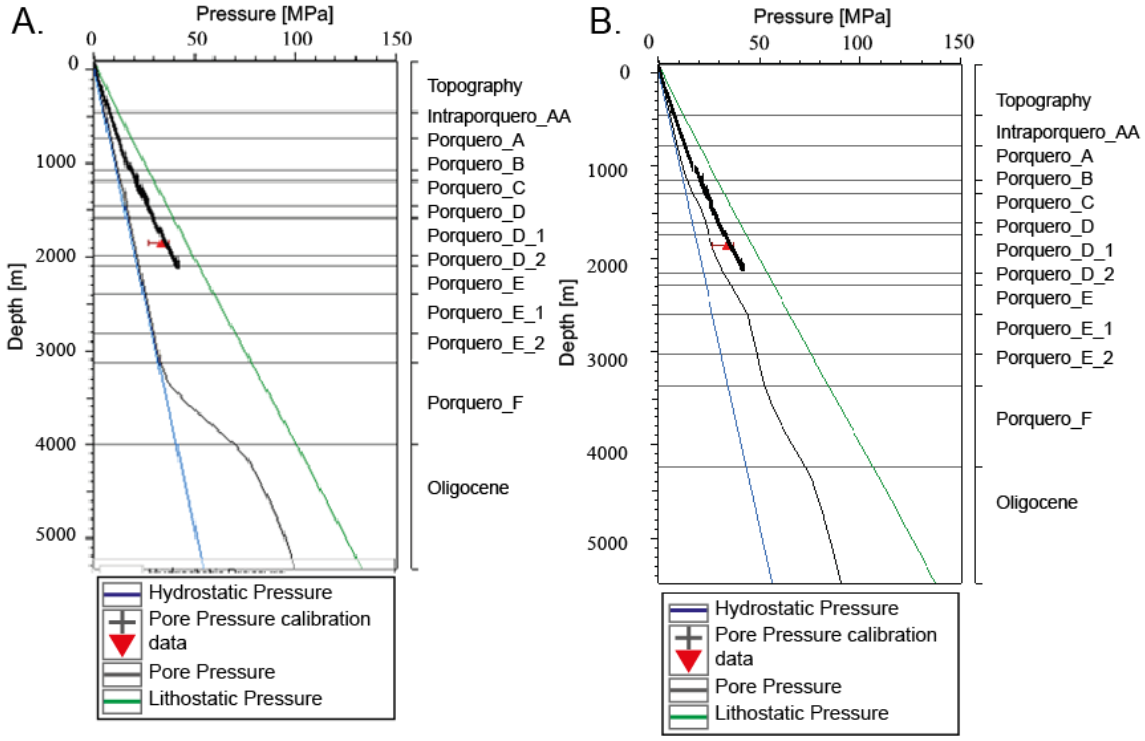

Fig. 75 Pore pressure behaviour with faults inclusion (A) all faults open and (B) all faults closed. Faults when open, act as preferred drainage conduits of hydrocarbons. When they are closed, they act as sealing structures that may hinder fluids migration.

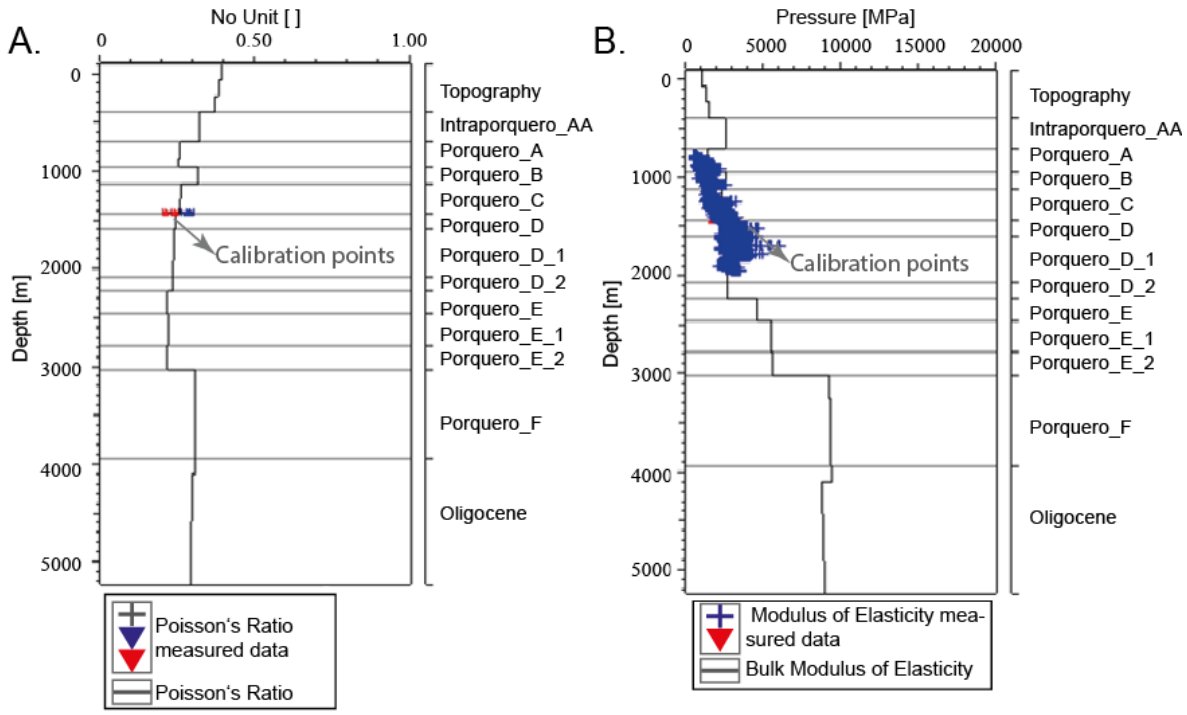

Fig. 76 Calibration of elastic properties (A) Young's modulus and (B) Poisson's ratio for well A. This well has data from rock mechanical laboratory results.

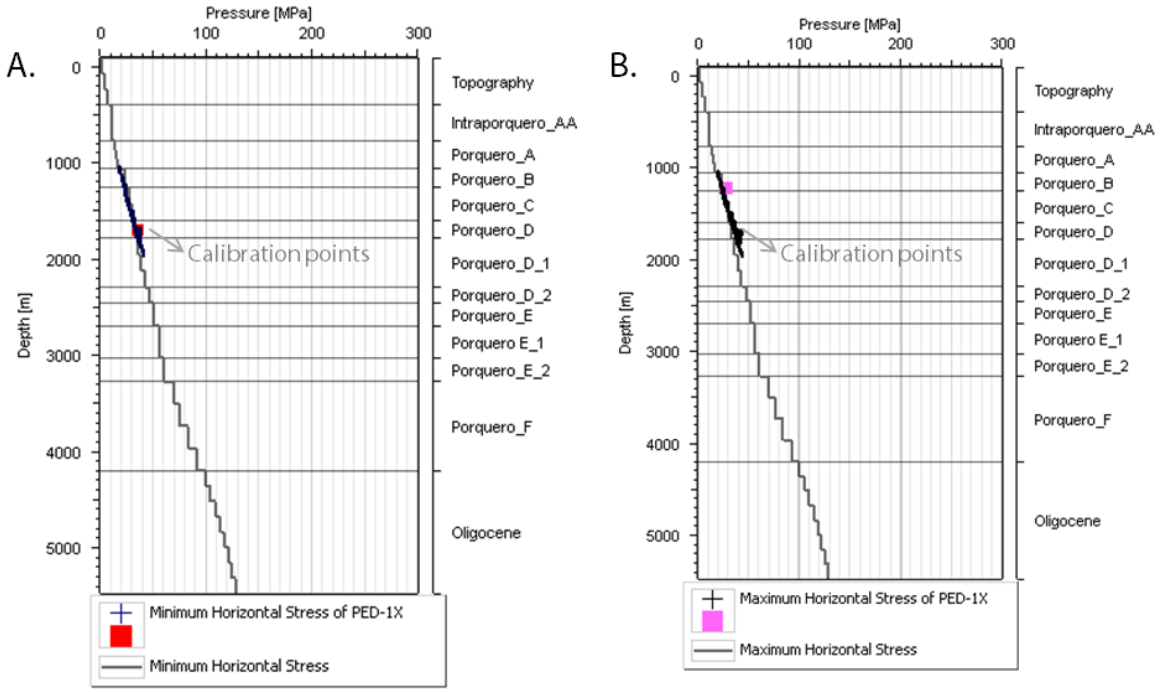

Fig. 77 Calibration of minimum and maximum horizontal stress for Well A. (A) Minimum horizontal stress S_{hmin}. (B) Maximum horizontal stress S_{Hmax}. Calibration data includes fracture closure pressure (F_{cp}) from hydraulic fracturing, and for S_{Hmax}, ranges were obtained from the stress polygon method. Thick line corresponds to results obtained from log-derived stress profiles for calibration.

5.4 Natural fracture modelling

Assessment of existing natural fractures in a reservoir is relevant since fractures represent primary pathways for hydrocarbon migration and production. Critical parameters in addressing the potential location of fracture occurrence are *in-situ* stress, rock strength properties and pore pressure. For drilling efficiency, it is relevant to understand whether the fractures are being generated *in-situ*, they are pre-existing or are being re-opened. Single present-day measurements of rock properties may add little to none information regarding the *in-situ* fracture generating properties, if there is no further knowledge on the tectonic evolution. Conventional and successful modelling includes the use of fracture predictors and detectors: curvature (Chopra and Marfurt, 2007; Dengliang, 2013), and S-wave or coherency methods (Chopra, 2002; Neves et al., 2004). These methodologies, while delivering good first-approximation approaches, often lead to oversimplified "sugar-cube" models. Geomechanical models, as the ones presented in this work, represent a vast amount of information that serve as input data to generate geologic and stress consistent fracture models.

The main objective of this section is to present systematic alternative methodologies that add a geomechanical instance to contribute in the uncertainty reduction of the fracture models. Such reduction may allow improved field development through: (i) better assessment of the recovery mechanisms, (ii) more reliable production forecasts, (iii) well placement for optimal drainage and (v) recognition of drilling hazards associated with fractures (Bourne et al., 2000). The resulting geometrical networks are base models to use in further property analysis and fluid flow simulation.

To accomplish this, two methodologies were performed to obtain discrete natural fracture networks (DFN) orientation and intensity parameters. The first approach works with a present-day configuration under a boundary element method approach and allocates the paleo-stress through an inversion using fault and fracture data. The second methodology considers a forward mechanical modelling approach and geomechanical extractions from a poro-plastic basin and petroleum systems model (BPSM) to estimate the accumulated equivalent plastic strain and indicate potential failure zones. The methods are applied in the study area of Block A, where there is interpreted fracture data for two wells.

5.4.1 Natural fracture prediction workflow

The natural fracture prediction workflow (NFP) generates a fracture network through a methodology that uses wellbore data, far-field tectonic setting and faults that were active at the time of the fracture generation. This methodology is based on the work developed by Maerten (1999). The method relies on the assumption that sub-seismic faults and fractures were developed at the same time or later that the larger structures.

The workflow (Fig. 78) begins with the analysis of wellbore imaging logs (OBMI[8]). The existing fractures for a specific interval of a well are visualized and categorized according to the proposed tectonic environment (tensile or shear fractures). The overall model is based on the continuum approach at large-scale, where the only disturbance is given by the faults.

[8] Oil-based Mud-Imager®

The selection of a suitable fracture generator-stress requires the definition of a tectonic model in consonance with present-day faults and well fracture data. Thousands of simulations were executed testing all potential configurations of stress perturbation caused by faults. The approach ensures a fast and convenient computation of paleo-stress and is suitable for a first approximation, especially in low-deformation areas (Maerten et al., 2016).

At each simulation the engine performs a comparison between the modelled stress and the measured fracture orientation and intensity. The final output corresponds to the best fit between datasets. Output of these steps includes full stress and strain tensor variables necessary to define fracture intensity and respective fracture orientation. Such fracture drivers were obtained through a forward modelling run constrained by the present-day structures and the resulting paleo-stress. These variables: intensity, orientation properties, statistical parameters and concentration factors were used to stochastically generate a discrete fracture network into the selected target unit (Maerten et al., 2014; Maerten et al., 2016).

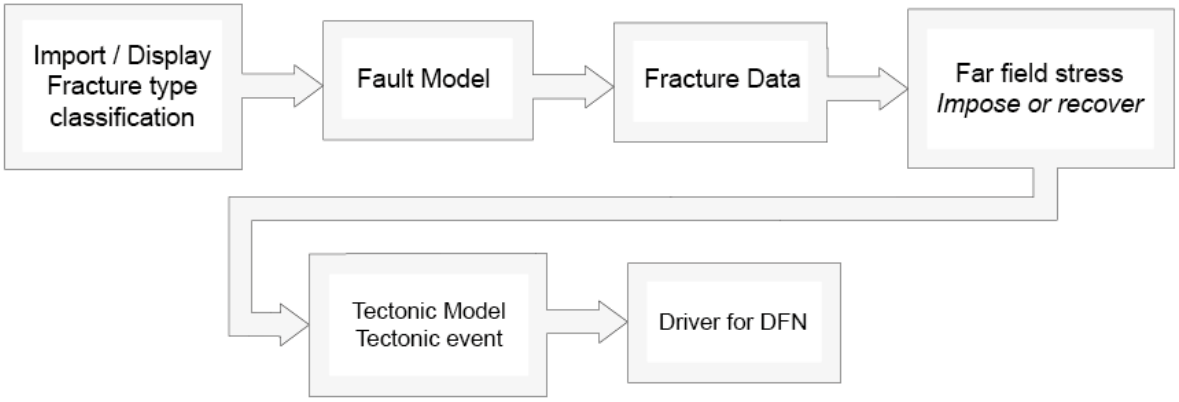

Fig. 78 Natural fracture network prediction workflow. The sequence adds geomechanical constrains, as imposed paleo-stress that potentially generated the well-derived fractures.

5.4.1.1 Well data analysis

Within block A, there are two wells available with fracture data. The analysis of image logs, performed by the industrial partner, derived in the detection of natural fractures, bedding orientation and induced events location (induced fractures and borehole breakouts).

Considering the interval logged the density is classified as low to moderate. In Fig. 79-A and Fig. 79-B, the selected metric analytics, striking orientations and dip angle are displayed for well B and well C as a jointed dataset. 193 Natural fractures were identified in well C and 251 for well B. Fig. 79-A display a rose diagram exhibiting a major strike trend of WNW-ESE orientation (~100-115°). Fig. 79-B shows a histogram of interpreted dip angle, which predominantly range between 20 and 50 degrees.

A section of this dataset (one well) is used as input data for the NFP workflow and the rest (second well) serves later as a calibration data for orientation and intensity parameters.

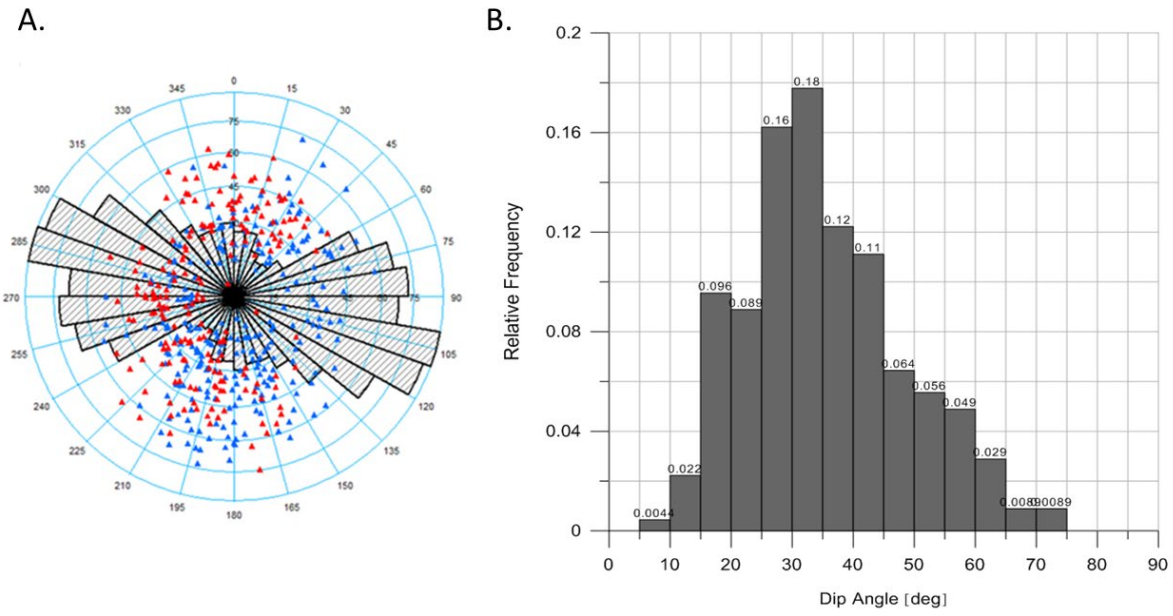

Fig. 79 Natural fracture analysis from well B and well C. (A) Rose map with fracture strike orientation and (B) Dip angle orientation histograms. These plots were generated after image log interpretation of well data provided by industrial partner.

5.4.1.2 Tectonic model and fracture drivers

To perform the analysis in target units Porquero C and D, 8 faults were selected to be the "active structures". The faults are kept continuous structures and are not trimmed. There are two distinctive fault patterns (Fig. 80). The first group, in black, has a preferred orientation of ENE-WSW. The second, conformed by coloured faults, has a governing orientation of WNW-ESE. The selection of different tectonic events per faulting pattern or one single tectonic event for the entire dataset is possible, but discretised tectonic events capture more information to feed the final fracture networks. Output properties of this stage include displacements and full stress and strain tensors.

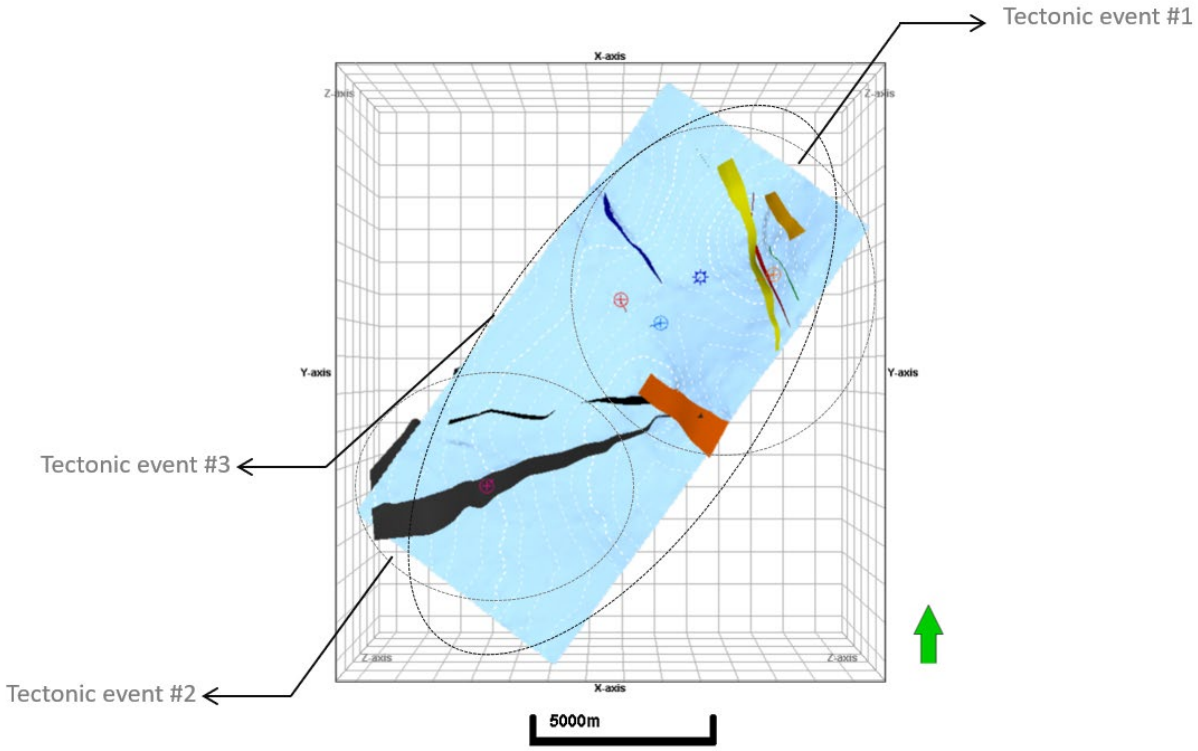

Fig. 80 Selection of different tectonic events according to fault orientations. Two different faulting patterns are recognized for the active faults on top of Porquero C. Each fault group may represent a tectonic event, or one single tectonic event may be defined, including all modelled faults.

Paleo-tectonic stresses

The identification of a stress state that promoted fracture generation in previous geological ages is a very complex process. For this exercise, the *far-field* stress is recovered through a geomechanical stress inversion using fracture data and selected faults (Maerten et al., 2016). The concept is to run thousands of simulations covering the range of all possible tectonic configurations and, for each simulation, compare the attributes of the modelled stresses with the observed fracture geometry (from borehole images). This step works under an engine called iBEM 3D (originally Poly3D) (Bourne et al., 2000; Maerten, 2010).

The engine iBEM3D is developed under a boundary-value problem of an angular dislocation in an infinite whole space or semi-infinite half space composed of a homogenous and isotropic linear-elastic material (Maerten et al., 2014; Maerten et al., 2006). This means that fractures generated due to mechanical heterogeneity are neglected of the simulation, and the disturbance of the stress field is caused by faults. Default values of mechanical properties are a Young's modulus of 30 GPa and Poisson's ratio of 0.25. In contrast with the metrics analysed through log-base and seismic-driven geomechanical models these magnitudes are not fully representative of the target units but will be regarded as a first approximation. The method has its best performance in regions with low deformation (Bourne & Willemse, 2001), such as this case, which may indicate a balance with respect to the lack of heterogeneity. Application for strongly deformed areas is not recommended (Maerten et al., 2016).

The simulations are analysed and sorted to select the simulation providing the best fit with measured data. At the end of each simulation corresponding to a specific tectonic event, a set of attributes, such as fracture dip angle, dip azimuth, stress, strain and displacement are generated. These geomechanical simulations provide local stress tensors on each point of the 3D grid. Finally, a calibration of fracture density can be generated. Fig. 81 displays the tectonic stress selection for one tectonic event.

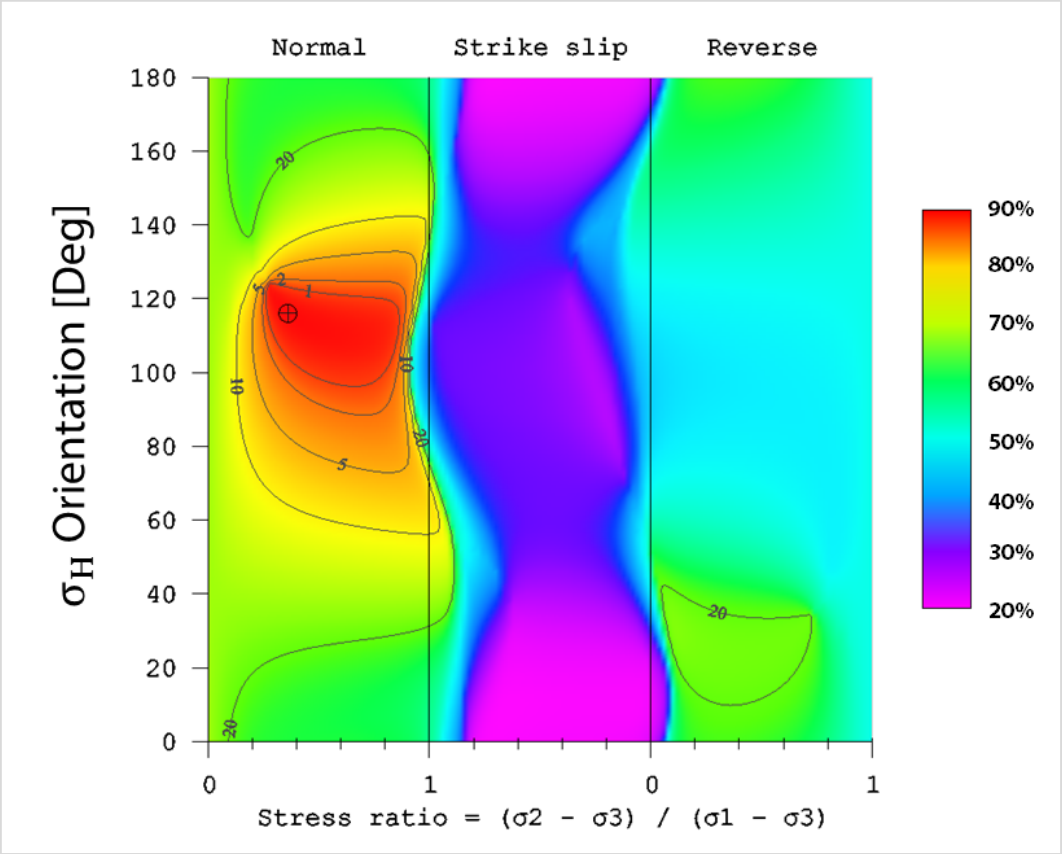

Fig. 81 Paleo-tectonic-stress calculation for discrete fracture network through stress inversion. The iso–contours and colour scale show the best fit between estimated tectonic stress and measured data. The result corresponds to a normal faulting regime, as estimated under an Andersonian assumption. The approximate S_{Hmax} is oriented 120°.

Intensity distribution

Considering the fracture network drivers, including local and regional constraints, fracture intensity per tectonic event is generated as a 3D grid. Fig. 82 shows an intensity grid that displays an increased intensity in the surrounding of major fault structures. This result is reasonable as the fracture intensity increases the closer it gets to the fault surface.

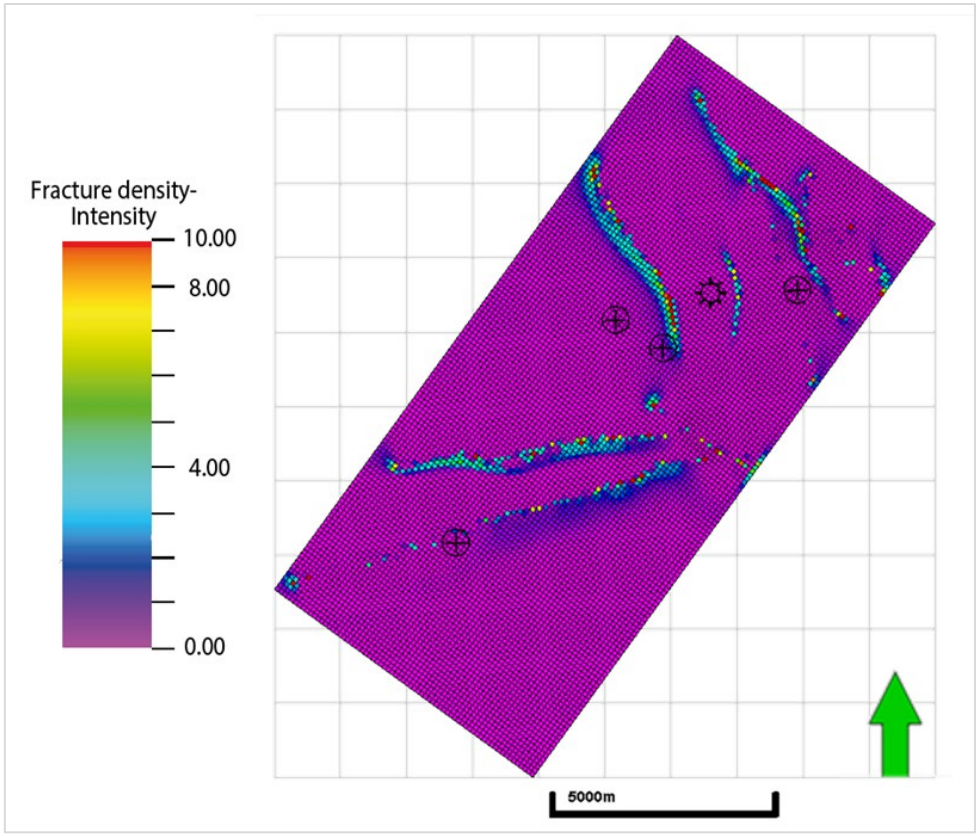

Fig. 82 Fracture intensity resulting from NFP workflow. The higher fracture intensities are located near major fault structures. This screenshot corresponds to a single tectonic event assignation including all the faults. The plane corresponds to the top of Porquero C unit. Arrow points to North.

Fracture orientation calibration

The modelled fracture strike is computed based on a Mohr-Coulomb failure criterion. To confirm that the model is properly capturing the orientation as inferred from hard data (well B), an extraction is done at a well which has interpreted fracture data and was kept aside to perform a blind test (well C). The extraction is performed by the selection of the specific cells that the well intersects and the selection of the fracture planes corresponding to such cells.

Fig. 83-A displays the interpreted fracture striking orientation, while Fig. 83-B shows the orientation obtained through the stochastic fracture network generation. Fig. 83-C shows the sample where the extraction was made. The difference in fracture density is inferred to happen because of the grid resolution, besides the fact that the well sampling is larger than the interval selected for simulation. Overall the fracture orientation coincides with the well interpreted data.

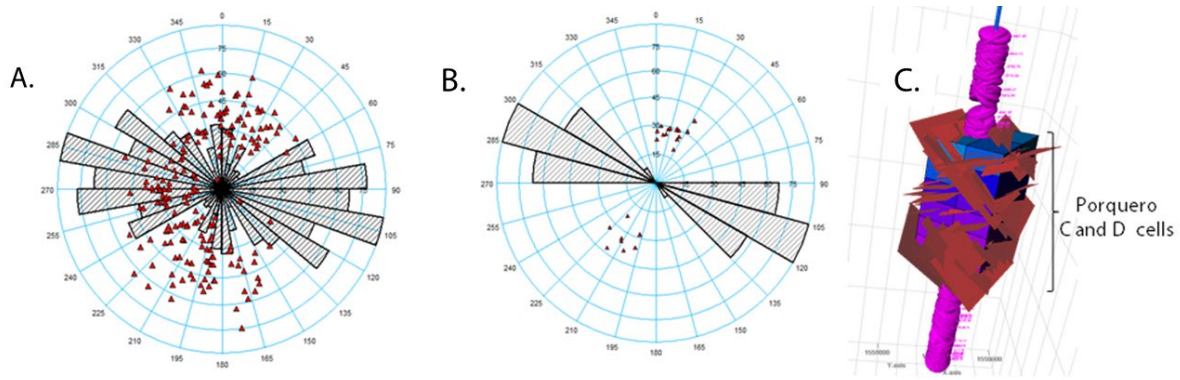

Fig. 83 Resulting natural fracture network at Porquero C level. (A) Dip azimuth of well C interpreted fracture planes. (B) Dip azimuth of the fracture planes extracted from the model at well C location. (C) Sketch of the intervals for extraction.

Discrete fracture network

A discrete fracture network is generated stochastically considering the fracture drivers, namely: preferred orientations of dip angle and dip azimuth, a concentration factor and fracture intensity map. The network is constructed on selected target units to ease computational efforts. There are three metrics necessary to build the DFN: a measure of distribution, geometry parameters and orientation constrains. The fracture distribution is defined by the fracture intensity volume (Fig. 82). Orientation constrain is also derived from the fracture drivers, mainly dip angle and dip azimuth. The engine utilizes statistical correlation to adjust orientation restricted by mean dip angle and azimuth. A concentration value is added which controls the dispersion of the fractures. Upscaling rigurosity of the remaining sedimentary units was not covered in this phase of the project. Fig. 84 displays the resulting discrete fracture network model for the sedimentary units of Porquero C and D.

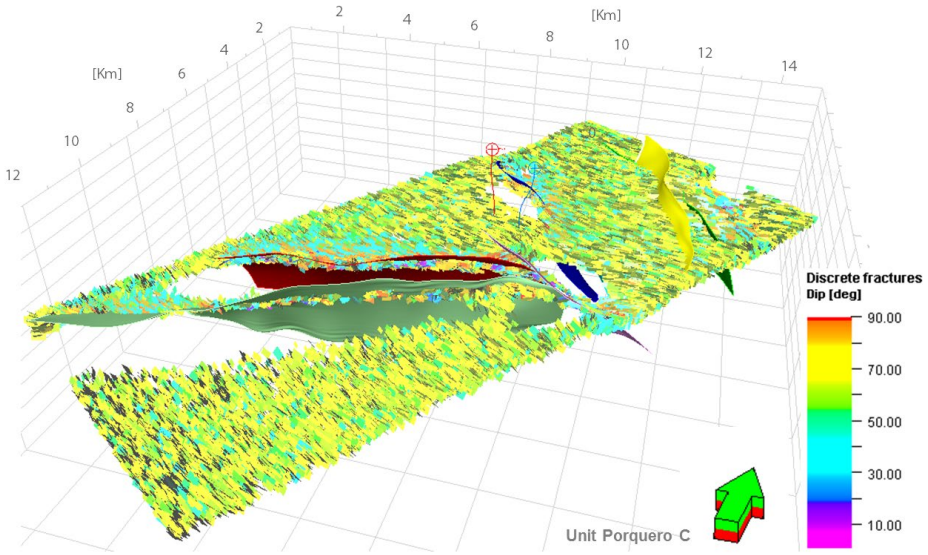

Fig. 84 Resulting discrete fracture network at Porquero C unit. Colour scale corresponds to fracture dip angles. Arrow points to the North.

5.4.2 Fracture network from basin and petroleum system model (BPSM)

The general premise that fractures are associated with major reservoir structures is not always valid. Fractures are affected by a corresponding in-situ stress, pore pressure and the mechanical properties of the material. It is known that rock properties change on scales of tens to hundreds of millions of years (diagenesis, deformation, uplift, burial, and alterations) (Maerten et al., 2016). Basin and petroleum system modelling is an approach that can capture the deformation suffered by a sedimentary basin through geological time. In this approach a convergence between basin dynamic events, chemical events, generation and migration of hydrocarbons and geomechanics is considered. Geomechanical forward modelling, an inherent modelling piece available in the basin modelling approach, allows the evaluation of physical laws dictating the formation of faults and fractures under chronologically-appropriate *in-situ* conditions (Noufal et al. 2015).

As background variables, there are all sorts of geomechanical features that are being regularly modified by the convergence of the mentioned processes. Through the temporal discretization of events and the finite element method implementation, it is numerically possible to capture the deformation suffered by the area through geological time.

An equivalent plastic strain was calculated with the mechanical outputs of the model. The equivalent plastic strain concept is a bulk value of the unrecoverable deformation fraction of the total strain suffered by a material. The premise of the model is that an area with high equivalent plastic strain will potentially allocate higher fracture density

On a first instance, the model is constructed to reproduce the deformation history of the basin by the addition of geomechanical boundary conditions, derived from the tectonic evolution analysis (Fig. 85). This means that approximate maximum horizontal stress orientation is added per geological age. The mechanical behaviour per age is derived from facies maps assigned to the stratigraphic horizons. The model works under a Drucker-Prager failure criterion.

Afterwards, with the full 3D mechanical properties, fracture orientation and stress-strain tensors, it was possible to compute fracture intensity for the target unit. On the final stage, an extraction was made on well level and the potential of the synthetic data to generate fracture networks was tested.

This approach gathers a robust set of data such as mathematical algorithms, stratigraphic, palaeontology, petrophysical, well logging, tectonic evolution and other sorts of data to reconstruct the basin evolution. These premises lead to the assumption that the most reliable approximation regarding pore pressure and fracture models is accomplished through this approach. The efforts of the BPSM derived fracture networks often target strongly deformed areas, considering the high computational demand required to develop the models.

The reason for the later statement is because conventionally, the data necessary to construct such models is not entirely available, and low-to-mildly deformed areas can benefit from a much faster and simple approach (see section 5.4).

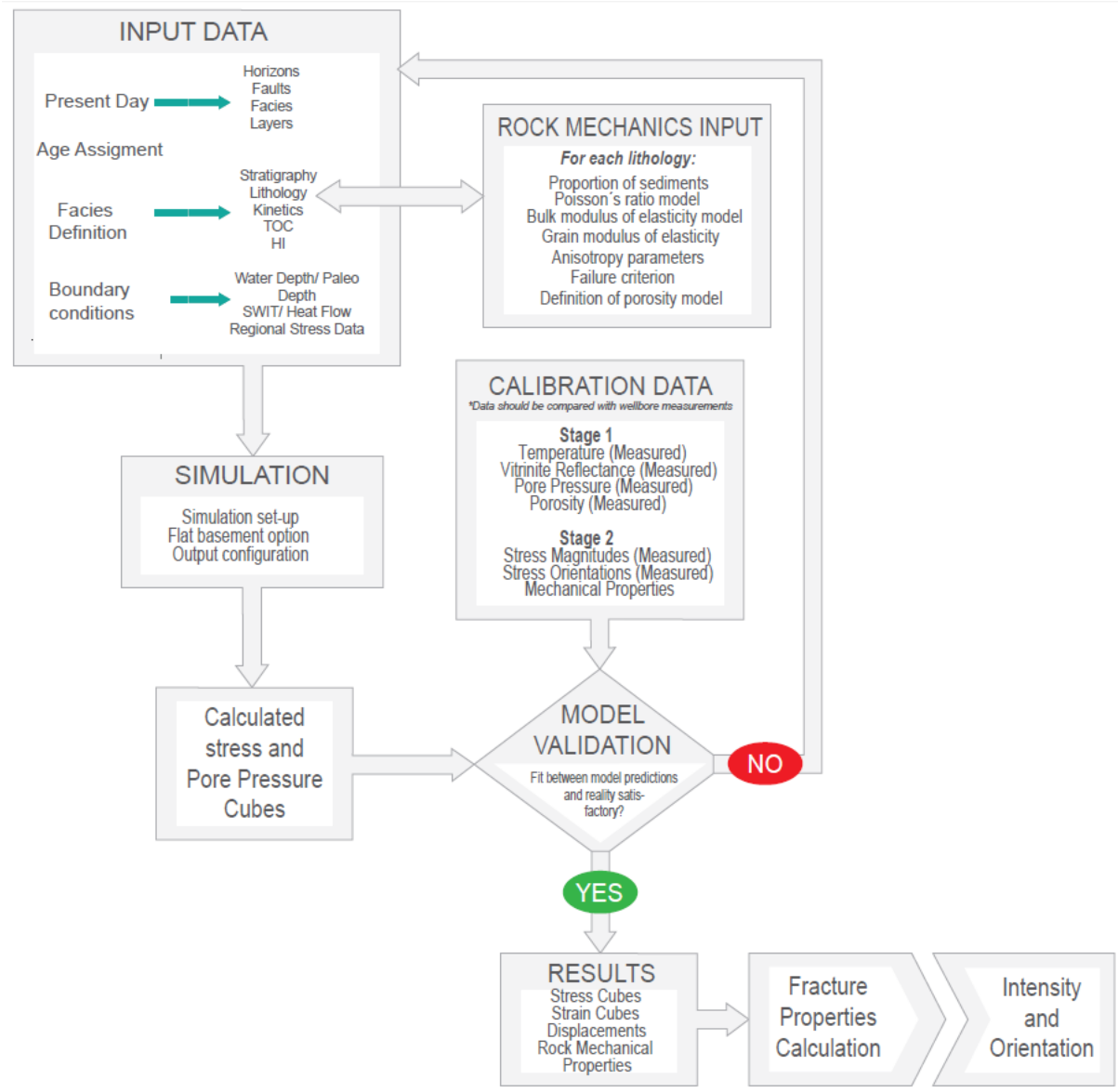

Fig. 85 Natural fracture network modelling from basin and petroleum systems model. The fracture network approach takes advantage from the basin model construction, specifically from the mechanical approach, leading to temporally accurate boundary conditions and enhanced fracture prediction.

5.4.2.1 Fracture drivers from forward modelling and discrete fracture network generation

From the poro-plastic run of the basin and petroleum system model (BPSM), several property volumes were extracted, which were used as input towards the natural fracture network prediction. The mentioned properties include effective and total stress tensors, friction angle, yield modulus and plastic strain tensor. These property volumes are transferred to Petrel ® for its visualization advantages. An equivalent plastic strain is calculated funded in the Von Misses equivalent strain theory (Barnichon, 1998). This property serves as a representation of the amount of deformation suffered and accumulated by different areas of the basin through the defined geological stages. A linear relation is established between the equivalent plastic strain and fracture intensity. The assumption is that zones where there is a high plastic strain, are likely to have higher fracture intensity. Fig. 86 depicts a filtered area of the model's intensity volume. The resulting volume

alongside with orientation outputs are used to compute a discrete fracture network. The engine utilizes intensity volume, orientation volumes, default geometrical and aperture parameters.

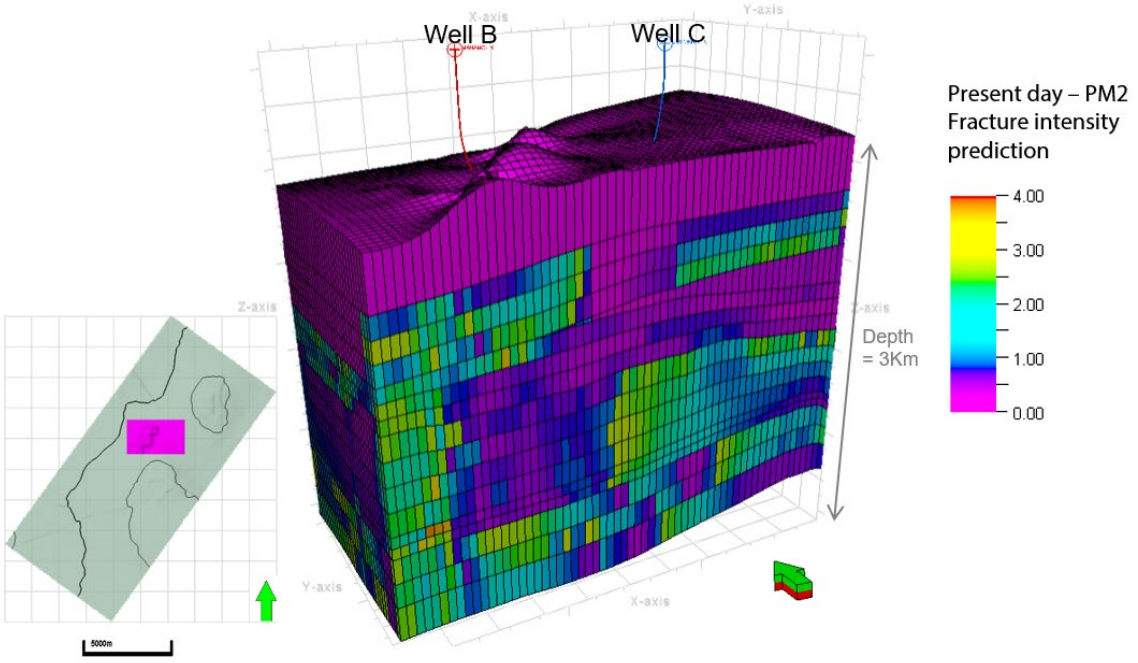

Fig. 86 Fracture intensity prediction from BPSM for a filtered section of the cube. The map on the left display the area filtered for display purposes. This area contains the two wells with measured data.

In Fig. 87 it can already observe the computed fracture orientation metrics. The maps display colour-scaled fracture dip angle and dip azimuth. A fracture concept is performed at each cell considering the stress and strain tensors and the Drucker- Prager failure model. For each cell, regardless of the size, one single fracture plane is generated (Fig. 88). At this point the first calibration is performed with orientation metrics, filtered in the units where fracture measurements are available.

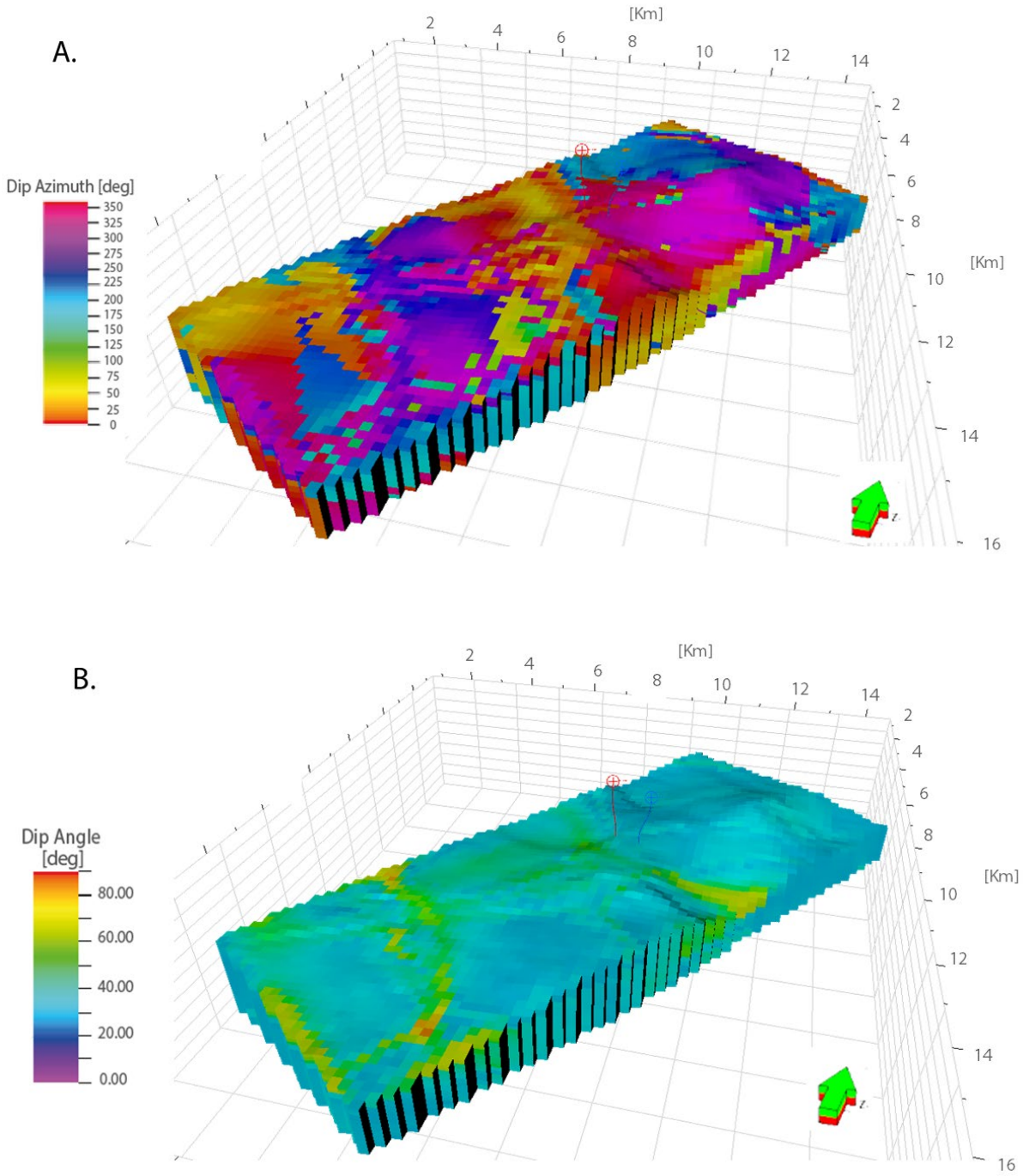

Fig. 87 Fracture orientation outputs from the basin modelling approach. (A) Fracture dip azimuth and (B) fracture dip angle. Layer corresponds to Porquero C unit. Arrow points to the North.

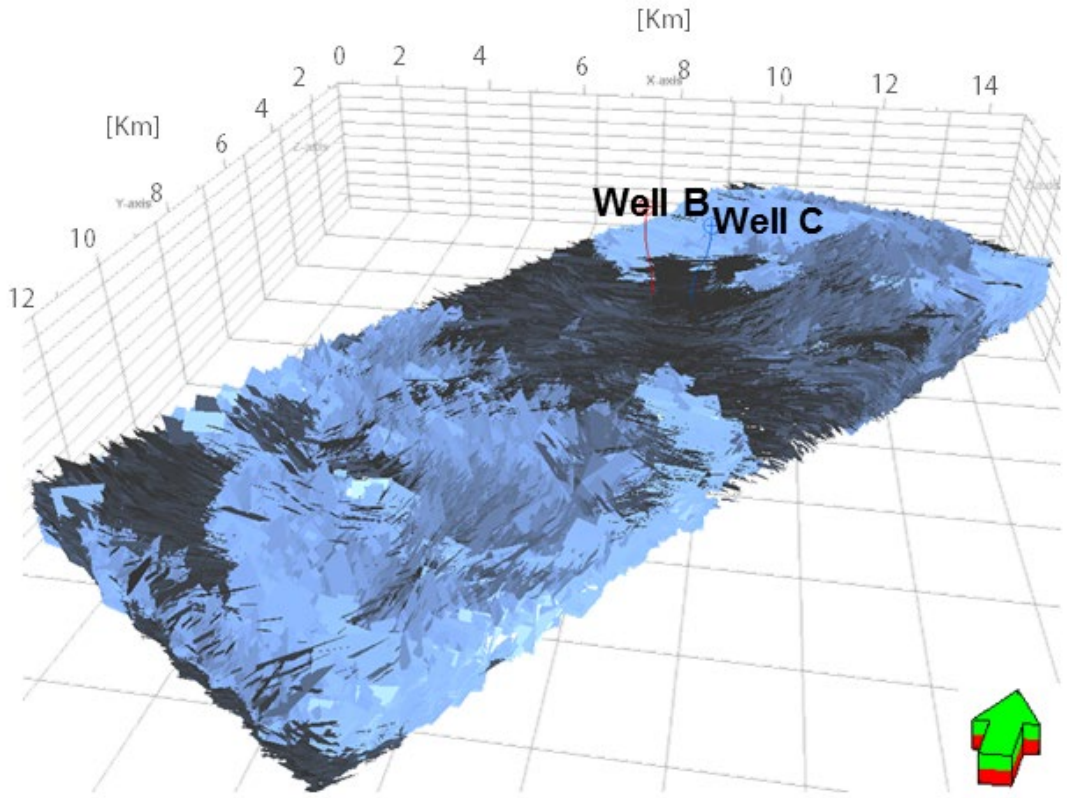

Fig. 88 Resulting discrete fracture network model from BPSM for a filtered section corresponding of Porquero C unit. Colour corresponds to a single fracture set with different visual perspective.

5.4.2.2 Model calibration

The first calibration is performed in terms of orientations metrics: dip angle and dip azimuth. Fig. 89-A and Fig. 89-B display the comparison between the dip azimuth corresponding to the fracture measurements from well logs and the simulated fracture network. The BPSM approach does not used the measurements as input data.

To test the reliability of the generated fracture network from this approach, an extraction is made at the location of the two wellbores with hard-data available (wells B and C). Fracture intensity, as a cell property is filtered and fracture planes along the wellbore are graphed (Fig. 90-A). Afterwards, the fracture planes extracted are compared to the corresponding measured data. Cumulative intensity is used as calibration metric (Fig. 90-B). Resulting BPSM-derived fractures along a wellbore can potentially be used to feed a discrete fracture generation engine (Fig. 91-A) leading to the calculation of a BPSM-derived synthetic discrete fracture networks (Fig. 91-B).

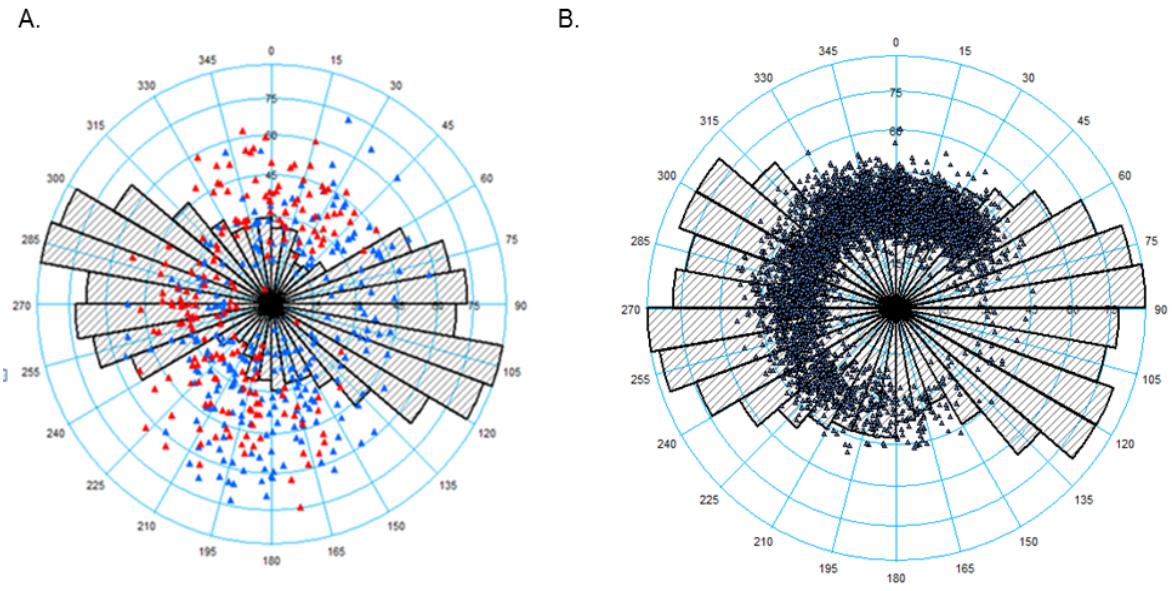

Fig. 89 (A) Azimuth of fracture planes interpreted from well image logs (B) Fracture plane azimuth extracted from the BPSM forward model. Orientation of fracture coincides in a WNW-ESE direction.

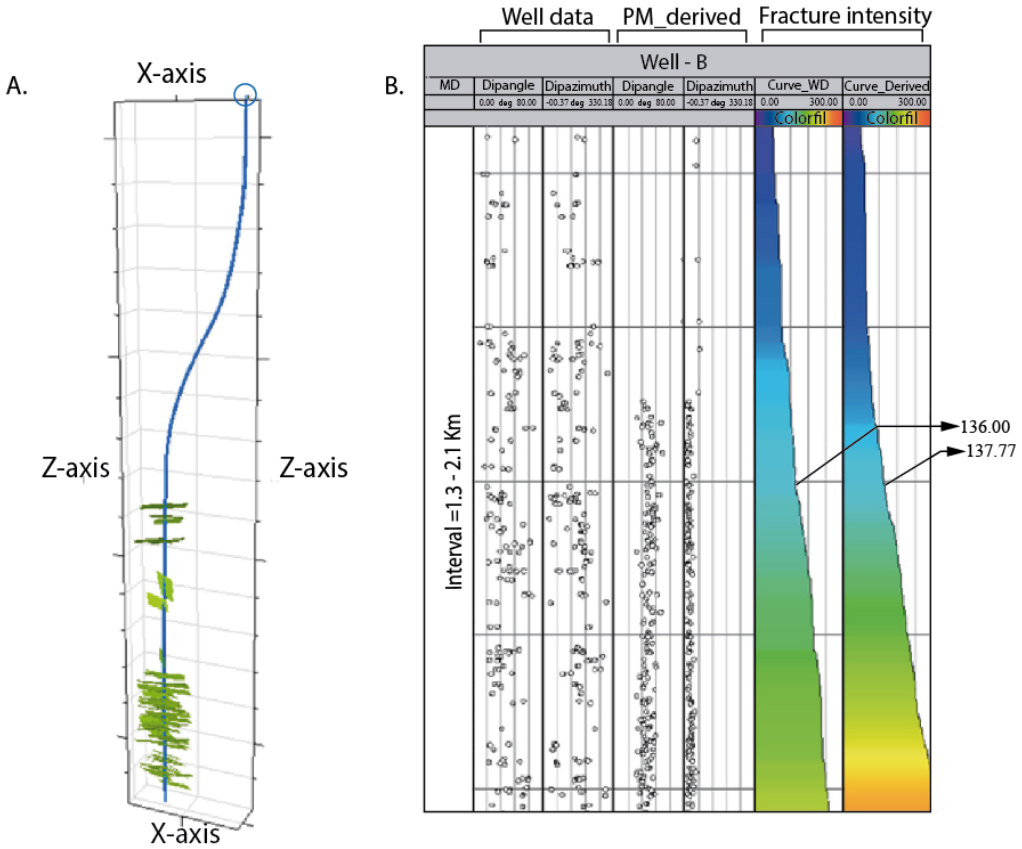

Fig. 90 (A) Extraction of fracture planes from BPSM along well B drilled trajectory. (B) Comparison between intensity derived from original well data (Wells C and D) and BPSM derived fracture planes.

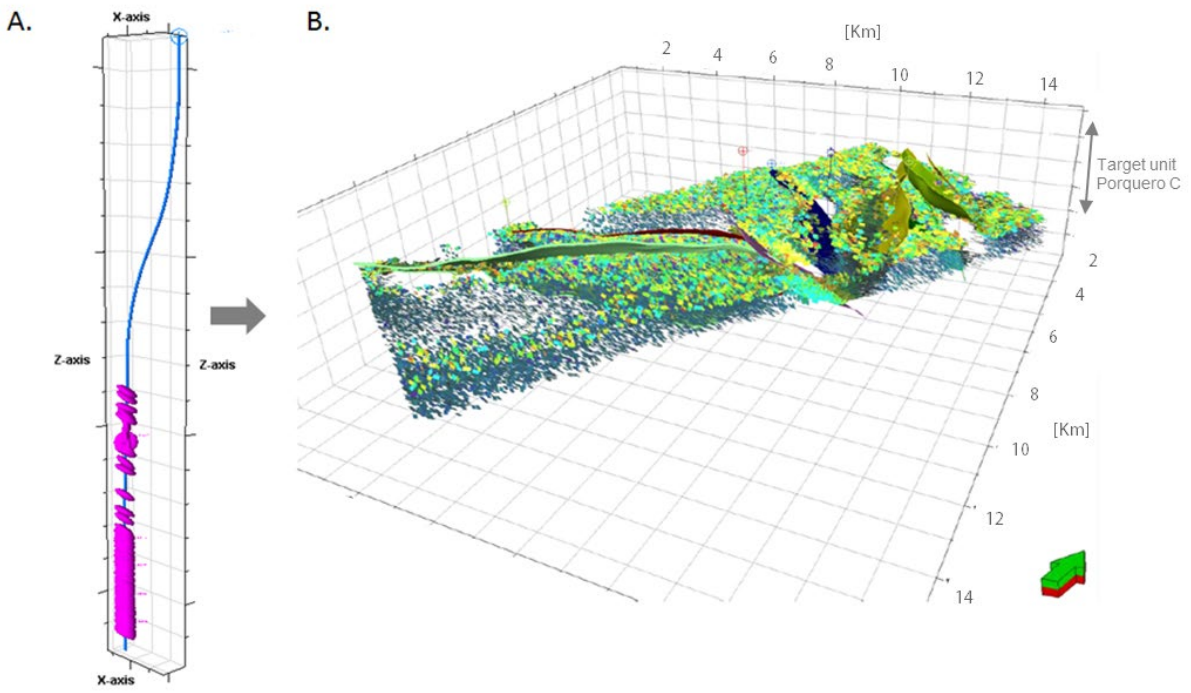

Fig. 91 (A) Synthetic fracture planes generated through BPSM for well B. (B) Fracture network generated from synthetic data.

Chapter 6 Results and analysis

The results of this study describe a fundamental geomechanical analysis performed through different approaches, applied in the case study area Block-A. The target of the models was the estimation of fundamental variables, including mechanical properties, pore pressure and *in-situ* stress state, necessary for any further geomechanical application.

The geomechanical assessment of Block A involved the construction and management of three distinct finite element models populated with three different datasets: (1) a log-based mechanical earth model (6.1), (2) a seismic-driven mechanical earth model (6.2) and (3) a basin and petroleum systems geomechanical model for Block A (6.3).

Log-based and seismic-driven models make part of the industry-standard ways to assess 3D geomechanical models and represent accurate approaches from present-day onwards. On the other hand, basin and petroleum system modelling approach (BPSM) aims to recover the geological history of the basin shedding light in causing mechanisms for present-day phenomena.

Each model deals with an outstanding amount of data, being capable of providing key geomechanical insights of the area independent of each other. This working approach allows comparing of synergies and overlaps and understanding of the advantages and disadvantages of each modelling methodology.

The second section (6.4) covers the results from the fracture network methodologies through two approaches. The first one is performed through stochastic calculations and paleo stress inversion. The second approach is derived from forward modelling, considering the basin and petroleum system model construction. Main outputs of this section include orientation metrics and derived fracture intensity. This section is of major importance to promote the optimization in well placement and efficient identification of better drainage zones.

6.1 Log-based mechanical earth model

6.1.1 Mechanical properties

Fig. 92 shows an extract of 1D mechanical earth models (MEM) results including calibration data exemplary for well A. It depicts the density log (DEN) as well as the compressional and shear slowness (DT and DTS) logs, which were used to calculate the dynamic elastic properties according to Eq. 36 and Eq. 37, which subsequently were converted to static values.

At well A, trend changes of E_{stat} (static Young's modulus) are thought to be associated with lithological composition and compaction conditions. As depth increases, from ~ 1300 m, at the top of Porquero C unit, the stratigraphic sequence shows an abrupt lithological change that goes from a claystone package and fine-grained sandstones to clay-matrix fine-to-fine-to-course grained sandstone, saturated with gas (gas flow registered in drilling journals). At this depth there is a variation in the E_{stat} behaviour going from an average of 1.2 to 2.5 GPa. These averaged values are sustained across the interval between 1360-1600 m. However, an abrupt shift is observed in the lower section of Porquero C unit (~1600-1620 m) where E_{stat} reaches values of 4.8 GPa which may correspond to less plasticity of the rock. With respect to Poisson's ratio variations are sustained between 0.22 and 0.25. In areas where limestone content increase tends to drop to 0.20. At the

calibration points, the log-derived mechanical parameters are in accordance with the rock mechanical properties measured triaxial testing and acoustic velocities at triaxial stress conditions (as observed in tracks 5, 6 and 7 in Fig. 92). This data served as correlation between dynamic and static properties.

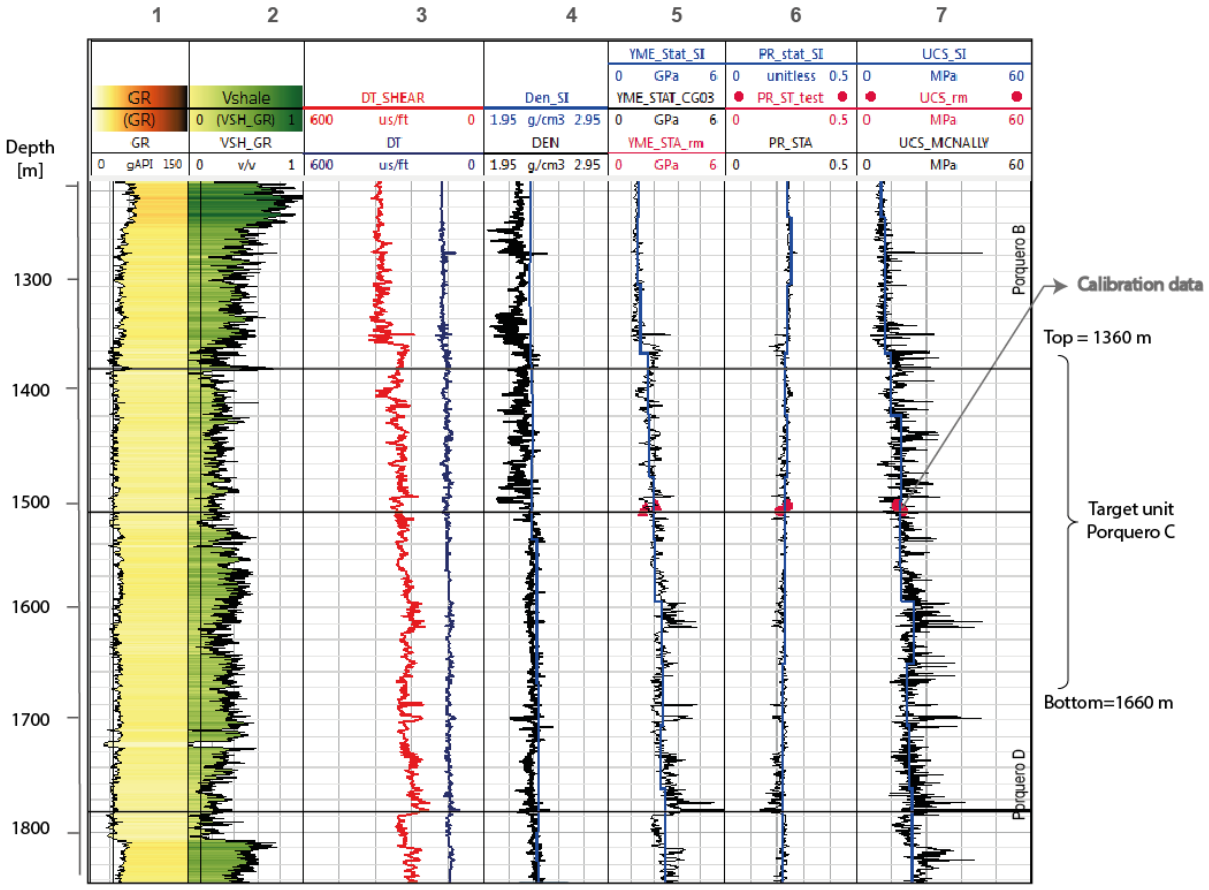

Fig. 92 Overview of mechanical properties for Well A with calibration data. Comparison between data derived from logs and from seismic inversion (black and blue curves in tracks 4, 5 and 6). Track 1= Gamma ray, 2= Shale volume, 3=Compressional and shear slowness, 4= Density, 5= Young's modulus, 6= Poisson's ratio, 7= Unconfined compressive strength. The red points represent the calibration between mechanical properties and laboratory measurement.

One of the main causes of uncertainty with the log-based mechanical earth model is the restricted calibration data, considering that only one well accounted for rock mechanical testing data. The reasoning and validation of mechanical properties were reinforced with lithological trend analysis and palaeography of the basin using the wells within the model and some others available in the vicinity. Considering the well cluster proximity, between Wells A to D, the same dynamic-to-static correlations were implemented. A detailed extraction of magnitudes for each formation top from the extrapolated properties is shown in Table 10 and Table 11.

Table 10: Young's modulus per sedimentary unit and per well. Data extracted from the log-based approach.

Young's Modulus [GPa]					
Unit/Well	**Well A**	**Well B**	**Well C**	**Well D**	**Well E**
Topography	1.31	1.31	1.31	1.31	1.31
Porquero A	1.17	1.24	1.24	1.17	1.03
Porquero B	1.38	1.45	1.72	1.31	1.45
Porquero C	1.65	2.07	2.69	1.52	1.45
Porquero D	2.76	2.48	2.76	2.07	2.41
Porquero E	3.79	3.65	3.72	3.86	4.76
Porquero F	7.86	4.27	4.41	4.21	9.58

Table 11: Poisson's ratio per sedimentary unit and per well. Data extracted from the log-based approach

Poisson's Ratio					
Unit/Well	**Well A**	**Well B**	**Well C**	**Well D**	**Well E**
Topography	0.25	0.25	0.25	0.25	0.25
Porquero A	0.25	0.25	0.25	0.24	0.25
Porquero B	0.25	0.25	0.24	0.24	0.25
Porquero C	0.24	0.24	0.22	0.25	0.25
Porquero D	0.22	0.23	0.22	0.23	0.23
Porquero E	0.22	0.22	0.22	0.22	0.22
Porquero F	0.22	0.22	0.22	0.22	0.18

Fig. 93 shows the spatial distribution of E_{stat} and ν_{stat}on the Porquero C, obtained through the log extrapolation (Fig. 93-A and Fig. 93-B). The reliability of the estimated properties is high for a restricted area surrounding the wells, while the inter-well space (well C and well E) may hold low uncertainty. The higher Young's modulus is found towards the western side of the model may coincide with lithological conditions pointing to less plastic rocks. Towards this area it is assumed an increase in more compacted shales and micritic-matrix limestone, while towards the eastern side of the model claystones, siltstones and clay-matrix fine-grained sandstones may imply an increase in rock ductility.

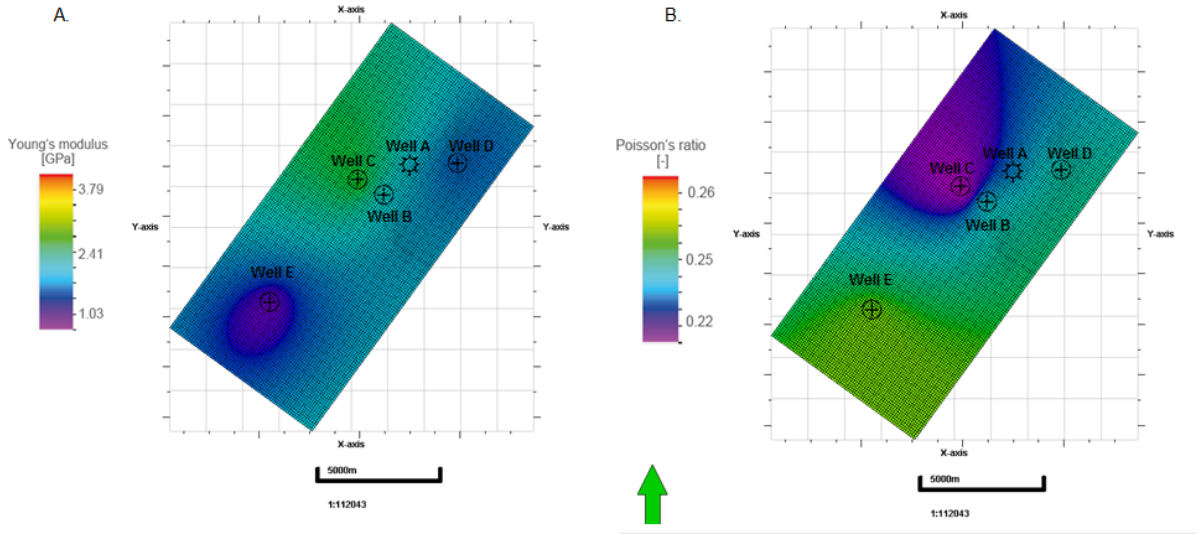

Fig. 93 3D log-base distribution of mechanical properties resulting from log extrapolation. (A) Young's modulus. (B) Poisson's Ratio at the top of Porquero C unit.

6.1.2 Pore pressure

The pore pressure model was estimated through the extrapolation of pressure gradients obtained from well logs through sonic trend-line methods. These values were calibrated with formation pressure magnitudes obtained from drilling stem test (DST) (summarized in Table 2), integrity tests and, with lower accuracy, pressure behaviour from registered drilling breaks or inflows during drilling. Pressure gradients used for the calculation vary with depth and are mainly associated with tectonic evolution, compaction and facies changes through the sedimentary column. Pore pressure per well on each stratigraphic top, extracted from the extrapolated model is described in Table 12. Elevated pore pressure in the lower interval is assumed to be a result of fast subsidence, filling and abrupt compaction occurred in the basin during Early to Middle Miocene.

Table 12: Pore pressure per sedimentary unit and per well. Data derived from the log-based approach

Pore pressure [MPa]					
Unit/Well	**Well A**	**Well B**	**Well C**	**Well D**	**Well E**
Topography	0.52	0.53	0.63	0.47	0.68
Porquero A	10.53	11.76	14.59	7.06	10.72
Porquero B	14.25	13.92	21.86	11.37	18.83
Porquero C	18.13	14.55	20.65	12.86	18.83
Porquero D	23.65	17.53	28.09	19.35	19.34
Porquero E	35.39	45.44	48.95	39.74	34.54
Porquero F	30.45	44.82	47.79	39.93	54.08

Fig. 94 shows the pore pressure distribution in units Porquero C to F. At reservoir level mean values are approximately 18-20 MPa. The highest pressure magnitudes can reach up to 26 MPa, corresponding to the areas of stronger subsidence. The grey arrow is highlighting an approximate

region where the pressure starts to increase in an abrupt fashion towards the bottom intervals of the stratigraphic column, mainly from Porquero D to bottom of the wells. This behaviour is more evident at well E where from 2200 m pore pressure increase dramatically, reaching magnitudes of 40-54 MPa and showing peaks of >60MPa in unit Porquero F. This trend is also registered in wells surrounding the case study area.

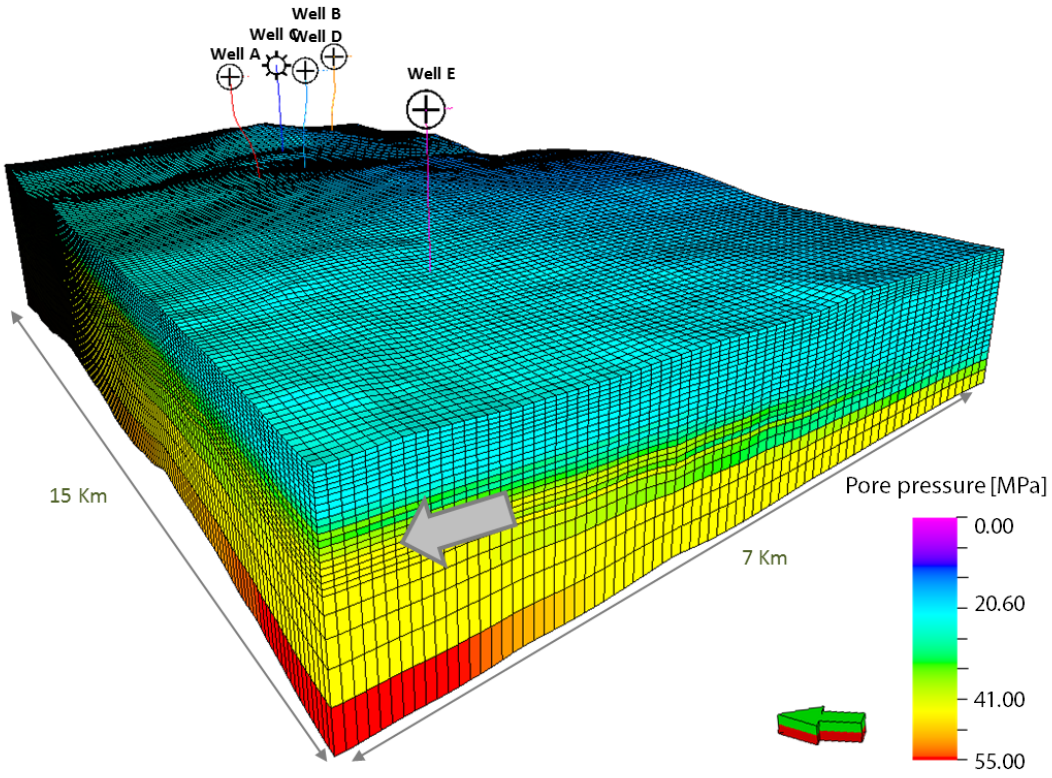

Fig. 94 Pore pressure distribution on Porquero C-F. The grey arrow points to the approximate beginning of increase in pore pressure, which may be correlated to abrupt subsidence process in the unit. Green/red arrow points to the North

Fig. 95 displays a horizontal pore pressure obtained through the kriging extrapolation method. The pore pressure increases towards the western side of the Block A, following the sedimentation of large thicknesses, compaction increment and estimated lithological changes to a rock rich in shales, micritic limestones and sandstone intercalations with less percentage of clay, very compacted and overpressured.

Wells E and C, located paleo-geographically in the deepest part of Block A, laterally register the highest pore pressure values in the Porquero C unit. The coincidence between both trends could indicate the pore pressure values estimated with the technique, in areas far from the wells, was reproduced with low uncertainty.

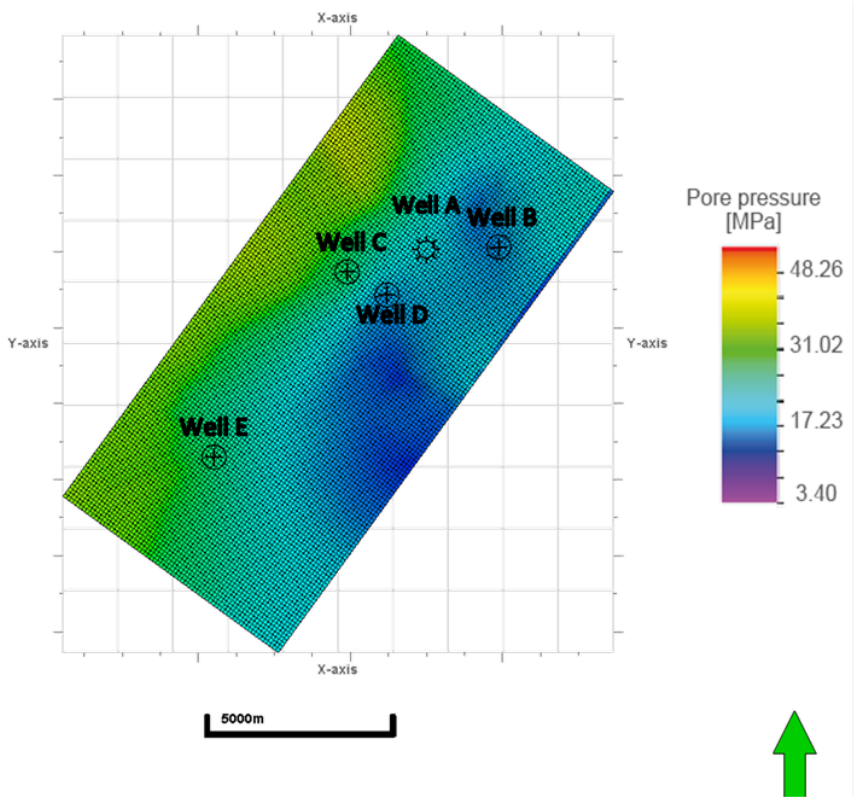

Fig. 95 Pore pressure distribution estimated from well extrapolation on the top of Porquero C.

6.1.3 In-*situ* stress magnitudes

The stress state along the wellbore will strongly condition the drilling performance. The knowledge of well-profile *in-situ* stress state becomes of paramount relevance for wellbore stability control. Fig. 96 displays a detailed section on well A, which is the well with the strongest calibration dataset, covering target units Porquero C and Porquero D. Sv, S_{Hmax} and S_{hmin} magnitudes at reservoir level are approximately 32 MPa, 26MPa and 24 MPa, respectively.

The magnitude profiles predominately show S_v as the largest principal stress, indicating a normal faulting regime; condition associated with a tectonic regime that characterised the Early Miocene period in the reservoir units. This is good agreement with stress data derived from *mini-frac* data and the stress polygon approach outlined in section 5.1.4. The observed behaviour at the target units is a normal stress regime, a trend that is sustained across wells at the same depth up to the bottom of Porquero D. From this depth onwards the behaviour in units Porquero E and F changes as stresses increase abruptly in association to an increase in the pore pressure. This is referred to a transitional tectonic regime of normal/strike-slip faulting, considering the relative magnitudes of the stresses (Zoback 2007).

This behaviour is more obvious as depicted in Fig. 97, for Well E. This well shows a strike/slip regime for the bottom part of the well section, corresponding to the bottom of the Porquero D unit onwards. This area is associated with abnormally high pore pressure and is linked with recurrent drilling issues. The horizontal stress ratio (S_{Hmax} / S_{hmin}) shows values of approximately 1.1 up to Porquero D. At well E, from approximately 2 Km onwards the horizontal stress ratio can reach up 1.3. Changes in the stress state with depth determine the mechanical stratigraphy of rocks with widely contrasting mechanical attributes, which in turn influence completion strategies (Tavener et al., 2017).

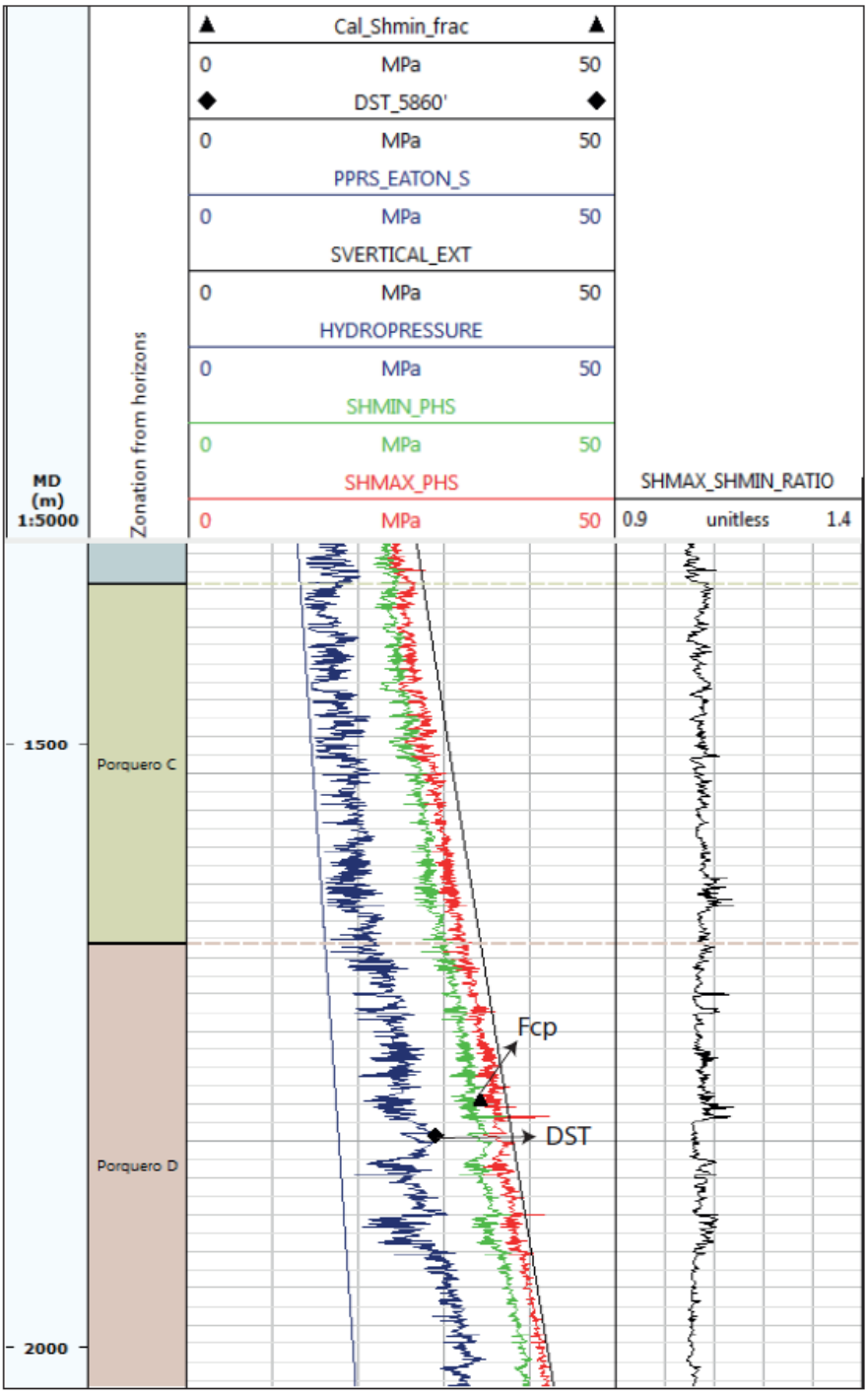

Fig. 96 1D MEM results showing pore pressure and stress magnitude variations with depth for a section of well A. SVERTICAL_EXT corresponds to the maximum principal stress indicating a normal faulting regime. The scatter in the S_{Hmax}, and S_{hmin} curves results from the different mechanical properties of shales and sandstones. Stress ratio (S_{Hmax}/S_{hmin}) consistently range between 1 and 1.1.

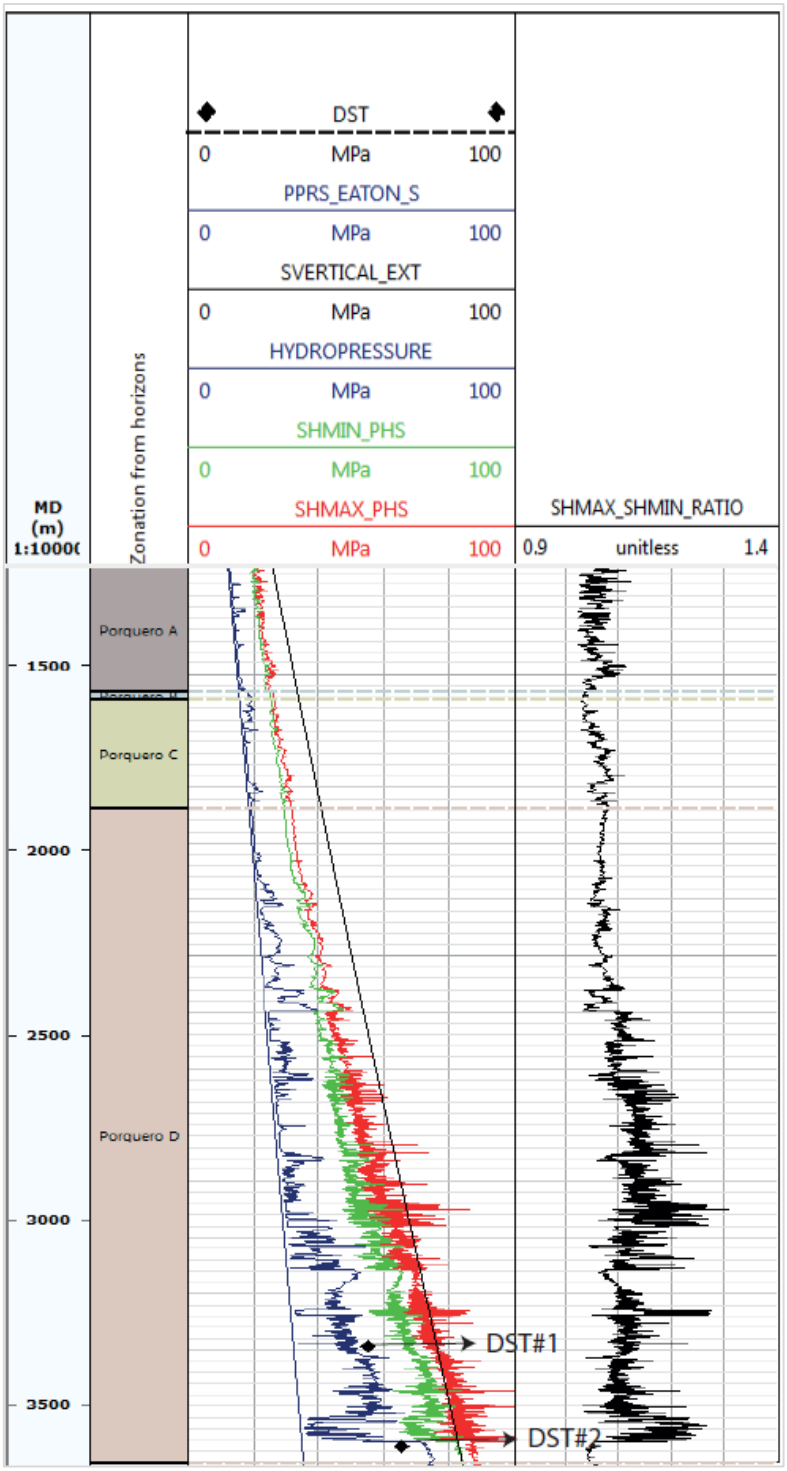

Fig. 97 1D MEM results showing pore pressure and stress magnitude variations with depth for a section of well E. SVERTICAL_EXT corresponds to the maximum principal stress indicating a normal faulting regime. The scatter in the S_{Hmax}, and S_{hmin} curves results from the different mechanical properties of shales and sandstones. Stress ratio ranges between 1 and 1.1 up to ~2500m. From this depth onwards, it may reach values of 1.3.

3D stress models are a result of the extrapolated properties (mechanical properties and pore pressure), and the estimation of stresses through a poro-elastic approach. The resulting principal stress volumes are considering tectonic strains as boundary conditions. Seed values of tectonic strains are obtained from the calibration approach made in the log analysis. The assumptions are confirmed through the calibration with hydraulic fracturing closure pressure (F_{cp} in Table 3) for S_{hmin}. S_{Hmax} on the contrary, is constrained through wellbore failure assumptions and the stress polygon approach.

Fig. 98 (A-D) displays the principal stress distribution (S_{Hmax}, S_{hmin} and S_v) obtained for the Porquero C unit, in addition to calibrated orientation of S_{Hmax} through comparison with DIFs. Generally, magnitudes show a good correlation with depth, increasing to the north-western part of the model, showing S_v values of >43 MPa, while the lowest magnitudes are found in the eastern side of the model with S_v values of >25 MPa. The same trends apply to S_{Hmax} and S_{hmin}. S_{Hmax} values range from 20.00 to 34.7 MPa, while S_{hmin} values range between 19.20 and 32.00. The governing tectonic regime is a normal faulting regime. The trend is clearly correspondent with the field subsidence.

Considering the numerical representation of fault surfaces as cell properties within the engine (VISAGE ®), the resulting magnitudes do not show abrupt variations correlated to such structures, but rather a continuous distribution. The accurate representation of discontinuities is relevant for exploration purposes. Considering this, it is adequate to mention that there is poor effect of faults presence in the stress orientation.

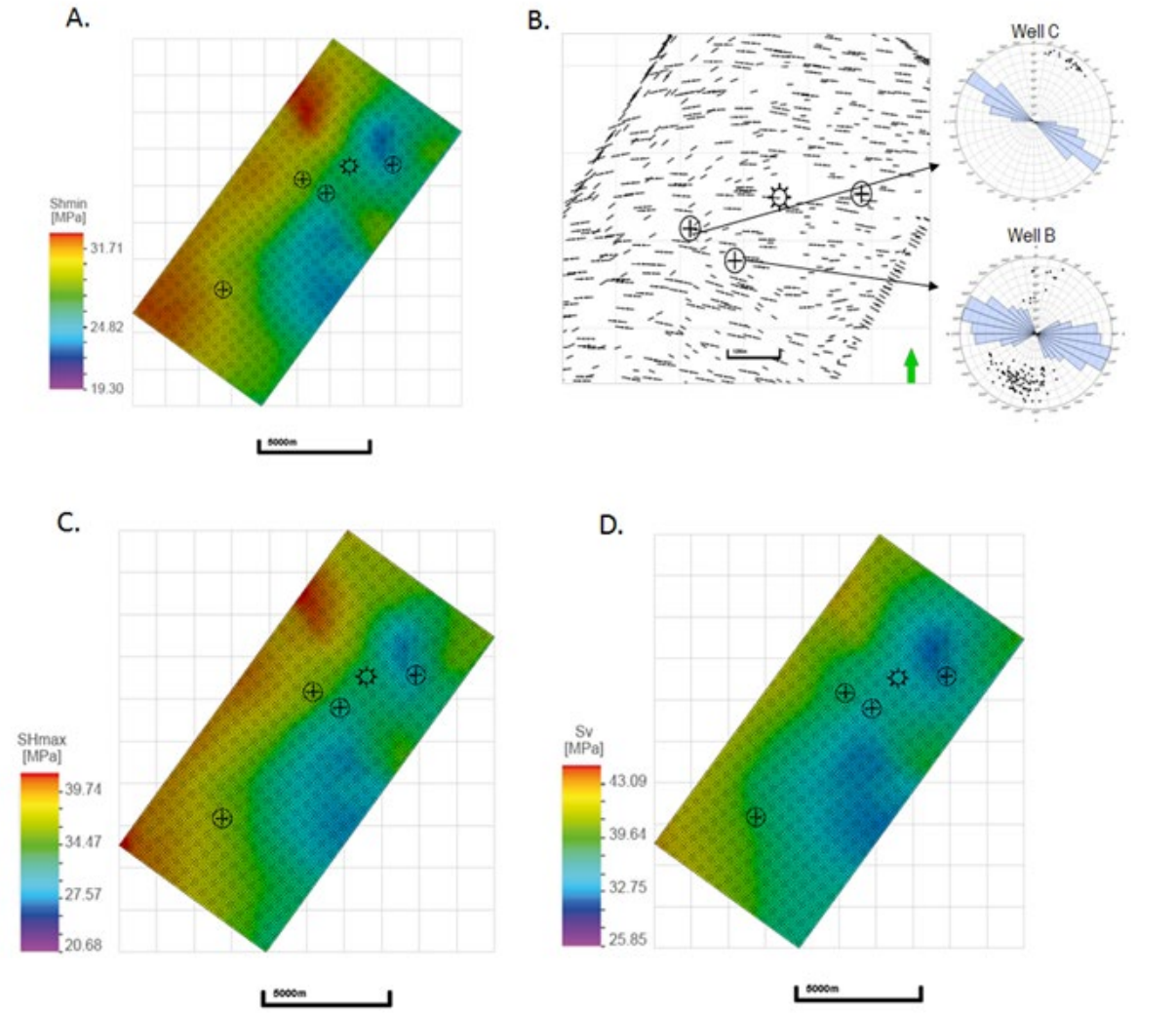

Fig. 98 3D distribution of principal stresses (A) Shmin, (B) orientation of SHmax, calibrated with DIF measurements (C) S_{Hmax} and (D) Sv. Map view of top of Porquero C.

6.2 Seismic driven mechanical earth model

For this modelling approach, the final mechanical configuration is based on an integrated population using default lithological values, log-derived mechanical properties from the previous section, depth trends and the resulting application of seismic inversion and AVO methodologies targeting reservoir units, Porquero C and D. Pore pressure model for this approach utilizes the same approximation performed for the log-based approach. Even though it neglects the horizontal heterogeneity, it is a good first approximation for the pore pressure behaviour. *In-situ* stresses are calibrated at well location with hydraulic fracturing closure pressure log profiles for vertical accuracy, rock mechanical laboratory results and field measurements.

The integration of seismic inversion and AVO methodologies with log-derived mechanical earth models allows for a better spatial property population. Moreover, it allows an uncertainty decrease in areas with little or no data. Generally, the punctual data extracted at formation tops, correlates with the log-derived approach, likewise with the calibration data for mechanical properties and stresses. However, a point of analysis arises in formations E, F and onwards due to the lack of measured data for such formations.

6.2.1 Mechanical properties variation

The results obtained through the application of an integrated workflow show a match between the calibration data and the estimated geological/lithological relationships. The general behaviour of the modelled properties shows an increase in Young's moduli corresponding to an inferred decrease in rock plasticity, alongside an increase in Poisson's ratio. In Table 13 and Table 14 it is displayed the resulting punctual magnitudes of properties for the top of each stratigraphic unit.

According to the magnitudes extracted at well locations, there is a drop of approximately 5 GPa in E_{stat} and a minor variation of υ_{stat} with respect to the log-based model. The cause of this difference may be a consequence of the population data available for Porquero E and F, as it is obtained using log data just from well E and a small section of seismic inversion. Moreover, well E is poorly constrained in terms of mechanical properties, especially in the lower units of Porquero E and F. The entire interval of Porquero E-F only accounts for well E to feed parameter information. Despite the lack of calibration data, the estimation of mechanical properties follows the same correlations as for the well cluster (wells A-D).

Table 13: Young's modulus per sedimentary unit and per well. Data derived from the seismic-driven approach.

Young's Modulus [GPa]					
Unit/Well	**Well A**	**Well B**	**Well C**	**Well D**	**Well E**
Topography	1.24	1.24	1.24	1.24	1.24
Porquero A	1.24	1.24	1.24	1.17	1.17
Porquero B	1.38	1.45	1.45	1.31	1.45
Porquero C	1.65	1.86	2.07	1.38	1.45
Porquero D	2.83	2.48	2.55	1.86	2.34
Porquero E	2.69	2.55	2.48	2.28	1.65
Porquero F	7.86	3.03	3.03	1.65	4.96

Table 14: Poisson's ratio per sedimentary unit and per well. Data derived from the seismic-driven approach.

Poisson's Ratio					
Unit/Well	**Well A**	**Well B**	**Well C**	**Well D**	**Well E**
Topography	0.25	0.25	0.25	0.25	0.25
Porquero A	0.24	0.24	0.24	0.24	0.24
Porquero B	0.25	0.25	0.25	0.24	0.25
Porquero C	0.24	0.24	0.23	0.25	0.25
Porquero D	0.22	0.23	0.23	0.24	0.23
Porquero E	0.22	0.23	0.23	0.23	0.23
Porquero F	0.21	0.21	0.21	0.23	0.23

Fig. 99 A-B illustrates the 3D distribution of the mechanical properties between the top of Porquero A and the bottom of Porquero D units for the seismic-driven population approach. Static Young's modulus (E_{stat}) and Poisson's ratio (υ_{stat}) vary vertically, according to the sedimentary sequence, in the following way: (1) in the underburden section (beneath Porquero D), lateral variation of E_{stat} are about 12.5 GPa and υ_{stat} about 0.22. (2) At reservoir depth (Porquero C and D), lateral variations of E_{stat} are between 2.5 and 3.5 GPa and υ_{stat} are between 0.21-0.25. (3) In the upper stratigraphic levels, conforming to the overburden (Porquero A and B), values of E_{stat} range horizontally between 1.03-2.20 GPa and υ_{stat} is about 0.26.

In Fig. 100-A and Fig. 100-B it is displayed the seismic-driven distribution of mechanical properties, i.e. E_{stat} and υ_{stat} on top view for the top of Porquero C. The Young's modulus parameter (E_{stat}) shows a tendency to increase toward the west where the overpressure in the sediments increases and it is estimated that the plasticity of the rock decreases laterally. The Poisson's ratio (υ_{stat}) follows a slight tendency to increase towards the east of Block A.

Besides matching the geological framework, the highlight of this modelling approach is the ability to capture inter-well property distribution. This feature is especially important for future well placement. Another differential feature is the recognition of major structures like faults. The models display the drop in E_{stat} and the rise in υ_{stat}. A prominent change in mechanical properties is observed at the eastern side of the model where a drop in Young's moduli and corresponding rise in Poisson's ratio is observed.

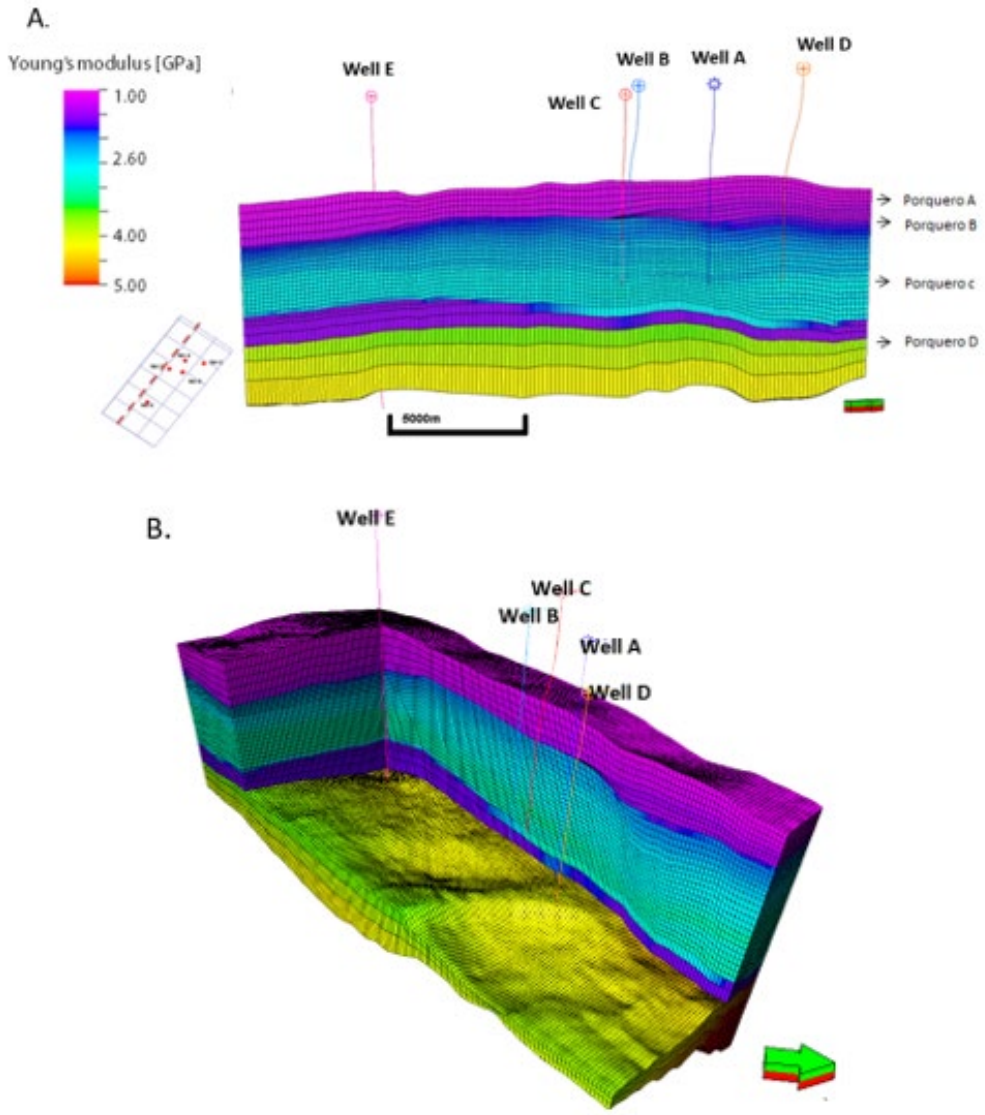

Fig. 99 (A) cross section of Young's modulus distribution (B) Diagram depicting the variations captured along and across the model. The property population is a result of an integrated approach between seismic inversion, well-log derived properties and depth-trends.

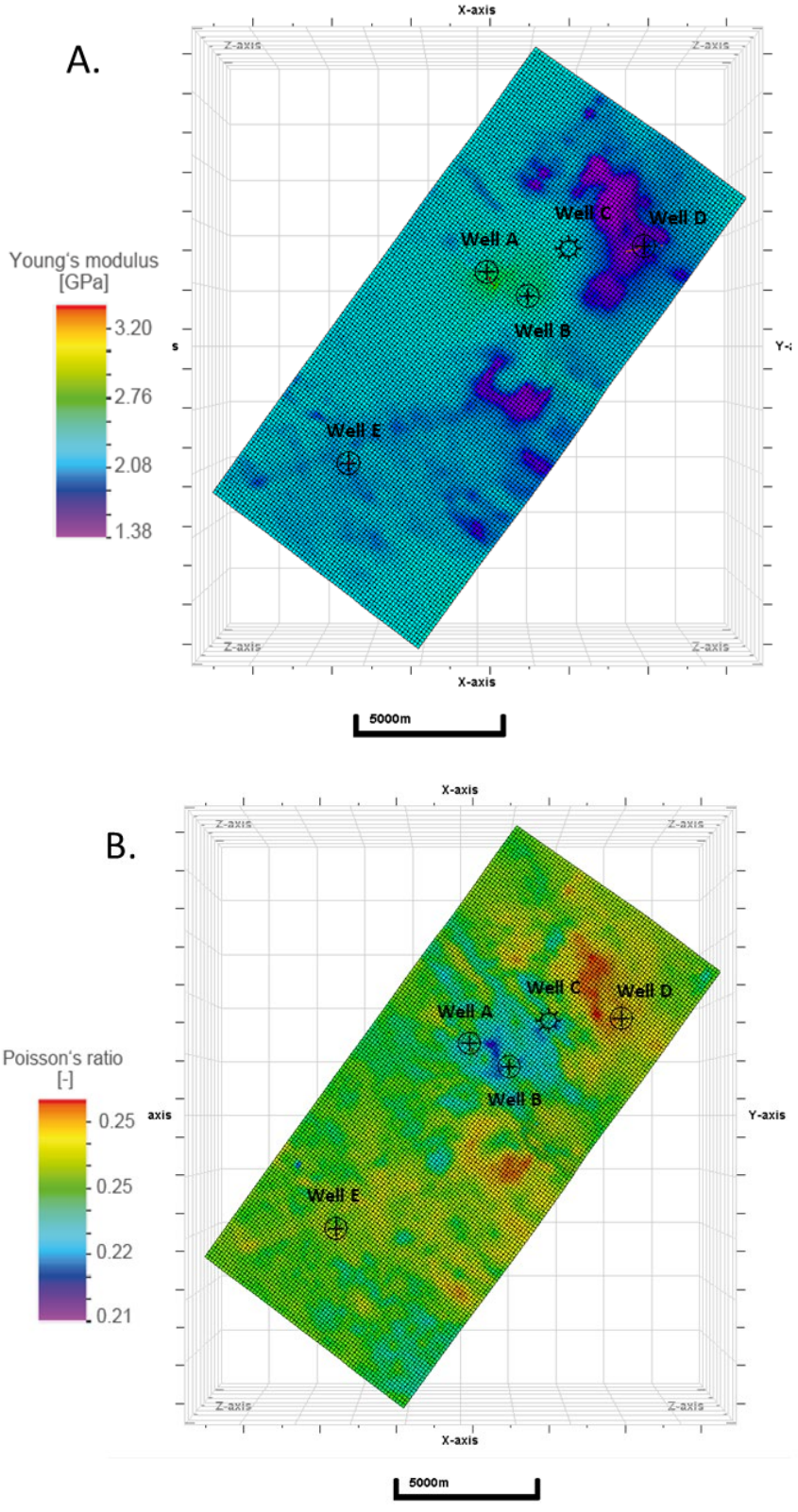

Fig. 100 3D Seismic-driven distribution of mechanical properties. (A) Young's modulus. (B) Poisson's Ratio. Both profiles correspond to the top of Porquero C unit.

6.2.2 3D In-situ stress characterisation

Modelling results, e.g., the complete stress tensor, are available for the entire model domain and can be derived for any desired section or path through the 3D MEM. As an example, Fig. 101 (A-D) shows the spatial distribution of the components of the stress tensor, i.e., magnitudes of S_v, S_{Hmax} and S_{hmin}, along with the S_{Hmax} azimuth for the top Porquero C level. Vertical stress (S_v) values are between 24 and 41 MPa. S_{Hmax} magnitudes range between 19-37 MPa, whereas S_{hmin} values are between 17 MPa and 33 MPa. The S_{Hmax} azimuth is mostly WNW-SE, with some local rotations to W-E direction. The modelled stress tensor components can also be used to characterize the stress and mechanical state of the subsurface further. Stress ratios were used to describe the stress anisotropies across the model. In the overburden section, S_{Hmax} can be up to 2.2*S_{hmin}, while at reservoir level it is between 1-1.2*S_{hmin}. The general trend is a decrease in horizontal stress anisotropy with depth while the ratio of S_{Hmax} to S_v is changing from ~0.93 in the overburden to ~0.75 at the reservoir level.

Fig. 102 displays a comparison of the extracted profiles for well A from the seismic-driven model (colour-scale), in addition to the log-based approach (red-dashed line) and the original raw data (black line). The differences among models, with respect to the original data are below 5%. This difference is mostly due to resolution associated with data sources.

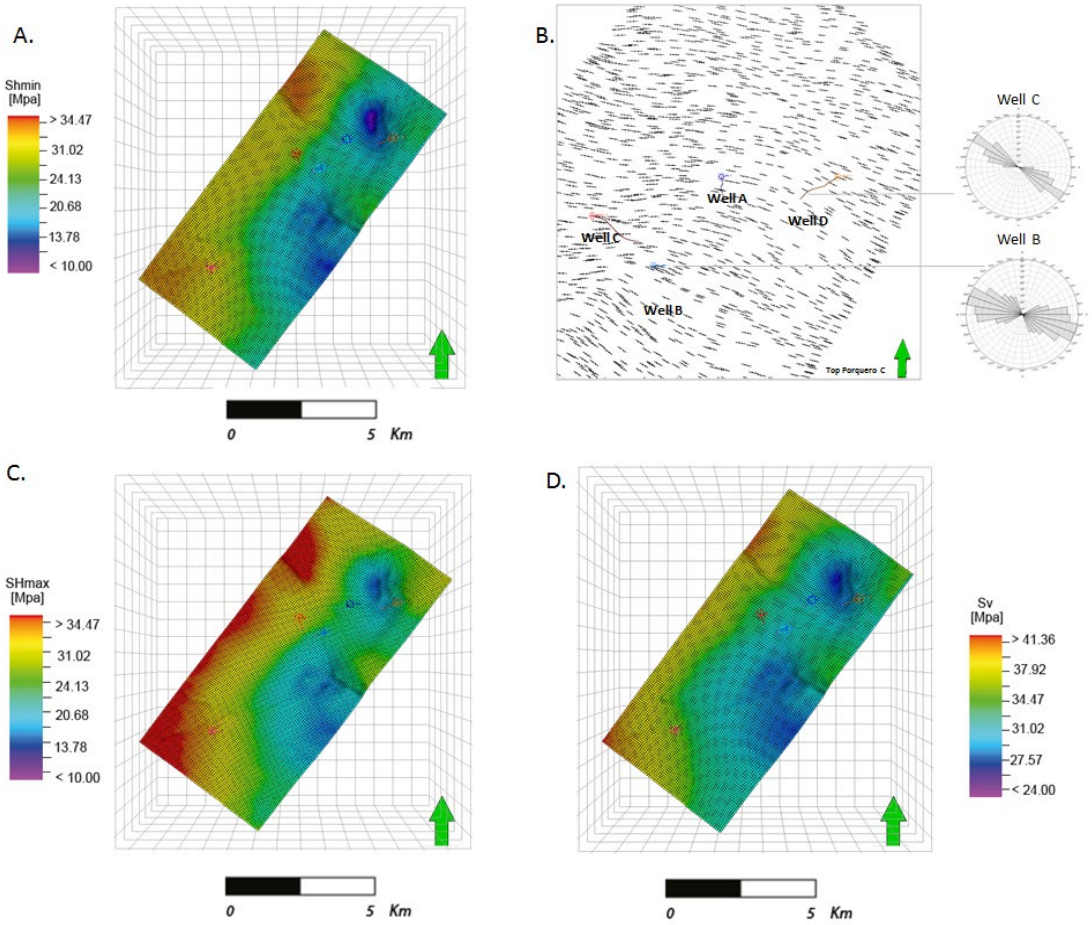

Fig. 101 Map view of (A) S_{hmin}, (B) S_{Hmax} orientation at reservoir level with calibration data for reference, (C) S_{Hmax} and (D) S_v spatial distribution and magnitudes.

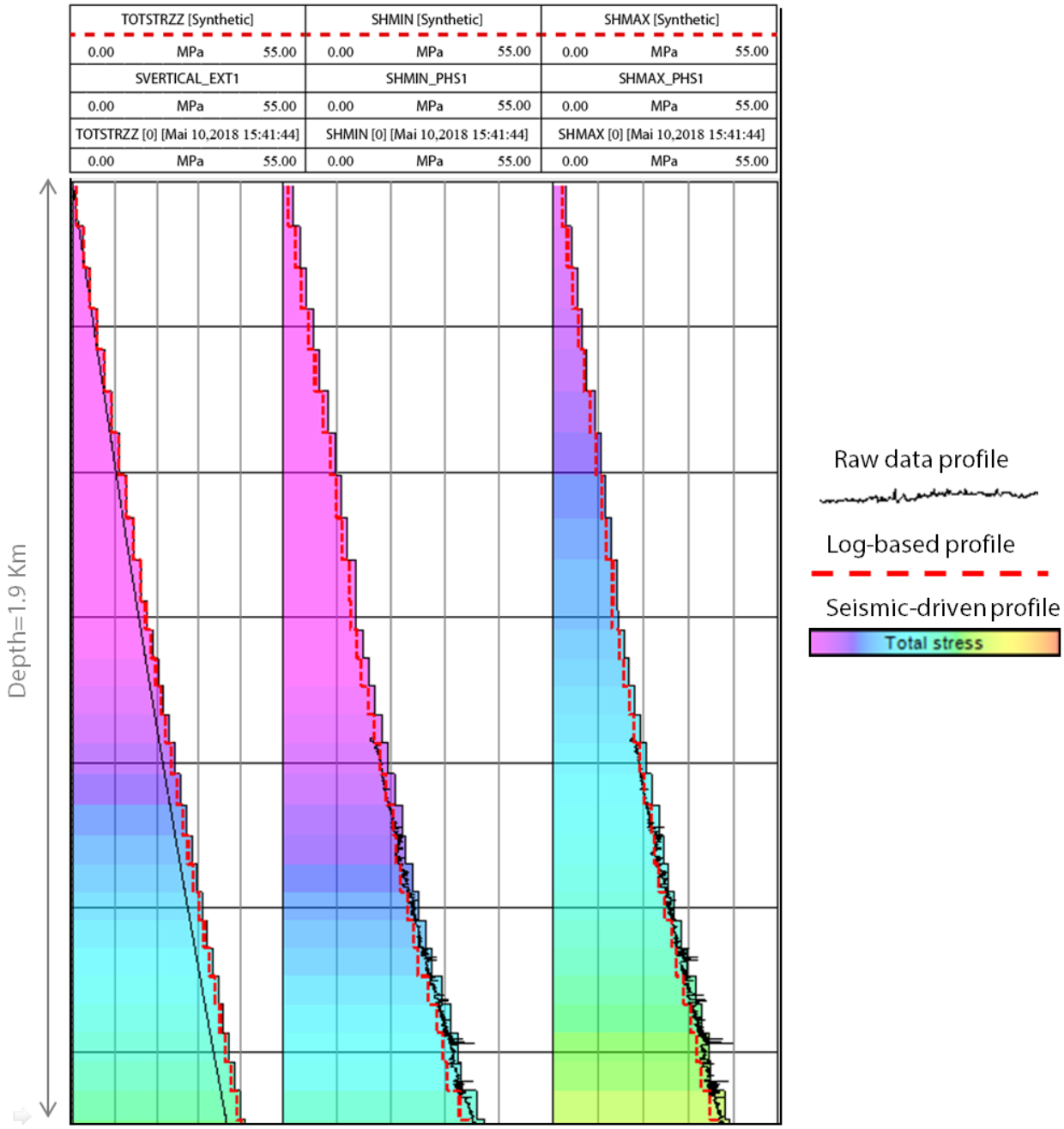

Fig. 102 Stress profiles extracted at well A location from log-based and seismic driven approach with respect to the original raw data. The stresses display good correspondence among each other.

6.3 Basin and petroleum system models: Geomechanical approach

Basin modelling is presented as an alternative methodology to assess geomechanical behaviour of a formation at well, reservoir, field and basin scale. The model construction works under the integration of several datasets including: structural elements, facies modelling, thermal, geochemical models and geological evolution studies tied to temporal constraints, to assess the hydrocarbon generation, migration and accumulation route.

Mechanical properties and pore pressure were estimated through the detailed description of facies and paleogeography interpretation through the geological time. This means it is possible to honour the physical-chemical transformations and track mechanical variations from the basin origins until today, making it great proxy models for further reservoir predictive simulations. The dynamic nature of the simulation approach implies that every geological age defined comprise a simulation on its own. This means that in every step each of the selected properties can be analysed independently and therefore a cumulative effect can be tracked up to present-day configuration. The results of this section are crucial for natural fracture –faulting studies.

6.3.1 Mechanical property distribution

Mechanical properties were derived from facies models that work with lithology changes compaction curves to estimate porosity and paleogeography variations through the geological time. The two governing properties are calibrated using rock mechanical laboratory results for one well (Well A). The surrounding well cluster (wells B, C and D) are calibrated using laboratory rock mechanical tests data. Fig. 103 displays the spatial distribution of mechanical properties. Young's modulus at reservoir level (Porquero C) ranges between 2.28 and 3.5 GPa, following the decrease in the plasticity of the rock to the western side of Block A. On the other hand, Poisson's ratio ranges between 0.22 and 0.24. These results agree with the highly-constrained reservoir section of the seismic-driven geomechanical approach (Table 13 and Table 14). A significant result of this stage is the possibility of restricting further the mechanical properties of wells in poorly constrained areas. Fig. 104 and Fig. 105 display the variation across the field of Young's modulus and Poisson's ratio respectively for the cross-section A-A'. Horizontal variation of the properties does capture the lithological pre-estimated trends. The extracted 2D section displays the mechanical properties variations in SW-NE direction across the stratigraphic column. Additionally, shows the estimated mechanical magnitudes in the yet-undrilled areas, potentially corresponding to Oligocene to Early Miocene age.

Young's modulus varies with depth in correspondence with the increase in compaction. From the surface until approximately 2000 m, values range between 1.7 – 2.2 GPa; this is an interval characterised by a high shale and clay percentage. In the interval between 2100-2500 m, the lithology changes to shale levels, calcareous mudstone, thin levels of micritic limestones, and the values increase to ranges between 2.5 and 3.5 GPa. From 2500 m to final depth, an abrupt increase in Young's modulus is observed, probably associated with the processes of subsidence, fast compaction and overpressure occurring in the lower sequence of the stratigraphic column, where the simulation indicates that Young's modulus values could potentially reach values up to 11.5 GPa. In the same way, the Poisson's ratio varies with depth and lithological changes, towards the top of the column reaches values up to 0.34, associated with the high percentage of clays and siltstones. As the depth increases, the values end to decrease in a range between 0.25-0.22.

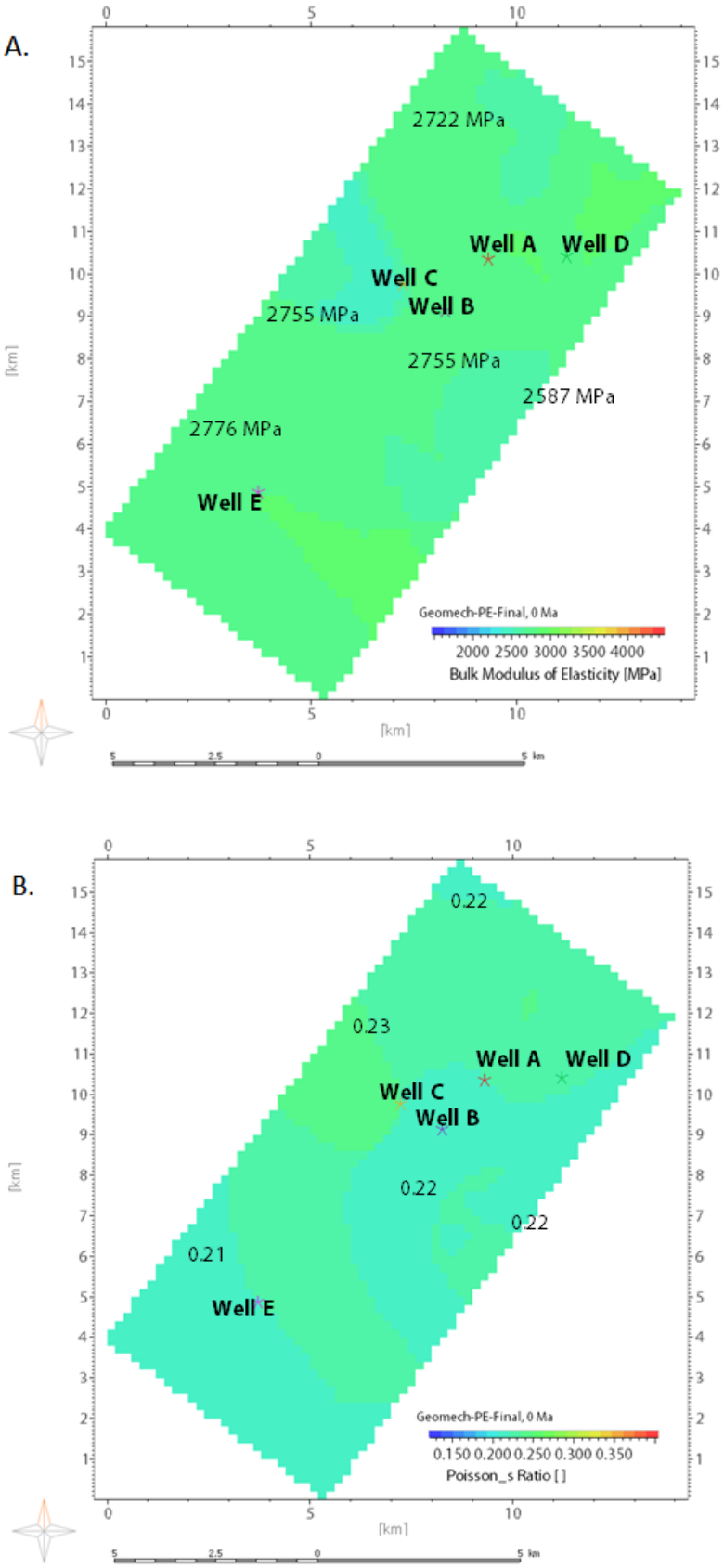

Fig. 103 Distribution of static elastic mechanical properties on present-day (A) Bulk modulus of elasticity and (B) Poisson's ratio. Top of Porquero C unit.

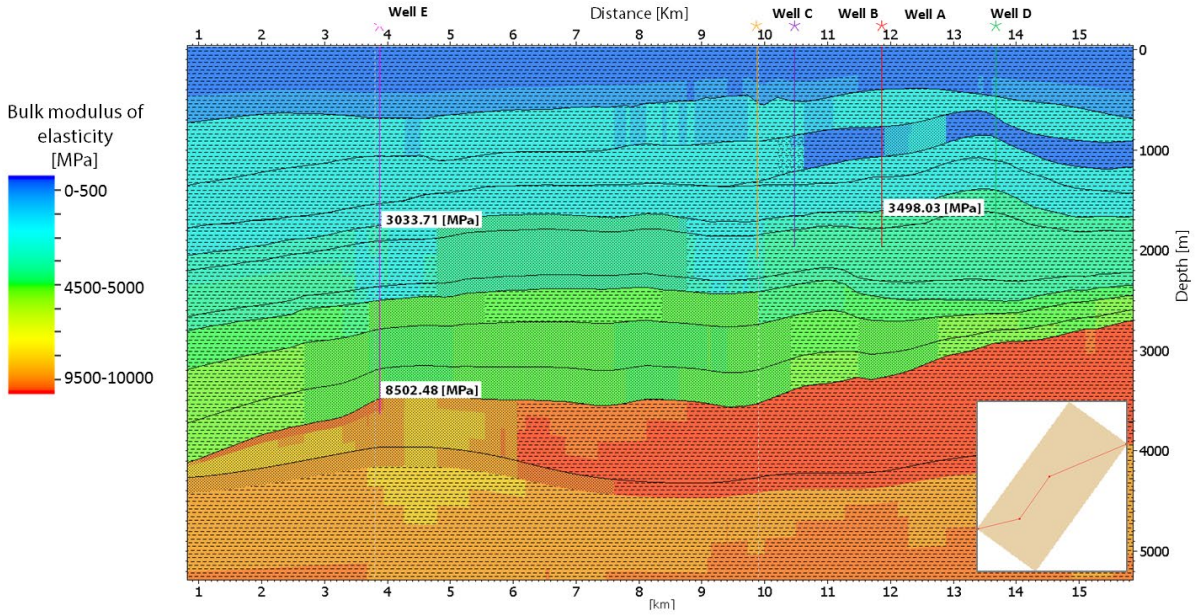

Fig. 104 Young's modulus vertical distribution over cross section A-A'.

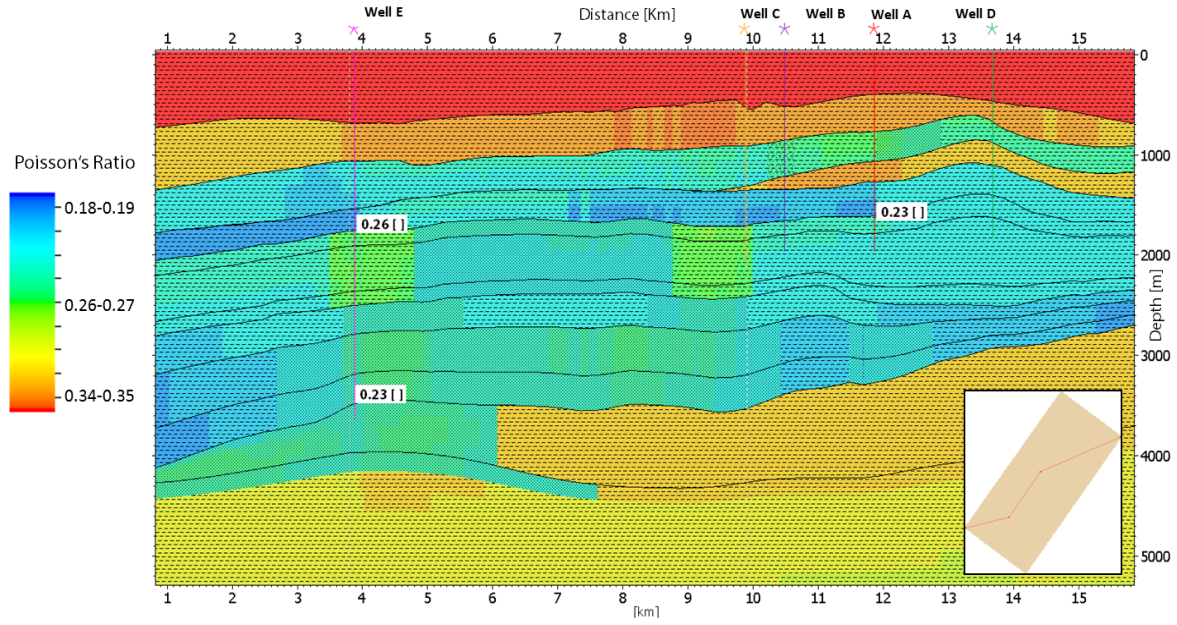

Fig. 105 Poisson's ratio distribution over cross section A-A'.

6.3.2 Pore pressure

This pore pressure estimation approach depends on many parameters responsible of paleogeography transformation of the basin trough geological time. It comprises several variables that consider the vertical and horizontal variations of permeability, porosity reduction from compaction and the interaction of such properties through porosity-permeability multipoint relations.

Pore pressure model is calibrated against field testing data in each of the wells within the seismic survey and several wells outside in the periphery for trend validation. Facies definition and compaction relations interaction will derive in low uncertainty pressure model and proper

identification of overpressured areas. Calibration of pressure profiles on well E ensures that the model is capturing the pressure variations along the target units. Higher pressure gradients, as reported in internal reports of well E and in wells surrounding the study area, are being reproduced in older units, Porquero F onwards.

Fig. 106-A and Fig. 106-B display the resulting pore pressure distribution in an oblique view and on top of Porquero C unit. Laterally, pore pressure increase occurred from east to west in function of lithological changes, subsidence and more compaction in the area. Vertically, increase with the depth. Porquero C unit displays pressure magnitudes approximately between 18.46 MPa to >28 MPa (~1000-1700 m), slightly higher than the log-derived pressure magnitudes. Pressure increase is observed form Porquero D unit onwards, where magnitudes averaging 50-60 MPa (>1550 m) are registered, with peaks of approximately > 60-80MPa (3900-4300m). This is in consonance with the reports of abnormally high pressures in the area, and the constant drilling issues occurrences from 2000 m onwards. Overall, the trend is compliant with the log-derived pore pressure state which is reasonable considering the low deformation configuration of the modelled area.

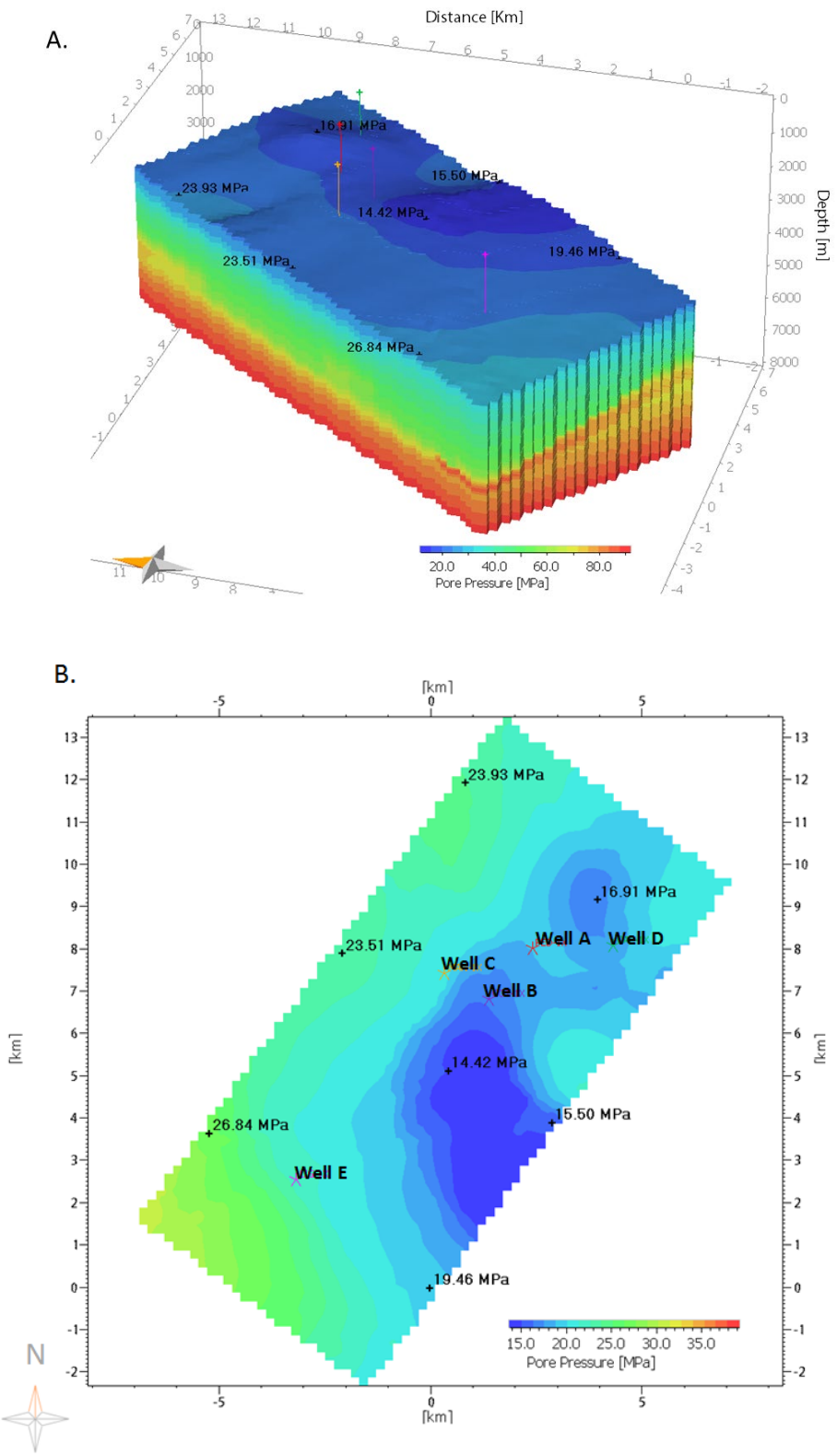

Fig. 106 3D pore pressure distribution covering from top of Porquero C unit. As observed, highest pressure is captured in the western side of the model, at Porquero D and F units. (A) Oblique view of pore pressure gradients and (B) Top view of lateral variations pore pressure magnitudes

6.3.3 Paleo stress models

A highlight of the basin and petroleum systems technology is the ability to simulate time-constrained geological events. The applied sequential solution approach within a single analysis offers the possibility to post-process all results individually for each load step in context with each other. The modelling approach takes advantage of the present-day setup and properties to estimate a past-event configuration. Mechanical properties and pore pressure are available for each time step through backstripping and forward modelling. Stress computation is performed at each step considering the properties estimated for the corresponding age. Vertical stress is the result of the integration of the density of overlaying sediments, while horizontal stresses are solved through a poro-elastic approach.

In the Block A study area of approximately 100 Km^2, distinct tectonic regimes occurred in the basin from the Oligocene to recent period. During Late Oligocene-Early Miocene (~26-16 Ma.), it is characterised by extension along WNW striking normal faults, which controlled the subsidence, sedimentation and abrupt compaction. At the beginning of Middle Miocene (~15-11 Ma) ceases the extension and a regional east / west convergence initiate. During the Late Miocene / Recent (~11-0 Ma) continued the northwest / southeast shortening. This compressive event has been correlated with the Andean Orogeny. Three regional stress orientations were imposed as boundary conditions to constrain further the simulation (explained in section 5.3.10).

Fig. 107 displays the paleo stress setting extracted at 15 Ma and present-day setting for vertical and horizontal stresses (S_v, S_{Hmax} and S_{hmin}) measured at the middle of the cell group that correspond to Porquero C marked with a red cross. The governing tectonic regime within block A is a normal faulting regime. The imposed sequence and the resulting stresses are summarized in Table 15.

Fig. 108 and Fig. 109 display the distribution of S_{Hmax} and S_{hmin} on top of the corresponding unit per age: for 20 Ma, the sedimentation sequence covers Porquero E and F units, while 15 Ma covers the sedimentation of Porquero C.

Regarding the maximum stress orientation in past events, the boundaries are constrained with the associated stress orientation for the specific ages. Across the model, stress rotation is appreciated considering the small difference between horizontal stresses. The overall concept stands that when there is low-stress anisotropy, structures will govern stress rotation, whereas a high-stress difference often shows consistency with the imposed regional stress field (Yale, 2003).

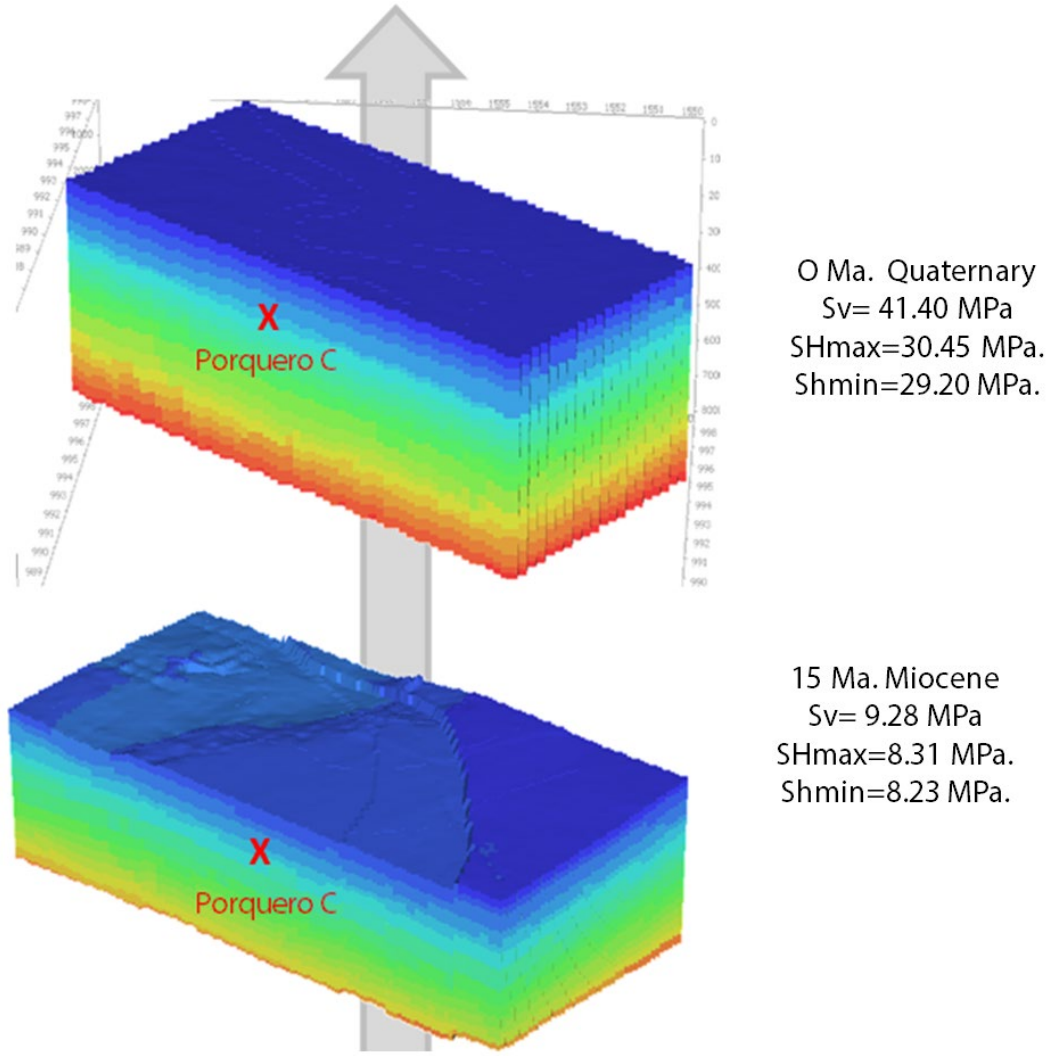

Fig. 107 Paleo-stress state magnitudes. The sequence corresponds to the steps defined for 15 and 0 Ma configuration. The red cross corresponds to cell selection point at Porquero C level.

Table 15 Summary of the paleo stress models and their characteristics in terms of stress orientation and stress magnitudes at the reservoir level.

	Paleo-model 3	**Paleo-model 2**	**Present-day**
S_{Hmax} orientation	130° N	125° N	120° N-115 ° N
Stress regime	Normal	Normal	Normal
S_V at reservoir level	1.70 MPa	16 MPa	35 MPa
S_{Hmax} at reservoir level	1.23 MPa	6.72 MPa	20.38 MPa
S_{hmin} at reservoir level	1.16 MPa	5.94 MPa	19.97 MPa

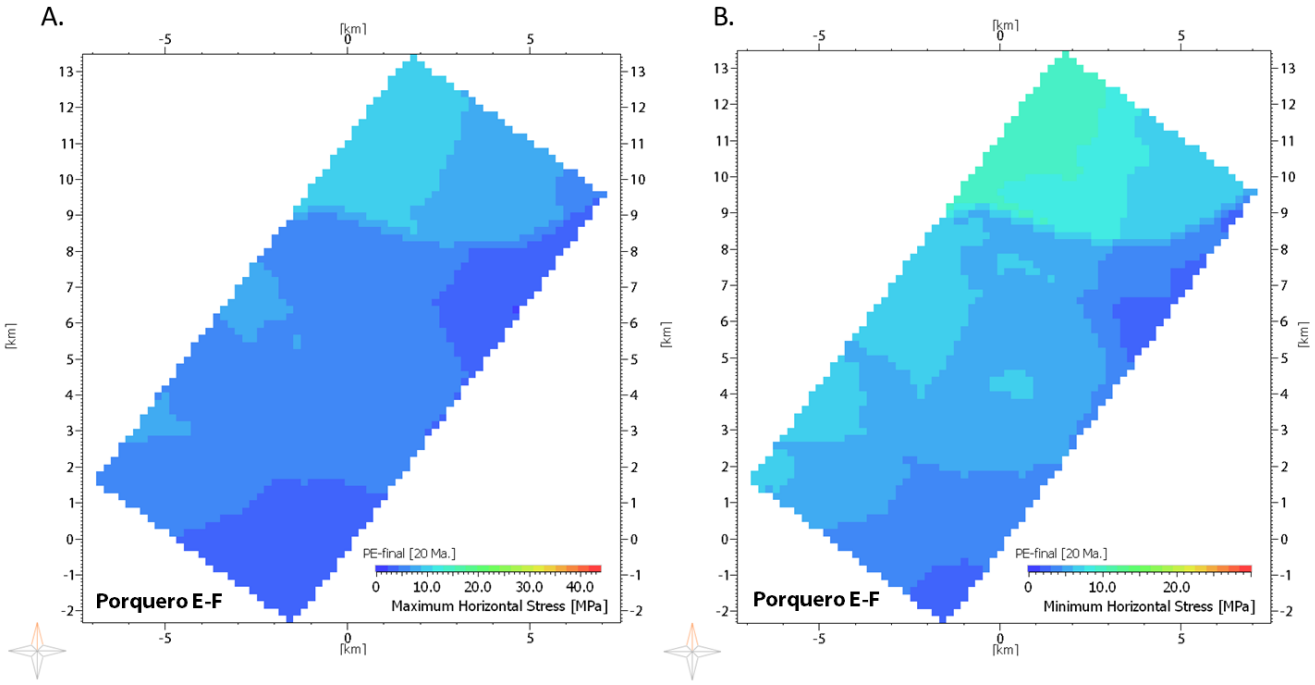

Fig. 108 Paleo-stress state magnitudes at 20 Ma. (A) Maximum horizontal stress and (B) Minimum horizontal stress. Top of Porquero E unit.

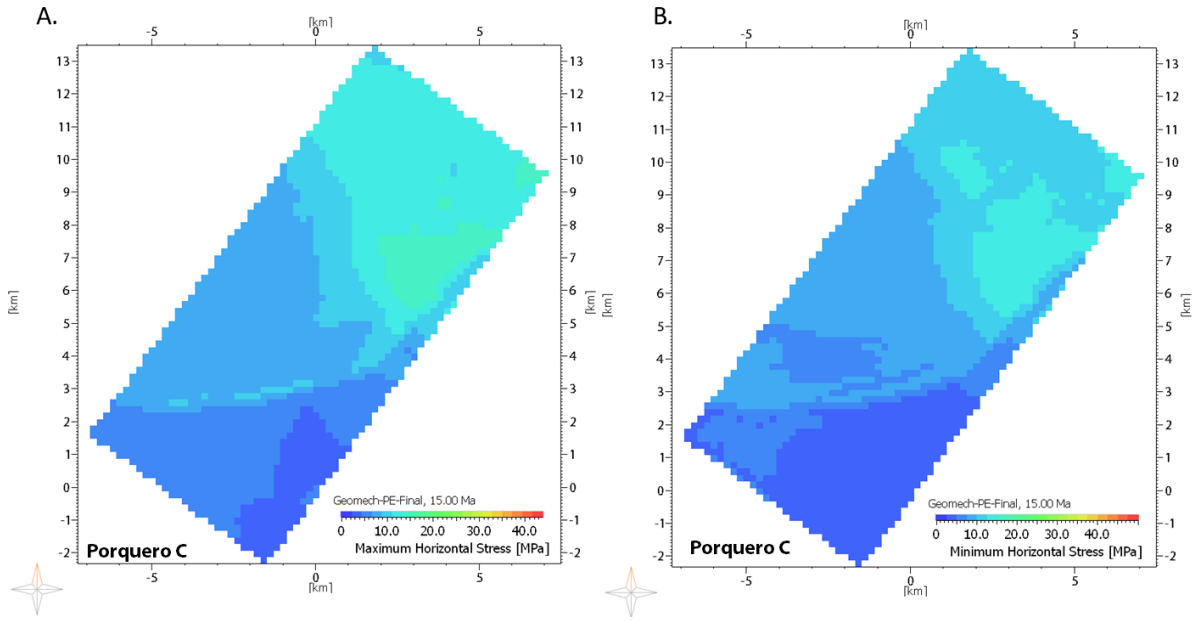

Fig. 109 Paleo-stress state magnitudes at 15 Ma. (A) Maximum horizontal stress and (B) Minimum horizontal stress. Top of Porquero C unit.

Maximum horizontal stress orientation for three paleo-events is displayed in Fig. 110, for the pre-imposed of 20 Ma, 16.4 Ma and 15 Ma. Early sedimentations sequence (~20Ma.) displays a stress orientation in an E-W direction for well B. For the following ages, in well B, there is a rotation towards NW-SE. For well C the orientation goes from a WNE-ESE to a W-E direction. At 15 Ma there is another rotation towards WNW-ESE sustained through the evolution until present-day state.

The stress rotation and changes may be a consequence of fault generation associated with regional tectonic stresses and events.

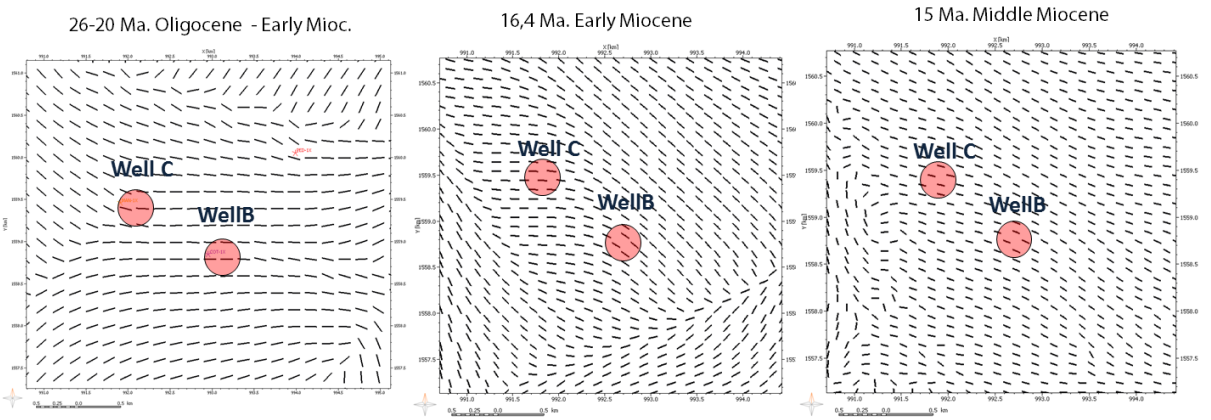

Fig. 110 Maximum stress orientation for defined paleo-stresses at wells B and C location. Selected paleo stresses correspond to 20, 16.4 and 15 Ma. Stress abrupt rotation across the map is associated with facies changes and fault occurrence related to the tectonic evolution of the basin.

6.3.4 3D Present-day stresses

Stresses are calculated through a poro-elastic stress approach. Tectonic strains serve as a tuning parameter and are assumed to be calibrated with the calibration of principal stresses. Main outputs available are all the components of the total and effective stress tensor. Fig. 111 displays the distribution of principal stresses on top of Porquero C and the distribution of stress tensors across the layer (big arrows display the defined present-day stress orientation. As a general trend, at the top of the reservoir level (Porquero C), stress variation is associated with depth, reaching the highest values in the north and south-east regions of the model, coinciding with the regions of highest subsidence and higher sediment thickness.

Simulated S_{hmin} (Fig. 111-A) magnitudes vary between 16 MPa and 32 MPa, in the shallowest and deepest areas, respectively. S_{Hmax} values (Fig. 111-C) range between 19 MPa and 37 MPa. Finally, Vertical stress (Fig. 111-D), ranges between 29 MPa and 46 MPa. These trends selected across the layer display a governing normal faulting regime.

Fig. 112 and Fig. 113 display the potential of the model to capture the maximum horizontal stresses at well locations. Two rose diagrams are added showing the calibration of stresses with drilling-induced fractures (DIF's). The area where wells B and C are located, display a governing maximum horizontal stress of WNW-ESE orientation. Vectors spacing is uniform across the model as the finite element mesh is structured and uniform.

Even though the Lower Magdalena Valley Basin did suffer large tectonic deformations, the area available for simulation (Block A) was affected with less intensity during the history of the basin. Expanding on this, from Oligocene age, the stratigraphy is a product of depocenter filling generated after an extensive tectonic dynamic that resulted in subsidence, fillings and abrupt compaction towards the west. During Middle to Late Miocene, in a compressive tectonic stage, relative unconformities were generated as a result of sedimentation within paleo-canyons and close-to-vertical faults with minor displacements. In Late Miocene to Recent the region registered the strongest effect

of the Andean orogeny leading to an interpretation of compressive tectonics supported by erosive events in the upper formations.

Considering this, the stress orientation variations at different locations are attributed to the presence of faults intercepting the sedimentary unit. An enlargement considering these stress rotations is clearly seen in Fig. 113. The stress field is often disturbed in both magnitude and orientation in the vicinity of mechanical heterogeneity or disturbed areas as it happens with fault surfaces. In this case S_{Hmax} becomes distorted at the fault surface. The variations are traceable along with the entire geometry of the fault.

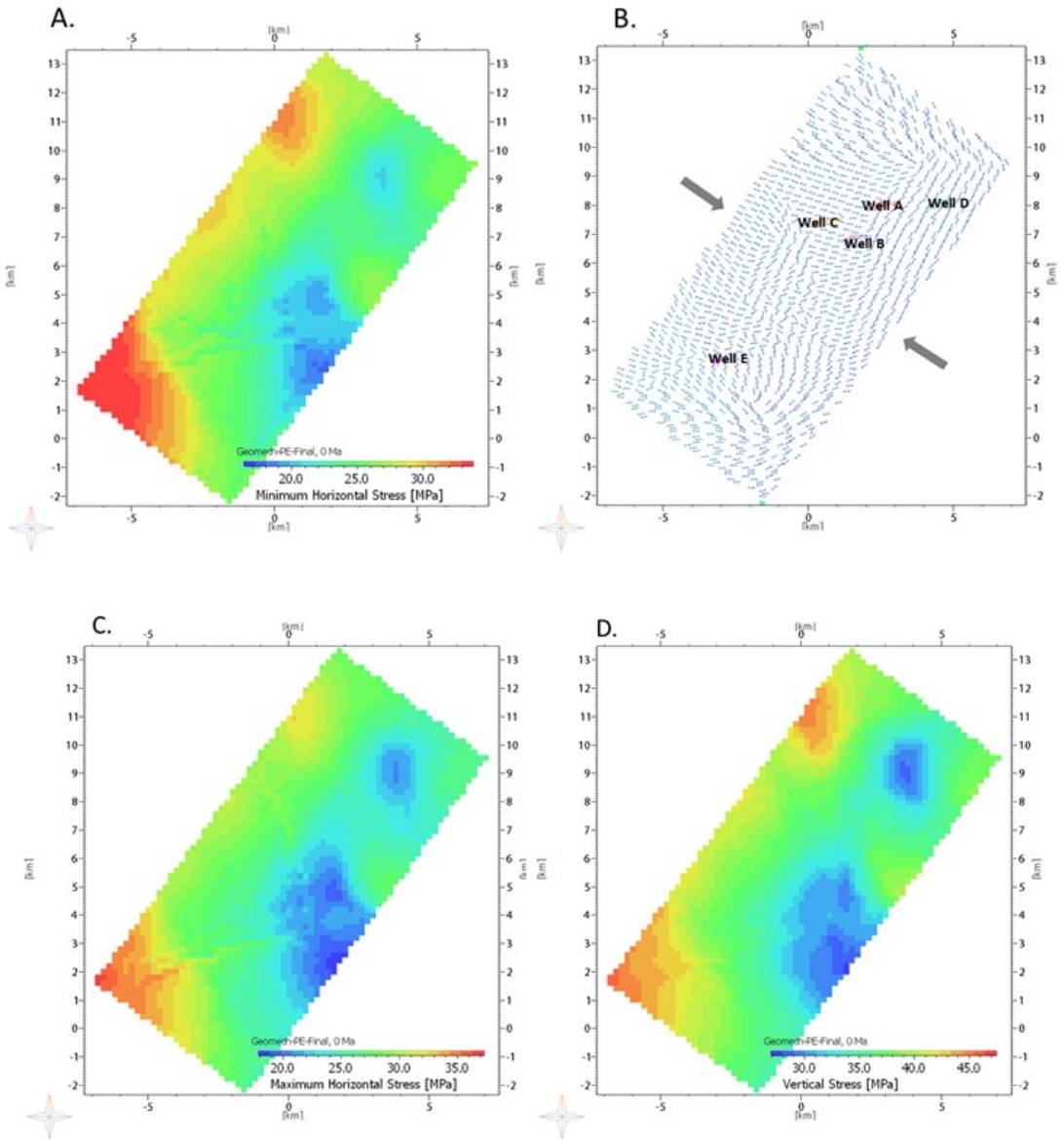

Fig. 111 (A) S_{hmin} magnitude, (B) S_{Hmax} orientation, (C) S_{Hmax} magnitude and (D) Vertical stress magnitudes on top of Porquero C unit. Higher stress magnitudes coincide with the regions of higher subsidence in the area.

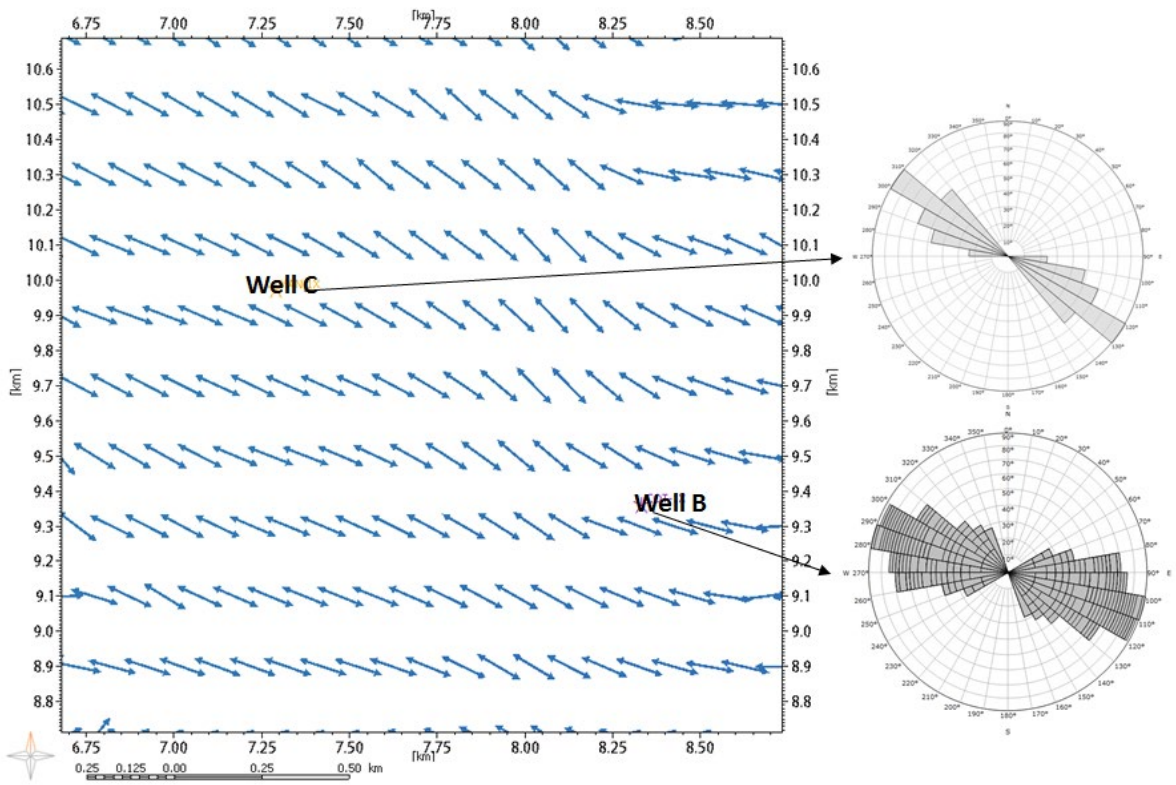

Fig. 112 S_{Hmax} orientations calibrated with drilling induced fracture (DIF) orientations on wells B and C.

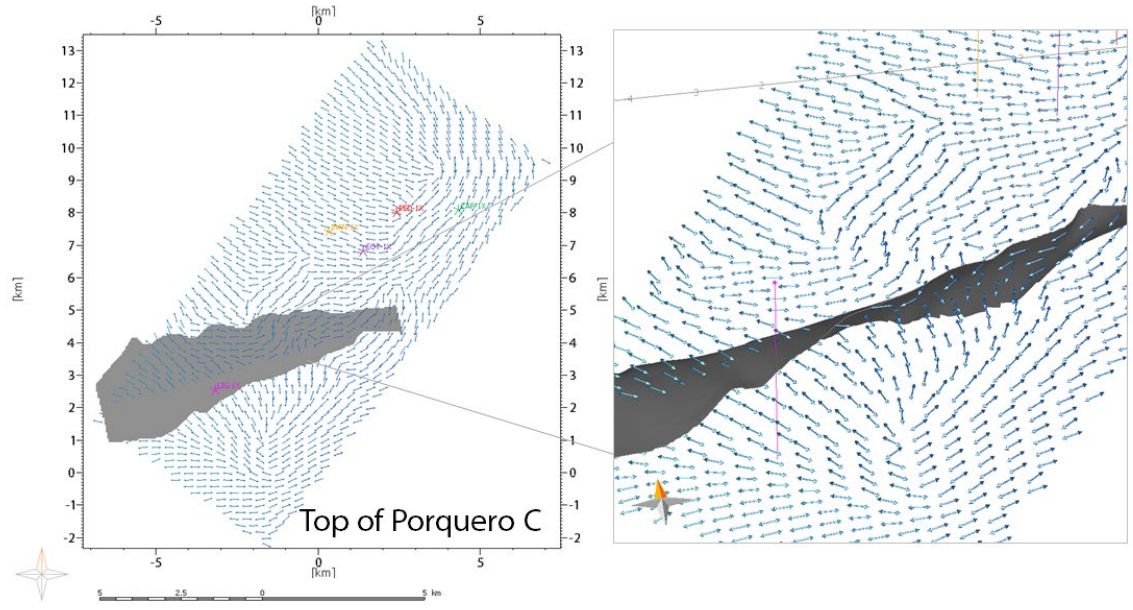

Fig. 113 Maximum horizontal stress tensor component variation with the presence of a NE-SW striking fault. The stress tensor is displayed on the top of the Porquero C unit.

6.4 Natural fracture modelling

Contrary to drilling induced fractures (DIF), natural fracture systems are any randomly oriented break or crack occurring in the rock. Conventionally, natural fractures in reservoirs are analysed in terms of dip angle or dip azimuth, alongside the spatial variation between fracture planes. These variables link the fracture systems and networks to the environmental conditions of a specific geological setting. The following results add to the lack of understanding regarding the replication and predictive potential of geomechanical models to address natural fracture presence and distribution.

6.4.1 Natural fracture prediction (NFP)

This workflow presents the generation of a fracture network using as input data: faults from seismic interpretation and wellbore fracture data. An automatic generation of the *fracture-generating-stress* or paleo-stress is performed through a stress inversion method (Maerten et al., 2016). The paleo-stress setting is estimated through thousands of simulations until one setting matches the orientation of the fractures registered from well data (Image logs). The method is established under a boundary element method (BEM) approach. This implies that mechanical properties were constant, which may mean a limitation if the rest of the variables are not properly constrained. The results are obtained through an iterative process which is calibrated with the wellbore fracture data.

Fig. 114-A shows the orientation of natural fractures and dip angle, for the two wells available as a reference. Fig. 114-B presents for the fracture network using a single tectonic event. The point cloud in the rose plots represents the striking orientation of fractures generated for Porquero C and D units. In general, the modelled fracture network captures the WNW-ESE strike of the measured fracture orientations. Considering the mild deformation of the modelled area (block A) in the present-day setting, it can be observed that the natural fracture network reproduction is reliable.

As the model is constrained further and the active structures are fixed, is important to mention that the results are fault-related fractures, as these are the only disturbances in the model volume. While this modelling approach works substantially well for low-deformation areas, as is this case, in highly deformed settings the results may be misleading (Maerten et al., 2016). For this case, adding the geomechanical constraints and using wellbore data, profoundly reduce the uncertainty in the vicinity of the well.

Another important metric is the fracture intensity. Fig. 115-A and Fig. 115-B show the statistical representation of fracture intensity corresponding to Porquero C and D units. Stochastic fracture generation (NFP workflow) can capture the near-fault fracture presence, considering the homogeneity in the mechanical property distribution; faults are the only disruption in the units.

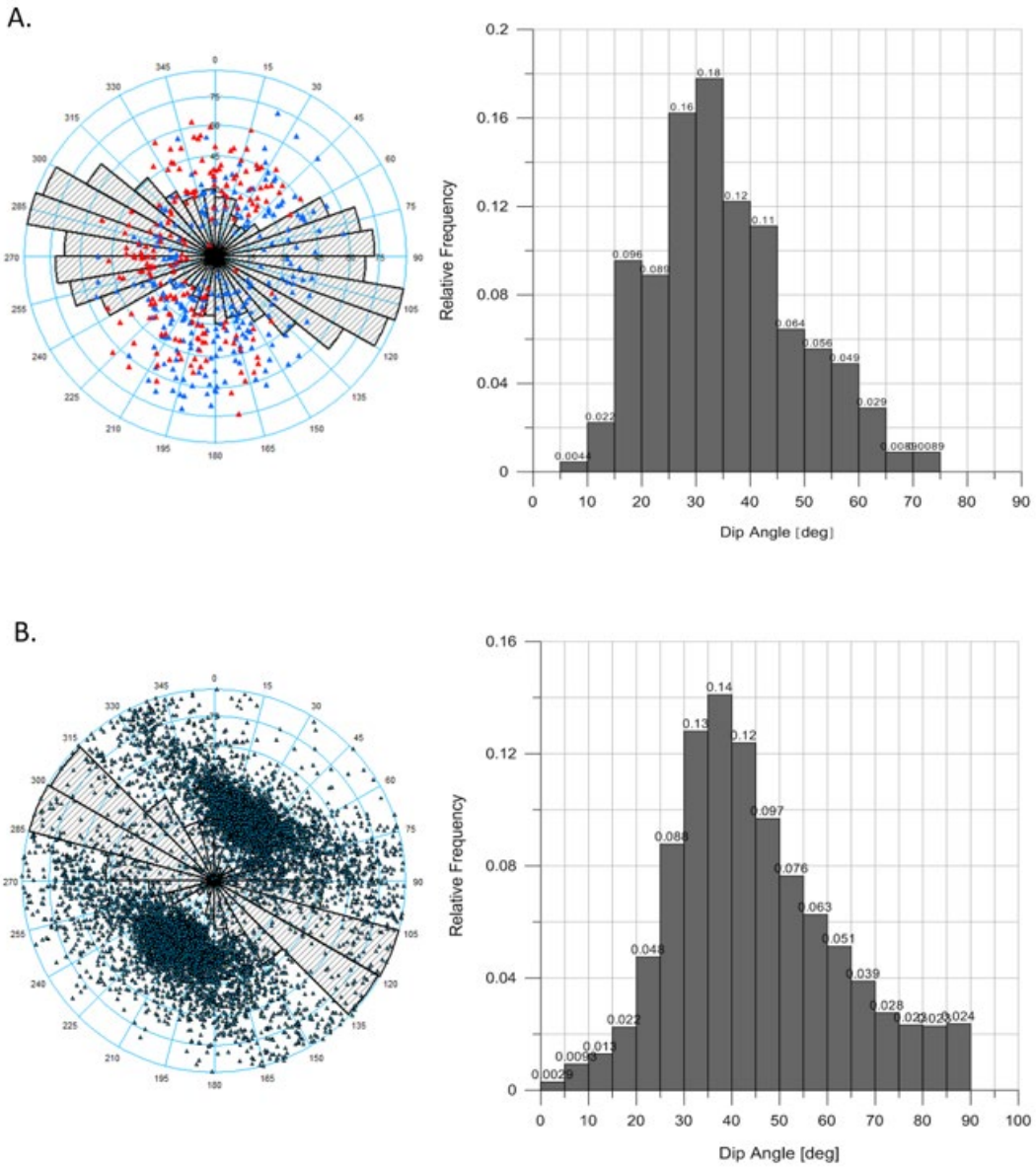

Fig. 114 Comparison between wells B and C measured fracture data and simulated fracture network using the NFP workflow for a double tectonic stress configuration. (A) Wells B and C natural fracture data. (B) Fracture network model obtained through NFP workflow.

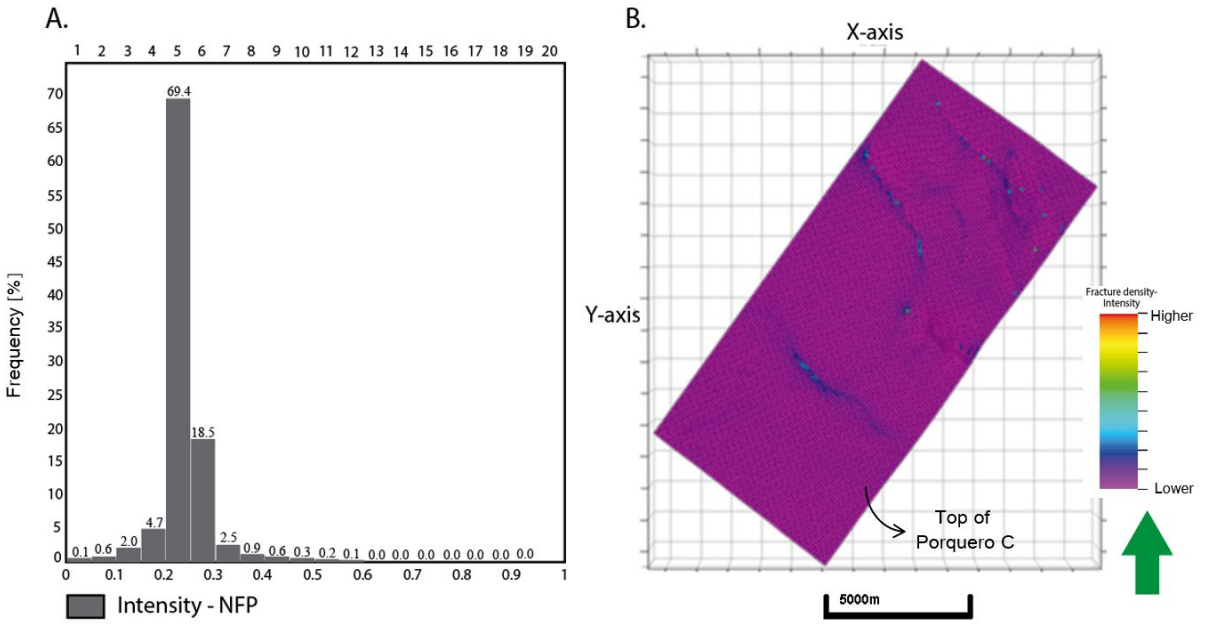

Fig. 115 Fracture intensity from stochastic simulation (A) Intensity histogram. (B) Fracture intensity map for the top of Porquero C associated with the presence of faults. Green arrow points to the North

6.4.2 Basin and petroleum system-derived fracture network.

A forward geomechanical model was used to derive fracture orientation and density metrics. The overall goal of this simulation is to constrain further the geomechanical boundary conditions through geological time to better estimate present-day natural fracture networks. For this, decompaction and backstripping were implemented and the temporal geometry changes were constrained with paleo-water depth maps. The generation of a fracture plane is done under the considerations of rock strength and failure criteria. The engine generates one fracture plane per cell. Fig. 116-A and Fig. 116-A show the original measured data and the resulting orientation and dip angle for a representative filtered section of the model (corresponding to Porquero C and D).

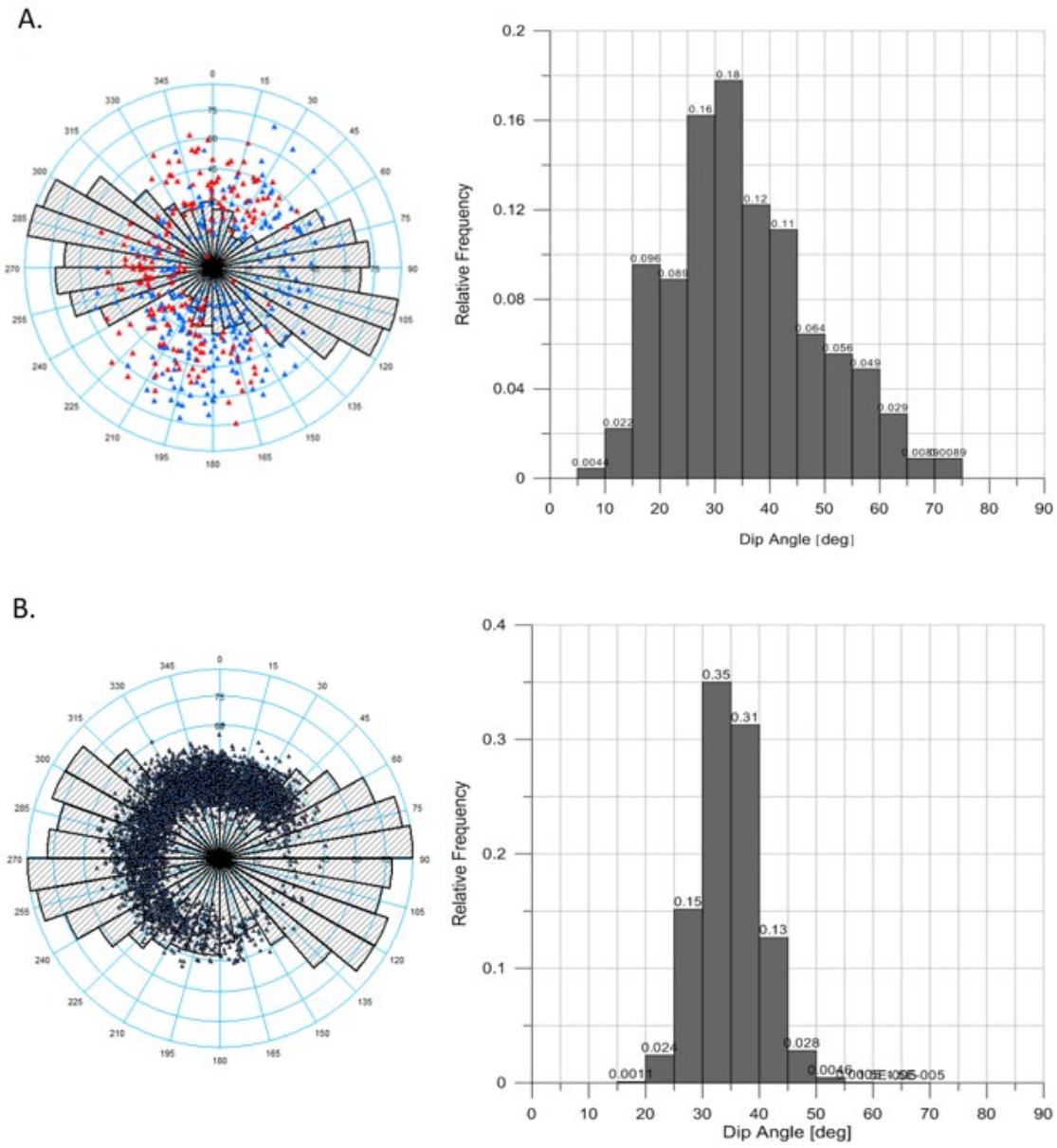

Fig. 116 Orientation metrics and rose map for BPSM derived fracture network. Target zones Porquero C and D. (A) Wells B and C measured natural fracture data (B) BPSM modelled fracture network

The basin and petroleum systems modelling approach was developed in two different instances through a poro-elastic and a poro-plastic approach. The plastic strain used in this approach is a mean to represent the cumulative deformation suffered by the rock through geological evolution. A higher plastic strain indicator implies that the area is most likely to have a fracture presence. This serves as a good parameter to identify well placement spots.

Such forward model simulations (BPSM workflow) was able to represent the heterogeneity through the facies maps beyond the existence of the faults, therefore was able to capture *away-from-fault* fracture generation. Fig. 117 shows the histogram and top view intensity map of Porquero C unit estimated with the forward model (BPSM). While there are some computational constructs, the fault presence indicator does not follow exactly the fault trends.

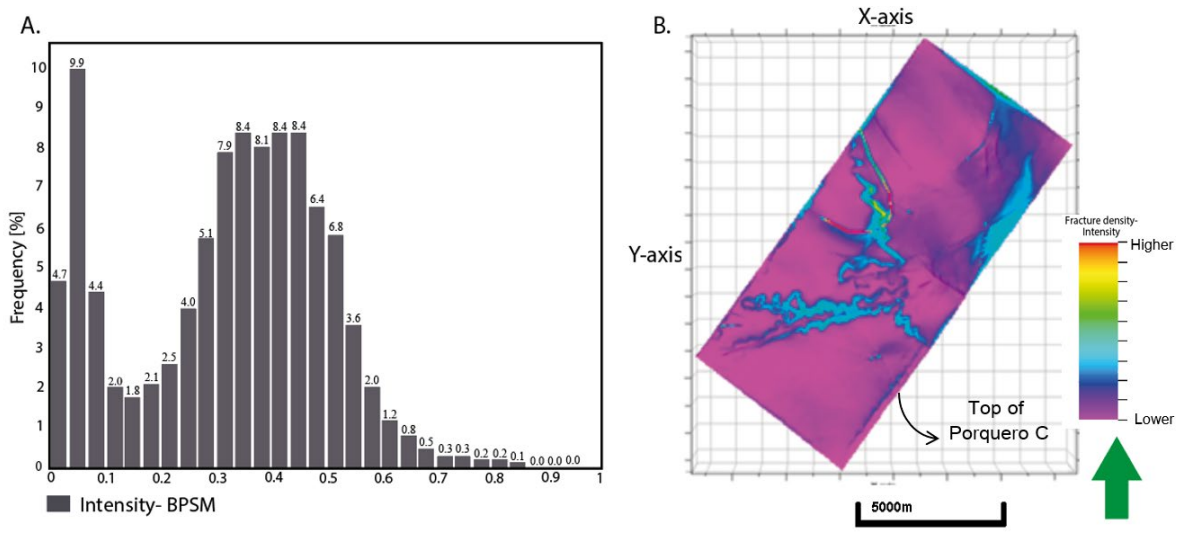

Fig. 117 Fracture intensity from forward-model simulation (A) Fracture intensity histogram. (B) Fracture intensity map for the top of Porquero C.

6.4.3 Fracture network temporal correlation

According to theory, generation and development of fractures is mainly controlled by the tectonic stress field. The type of fracture is normally defined by the stress regime and the orientation of the principal stresses. It is therefore arguable that the fracture setting analysed in present-day does not solely answer to a present-day stress regime, but certainly has registered past tectonic events. The BPSM approach temporal analysis and the possibility of imposing stress regional orientation for different tectonic stages make the simulation consistent with the inferred stress evolution.

Two wells in the area have natural fracture interpreted data, extracted from image log analysis. Fracture interpretation was performed by the industrial partner at wells B and C (Fig. 118). Through the examination of maximum horizontal stress, following the defined paleo-stresses in section 6.3.3, it is possible to associate potential fracture occurrence per age. Fig. 119 displays the maximum horizontal stress azimuth for the selected geological paleo-steps. The coloured regions correspond to the area of the two wells that have natural fracture interpretation.

Extensional fractures tend to form in a plane normal to the least principal stress, whereas the strike of shear fractures depends on the tectonic stress regime. As it was theorized by Anderson (1905), in a normal faulting regime conjugate sets of shear fractures are expected to strike nearly parallel to the direction of maximum horizontal stress (S_{Hmax}) and to dip ~60°. In the case of a strike-slip faulting regime, conjugate sets of shear fractures are nearly vertical and strike at an angle of ~30° with respect to the S_{Hmax}. Likewise, conjugated sets of shear fractures in a reverse faulting regime are expected to show low-angle dips of approximately 30°. These cases are subjected to the most common occurrences in analysed datasets. However, in practice there are working ranges within these categories that often overlap, reflecting lithological heterogeneities and non-ideal stress conditions (Aruffo, 2014; Lorenz & Cooper, 2017; Nelson, 2001).

The predominant orientation for both wells is WNW-ESE. Within the two groups interpreted orientations include sets striking in E-W, NW-SE and minor strikes in NE-SW. The governing fracture set falls within the stress evolution and the representative regional S_{Hmax} orientation is

between ~100°-130° WNW-ESE. The fractures are assumed to be shear fractures or hybrid between shear and extensional fractures.

The fracture dip angle for both fracture groups spans between low dip angles, intermediate-dip and in minor proportion high-angle dips. The governing dipping angles are associated with a normal faulting regime (>35°). Low-dipping conjugated sets of shear fractures are observed implying deformations occurred under reverse to normal faulting regimes and covered dipping angles of 0 to 40°. This set of fractures is present in both wells and are potentially associated with the shift from an extensional to a compressional regime (~15 Ma), which turned into abrupt deformation on the western side of the Plato sub-basin.

In well C, there is a distinct group of fractures striking approximately N-S. According to literature such orientation perpendicular to the governing maximum horizontal stress may be associated with release/unloading events that cause local stress reorientation (Fossen, 2010; Ritter, 2016; Thöny, 2014). These are presumably associated with compression reactivation as a consequence of the Andean Orogeny which lead to abrupt unconformities and large eroded intervals (Arminio et al., 2011).

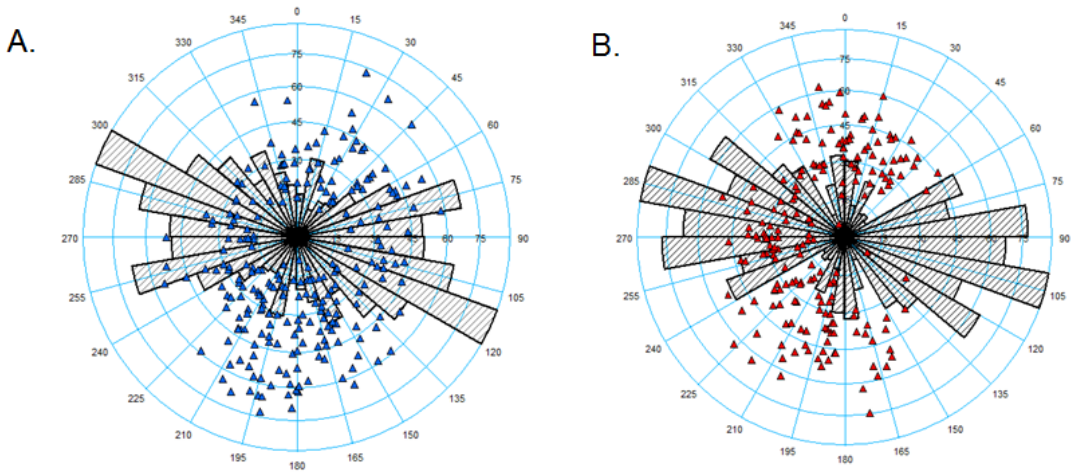

Fig. 118 Details fracture strike obtained through the interpretation of image logs. (A) Well B and (B) well C.

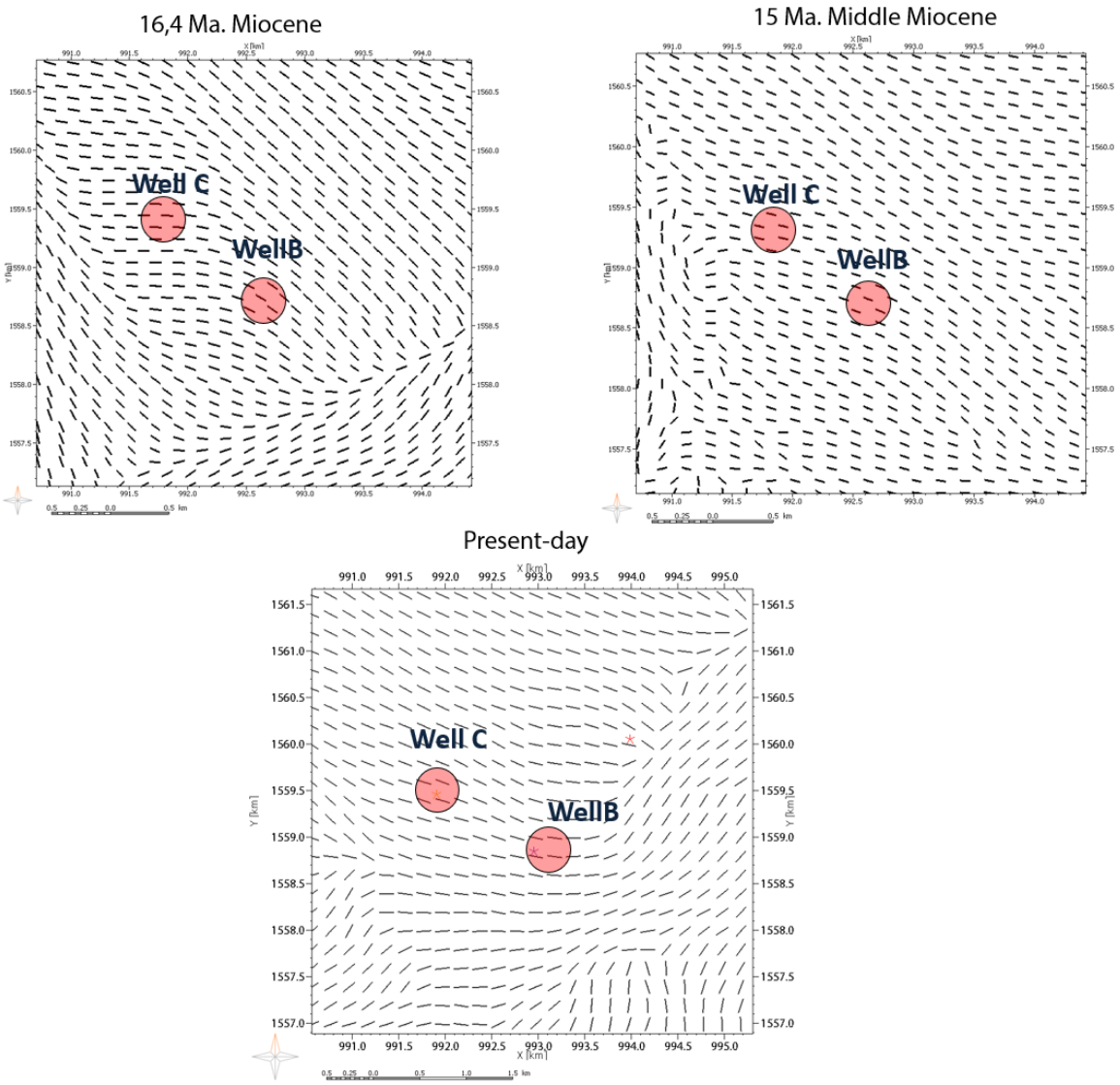

Fig. 119 Maximum stress orientation for defined paleo-stresses at wells B and C location. Selected paleo stresses correspond to 15 and 16.4 Ma. Reorientation of stresses is probably associated to tectonic regime changes in the basin (extensive to compressive), offsets planes due to fault generation and the increment of erosive events.

Chapter 7 Summary and discussion

The work developed in this thesis described different geomechanical approaches applied to a tight sand gas field in the Lower Magdalena Valley area in northern Colombia, in order to predict in 3D distribution of geomechanical parameters through the construction of models from different data sources. The key results of this work prove that alongside conventional geomechanical predictive methods, the integration of geological processes through basin modelling techniques, provide an alternative approach for pore pressure prediction and mechanical property assessment based on geological interpretation which consequently derives in better geomechanical models. The strong geological association, alongside field and laboratory data makes up for a valuable and consistent spatial prediction of properties. The thorough calibration of the model ensures that the basin and petroleum system model, besides fulfilling its original goals of hydrocarbon generation, migration and accumulation analysis, can serve to bring about physically accurate geomechanical description of a reservoir.

Modelling results show substantial variation along and across the modelled stratigraphy in terms of stress magnitudes, between log-derived, seismic-driven and basin modelling approaches, which do not merely result from different depths but also from the spatial representation of mechanical properties. The modelling work steps allowed assessing the property variations and the differences in the stress prognosis which result from a model population based entirely on well log data versus one that uses seismic inversion and AVO analysis in addition to the well logs, and at the same time, these are compared to one that implements regional correlations to define lithological trends, pore pressure generation mechanisms and mechanical behaviour. The performed approaches had three principal objectives to assess, which were: mechanical properties, pore pressure and *in-situ* stress distribution at field and wellbore scale. The fundamental variations and highlights among modelling approaches can be grouped into three categories (1) Model construction-used database, (2) Pore pressure modelling and (3) Mechanical properties definitions.

The log-derived and seismic-driven models were developed with present-day data from exploration and production. These modelling approaches are the current preferred tools in industry practice, considering its versatility and the conventional datasets available. These models serve also to work from present-day setting to future predictive scenarios, but when the information is scarce, there may be high uncertainty in the estimation of parameters in areas far from the wells. In many cases it is necessary to integrate results between both approaches to generate integrated gradients. The third approach, basin modelling, worked with a governing data that was extracted mostly from geological interpretations. The possibilities of local calibration, from field and laboratory data, represent an advantage. The usage of detailed regional geological trends in addition to interpreted structures, geochemical data, paleogeography, compaction trends, facies maps and thickness changes etc., provides an educated prediction of what occurs at the inter-well areas. This concept constitutes a dynamic modelling approach, able to represent the geological time scales and variations suffered by the area.

Regarding pore pressure modelling (Pp), the differences among modelling approaches imply, on one hand that the application of empirical models derived from seismic velocities are useful for local interpretation, first approximations and specific drilling purposes, as the thorough calibration demonstrate that the overall trend is being captured. Nevertheless, regional extrapolation may benefit

from more elaborated methodologies that consider the spatial heterogeneous nature of rocks. On the other hand, basin modelling approach utilizes compaction laws that intend to represent the natural compacting behaviour of sediments and porosity-permeability relationships, that considers the inter-relation of properties along and across a sedimentary unit. Such interaction enables pore pressure generation or release mechanisms throughout the geological evolution which control the present-day pressure state. Additionally, faults act as drainage conduits or compartment seals depending on the permeability conditions and have a strong influence in pore pressure build-up. While a proper assessment would require a further knowledge of the active/inactive faults and the type of filling or cementation, the simplifications applied in this research provided a good first approximation to its behaviour. The final pressure model relies strongly on the facies definition which derived in further cross-discipline assessments to generate it with considerable accuracy.

A critical distinction among the simulated approaches is the mechanical property definition. In general, one may be more accurate than the other, especially in the inter-well regions, but in terms of practical applications they are all capable of delivering valuable information and its implementation depends on the data availability and the specific case study. Property modelling of a finite element model can start with a basic approach through extrapolation of scarce data. The great advantage of being capable to work with different datasets is the possibility to obtain early spatial information that tied to geological analysis may provide insights of the inter-well regions and early warning of potential risky areas. The associated uncertainty will decrease as data density increase during the reservoir life-cycle.

The use of diverse data integration (seismic surveys, laboratory testing results, geological and well log-derived data) intends to reduce the uncertainty of the spatial heterogeneity and increase the reliability in the inter-well regions. The quality and accuracy of the seismic inversion is therefore of major importance. After such property population methodology, there is warranty that the highest quality data is assigned to each to a stratigraphic column in any place of the simulated domain.

7.1 Log-based vs. seismic driven approach

The differences between the two approaches for the mechanical characterization of the Porquero C reservoir unit are shown in Fig. 120 A and B for static Young's modulus and Fig. 120 C and D for static Poisson's ratio, in top and side views. Comparing the two property population methods, the differences in Young's modulus and Poisson's ratio are below 5% in the well-cluster (wells A-D) and can rise to <15% in poorly constrained inter-well areas for which no well data is present. These results are representative for the overburden and target units.

A highlight is necessary for the region where well E is located. Well E is an old and poorly constrained, but is the single well within the model that drilled through Porquero E and F. As observed in Fig. 121, a comparison between well A (the only well with rock mechanical tests) and well E (no mechanical data for calibration) the behaviour of the properties coincides up to a depth corresponding to Porquero D unit. From this depth onwards, abrupt changes are registered in the log-derived properties, while the behaviour of the seismic-derived data varies progressively.

The difference between the Young's modulus and Poisson's ratio derived from the two approaches are thought to be caused by several reasons: regarding the population approach, the population methodology applied in E and F units only uses well E data, which is scarce and does not have any kind of calibration data. Moreover, reports describe behaviour of abnormally-high−pressure regime,

numerous drilling accidents (including stuck pipe, well flow, kicks and stabilization problems). For this reason, it can be assumed that the data exceeding 2400 m has a lower reliability.

Regarding the sensibility between log data and seismic data, it is logic to infer that vertically, electric logs are more sensible, as they are capturing abrupt transitions as it passes through interlayered strata, which are not accounted in the seismic data. However, horizontally the seismic inversion and AVO methodologies allows for a better spatial property population, allowing an uncertainty decrease in areas with little or no data. Log-derived elastic properties can be used as a reference and may represent an upper-bound for the properties in the stratigraphic unit of Porquero F, in the vicinity of well E. Even though the resulting behaviour is compliant with the geological setting, there is no calibration data available to ensure the precision of the mechanical properties, further than 2400 m. Considering this, the highest reliability of the model can be guaranteed from the model surface to Porquero D, since this section of the model domain guaranties low uncertainty properties.

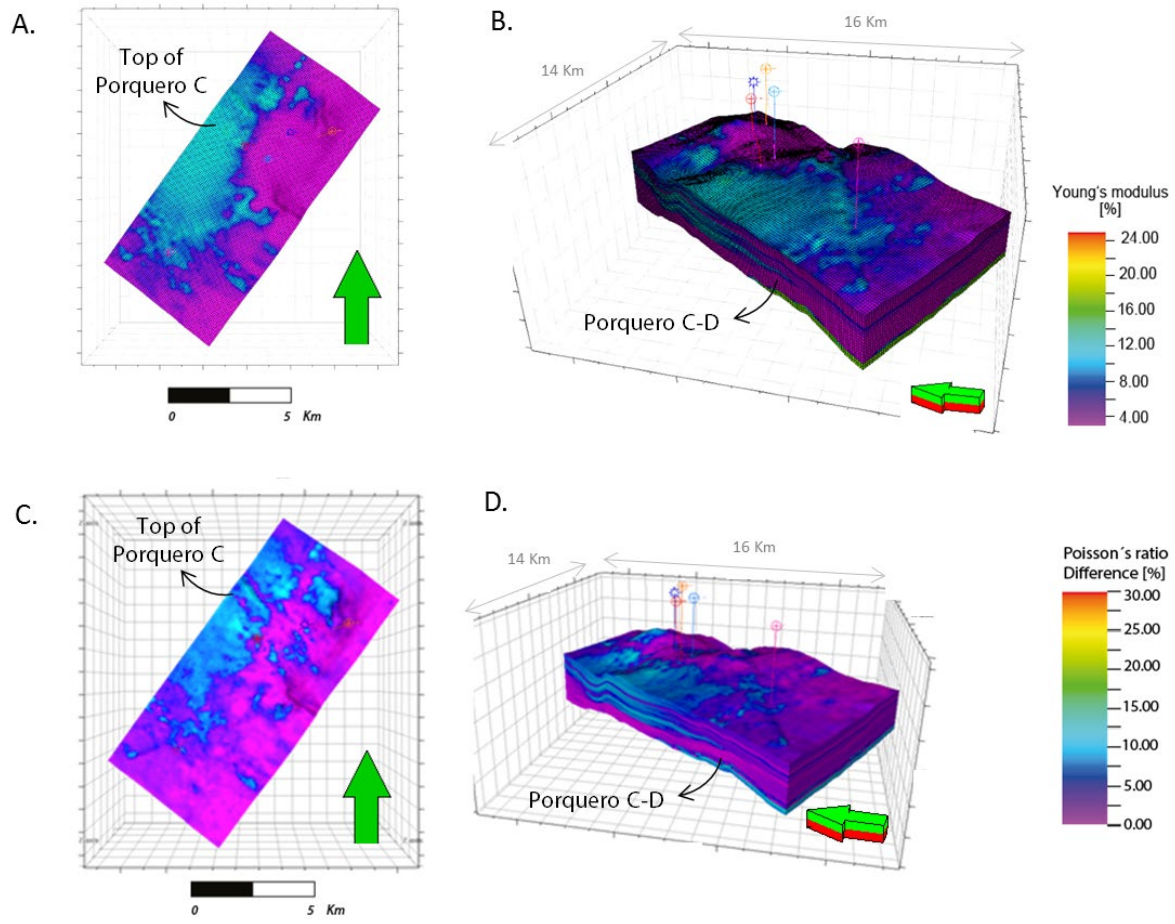

Fig. 120 (A) and (B) show the absolute difference of static Young's modulus between the two approaches. (C) and (D) show the absolute Poisson's ratio difference between the two approaches.

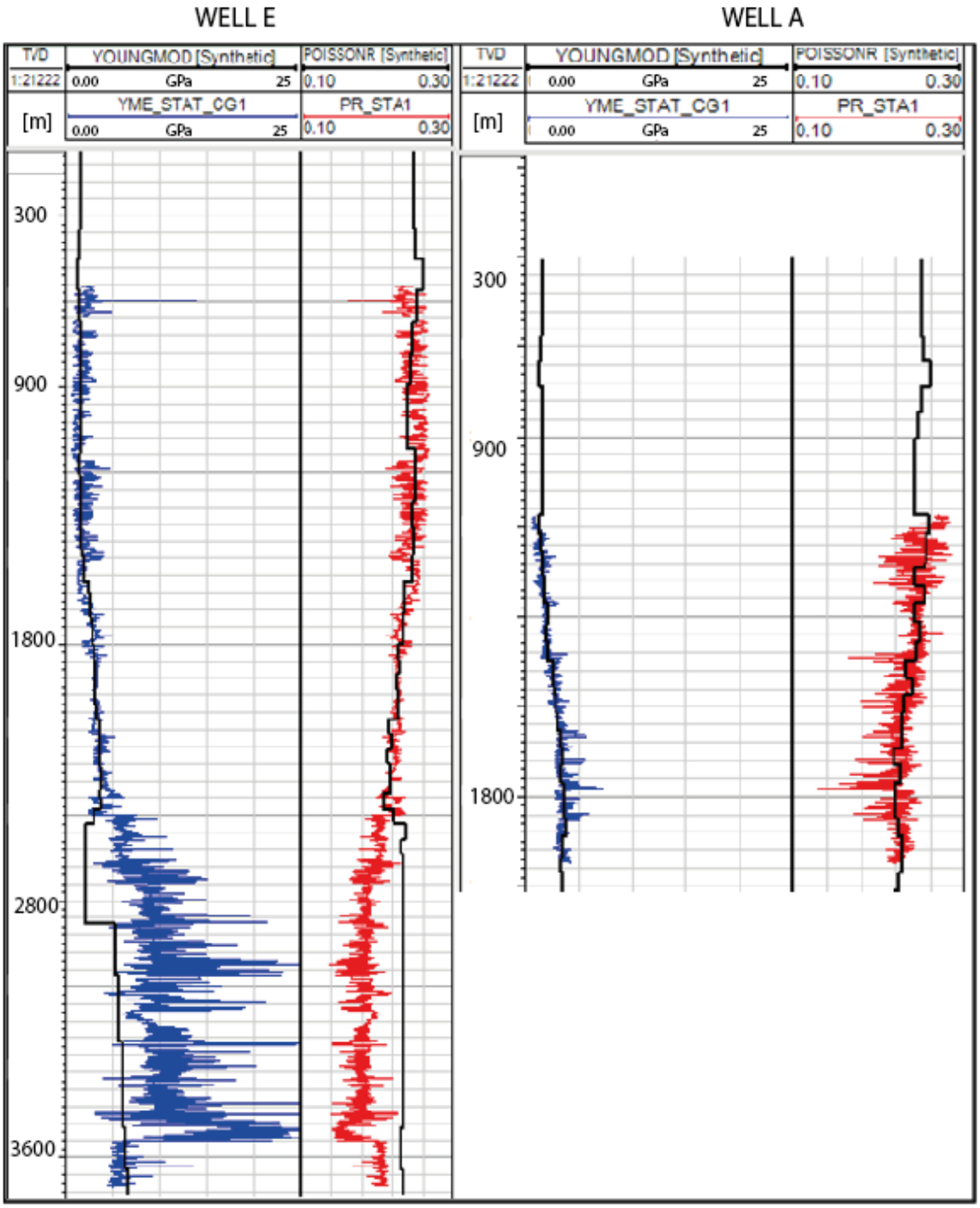

Fig. 121 Well profiles displaying the correspondence of mechanical properties obtained from logs with respect to the final population of the seismic-driven model. There a correspondence between approaches up to a depth corresponding to Porquero D unit. A difference is observed from this depth onwards associated with abnormally high pressure regime.

Fig. 122 displays the property extraction for formation tops on well A, which is considered the best mechanically constrained well. These results were obtained from the seismic-driven and the log-based approach. The seismic-driven approach follows a progressive variation of properties as the end of the seismic data is reached. Even though the variation is noticeable, it fits the setting and trends of the upper units. On the log-based approach, units E and F are being populated with data extracted from

well E only, showing abnormal peaks in the mechanical properties. This well was not part of the seismic inversion calibration workflow and there is no rock laboratory test available for calibration on the bottom units (E and F). A single well populating an area of 100 km^2 implies high uncertainty, but on the other hand, it may be the case that well resolution is capturing behaviour not recognizable by the seismic data. Presumably, because of these reasons, the accurate fit between log data and seismic driven data for wells A to D, is not observed in well E bottom units. However, considering the coverage of the seismic inversion and the good fitting/adjustment that exist with the log-based approach in the C and D units, it can be stated that the best trends in the mechanical properties, are obtained from the integration of both methodologies.

Regarding the resulting modelled stresses, the most significant differences, for example, in the predicted S_{hmin} magnitudes can be up to ~17% and are found on the eastern side of the model and between well A and E. In areas closer to wells, especially wells A, B, C, D differences remain below ~5%. Again, it is a noticeable remark that the integrated approach is able to capture the change of stress behaviour in two distinct locations (Fig. 123-A), whereas in the well-log only approach this variation remains poorly delimited (Fig. 123-B).

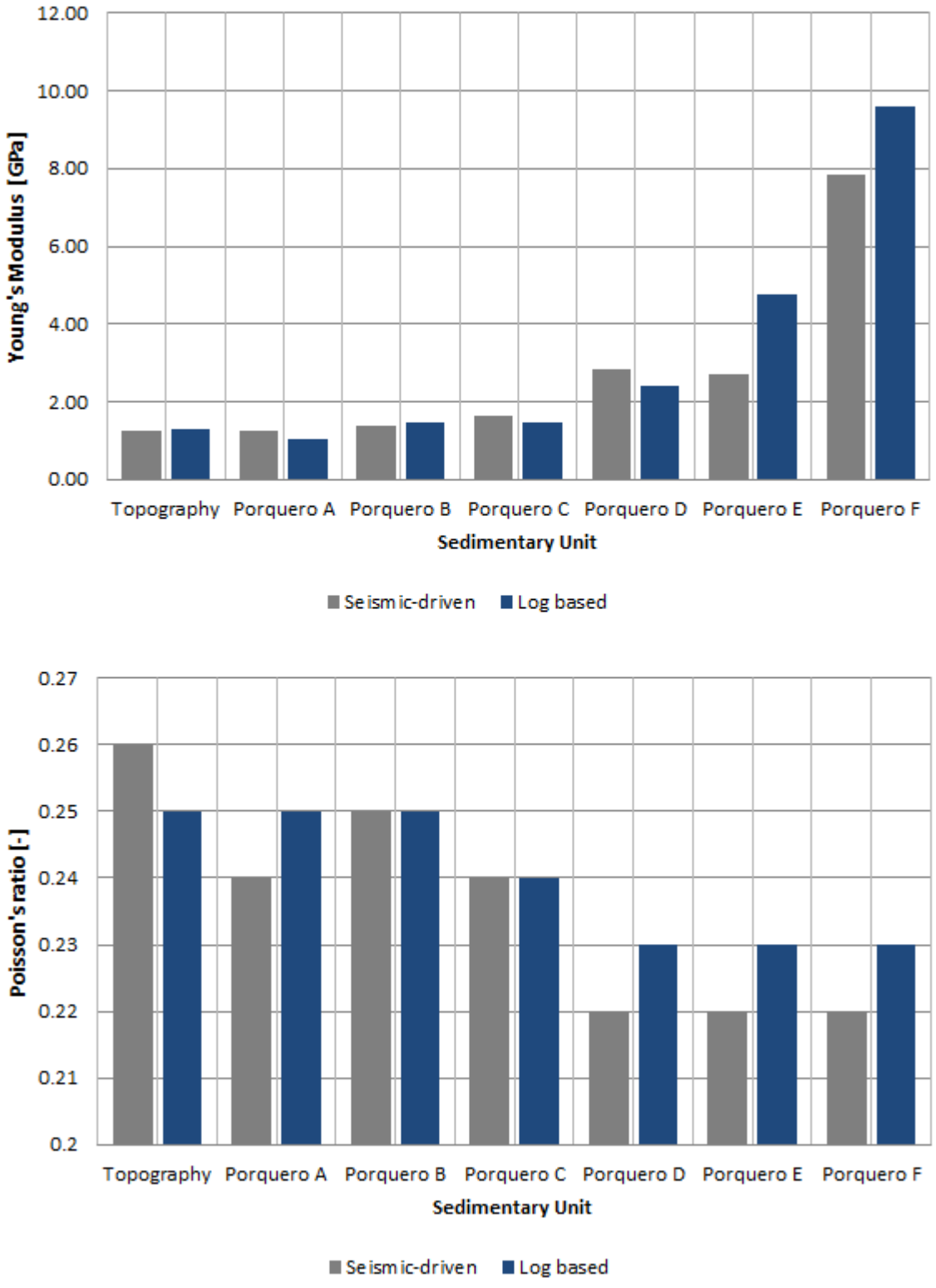

Fig. 122 Bar graphic displaying the variation of Young's modulus (Top) and of Poisson's ratio (Bottom) from log-derived and seismic-driven mechanical earth model. Extraction on well A.

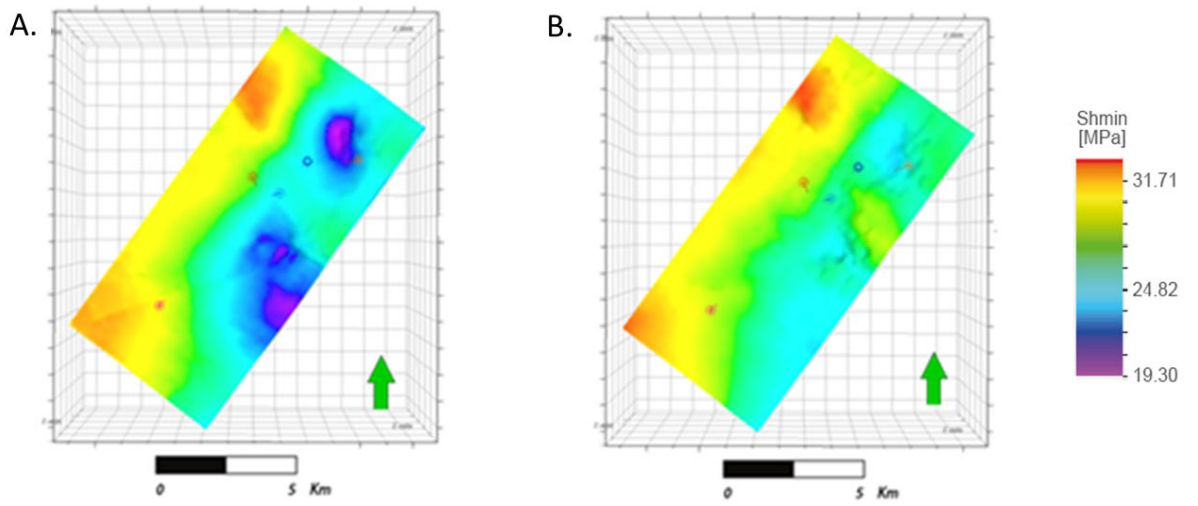

Fig. 123 (A) S_{hmin} distribution obtained from the integrated approach and (B) S_{hmin} obtained using well logs only. Top of Porquero D unit.

7.2 Basin modelling approach vs. conventional methods

The main comparison points between basin modelling, seismic driven and log-based approaches are the features concerning the mechanical property and pore pressure definition. Pore pressure in the seismic-driven approach utilized a log-derived pressure gradient extrapolation based in seismic empirical correlations. This approach works in an acceptable way for a first approximation and trend estimation, but it fundamentally neglects the possibility of capturing permeability- and structure-derived spatial variations across the model.

Basin modelling-derived pore pressure does not rely on well data as input but involves it for calibration in later stages. The pore pressure model is the result of the numerical representation of several mechanisms and interactions among properties, which are neglected in the seismic-driven model. Porosity, permeability, loading and unloading events are considered in the final pressure magnitudes. The results presented in this work display high concordance among each other, but the physical constrains associated with compaction-driven pore pressure are only represented in the basin modelling approach. Alongside well and field measurement calibration, BPSM demonstrates to be the approach that considers the most variables to estimate pore pressure. Fig. 124 displays the comparison between log-based derived and BPSM pore pressure. Variations between approaches can be of up to 15%, whereas in poorly constrained areas differences can reach up to 30%. However, the increasing pore pressure trend was captured by the two approaches for the selected well location

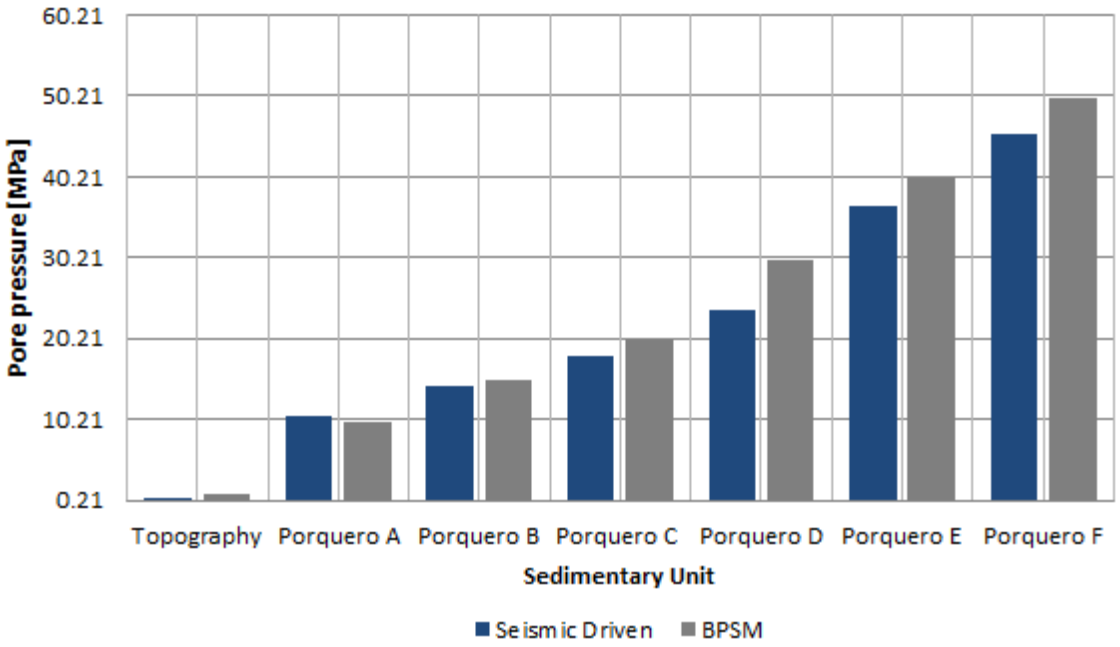

Fig. 124 Pore pressure comparison between seismic-driven model (log-based derived pressure) and basin and petroleum system modelling approach. Extraction on well A.

Mechanical properties are a second highlight of the model. Log-based mechanical properties are directly calculated from a continuous record of the wellbore. This means that minimal disturbances are being captured in the log as well as abrupt responses associated with lithological changes. In the seismic-driven approach, mechanical properties are derived from impedance and density volumes, extracted from a seismic inversion procedure. This method leads to a high resolution, calibrated elastic property cubes, which captures of heterogeneities away from the well cluster and well location. Regarding resolution, this property definition constitutes the most reliable way to describe the non-homogenous nature of a rock formation laterally. In the basin modelling approach, elastic properties are estimated as a function of porosity and linked to a specific geometrical constrain related to the facies maps, in present-day state, in addition to burial depth and subsidence history and other mechanisms. Regarding consistency, this modelling approach constitutes the most geologically-consistent derivation of properties.

It is reasonable to expect mild to high variations between these approaches, depending on the calibration data available per unit. Fig. 125 displays a comparison between Young's modulus and Poisson's ratio magnitudes obtained from the three different approaches. In the target units Porquero C and D relative variations with respect to seismic-driven and log-based approach are approximately <10-15%. This variation with respect to hard-data can be adjusted with higher resolution facies maps and increase in calibration data.

There is a mild over estimation of Young's modulus along the profile and an abrupt over estimation of Poisson's ratio observed in the shallow layers, as derived from the BPSM approach. These properties are directly associated with the compaction behaviour and porosity assigned for the facies maps. In the case of Poisson's ratio is this result is representing loose sediment.

A distinct trend, opposite to the seismic-driven and log-based methods is observed in the poorly constrained units E and F. The lack of calibration data of the lower units hampers the possibility of giving absolute results, but it provides a working range of mechanical properties. In unit E, for

example, Young's modulus varies approximately between 5 to 8 GPa, while Poisson's ratio stands between 0.21 to 0.23.

The over- and under estimation of mechanical parameters can lead to variations of ± 5 to 15MPa in the horizontal stress profiles. The direct consequence of these miscalculations is observed in the wellbore stability assessment, as mechanical properties determine the mechanical integrity limits of the wellbore wall.

Faults

One key aspect worth mentioning is the faults numerical interpretation. In the seismic-driven approach worked using the Petrel-Visage ® simulator, faults are considered as cell properties. The resulting profiles are continuous and do not show abrupt stress orientation changes. In the BPSM engine PetroMod ®, numerical consideration of faults allows the reproduction of more visible effects of faults in the stress orientation and magnitudes. This feature is relevant for directional drilling procedures, depending on the faulting environment, as a wellbore will be more stable in the direction of the maximum horizontal stress S_{Hmax} (Fjaer et al., 2008; Tiwari, 2013).

Fig. 125 Bar graphic displaying the variation of Young's modulus (Top) and of Poisson's ratio (Bottom) from log-derived, seismic-driven and BPSM mechanical earth models. Extraction on well A.

7.3 Comparison between NFP and BPSM-derived fracture models

An important application, relevant for optimizing well placement, was the estimation of a natural fracture network, which was generated for the target sedimentary units (Porquero C and D). Two modelling approaches were implemented: one based in geostatistics and stress inversion (NFP) and the second, based on forward modelling from the basin and petroleum systems approach (BPSM). Fig. 126-A and Fig. 126-B displays the comparison of the orientation metrics obtained from the two approaches. The difference in data density is a result of the filtering and the resolution of modelling meshes.

Original measured data orientation has an average strike orientation of ~108° (ranging between 60° to 120°). Generally, both approaches can capture the striking tendency of the target units in WNW-ESE orientation. In one hand, the NFP-derived fracture network displays a high concentration of data around the approximate present-day stress state (~100-120 NW-SE). The NFP workflow uses the well data as input for their calculations as well as fault surfaces. This approach is useful when there is existing data. For areas with low deformation degree and constant structural patterns like is this case, the results are close to the reliable limit. A great limitation that exists in the NFP workflow is the lack of heterogeneities representation in mechanical properties. Nevertheless, considering the geological context, with increase details in modifiable variables (tectonic events per group of faults, good definition of active faults) it is possible to catch the fracture trend according to the well data.

On the other hand, BPSM-derived fracture network holds high scattering with a dominant striking orientation of approximately ~105°. BPSM approach does not utilize wellbore fracture data to construct the model, which is a highlight of the method since the results are a response of geological and tectonic approximations. The heterogeneity across the unit is represented through the facies–derived mechanical properties, but additionally, the model is capturing porosity-permeability relations variations vertically and horizontally. Moreover, the resulting network is recognizing the temporal changes in lithology as well as stress variations through time, as per imposed in the geomechanical boundaries.

Fig. 127 and Fig. 128 display the ability of the two models to capture and reproduce wellbore fracture orientation data. The two models correspond to extractions made from the models at wells B and C. Original measured data is displayed for reference. The data density is affected by the resolution difference between the measured data coverage from the measurements and the extraction made for units C and D.

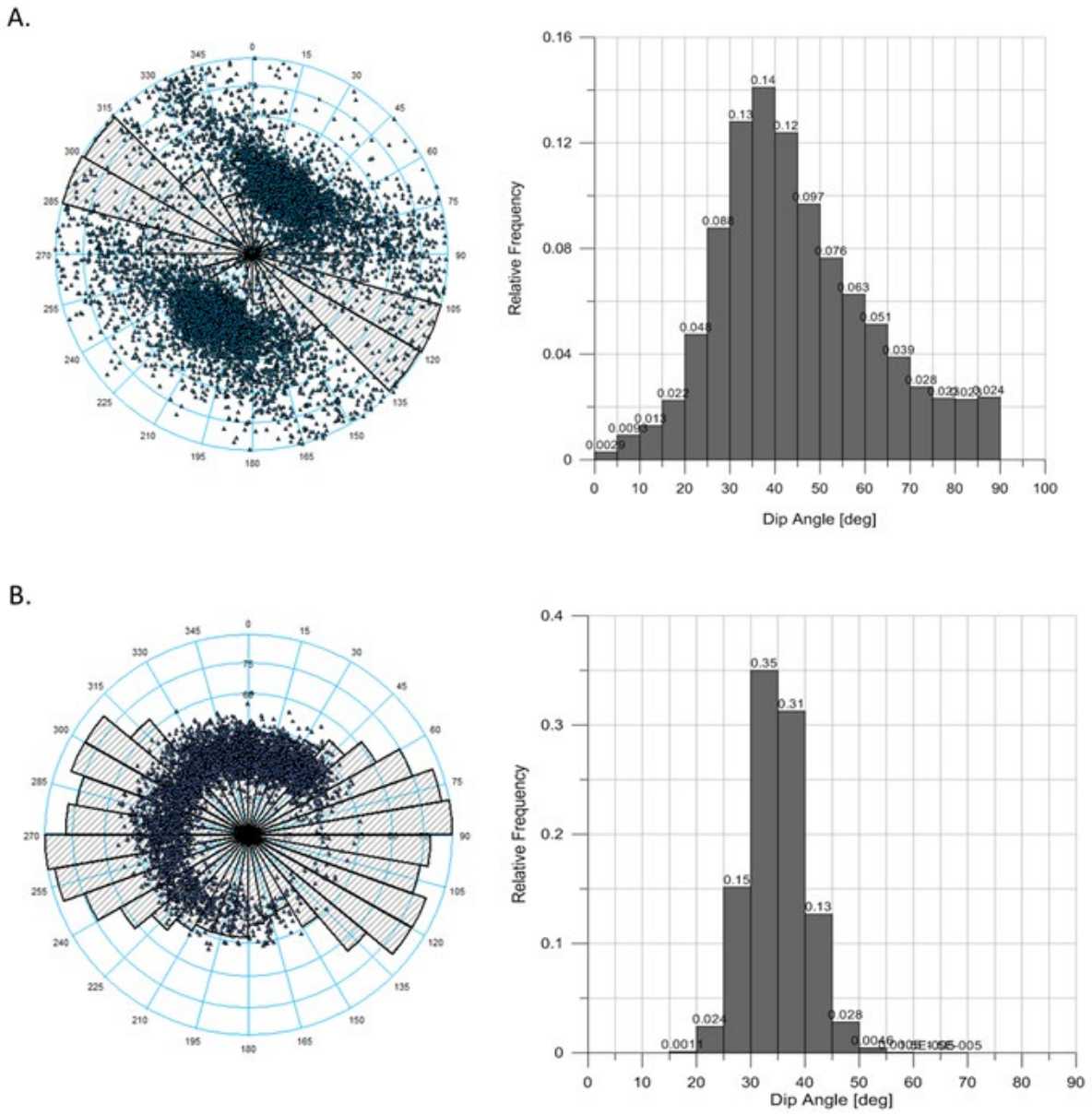

Fig. 126 Comparison of orientation metrics obtained from (A) Natural fracture prediction and (B) BPSM-derived fracture models. The selection covers the units of Porquero C and D.

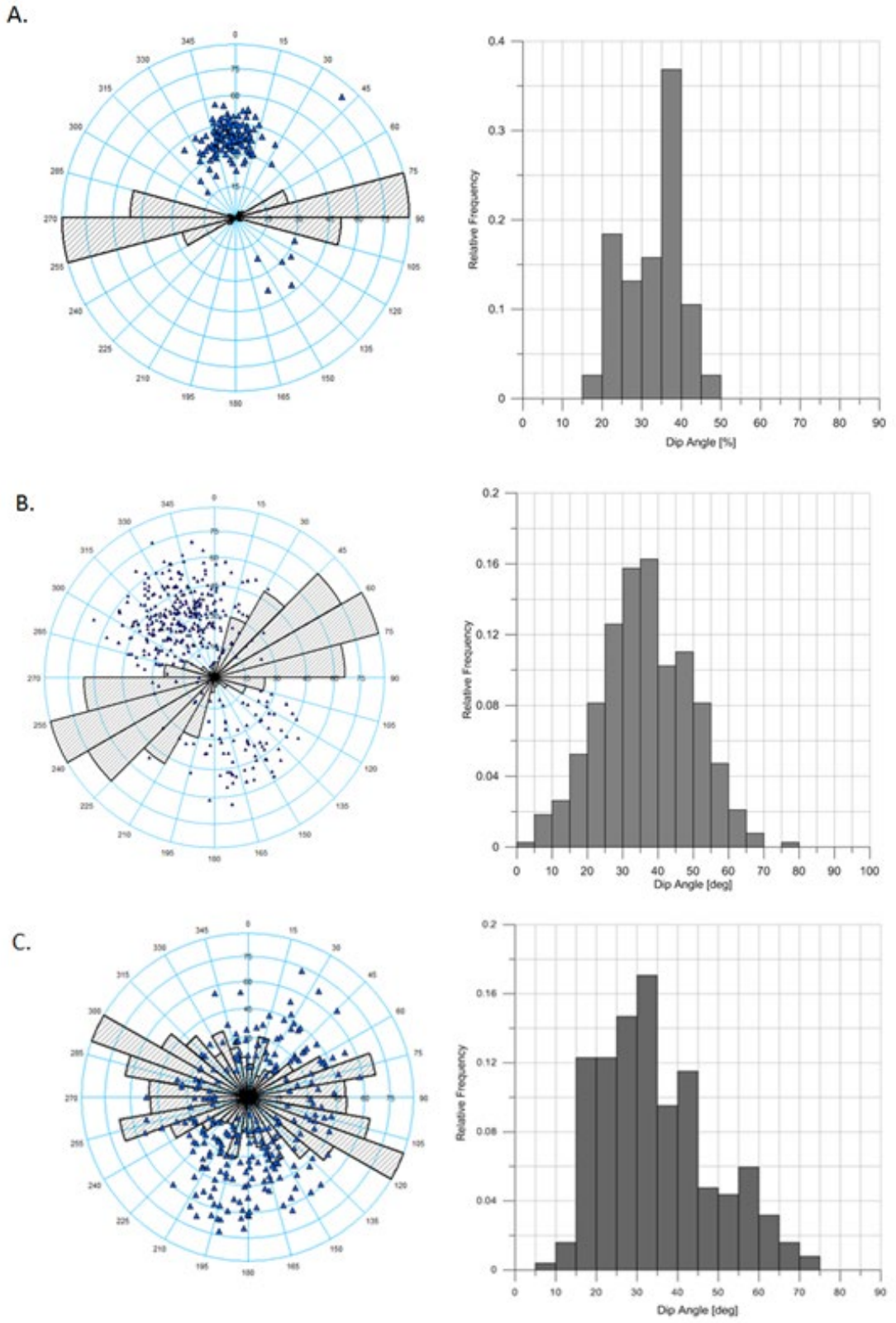

Fig. 127 Comparison of resulting fracture plane intersection at well B location extracted from for a filtered section of Porquero C unit (A) NFP, (B) BPSM workflow and (C) well B measured data for reference.

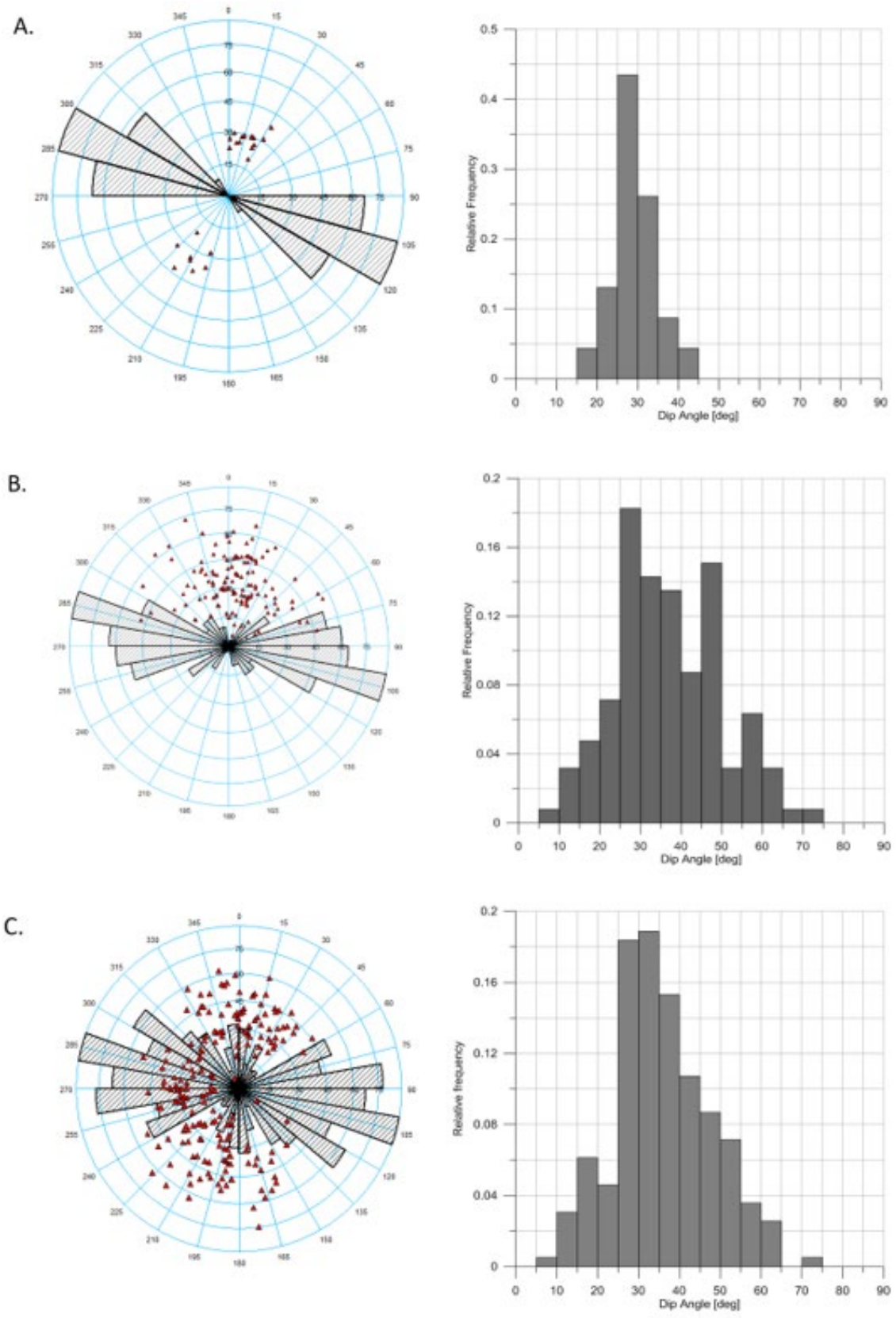

Fig. 128 Comparison of resulting fracture plane intersection at well location extracted from (A) NFP, (B) BPSM workflow and (C) measured data from well C for reference. Extraction at well C.

7.4 Practical potential of the developed geomechanical models: Pore pressure prediction in a new well.

The objective of this section is to showcase the potential applications of the catalogue of models developed in previous chapters. A way to assess the potential benefits of using the models is through the prediction of selected properties for a random well and comparing it to field data. Outpost's wells normally do not have hard data to calibrate and rely heavily on geological interpretations and educated guesses. Log-based and basin and petroleum system models were used for the generation of a well pressure profile for a new, randomly located well. This well will serve as a comparison point between the modelling approaches in terms of pore pressure, considering the dataset available. Pore pressure is the only property with measurements available in all wells.

Well X is located approximately 4 Km away from the well cluster, towards the north corner of the model (Fig. 129) and covers a depth of 3 Km reaching unit Porquero F. Wells Y and Z do account for pressure measurements and are close to the well X by ~2.5 Km. These wells were not considered in the simulations as they are outside the seismic volume but, represent additional data for further constrain of the property as they account for drilling stem tests (DST) and registered pressure gradients.

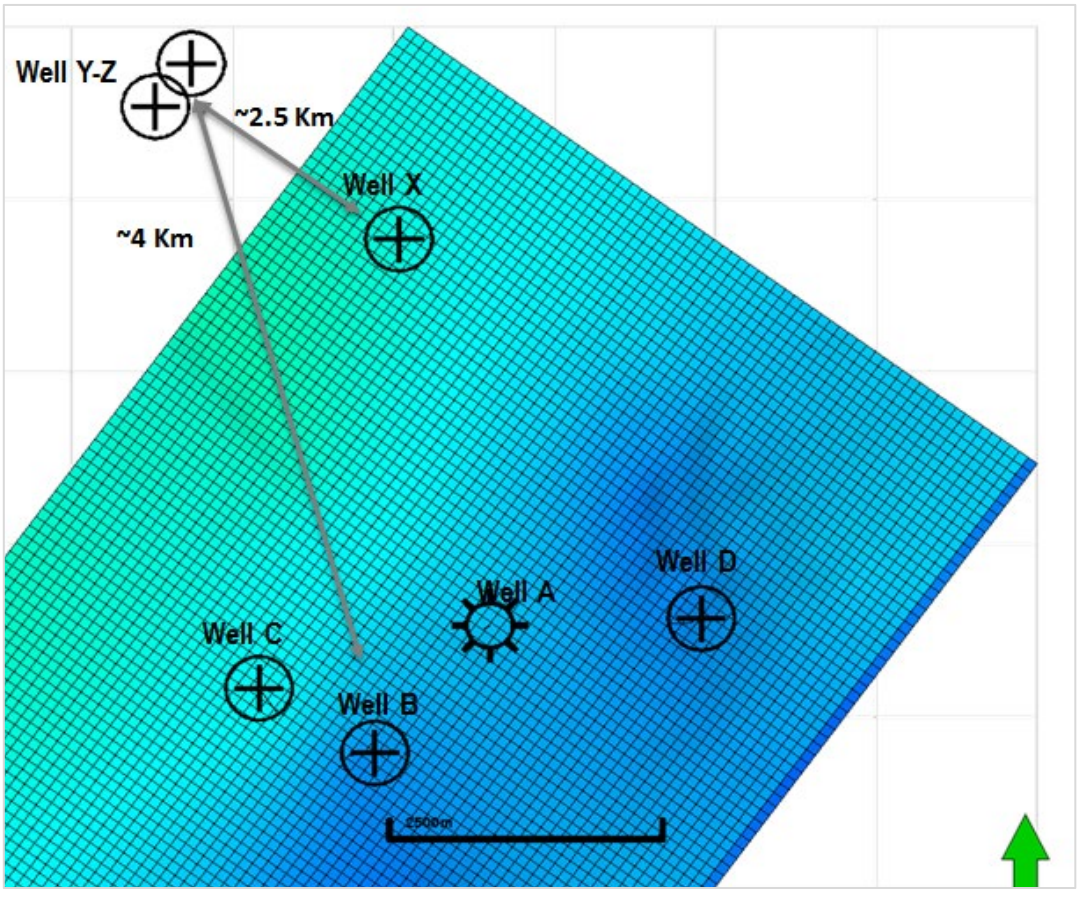

Fig. 129 Well X, Y and Z location. Well X is approximately 4 Km away from the well cluster (wells A-D) and ~2.5Km from wells Y and Z. Wells Y and Z are approximately 6 Km from the well cluster.

Fig. 130 presents a comparison between the extracted pressure profiles at well X location from BPSM and seismic-derived models. Calibration data from the well cluster and wells Y and Z were used to constrain the pressure profile of well X (see Table 2). The pressure trend satisfies calibration data with

minimum deviation up to the top of Porquero D unit. At the corresponding depth of Porquero E, a difference is observed between the BPSM derived pressure and the calibration data, reporting a difference of ≤ 10 MPa and > 10 MPa in the lower units. Such difference may be attributed to local events occurring in the calibration data well. This is an area subject to abnormally high pressures. Nevertheless, the differences in the results indicate that the BPSM approach reproduced the prediction of parameters in an acceptable range to be used in the different operational activities in the reservoir, such as wellbore stability.

The simplified log-based pressure model can be used to discuss some fundamental processes of overpressure generation and compaction; nevertheless, such solutions are less practical since most overpressure distributions are strongly influenced by horizontal fluid flows along highly permeable layers (Hantschel & Kauerauf, 2009). Another relevant aspect is the resolution. While well logs can have high resolution, profiles derived from mechanical models are constrained with the data-mesh resolution relation. This means that, for example in BPSM, the approach may assign constant property behaviour to thick intervals, which may result in higher uncertainty. This exercise helps in the identification of outliers and non-compliant trends across the model.

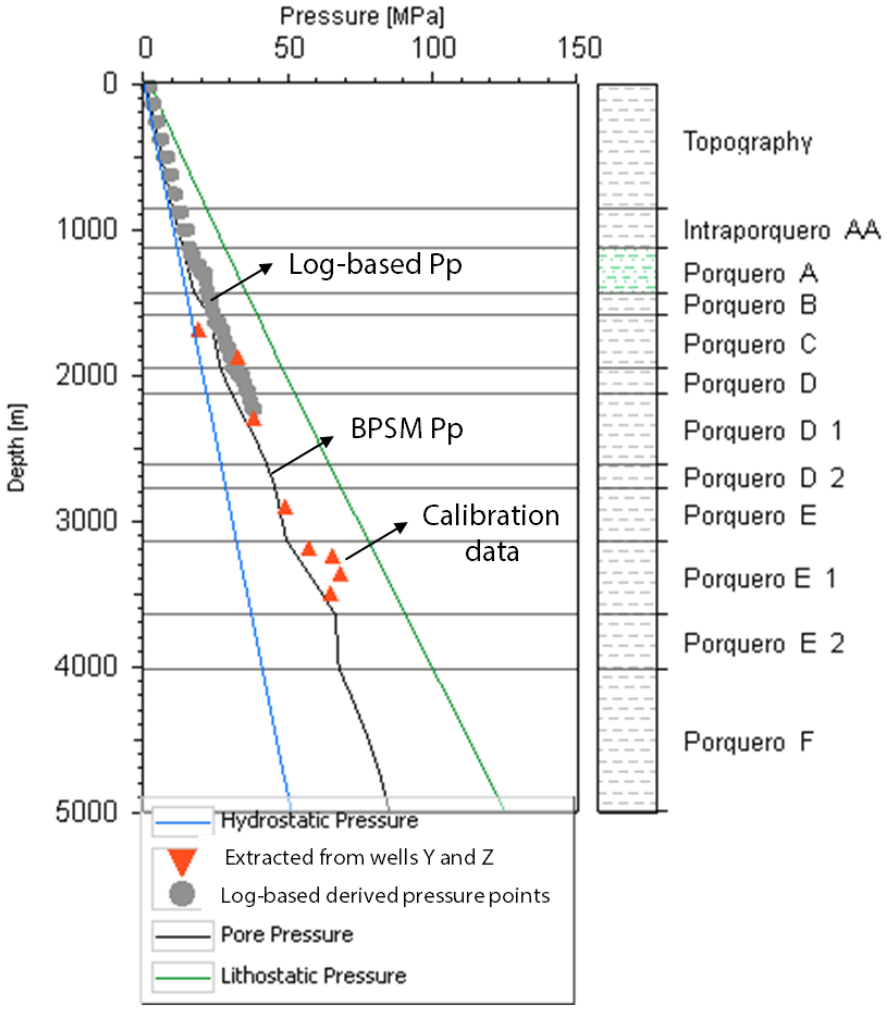

Fig. 130 Pore pressure predictive model for well X from geomechanical integrated approaches: Log-based (grey) and BPSM (black dashed). Blue and green curves correspond to hydrostatic and lithostatic pressures respectively. Calibration data of neighbouring wells was added for reference.

7.5 Limitations on simulations

The main limitation encountered in the construction of the models presented in this work, is related to it the scarcity of data, both for input and calibration. While the methods were developed fully and delivered results in correspondence with the geological trends, the lack of calibration points makes it complex to ensure full reliability in the entire modelled volume. On the contrary, high reliability of the models can be allocated to the target units and especially in the well cluster area (wells A-D).

The sample size of wells within Block A and its distribution across the formations is not consistent, leaving a well cluster on the north-eastern side of the block and a single well in the opposite direction. While from the surface and up to the target formations, the logging record shows a consistent behaviour, none of these wells (wells A-D) reach units E and F. The only well recording data from this point onwards is well E.

Well E sonic record is a simple one (no shear slowness available) and the corresponding shear slowness had to be derived from empirical correlations. This specific property definition on units E and F implies that the uncertainty in this section is high across the units, and the ultimate property results will be possible once further calibration data is gathered. This limitation can also be solved by the planning and drilling of wells in the vicinity of well E, adding up to the existing information to compare and validate the behaviour of the influence area.

Seismic inversion models comprise an independent procedure on their own, with many variables subjected to conditioning, filtering, cleaning and processing to derive lithology-related elastic properties. Overall, the data is suitable and in general correspondence with the geology. However, in detail, there are aspects that condition the results, like resolution or noise problems present in the original reflection survey that remained despite the conditioning. On top of that, the internal calibration was performed using wells A and B as references; therefore, the quality of the inversion and corresponding reliability is higher in the influence areas of those wells, and the well cluster zone. The area in the vicinity of well E holds high uncertainty due to the lack of dipole sonic-shear slowness data and was not included in the seismic inversion calibration.

Rock mechanical testing available for this study comprised only three measure points distributed along the target units Porquero C and D for one well. This information is highly reliable for the area of the well cluster, given the proximity of wells and mild variation of structures. The complex stratigraphy of the region, involving fine layering of sandstones and shales, hinders the common practice of extrapolating the value to an entire unit, and for this reason is strongly encouraged the gathering of more rock mechanical data.

Faults, on the other hand, are structures that heavily condition the pressure distribution across a formation. For this study, a limitation concerning fault structures are related to the description of the filling material, or quantification of the shale gouge ratio (Hantschel & Kauerauf, 2009). The characteristics of the filling sediments can modify the behaviour of fluid flow along and across a sedimentary unit, as well as the pressure development in areas near to faults. A thorough geological description of the sealing capacities of faults will improve the pressure models obtained through basin and petroleum systems approach (BPSM).

Regarding fracture network estimation, this is a process that carries high uncertainty considering the random nature of the fracture occurrence. The models presented in this work intend to shed light in potential approaches to estimate fracture occurrence and orientation in a pre-drilling state, acknowledging the existing uncertainty in the results. Further fracture analysis from image logs in

strategic points of the model would benefit greatly the estimation of potential fracture networks. In the case of the NFP workflow, heterogeneity definition of the mechanical properties would be filling the gap of information for this specific approach. In the case of BPSM, likewise NFP, horizontal resolution of lithologies hinders the possibility of high accuracy mechanical property estimation. However, an advantage of this approach is the ability to record different evolutionary treats in the modelled area.

Chapter 8 Conclusions and perspectives

8.1 Conclusions

Three methodologies were applied for the characterization of the geomechanical parameters in the Oligocene-Miocene tight gas sands reservoirs of the Porquero formation in the study area Block A, within the Plato Sub-basin in the Lower Magdalena Valley Basin (LMVB). A geomechanical workflow applied in this case study is presented targeting *in-situ* stress and natural fracture prediction through the implementation of log-based, seismic driven and basin and petroleum systems modelling technology. The methods were feed with a diverse and relevant dataset that included well logs, field and laboratory data, tectonic evolution and 3D seismic surveys with a correspondent seismic inversion.

Five one-dimension mechanical earth models (1D MEM's) delivered a detailed characterization of the mechanical properties, pore pressure and stress state at existing well locations, whereas a seismic-driven model provided a prognosis of these parameters for the entire Block A field. Calibration of the models ensures that simulation results are in full accordance with the observed parameters presently available. Log-derived pore pressure was constrained with DST measurements, drilling events and drilling mud weight equivalent density, showing a general tendency of hydrostatic to overpressured regimes. Specifically, it displays a hydrostatic pressure regime in units from the top up to Porquero C, and mild to abnormally high pressures in the reservoir area and units below.

The log-based approach is routinely performed in industry depending on the data availability originally at an exploratory stage. The transfer and extrapolation into 3D models make them useful as local calibration points throughout the model construction. An enhancement of this model is achieved by the inclusion of seismic inversion-derived mechanical properties. With this information, local and spatial variations were captured, and the mechanical earth models validated and updated. The log-based mechanical earth models are key elements to assess wellbore stability or drilling-related issues.

It was confirmed that seismic-derived models can capture the general mechanical trends along and across the entire model providing awareness in inter-well and undrilled areas of Block A. Modelling results show that the mechanical characterization and stress prognosis benefits significantly from the integrated property population approach combing seismic-derived and well-derived mechanical parameters. This deterministic model population can better capture mechanical property variations, especially in undrilled areas, in comparison to entirely geostatistical methods (e.g., kriging) for property inter-and extrapolation, respectively. Consequently, the stress prognosis of a 3D MEM populated in such a way will be more reliable. Differences among models can rise to 15% which can dramatically vary completion strategies.

The third and most important methodology was based on the integration between the basin and petroleum system modelling (BPSM) with rock mechanical analysis. The accomplishments of these objectives ensure the best mechanical description of study area. This methodology used the strong geological and geophysical interpretation as input data, and the information of the origin of the basin and most the evolutionary processes and driving mechanism that the basin suffered until present-day. This approach gathers most of the variables and datasets that describe the subsurface, as well as taking advantage of widely used methodologies to refine the results.

It was demonstrated in Block A, that basin and petroleum systems technology can be used to predict porosity-dependent pressure variations on an unconventional play. A significant enhancement on the mechanical property definition comes from the definition of suitable compaction curves for each lithology. Such definition per sedimentary unit leads to the representation of the basin heterogeneity vertically and horizontally. Paleo-geometries were constrained using geological interpretation of paleo water depth and facies maps for each chronological age. Estimated stress orientations were included to recreate the recent LMVB regional tectonic history. Like this, it was possible to highlight that the basin and petroleum systems modelling technique is suitable and convenient given the consistent geomechanical constrains.

Through reproduction of burial history, consideration of porosity-permeability relationships and fault presence, it was possible to associate the results with geologically consistent pressure-formation mechanisms. Critical parameters like porosity and pressure were calibrated at well locations with field-measured data, ensuring that the general regimes were being adjusted to the case study. The calibration process ensured constrained spatial results in undrilled areas and in the entire modelling domain. The validity of the pore pressure calibration was confirmed by a prediction exercise using a randomly generated well. Overpressured zones were later compared with wells surrounding the modelling domain, as well as with log-based derived profiles, confirming the registered trends.

With the use of presented methodologies, it was possible to benchmark the model to registered trends and use it as starting point for the basin and petroleum systems modelling approach. Data management and pre-processing was carried out to ensure the best quality of the information. Extensive description of the geological and tectono-stratigraphic history of the basin is included as a fundamental element of the geomechanical modelling ensuring a stress and geology-consistent simulation. This worked-geomechanical modelling example from northern Colombia illustrates the potential of geomechanical models for the assessment of mechanical properties, pore pressure and *in-situ* stress characterisation.

In-situ stresses

S_{Hmax} was constrained through drilling induced fractures, shear wave splitting analysis and regional stress data and showed a governing WNW-ESE orientation. S_{hmin} magnitude was constrained using hydraulic fracturing closure pressure. It was found that the area is associated with a ruling normal faulting regime. At reservoir depth, vertical stress gradient (S_v) has a mean value of 23.29 MPa/km, and S_{Hmax} is on average $1.2*S_{hmin}$. Pore pressures show a hydrostatic pressure regime in units up to Porquero C and mild to abnormally high pressures in the bottom reservoir interval (Porquero D) and units below (Porquero E and F). By means of the comparison of mechanical properties and calculated stress, it was proven how seismic surveys represent critical input information to characterise the horizontal heterogeneities in inter-well and poorly constrained areas.

Natural fracture modelling

With regards to natural fracture modelling, two modelling approaches were tested. One involving stochastic simulation and paleo stress calculation through stress inversion and the second through forward modelling (derived from the BPSM). Through both approaches a discrete fracture network gas generated for the target unit Porquero C. Moreover, it was possible to closely reproduce the fracture orientation found in wellbore image analysis.

Both of the methods were compared, showing good resemblance among each other, attributed to the mild deformation of the modelling domain. The stress inversion modelling approach does provide a

good approximation as it is a method well suited for low-deformation areas and a dense measured dataset. Nevertheless, the benefits that represent the basin model construction and simulation towards geomechanically constrained fracture prediction are of high relevance, as this modelling endeavour can consistently correlate fracture groups with stresses, its corresponding rotation through geological time and a complete set of variables that describe the temporal mechanical variations.

Wellbore stability

To showcase potential applications of the results and considering the generated mechanical earth model for well A, it was possible to estimate a safe mud weight window for the target units Porquero C and F. A lower bound is given by the breakout pressure of ~15-17 MPa, to avoid breakout generation or risk of kick. The upper bound corresponds to the breakdown pressure of ~35MPa, to avoid fracturing the rock or causing undesired damage. This was performed on the better constrained well. Furthermore, a new well was suggested at a random location and its pressure profile was extracted, which showed a match with selected calibration data. Further work is intended for poorly constrained wells in the area and wells in the vicinity of Block A.

Outlook

The work displayed in this thesis fills in the existing gap of geomechanical characterisation for the selected area within the Lower Magdalena Valley Basin using a forward basin modelling approach for rock stress, pore pressure and mechanical properties characterisation, panning through mainstream methodologies and integrating approaches to achieve the best results possible (Fig. 131).

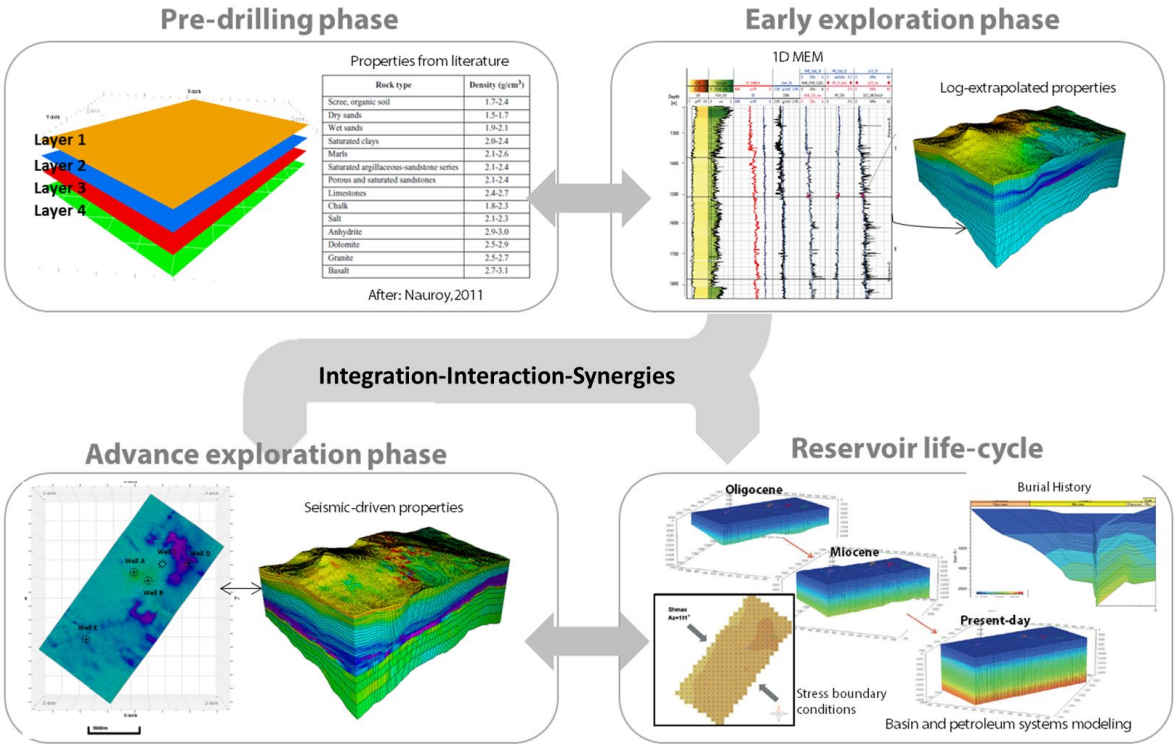

Fig. 131 Geomechanical approaches applied to the Lower Magdalena Valley Basin case study area and allocation of basin and petroleum system modelling approach within the geomechanical modelling catalogue.

The final present-day stress and fracture models of Block A can be used for various aspects during future exploration and possible production stages, like wellbore stability analysis, hydraulic fracture

design, depletion, and subsidence studies, among others. As is the case with any other model, the prediction quality increases with the increasing availability of calibration data, so the models can and should be updated each time new data becomes available in course of the field development. The presented geomechanical models promote the data and discipline integration taking advantage of various datasets to enhance quality of reservoir characterization. The overall research concept is relevant for oil and gas exploration and production. The tools and methodologies implemented represent a great endeavour useful to assess the current state of an area and subsequent implementation in predictive production scenarios.

8.2 Perspectives and further work

The catalogue of models displayed in this work represent base models for further predictive scenarios; being the most relevant those related to hydrocarbon production processes and associated transient deformation. The applications of the models presented in this work can play a key role in the entire life-cycle of a reservoir. The following list just mentions a few applications:

- Wellbore stability assessment: this can be achieved by analysing the hydraulic and mechanical boundaries of the wellbore wall, using the elastic mechanical properties and pore pressure from the log-based approach.

- Anisotropy analysis: Though advanced 3D seismic survey analysis, it can be calculated accurate definition of longitudinal and transverse mechanical properties.

- Migration and geomechanics synergy assessment: This can be accomplished by advancing the study of fluids and fluid flow for the BPSM approach to understand the variations caused by the occurrence, migration and accumulation of hydrocarbons.

- Hydro-mechanical model coupling: The geomechanical models are set to be fully coupled fluid-flow simulations and study the temporal effects of production in the reservoir, for example: compaction and subsidence analysis.

- Well location related to fracture presence: well placement can be enhanced by targeting areas with potentially high fracture occurrence, as these will as act as preferential drainage conduits.

- Fracture pattern estimation and “fracability” of a rock: Geomechanical model associated with petrophysical and brittleness study can add information on how easy or complex it can be to open and sustain a hydraulic fracture, as well as the potential pattern that the fractures may follow.

Systematic calibration through the model’s construction ensures that these are reliable and of the best quality considering the data and resources available. However, in order to move forward in this research line, data improvement and enhanced methodologies will help overcoming the current model limitations and exploit the existing dataset.

The overall geomechanical modelling approach using either methodology would benefit from the addition of further well and core data. Specifically, deeper wells that reach to the Ciénaga de Oro formation would add calibration information for Porquero E and F units, which current mechanical state and pore pressure is highly uncertain. Several cores per unit and associated laboratory testing, as possible, would increase the certainty of the log-derived mechanical properties and the conversion of dynamic-to-static properties, necessary to populate the models. Regarding the type of well data

required to improve the models, image logs for target units would represent an additional source to constrain minimum and maximum horizontal stress, as well as shedding light in further natural and induced fractures or breakouts information.

Pore pressure models developed in this study comprise the main method to obtain a 3D pore pressure distribution, which is from acoustic models (sonic logs). Nevertheless, a great improvement to the modelled pressure would come from the use of 3D seismic survey to derive a pressure volume, a process known as seismic-to-pore pressure (Dutta, 1997; Sayers et al., 2002). In addition to well data and seismic inversion methods, this would represent the highest quality pressure model. Biot coefficient heterogeneity can be honoured through seismic inversion and rock physics methodologies as presented in Cho et al. (2016).

Stress prediction in the overburden section of the model (e.g., for borehole stability issues) and an enhance sideburden mechanical description, would benefit from further rock mechanical lab tests and stress measurements. The same holds for better constraints on the boundary conditions. Thus, tectonic strains for the poro-elastic stress model would benefit from GPS measurements (Liu et al., 2017) and extended tectonic analysis in the area for better representation of the far-field stress field.

Through this work, it was presented how mechanical properties distribution improves when taking advantage of seismic data, but also how a basin modelling approach represents the actual tectono-stratigraphic evolution processes that lead to present-day condition. One of the complexities of the approach lies on the interpretation of mechanical properties from different types of maps, as it strongly depends on the subjectivity of geological interpretation. A way to move a step forwards in the property definition would be an inclusion of seismic data into the characterisation workflow of basin modelling, i.e.: a 3D seismic-driven basin model (Prisco et al., 2015; Szydlik et al., 2015). Like this, inter-well areas would be properly constrained in present-day state and serve as additional constraint for the parameters and transient conditions development. This would capture even better the heterogeneities in broad and detailed scale for any area of the model. However, this is often an approach that requires extensive cross-discipline interaction and repeated feedback loops that would derive in longer model generation.

References

Afsari, M., Amani, M., Razmgir, S., Karimi, H., & Yousefi, S. (2010). Using Drilling and Logging Data for Developing 1D Mechanical Earth Model for a Mature Oil Field to Predict and Mitigate Wellbore Stability Challenges (SPE 132187). *Proceedings of SPE Unconventional Gas Conference*, 1–12.

Aki, K., & Richards, P. (2002). Quantitative seismology. In J. Ellis (Ed.) (pp. 123–192). California: University Science Books. https://doi.org/10.1016/S0065-230X(09)04001-9

Al-Hajeri, M., Al Saeed, M., Derks, J., Fuchs, T., Hantschel, T., Kauerauf, A., … Wygrala, B. (2009). Basin and petroleum systems modelling. *Oilfield Review*, *21*(2), 14–29.

Allen, P., & Allen, J. (2013). Basin Analysis: Principles and applications to petroleum play assessment (Vol. 53, pp. 326–339). https://doi.org/10.1017/CBO9781107415324.004

Anastasopoulos, I., Gelagoti, F., Kourkoulis, R., & Gazetas, G. (2011). Simplified Constitutive Model for Simulation of Cyclic Response of Shallow Foundations: Validation against Laboratory Tests. *Journal of Geotechnical and Geoenvironmental Engineering*, *137*(12), 1154–1168. https://doi.org/10.1061/(ASCE)GT.1943-5606.0000534

Antes, H. (2010). Lecture notes: A Short Course on Boundary Element Methods (pp. 1–25). Institut fuer Angewandte Mechanik, Technische Universität Braunschweig.

Archer, S., & Rasouli, V. (2012). A log-based analysis to estimate mechanical properties and in-situ stresses in a shale gas well in the Northern Perth Basin. *WIT Transactions on Engineering Sciences*, *80*, 163–174. https://doi.org/10.2495/PMR120151

Arminio, J., Talukdar, S., Castillo, L., Vega, R., Ruiz, D., Azuaje, V., … Betancourt, J. G. (2016). Petroleum Geology and Exploration of the Guama Field, Lower Magdalena Basin. In *ACGGP Technical Committee* (p. 23).

Arminio, J., Yoris, F., Porras, L., Garcia, E., & Di Luca, M. (2011). Geology and hydrocarbon potential: Lower Magdalena Basin. In F. Cediel (Ed.), *Petroleum geology of Colombia* (Fondo Edit, Vol. 10, pp. 23–189). Medellin: Fondo Editorial Universidad EAFIT.

Aruffo, C. (2014). *Geomechanical characterization of the CO2CRC Otway Project site, Australia*. Technische Universität Darmstadt.

Asquith, G., Krygowski, D., Henderson, S., & Hurley, N. (2004). Basic relationships of well log interpretation. In *Basic Well Log Analysis* (pp. 1–10). Tulsa, Oklahoma: American Association of Petroleum Geologist.

ASTM International. Laboratory Determination of Pulse Velocities and Ultrasonic Elastic Constants of Rock, 14 Designation: D 2845 – 00 § (2000). Retrieved from https://www.astm.org/

ASTM International. ASTM E10-12 Standard Test Method for Brinell Hardness of Metallic Materials (2012). West Conshohocken, PA. https://doi.org/https://doi.org/10.1520/E0010-12

Athy, L. F. (1930). Density, Porosity, and Compaction of Sedimentary Rocks. *AAPG Bulletin*, *14*(1), 194–200. https://doi.org/10.1306/3D93289E-16B1-11D7-8645000102C1865D

Ávila-carrera, R., Spurlin, J., & Valle-molina, C. (2011). Simulating elastic wave propagation in boreholes : Fundamentals of seismic response and quantitative interpretation of well log data. *Geofísica Internacional*, *50*(1), 57–76.

Avseth, P., Mukerji, T., & Mavko, G. (2008). Introduction to rock physics. In *Quantitative Seismic Interpretation: Applying Rock Physics Tools to Reduce Interpretation Risk* (pp. 24–29). Cambridge University Press.

Azadpour, M., & Manaman, N. S. (2015). Determination of Pore Pressure from Sonic Log : a Case Study on

One of Iran Carbonate Reservoir Rocks, *4*(3), 37–50.

Bacon, M., Simm, R., & Redshaw, T. (2012). 3D Seismic Interpretation (pp. 57–118). Cambridge University Press.

Baker Hughes. (1993). Origins of Abnormal Pressure. In *Formation Pressure Evaluation. Reference guide* (pp. 46–205). Houston, TX.

Baker Hughes. (1996). Wellsite Geology. Reference Guide (pp. 1-11 (Ch.11)). Houston, TX.

Balzarini, M., Nicula, S., Mattiello, D., & Aliverti, E. (2001). Quantification and description of fracture network by MRI image analysis. *Magnetic Resonance Imaging*, *19*, 539–541.

Barclay, F., Bruun, A., Rasmussen, K. B., Alfaro, J. C., Cooke, A., Cooke, D., … Roberts, R. (2007). Seismic Inversion : Reading Between the Lines. *Oilfield Review*, *20*(1), 42–63.

Barnichon, J. D. (1998). Finite Element Modelling in Structural and Petroleum Geology (pp. 24–41). Université de Liège.

Bassiouni, Z. (1994). Theory,Measurement,and Interpretation of Well Logs Volumen 4 (pp. 1–79, 92–202). Society of Petroleum Engineers Inc.

Basu, A., & Aydin, A. (2006). Evaluation of Ultrasonic Testing in Rock Material Characterization. *Geotechnical Testing Journal*, *29*(2), 1–9. https://doi.org/10.1520/GTJ12652

Berard, T., Desroches, J., Yang, Y., Weng, X., & Olson, K. E. (2015). High-Resolution 3D Structural Geomechanics Modelling for Hydraulic Fracturing. *Society of Petroleum Engineers*, 1–23. https://doi.org/10.2118/173362-MS

Bernal-Olaya, R., Mann, P., & Escalona, A. (2015). Cenozoic Tectonostratigraphic Evolution of the Lower Magdalena Basin, Colombia: An Example of an Under- to Overfilled Forearc Basin. *Petroleum Geology and Potential of the Colombian Caribbean Margin*, *Memoir 108*(January 2016), 135–398. https://doi.org/10.1306/13531943M1083645

Betancourt, J., Arminio, J., García, E., & Yoris, F. (2016). Modelo petrofísico integrado: Herramienta clave para la detección de yacimientos de gas condensado en capas delgadas y de baja permeabilidad - Cuenca del Valle inferior del Magdalena, Colombia. *Ingeniería Petrolera*, *56*(5), 256–276.

Bhinde, T., & Todman, S. (2016). The Effects and Modelling of Stress in Hydraulically Fractured Tight Reservoirs. In *Abu Dhabi International Petroleum Exhibition & Conference* (pp. 1–19).

Biot, M., & Willis, D. (1957). The elastic coefficients of the theory of consolidation. *Journal of Applied Mechanics*, 594–601. https://doi.org/10.1002/9780470172766.ch13

Bosch, M., Mukerji, T., & Gonzalez, E. F. (2010). Seismic inversion for reservoir properties combining statistical rock physics and geostatistics: A review. *Geophysics*, *75*(5), 165–176. https://doi.org/10.1190/1.3478209

Bourne, S. J., Brauckmann, F., Rijkels, L., Stephenson, B. J., Weber, A., & Willemse, E. J. M. (2000). Predictive modelling of naturally fractured reservoirs using geomechanics and flow simulation. In *9th Abu Dhabi International Petroleum Exhibition and Conference*. https://doi.org/10.2118/87253-MS

Bourne, S. J., & Willemse, E. J. M. (2001). Elastic stress control on the pattern of tensile fracturing around a small fault network at Nash Point, UK. *Journal of Structural Geology*, *23*(11), 1753–1770. https://doi.org/10.1016/S0191-8141(01)00027-X

Bowers, G. (1995). Pore Pressure Estimation From Velocity Data: Accounting for Overpressure Mechanisms Besides Undercompaction. *International Journal of Rock Mechanics and Mining Science & Geomechanics Abstracts*, *10*(02), 89–95. https://doi.org/10.2118/27488-PA

Bradford, I. D. R., Fuller, J., Thompson, P. J., & Walsgrove, T. . R. (1998). Benefits of assessing the solids production risk in a North Sea reservoir using elastoplastic modelling (SPE/ISRM 47360). In *SPE/ISRM Eurorock '98* (pp. 261–269). https://doi.org/10.2118/47360-MS

Brady, B., & Brown, E. (2005). Rock mechanics for underground mining (pp. 1–195). https://doi.org/10.1007/BF01238443

Briceno, R. (2013). *Evaluacion del gradiente geotérmico y flujos de calor en la cuenca Valle Inferior del Magdalena, Colombia*. Universidad de oriente.

Caro, M., & Spratt, D. (2003). Tectonic Evolution of the Jacinto Fold Belt, NW Colombia. *Recorder*, *28*(02), 36–43.

Chapra, S. C., & Canale, R. P. (2015). Numerical Methods for Engineers (pp. 873–912). McGraw-Hill Science/Engineering/Math.

Cheng, A. (2016). *Poroelasticity*. *Theory and Applications of Transport in Porous Media* (Vol. 27). https://doi.org/10.1007/978-3-319-25202-5

Cheung, P., Hayman, A., Laronga, R., Cook, G., Flournoy, G., Goetz, P., … Redden, J. (1994). Imágenes claras en lodos base aceite. *Oilfield Review*, (1986), 2–27.

Chilingarian, G. V., Serebryakov, V., & Robertson, J. O. (2002). Origin and prediction of abnormal formation pressures (pp. 24–42).

Christiansson, R., & Hudson, J. a. (2003). ISRM Suggested Methods for rock stress estimation—Part 4: Quality control of rock stress estimation. *International Journal of Rock Mechanics and Mining Sciences*, *40*(7–8), 999–1010. https://doi.org/10.1016/j.ijrmms.2003.07.012

Colmenares, L., & Zoback, M. (2003). Stress field and seismotectonics of northern South America. *Geology*, *31*(8), 721–724. https://doi.org/10.1130/G19409.1

Cook, R. D. (1995). Finite element Modeling for Stress Analysis (pp. 2–18).

Crouch, S. (1976). Solution of Plane Elasticity Problems by Displacement Discontinuity Method. *International Journal of Numerical Methods in Engineering*, *10*, 301–343.

Crouch, S., & Starfield, A. (1983). Boundary Element Method in Solid Mechanics with Application in Rock Mechanics and Geological Mechanics, (pp. 1–43). London.

Dahm, T., Hainzl, S., & Becker, D. (2010). How to discriminate induced , triggered and natural seismicity. *Proceedings of the Workshop Induced Seismicity*, 69–76.

De Gennaro, V., Amri, R., Brignoli, M., Kallel, N., Wielemaker, E., & El Ayeb, S. (2014). Integrated Unconventional Gas Evaluation Workflow: From Anisotropic Geomechanical Modeling To Completion Design. *SPE/EAGE European Unconventional Resources Conference and Exhibition*, (Figure 1), 1–16. https://doi.org/10.1017/CBO9781107415324.004

Dembicki, H. (2016). Basin Modeling. In *Practical Petroleum Geochemistry for Exploration and Production* (pp. 273–308). https://doi.org/10.1016/b978-0-12-803350-0.00008-8

Dershowitz, W., & Herda, H. (1992). Interpretation of fracture spacing and intensity. *Rock Mechanics*, 757–766.

Dershowitz, W. S., Pointe, P. R. La, & Doe, T. W. (2004). Discrete Fracture Network Modeling: Current Status and Future Trends.

Detournay, E., & Cheng, A. (1993). Fundamentals of Poroelasticity. *Comprehensive Rock Engineering: Principles, Practice and Projects*, *II*, 113–171. https://doi.org/10.1016/0148-9062(94)90606-8

Di Luca, M. (2016). Caracterización Geofísica de Yacimientos Heterogéneos de la Formación Porquero : Área Piloto Bloque A , Cuenca del Valle Inferior, pp. 5–34.

Di Luca, M., Salinas, T., Arminio, J. F., Alvarez, G., Alvarez, P., Bolivar, F., & Marín, W. (2014). Seismic inversion and AVO analysis applied to predictive-modeling gas-condensate sands for exploration and early production in the Lower Magdalena Basin, Colombia. *Leading Edge*, *33*(7), 936–943. https://doi.org/10.1190/tle33070746.1

Doornhof, D., Kristiansen, T., Nagel, N. B., Pattillo, P. D., & Sayers, C. (2006). Pressure drawdown in a producing field can lead to reservoir compaction , movement. *Oilfield Review*, *Autumn*, 50–68.

Duque-Caro, H. (1979). Major Structural Elements and Evolution of Northwestern Colombia: Small Basin Margins, *109*, 329–351. Retrieved from http://archives.datapages.com/data/specpubs/history2/data/a109/a109/0001/0300/0329.htm

Dutta, N. (1997). Pressure prediction from seismic data: implications for seal distribution and hydrocarbon exploration and exploitation in the deepwater Gulf Of Mexico. *Norwegian Petroleum Society Special Publications*, *7*(C), 187–199. https://doi.org/10.1016/S0928-8937(97)80016-1

Dutta, N. (2002). Geopressure Detection Using Reflection Seismic Data and Rock Physics Principles: Methodology and Case Histories From Deepwater Tertiary Clastics Basins. In *Proceedings of the 2002 SPE Asia Pacific Oil and Gas Conference and Exhibition*. Melbourne, Australia. https://doi.org/10.2523/77820-MS

Dutta, N. (2016). *Lecture II- Rock physics and geopressure*. Lecture notes.

Eaton, B. A. (1975). The Equation for Geopressure Prediction from Well Logs. *Fall Meeting of the Society of Petroleum Engineers of AIME*, 11. https://doi.org/10.2118/5544-MS

Evans, K., Zappone, A., Kraft, T., Deichmann, N., & Moia, F. (2012). A survey of the induced seismic responses to fluid injection in geothermal and CO2 reservoirs in Europe. *Geothermics*, *41*, 30–54. https://doi.org/10.1016/j.geothermics.2011.08.002

Fadipe, O. A., Bouhlel, A., & Noufal, A. (2016). Basin Scale Geomechanical Modeling of Tight Carbonate Reservoir in Abu Dhabi : Implications on Pore Pressure Development Geological Setting of Abu Dhabi Onshore Area. In *Abu Dhabi International Petroleum Exhibition & Conference held*. Abu Dhabi.

Fattahpour, V., Pirayehgar, A., Dusseault, M. B., & Mehrgini, B. (2012). Building a mechanical earth model: A reservoir in southwest Iran. *46th US Rock Mechanics / Geomechanics Symposium 2012*, *4*.

Fatti, J. (1994). Detection of gas in sandstone reservoirs using AVO analysis: A 3-D seismic case history using the Geostack technique. *Geophysics*, *59*(9), 1362. https://doi.org/10.1190/1.1443695

Fernández, A., & Alvarellos, J. (2011). Modelos geomecánicos 3D y su creciente aplicación en la industria petrolera. *Revista Internacional de Desastres Naturales, Accidentes e Infraestructura Civil*, *12*(1), 151–157.

Fertl, W. H. (1976). Developments in petroleum science 2 : Abnormal formation pressures (pp. 1–289). Houston, Texas: Elsevier Scientific Publishing Company.

Filippova, K., Kozhemkov, A., & Alabushin, A. (2011). Seismic Inversion Technique: choice and benefits. *First Break*, *29*(May), 103–114.

Finkbeiner, T., Barton, C., & Zoback, M. (1997). Relationships Among In-Situ Stress, Fractures and Faults, and Fluid Flow: Monterey Formation, Santa Maria Basin, California. *AAPG Bulletin*, *81*(12), 1975–1999. https://doi.org/10.1306/3B05C6FE-172A-11D7-8645000102C1865D

Fischer, K. (2013). Geomechanical reservoir modeling – workflow and case study from the North German Basin, pp. 47–74. Retrieved from url: http://tuprints.ulb.tu-darmstadt.de/id/eprint/3647

Fischer, K., & Henk, A. (2013). A workflow for building and calibrating 3-D geomechanical models-A case study for a gas reservoir in the North German Basin. *Solid Earth*, *4*(2), 347–355. https://doi.org/10.5194/se-4-347-2013

Fisher, R. (1953). Dispersion on a sphere. In *Proc. Royal Society London* (pp. 295–305).

Fjaer, E., Holt, R. M., Horsrud, P., Raaen, A. M., & Risnes, R. (2008). Petroleum Related Rock Mechanics. In *Developments in Petroleum Science* (Vol. 53, pp. 357–368). Elsevier publications. https://doi.org/10.1016/0148-9062(93)92632-Z

Fleitout, L., & Froidevaux, C. (1982). Tectonics and topography for a lithosphere containing density

heterogeneities. *Tectonics*, *1*(1), 21–56.

Flinch, J. (2003). Structural Evolution of the Sinu- Lower Magdalena Area (Northern Colombia). In *The Circum-Gulf of Mexico and the Caribbean: Hydrocarbon habitats, basin formation, and plate tectonics: AAPG Memoir* (Vol. 79, pp. 776–796).

Flinch, J., Amaral, J., Doulcet, A., Mouly, B., Osorio, C., & Pince, J. M. (2003). Structure of the Offshore Sinu Accretionary Wedge . Northern Colombia. *VIII Simposio Bolivariano de Cuencas Subandinas*, 76–83.

Fossen, H. (2010). Structural Geology. In *Structural Geology* (Vol. 1, pp. 1–359). Cambridge University Press. https://doi.org/10.1017/CBO9781107415324.004

Fox, A., Snelling, P., McKenna, J., Neale, C., Neuhaus, C., & Miskimmins, J. (2013). Geomechanical Principles for Unconventional Reservoirs, pp. 1–25.

Franquet, J., Stewart, G., Bolle, L., & Ong, S. (2005). Log-Based Geomechanical Characterization and Sanding Potential Analysis\non Several Wells Drilled in Southern Part of Oman. *Proceedings of SPE/PAPG Annual Technical Conference*, 1–10. https://doi.org/10.2523/111044-MS

Fredrich, J. T., Arguello, J. G., Thorne, B. J., Wawersik, W. R., Deitrick, G. L., de Rouffignac, E. P., … Bruno, M. S. (1997). Three-dimensional geomechanical simulation of reservoir compaction and implications for well failures in the Beldridge diatomite. *Proceedings - SPE Annual Western Regional Meeting*, 13–28. https://doi.org/10.2118/36698-ms

Frischbutter, A., & Henk, A. (2010). Predicting Stress and Fracture Orientations with Geomechanical Reservoir Models - Lessons Learned from a Case Study. In *AAPG Convention* (pp. 8–11).

Garcia-teijeiro, X., & Rodriguez-herrera, A. (2014). Dependence of Stress-induced Micro-seismicity on Natural Fracture Properties and In-situ Stress. In *SPE/CSUR Unconventional Resources Conference* (pp. 1–12). https://doi.org/10.2118/171632-MS

Gardner, G. H. ., Gardner, L. W., & Gregory, A. R. (1974). Formation velocity and density - The diagnostic basics for stratigraphic traps. *Geophysics*, *39*(6), 770–780.

Geertsma, J. (1973). Land subsidence above compacting oil and gas reservoirs. *Journal of Petroleum Technology*, *26*(06), 734–744.

Giroldi, L., Wallick, B., Rodriguez-Herrera, A., Koutsabeloulis, N., & Lowden, D. (2014). Applications of broadband seismic inversion in the assessment of drilling and completion strategies : A case study from eastern Saudi Arabia. In *SEG Denver 2014 Annual Meeting* (pp. 3153–3156). https://doi.org/DOI http://dx.doi.org/10.1190/segam2014-1358.1

Gluyas, J., & Swarbrick, R. (2004). Petroleum Geosciences (pp. 1–79). Blackwell Science Ltd.

Golf-Racht, T. D. (1982). Fundamentals of fractured reservoir engineering (pp. 66–68). Elsevie Scientific Publishing Company.

Goodman, R. E. (1989). Introduction to Rock Mechanics (pp. 55–87). Canada: John Wiley and Sons inc.

Goovaerts, P. (1997). Geostatistics for natural resources evaluation. In *Applied Geostatistics Series* (pp. 125–181). New York.

Gray, D., Anderson, P., Logel, J., Delbecq, F., Schmidt, D., & Schmid, R. (2012). Estimation of stress and geomechanical properties using 3D seismic data. *First Break*, *30*(3), 59–68.

Grover, A., Muhairi, L. Al, Al-shabibi, T. A., Madhi, A. El, & Dhabi, A. (2016). Integration of 3D Seismic , Structural Geology and Geomechanics to Model Naturally Fractured Reservoir A Case Study in Carbonate Reservoirs , UAE . In *Abu Dhabi International Petroleum Exhibition & Conference* (pp. 1–14). Abu Dhabi, UAE: Society of Petroleum Engineers.

Gudmundsson, A. (2011). Rock Fractures in Geological Processes (pp. 190–231). https://doi.org/10.1017/CBO9780511975684

Gutierrez, M., & Youn, D. (2015). Effects of fracture distribution and length scale on the equivalent continuum elastic compliance of fractured rock masses. *Journal of Rock Mechanics and Geotechnical Engineering*, *7*(6), 626–637. https://doi.org/10.1016/j.jrmge.2015.07.006

Haimson, B. C., & Cornet, F. H. (2003). ISRM suggested methods for rock stress estimation-part 3: Hydraulic fracturing (HF) and/or hydraulic testing of pre-existing fractures (HTPF). *International Journal of Rock Mechanics and Mining Sciences*, *40*, 1011–1020. https://doi.org/10.1016/j.ijrmms.2003.08.002

Hamid, O., Hall-thompson, B., Omair, A., Aramco, S., Ahmed, S., & Ahmed, M. (2016). Geomechanics on a Horizontal Well. In Society of Petroleum Engineers (Ed.), *Abu Dhabi International Petroleum Exhibition & Conference* (pp. 1–9). Abu Dhabi, UAE.

Hantschel, T., & Kauerauf, A. I. (2009). Fundamentals of basin and petroleum systems modeling. In *Fundamentals of Basin and Petroleum Systems Modeling* (pp. 1–476). Springer. https://doi.org/10.1007/978-3-540-72318-9

Hantschel, T., Wygrala, B., Fuecker, M., & Neber, A. (2012). Modeling Basin-scale Geomechanics Through Geological Time. In *International Petroleum Technology Conference*. Bangkok, Thailand. https://doi.org/10.2523/15286-MS

Heidbach, O, Hergert, T., Reiter, K., Giger, S., & Marschall, P. (2015). 3D stress field sensitivity analysis on the scale of geological siting regions in Northern Switzerland with focus on Opalinus Clay. In *Clays in natural and engineered barriers for radioactive waste confinement. 6th international conference* (pp. 110–111). Brussels. https://doi.org/10.1016/j.tecto.2009.07.023.Heidbach

Heidbach, Oliver, Rajabi, M., Reiter, K., & Ziegler, M. (2016). *World Stress Map Database Release 2016*. GFZ Data Services. https://doi.org/http://doi.org/10.5880/WSM.2016.001

Henk, A. (2008). Perspectives of geomechanical reservoir models-why stress is important. *Oil Gas-European Magazine*, *4*(July), 20–24.

Henk, A., & Nemčok, M. (2008). Stress and fracture prediction in inverted half-graben structures. *Journal of Structural Geology*, *30*(1), 81–97. https://doi.org/10.1016/j.jsg.2007.10.006

Herwanger, J., & Koutsabeloulis, N. (2011). Seismic Geomechanics: How to Build and Calibrate Geomechanical Models Using 3D and 4D Seismic Data (pp. 6–90). EAGE, 2011.

Hoedeman, G. (2015). Multi-scale Geomechanics : How Much Model Complexity is Enough ? In *Abu Dhabi International Petroleum Exhibition and Conference* (pp. 9–12).

Hoek, E., & Martin, C. D. (2014). Fracture initiation and propagation in intact rock - A review. *Journal of Rock Mechanics and Geotechnical Engineering*, *6*(4), 287–300. https://doi.org/10.1016/j.jrmge.2014.06.001

Hudson, J., Cornet, F. H., & Christiansson, R. (2003). ISRM suggested methods for rock stress estimation-part 1: Strategy for rock stress estimation. *International Journal of Rock Mechanics and Mining Sciences*, *40*, 991–998. https://doi.org/10.1016/j.ijrmms.2003.07.011

Hudson, J., & Harrison, J. (1997). Engineering rock mechanics: An introduction to principles (pp. 31–228). Great Britain: Elsevier science.

Iverson, W. P. (1992). Fracture Identification From Well Logs. *Proceedings of SPE Rocky Mountain Regional Meeting*, (24351), 359–367. https://doi.org/10.2118/24351-MS

Jaeger, J. C., Cook, N. G. W., & Zimmerman, R. W. (2007). Fundamental of Rock Mechanics (pp. 9–197). Blackwell Publishing. https://doi.org/10.1017/CBO9781107415324.004

Jing, L. (2003). A review of techniques, advances and outstanding issues in numerical modelling for rock mechanics and rock engineering. *International Journal of Rock Mechanics and Mining Sciences*, *40*(3), 283–353. https://doi.org/10.1016/S1365-1609(03)00013-3

Jing, L., & Hudson, J. A. (2002). Numerical methods in rock mechanics. *International Journal of Rock Mechanics and Mining Sciences*, *39*(4), 409–427. https://doi.org/10.1016/S1365-1609(02)00065-5

Jing, L., & Stephansson, O. (1995). Discrete fracture network (DFN) method. In *Developments in Geotechnical Engineering* (pp. 365–398).

Kesarwani, A., Malhotra, A., & Agarwal, V. (2013). Pore Pressure : Causes , Methods of Determination and their Limitations. *10Th Biennial International Conference and Exposition*, (117), 3–5.

Kolo, I., Abu Al-Rub, R., Sousa, R., Sassi, M., & Sirat, M. (2015). Numerical modelling of fold-related fractures. In *13th International Congress of Rock Mechanics* (pp. 1–10).

Koutsabeloulis, N., & Zhang, X. (2009). 3D Reservoir Geomechanical Modeling in Oil/Gas Field Production. *SPE Saudi Arabia Section Technical Symposium*. https://doi.org/10.2118/126095-ms

Kroehler, M. E., Mann, P., Escalona, A., & Christeson, G. L. (2011). Late Cretaceous-Miocene diachronous onset of back thrusting along the South Caribbean deformed belt and its importance for understanding processes of arc collision and crustal growth. *Tectonics*, *30*(6), 1–31. https://doi.org/10.1029/2011TC002918

Kumar, B., Niwas, S., & Mangaraj, B. (2012). Pore Pressure Prediction from Well Logs and Seismic Data. In *9th Biennial international Conference and exposition on Petroleum Geophysics* (pp. 1–7).

Lancellotta, R. (2009). Geotechnical Engineering (pp. 142–201). https://doi.org/624.151–dc22

Lefranc, M., Hussein, A., Tan, C. P., Legrand, X., Lee, B. C., Maerten, L., … Anis, L. (2014). *3D Structural restoration and Geomechanical Forward Modeling in a visco-plastic medium to natural fracture prediction in a Malay producing field, offshore Malaysia*. *Offshore Technology Conference-Asia*. https://doi.org/10.4043/24753-MS

Legarth, B., Huenges, E., & Zimmermann, G. (2005). Hydraulic fracturing in a sedimentary geothermal reservoir: Results and implications. *International Journal of Rock Mechanics and Mining Sciences*, *42*(7-8 SPEC. ISS.), 1028–1041. https://doi.org/10.1016/j.ijrmms.2005.05.014

Legrand, X., Joonnekindt, J. P., Lee, B. C., Lefranc, M., Maerten, L., & Anis, L. (2013). Innovative Natural Fracture Prediction using a geomechanically-based solution: Application to the Malay Basin (Malaysia). In *Second EAGE Workshop on Naturally Fractured Reservoirs*. Muscat, Oman.

Lei, Q., Latham, J. P., & Tsang, C. F. (2017). The use of discrete fracture networks for modelling coupled geomechanical and hydrological behaviour of fractured rocks. *Computers and Geotechnics*, *85*, 151–176. https://doi.org/10.1016/j.compgeo.2016.12.024

Li, Q., Xing, H., Liu, J., & Liu, X. (2015). A review on hydraulic fracturing of unconventional reservoir. *Petroleum*, *1*(1), 8–15. https://doi.org/10.1016/j.petlm.2015.03.008

Liu, J., Ding, W., Yang, H., Wang, R., Yin, S., Li, A., & Fu, F. (2017). 3D geomechanical modeling and numerical simulation of in-situ stress fields in shale reservoirs: A case study of the lower Cambrian Niutitang formation in the Cen'gong block, South China. *Tectonophysics*, *712–713*, 663–683. https://doi.org/10.1016/j.tecto.2017.06.030

Lorenz, J. C., & Cooper, S. P. (2017). Anderson's Shear Fracture/Fault Classification. In *Atlas of Natural and Induced Fractures in Core* (pp. 61–64). https://doi.org/10.1002/9781119160014

Lowrie, W. (2007). Fundamentals of geophysics (pp. 168–178). Cambridge University Press. https://doi.org/10.1029/98EO00138

Madatov, A. G., & Sereda, A. (2005). The effective basin model concept and fast 3D overpressure modelling in basin time scale. *Bulletin of the Murmansk State Technical University*, *8*(1), 5–43.

Maerten, F., Maerten, L., & Pollard, D. (2014). IBem3D, a three-dimensional iterative boundary element method using angular dislocations for modeling geologic structures. *Computers and Geosciences*, *72*, 1–17. https://doi.org/10.1016/j.cageo.2014.06.007

Maerten, Frantz. (2010). *Geomechanics to solve geological structure issues: forward, inverse and restoration modeling*. Universite Montpellier II.

Maerten, L., Gillespie, P., & Daniel, J. M. (2006). Three-dimensional geomechanical modeling for constraint of subseismic fault simulation. *AAPG Bulletin*, *90*(9), 1337–1358. https://doi.org/10.1306/03130605148

Maerten, L., & Maerten, F. (2006). Chronologic modeling of faulted and fractured reservoirs using geomechanically based restoration: Technique and industry applications. *AAPG Bulletin*, *90*(8), 1201–1226. https://doi.org/10.1306/02240605116

Maerten, L., Maerten, F., Lejri, M., & Gillespie, P. (2016). Geomechanical paleostress inversion using fracture data. *Journal of Structural Geology*, *89*, 197–213. https://doi.org/10.1016/j.jsg.2016.06.007

Magoon, L., & Beaumont, E. (1999). Treatise of Petroleum Geology, - Chapter 3. In E. Beaumont & H. Foster (Eds.), *Handbook of Petroleum Geology*.

Magoon, L., & Dow, W. (1994). The Petroleum System. In *The petroleum system - From source to trap. AAPG Memoir 60* (pp. 3–24). The American Association of Petroleum Geologists. Retrieved from http://archives.datapages.com/data/specpubs/methodo2/data/a077/a077/0001/0000/0003.htm

Mann, P. (1999). Caribbean sedimentary basins: Classification and tectonic setting from jurassic to present. In *Sedimentary Basins of the World* (Vol. 4, pp. 3–31). https://doi.org/10.1016/S1874-5997(99)80035-5

Mann, Paul, & Escalona, A. (2006). Regional geologic and tectonic setting of the Maracaibo supergiant basin, western Venezuela. *AAPG Bulletin*, *90*(4), 445–477. https://doi.org/10.1306/10110505031

Mann, Paul, & Escalona, A. (2011). Introduction to the special issue of Marine and Petroleum Geology: Tectonics, basinal framework, and petroleum systems of eastern Venezuela, the Leeward Antilles, Trinidad and Tobago, and offshore areas. *Marine and Petroleum Geology*, *28*(1), 4–7. https://doi.org/10.1016/j.marpetgeo.2010.07.003

Mata, O. (2014). Cenozoic structure, stratigraphy and paleography of the Lower Magdalena Basin, Colombia, pp. 28–99. https://doi.org/10.1007/s13398-014-0173-7.2

Mavko, G., Mukerji, T., & Dvorkin, J. (2009). The Rock Physics Handbook (pp. 43–47). https://doi.org/10.1017/CBO9780511626753

Meyer, J. J., & Payne, S. S. (2017). Using seismic inversion to predict geomechanical well behavior : a case study from the Permian Basin. In *GeoConvention 2017* (pp. 1–2). Canada.

Moeck, I., Kwiatek, G., & Zimmermann, G. (2009). Slip tendency analysis, fault reactivation potential and induced seismicity in a deep geothermal reservoir. *Journal of Structural Geology*, *31*(10), 1174–1182. https://doi.org/10.1016/j.jsg.2009.06.012

Mohamad, R., MacGregor, A. L., & Koutsabeloulis, N. (2015). Prediction of Carbonate Reservoirs Pore Pressure and Porosity in Onshore Abu Dhabi Using Petroleum Systems Modeling Technology. *Abu Dhabi International Petroleum Exhibition and Conference Held*. Abu Dhabi. https://doi.org/10.2118/177603-MS

Mora-Páez, H., Peláez-Gaviria, J., Diederix, H., Bohórquez-Orozco, O., Cardona-Piedrahita, L., Corchuelo-Cuervo, Y., … Díaz-Mila, F. (2018). Space Geodesy Infrastructure in Colombia for Geodynamics Research. *Seismological Research Letters*, *89*(2A), 446–451. https://doi.org/10.1785/0220170185

Mora, J. A., Oncken, O., Le, E., Mora, A., Veloza, G., Vélez, V., & Freitas, M. De. (2018). Controls on forearc basin formation and evolution : Insights from Oligocene to Recent tectono-stratigraphy of the Lower Magdalena Valley basin of northwest Colombia. *Marine and Petroleum Geology*, *97*(May), 288–310. https://doi.org/10.1016/j.marpetgeo.2018.06.032

Morales, R. H., & Marcinew, R. P. (1993). Fracturing of High-Permeability Formations: Mechanical Properties Correlations. *SPE Annual Technical Conference and Exhibition*, 467–475. https://doi.org/10.2118/26561-MS

Mosca, F., Djordjevic, O., Hantschel, T., McCarthy, J., Krueger, A., Phelps, D., … MacGregor, A. (2018). Pore pressure prediction while drilling: Three-dimensional earth model in the Gulf of Mexico. *AAPG Bulletin*, *102*(4), 545–547. https://doi.org/10.1306/0605171619617050

Narciso, J., Soares, A., & Costa, M. (2014). Pore Pressure prediction and modeling using seismic velocities. Universidade Técnica de Lisboa.

Nelson, R. A. (2001). Evaluating fractured reservoirs: Introduction. In *Geologic Analysis of Naturally Fractured Reservoirs* (pp. 101–124). https://doi.org/10.1016/B978-088415317-7/50005-1

Nikishov, G. P. (2007). Introduction to the Finite Element Method. In *Lecture notes at University of Aizu* (pp. 7–39). Aizu-Wakamatsu, Japan.

Noufal, A., Sirat, M., Steiner, S., Trubienko, O., Minton, J., Zhang, X., … Herrera, A. (2015). Estimates of In Situ Stress and Faults/Fractures in Carbonate Reservoirs in Onshore Abu Dhabi Using Geomechanical Forward Modeling. *Abu Dhabi International Petroleum Exhibition and Conference*, (January). https://doi.org/10.2118/177520-MS

Noufal, Abdelwahab, Sirat, M., Steiner, S., Trubienko, O., Minton, J., Zhang, X., … Herrera, A. (2015). Estimates of In Situ Stress and Faults/Fractures in Carbonate Reservoirs in Onshore Abu Dhabi Using Geomechanical Forward Modeling. In *Abu Dhabi International Petroleum Exhibition and Conference*. Abu Dhabi, UAE. https://doi.org/10.2118/177520-MS

Nur, A., & Byerlee, J. (1971). An exact effective stress law for elastic deformation of rock with fluids. *Journal of Geophysical Research*, *76*(26), 6414–6419.

O'Sullivan, C. (2011). Particulate discrete element modelling: a geomechanics perspective. In *Applied Geotechnics* (Vol. 4, pp. 1–30).

Orlic, B., Van Wees, J. D., & Van Ejis, R. (2001). Integrated Geomechanical Modelling for Prediction of Subsidence and induced Seismicity due to hydrocarbon extraction. In *Annual Conference of the International Association for Mathematical Geology* (p. 14). Cancún.

Orlic, B., Wassing, B., & Geel, C. (2013). Field scale geomechanical modeling for prediction of fault stability during underground gas storage operations in a depleted gas field in the Netherlands. *47th US Rock Mechanics/Geomechanics Symposium*.

Ouadfeul, S., & Aliouane, L. (2015). Wellbore Stability in Shale Gas Reservoirs , A Case Study fromThe Barnett Shale Wellbore stability - Mechanical stress : Pore pressure estimation using the Eaton's model. In *SPE North Africa Technical Conference and Exhibition*.

Ouellet, A., Berard, T., Desroches, J., Frykman, P., Welsh, P., Minton, J., … Schmidt-Hattenberger, C. (2011). Reservoir geomechanics for assessing containment in CO2 storage: A case study at Ketzin, Germany. *Energy Procedia*, *4*, 3298–3305. https://doi.org/10.1016/j.egypro.2011.02.250

Parent, A. (2012). *Modélisation 3D du système pétrolier du bassin nord-est de la Gaspésie, Québec, Canada*.

Pašić, B., Gaurina-Međimurec, N., & Matanović, D. (2007). Wellbore Instability: Causes and consequences. *Rudarsko-Geološko-Naftni Zbornik*, *19*, 87–98.

Perico, N., & Perico, N. (2014). Caracterización y recurrencia sísmica del Nido de Bucaramanga. In *V Congreso Internacional de Ingeniería Civil, Universidad Santo Tomás Seccional Tunja.* (pp. 1–19).

Perrodon, A. (1992). Petroleum Systems : Models and Applications. *Journal of Petroleum Geology*, *15*(July), 319–325.

Peters, K.E., Schenk, O., Schreier, A., Wygrala, B., & Hantschel, T. (2017). Basin and Petroleum System Modeling. In *Springer Handbook of Petroleum Technology* (Springer, pp. 381–413). Springer International Publishing AG 2017.

Peters, Kenneth E., Kacewicz, M., & Curry, D. J. (2012). An Overview of Basin and Petroleum System Modeling: Definitions and Concepts. *Basin Modeling: New Horizons in Research and Applications*, (4), 1–16. https://doi.org/10.1306/13311426H4139

Pindell, J. L., & Barrett, S. F. (1990). Geological evolution of the Caribbean region. A Plate-tectonic perspective. In *The Geology of North America* (Vol. H, pp. 405–432). https://doi.org/n/a

Plumb, R., Edwards, S., Pidcock, G., Lee, D., & Stacey, B. (2000). The Mechanical Earth Model Concept and Its Application to High-Risk Well Construction Projects. *IADC/SPE Drilling Conference*, 1–13. https://doi.org/10.2118/59128-MS

Prisco, G. De, Thanoon, D., Bachrach, R., Brevik, I., Clark, S. A., Corver, M. P., … Leirfall, O. K. (2015). Geophysical basin modeling : Effective stress, temperature, and pore pressure uncertainty. *Special Section: Earth Model: Effective Interpretation for Conventional and Unconventional Reservoirs*, *3*(3), 27–39. https://doi.org/10.1190/INT-2014-0287.1

Qiu, K., Gonzalez, J., Lalinde, G., Coste, B. J., Naas, A., & Fuller, J. (2008). Geomechanics Enables the Success of Horizontal Well Drilling in Libya: A Case Study. In *IADC/SPE Drilling Conference* (pp. 1–13). Orlando, Florida. https://doi.org/10.2118/111384-MS

Quek, S. S., & Liu, G. R. (2003). Fundamentals of finite element method. In *Finite Element Method: A Practical Course* (pp. 35–65). Singapur.

Ragan, D. M. (2009). *Structural Geology: An Introduction to Geometrical Techniques*. *Geology* (Vol. 22). https://doi.org/10.1017/CBO9780511816109

Rana, D., & Dvorkin, J. (2011). The link between seismic inversion, rock physics and geostatistical simulations in seismic reservoir characterization studies. *The Leading Edge*, (January).

Rees, S. Part One: Introduction to the triaxial testing, 1 www.gdsinstruments.com 1–4 (2013).

Reinecker, J., Tingay, M., & Müller, B. (2003). Borehole breakout analysis from four-arm caliper logs. *World Stress Map Project*, 1–5. Retrieved from http://extra.springer.com/2010/978-1-4020-8443-0/WSM Release 2008/WSM_website/pub/guidelines/WSM_analysis_guideline_breakout_caliper.pdf

Reiter, K., & Heidbach, O. (2014). 3-D geomechanical-numerical model of the contemporary crustal stress state in the Alberta Basin (Canada). *Solid Earth*, *5*(2), 1123–1149. https://doi.org/10.5194/se-5-1123-2014

Reyes Harker, A., Montenegro, G., & Gomez, P. (2000). Evolucion tectonoestratigráfica del Valle Inferior Del Magdalena, Colombia. In *Asociación Colombiana de Geólogos y Geofísicos del Petróleo (ACGGP)* (p. 293).

Reyes Harker, A., Montenegro, M., & Gómez, P. (2004). Tectonoestratigrafía y Evolución Geológica del Valle Inferior del Magdalena. *Boletín de Geología*, *26*(42), 19–38.

Reynolds, S., Mildren, S., Hillis, R., & Meyer, J. (2006). Constraining stress magnitudes using petroleum exploration data in the Cooper-Eromanga Basins, Australia. *Tectonophysics*, *415*(1–4), 123–140. https://doi.org/10.1016/j.tecto.2005.12.005

Ritter, A. N. (2016). Controls on Joint Formation During Glacial Unloading of the Sharon Sandstone At Gorge Metro Park, Akron, Ohio, pp. 2–4. https://doi.org/10.1130/abs/2016ne-272752

Rodriguez-herrera, A., Alford, J., Blyth, M., Tollefsen, E., Crowe, J., Loerto, J., … Höner, R. (2006). Sonic Logging While Drilling—Shear Answers. *Oilfielf Review*, *24*(1), 230.

Russell, B. (2014). Prestack seismic amplitude analysis: An integrated overview. *Interpretation*, *2*(2), SC19–SC36. https://doi.org/10.1190/INT-2013-0122.1

Russell, Brian. (2012). An overview of AVO and inversion. In *9th Biennial international Conference and exposition on Petroleum Geophysics* (pp. 1–5).

Rutqvist, J., Rinaldi, A., Cappa, F., & Moridis, G. (2013). Modeling of fault reactivation and induced seismicity during hydraulic fracturing of shale-gas reservoirs. *Journal of Petroleum Science and Engineering*, *107*, 31–44. https://doi.org/10.1016/j.petrol.2013.04.023

Rutqvist, Jonny, Rinaldi, A. P., Cappa, F., & Moridis, G. J. (2013). Modeling of fault reactivation and induced seismicity during hydraulic fracturing of shale-gas reservoirs. *Journal of Petroleum Science and Engineering*, *107*. https://doi.org/10.1016/j.petrol.2013.04.023

Saikia, K., Ikuku, C. E., & Sarkar, B. C. (2017). An integrated approach to discretized 3D modeling of

geomechanical properties for unconventional mature field appraisal in the western Canadian sedimentary basin. *Journal of Petroleum Exploration and Production Technology*, *8*(2), 1–13. https://doi.org/10.1007/s13202-017-0406-3

Satti, I. A., Ghosh, D., & Yusoff, W. I. (2015). 3D predrill pore pressure prediction using basin modeling approach in a field of Malay Basin. *Asian Journal of Sciences*, *8*, 21–31.

Sayers, C., Johnson, G. M., & Denyer, G. (2002). Predrill pore-pressure prediction using seismic data. *Geophysics*, *67*(4), 1286–1292. https://doi.org/10.1190/1.1500391

Sayers, C. M., & Schutjens, P. M. T. M. (2007). An introduction to reservoir geomechanics. *The Leading Edge*, *26*(5), 597. https://doi.org/10.1190/1.2737100

Schrefler, B. a. (2001). Computer modelling in environmental geomechanics. *Computers and Structures*, *79*, 2209–2223. https://doi.org/10.1016/S0045-7949(01)00076-1

Sengupta, M., Dai, J., Volterrani, S., Dutta, N., Rao, N., Al-Qadeeri, B., & Kidambi, V. (2011). Building a Seismic-driven 3D Geomechanical Model in a Deep Carbonate Reservoir. *SEG Technical Program Expanded Abstracts 2011*, 2069–2073. https://doi.org/10.1190/1.3627616

Singhal, B. B. ., & Gupta, R. P. (1999). Fractures and Discontinuities. In *Applied hydrogeology of fractured rocks* (pp. 487–492). Springer. Retrieved from http://ir.obihiro.ac.jp/dspace/handle/10322/3933

Słota-valim, M., Sowiżdżał, K., & Jedrzejowska-Tyczkowska, H. B. (2016). Seismic Driven 3D Geomechanical Model of Lower Paleozoic Shale Formation (Eastern Europe)-Case Study. In *Proceedings of the 78th EAGE Conference & Exhibition 2016*.

Smart, K. J., Ferrill, D. a., Morris, A. P., & McGinnis, R. N. (2012). Geomechanical modeling of stress and strain evolution during contractional fault-related folding. *Tectonophysics*, *576–577*, 171–196. https://doi.org/10.1016/j.tecto.2012.05.024

Soleymani, H., & Riahi, M. A. (2012). Velocity based pore pressure prediction-A case study at one of the Iranian southwest oil fields. *Journal of Petroleum Science and Engineering*, *94–95*(January 2010), 40–46. https://doi.org/10.1016/j.petrol.2012.06.024

Soroush, H. (2013). Discover a Career in Geomechanics. *The Way Ahead*, *9*(3), 15–17. https://doi.org/https://doi.org/10.2118/0313-015-TWA

Suarez, L. (2009). *Integrated geophysical studies in the Plato sub-basin, Lower Magdalena Basin, Colombia*. Universidad Simon Bolivar.

Swarbrick, R. E., Osborne, M. J., & Yardley, G. S. (2002). Comparision of Overpressure Magnitude Resulting from the Main Generating Mechanisms Generating Mechanisms. In *Pressure regimes in sedimentary basins and their prediction: AAPG Memoir* (Vol. 76, pp. 1–12).

Szydlik, T., Helgesen, H. K., Brevik, I., Prisco, G. De, Clark, S. A., Leirfall, O. K., … Cogan, M. (2015). Geophysical basin modeling : Methodology and application in deepwater Gulf of Mexico. *Special Section : Earth Model : Effective Interpretation for Conventional and Unconventional Reservoirs*, *3*(3), 49–58.

Tavener, E., Flottmann, T., & Brooke-barnett, S. (2017). In situ stress distribution and mechanical stratigraphy in the Bowen and Surat basins, Queensland, Australia. *Geomechanics and Geology*, *458*(1), 17.

Terzaghi, K. (1943). Stress conditions for failure in soils. In *Theoretical soil mechanics* (Vol. 1, pp. 7–26). https://doi.org/10.1680/geot.1964.14.1.1

Thöny, R. (2014). Geomechanical analysis of excavation-induced rock mass behavior of faulted opalinus clay at the Mont Terri underground laboratory (Switzerland), pp. 1–20.

Tingay, M. R. P., Reinecker, J., & Müller, B. (2008). Borehole breakout and drilling-induced fracture analysis from image logs. *World Stress Map Project*, (Guidelines: Image Logs), 8.

Tissot, B. P., & Welte, D. H. (1984). *Petroleum Formation and Occurrence. Second Revised and Enlarged*

Edition (Vol. 66). https://doi.org/10.1029/EO066i037p00643

Tiwari, R. R. (2013). Recognizing Horizontal Stress Orientation for Optimizing Well Placement and Well Completion Jobs. In *10th Biennial International Conference & Exposition*. Kochi. Retrieved from http://spgindia.org/10_biennial_form/P042.pdf

Tixier, M. P., Alger, R. P., & Doh, C. A. (1959). Sonic Logging. *Journal of Petroleum Technology*, *216*, 106–114.

Traugott, M. O., & Heppard, P. D. (1994). Prediction of pore pressure before and after drilling - taking the risk out of drilling overpressured prospects. In *AAPG Hedberg Research Conference Abnormal Pressures in Hydrocarbon Environments* (p. Abstract). Golden Colorado.

Trenkamp, R., Kellogg, J. N., Freymueller, J. T., & Mora, H. P. (2002). Wide plate margin deformation, southern Central America and northwestern South America, CASA GPS observations. *Journal of South American Earth Sciences*, *15*(2), 157–171. https://doi.org/10.1016/S0895-9811(02)00018-4

Vargas, C. A., & Duran, J. P. (2005). State of Strain and Stress in Northwestern of South America. *Earth Science Research Journal*, *9*(1), 43–50.

Vernette, G., Mauffret, a., Bobier, C., Briceno, L., & Gayet, J. (1992). Mud diapirism, fan sedimentation and strike-slip faulting, Caribbean Colombian Margin. *Tectonophysics*, *202*(2–4), 335–349. https://doi.org/10.1016/0040-1951(92)90118-P

Villamil, T. (1999). Campanian-Miocene tectonostratigraphy, depocenter evolution and basin deveploment of Colombia and western of Venezuela. *Palaeogeography, Palaeoclimatology, Palaeoecology*, *153*(1–4), 239–275.

Williams, M. J., Herve, J., Calvez, L., Conners, S., & Xu, W. (2016). Integrated microseismic and geomechanical study in the Barnett Shale Formation. *Geophysics*, *81*(3). https://doi.org/10.1190/geo2015-0077.1

Wygrala, B. P. (1989). *Integrated study of an oil field in the Southern Po Basin, Northern Italy*.

Yale, D. P. (2003). Fault and stress magnitude controls on variations in the orientation of in situ stress. *Geological Society, London, Special Publications*, *209*(1), 55–64. https://doi.org/10.1144/gsl.sp.2003.209.01.06

Yu, Z., & Lerche, I. (1995). Arcuate and growth faults in basin models, with an application to South Louisiana Roll-Over structure. *Mathematical Geology*, *27*(4), 513–547.

Zhang, J. (2011). Pore pressure prediction from well logs: Methods, modifications, and new approaches. *Earth Science Reviews*, *108*(1–2), 50–63. https://doi.org/10.1016/j.earscirev.2011.06.001

Zhang, S., Yin, S., Wang, F., & Zhao, H. (2017). Characterization of In Situ Stress State and Joint Properties from Extended Leak-Off Tests in Fractured Reservoirs. *International Journal of Geomechanics*, *17*(3), 04016074. https://doi.org/10.1061/(ASCE)GM.1943-5622.0000757

Zhao, X. G., Wang, J., Qin, X. H., Cai, M., Su, R., He, J. G., … An, Q. M. (2015). In-situ stress measurements and regional stress field assessment in the Xinjiang candidate area for China's HLW disposal. *Engineering Geology*, *197*(November 2017), 42–56. https://doi.org/10.1016/j.enggeo.2015.08.015

Zoback, M. (2007). Reservoir Geomechanics (pp. 3–445). Cambridge University Press. https://doi.org/10.1017/CBO9780511586477

Zoback, M., Barton, C., Brudy, M., Castillo, D., Finkbeiner, T., Grollimund, B. R., … Wiprut, D. J. (2003). Determination of stress orientation and magnitude in deep wells. *International Journal of Rock Mechanics and Mining Sciences*, *40*(7–8), 1049–1076. https://doi.org/10.1016/j.ijrmms.2003.07.001

Zoback, M., Moos, D., Mastin, L., & Anderson, R. (1985). Well bore breakouts and in situ stress. *Journal of Geophysical Research*, *90*(B7), 5523–5530. https://doi.org/10.1029/JB090iB07p05523

Zoeppritz, K. (1919). Über Erdbebenwellen Part VII b : Über Reflexion und Durchgang seismischer Wellen

durch Unstetigkeitsflächen. *Nachrichten von Der Gesellschaft Der Wissenschaften Zu Göttingen, Mathematisch-Physikalische Klasse*, (1919), 66–84. Retrieved from http://eudml.org/doc/59042

Statement of authorship

I hereby certify that this thesis has been composed by myself and describes my own work unless otherwise acknowledged in the text. All references and verbatim extracts have been quoted and all sources of information have been specifically acknowledged. This thesis has not been accepted in any previous application for a degree.

Hiermit versichere ich, dass ich die vorliegende Arbeit selbstständig und ohne Benutzung anderer als der angegebenen Hilfsmittel angefertigt habe. Stellen, die wörtlich oder sinngemäß aus anderen Schriften entnommen sind, sind als solche kenntlich gemacht. Die Arbeit ist in gleicher oder ähnlicher Form noch nicht als Prüfungsarbeit eingereicht worden.

Darmstadt _____. Signature ,_____

Resume/CV

CLAIRET I. GUERRA G.

Working experience

August 2019
Wintershall DEA
SPEAD graduate engineer

October 2015 – Early 2019
Technische Universität Darmstadt, Germany
Research Assistant

Feb 2017-June 2017
Schlumberger SIS, Geomechanics Centre of Excellence. London United Kingdom
Graduate Intern

June 2016- August 2016
Schlumberger Aachen technology centre. Aachen, Germany.
Graduate Intern

June 2013- December 2013
Baker Hughes Inc.
Graduate Intern

Education

October 2015- Current
Technische Universität Darmstadt, Germany
PhD Candidate in Reservoir Geomechanics.

January 2014 – July 2015
Pontificia Universidad Javeriana
Master of Science in Geotechnical Engineering

August 2009 – December 2013
Pontificia Universidad Javeriana
Civil Engineering.

Software

Petrel ® geomechanics module. Techlog ® geomechanics module. PetroMod ® for basin and petroleum systems analysis.

Finite Element Software: ABAQUS®, ANSYS®

Publications

(1) C. Guerra, K. Fischer, A. Henk. **2019**. Stress prediction using 1D and 3D geomechanical models of a tight gas reservoir – A case study from the Lower Magdalena Valley Basin, Colombia. *Geomechanics for Energy and the environment.* ISSN 2352-3808.

(2) C. Guerra, A. Henk, J. Hidalgo. **2017**. "Integration of petroleum systems and geomechanical modelling workflow. Case study: Lower Magdalena Basin (Colombia)". DGMK/ÖGEW-Frühjahrstagung, Fachbereich Aufsuchung und Gewinnung. Celle, Germany. Indexed abstract.

(3) Guerra C.I, Pinzón J.J., Prada L.F., Ramos A. **2016**. "Multiscale modelling of slope stability of block-in-matrix materials". Geo-Chicago 2016 Technical Papers: Sustainability, Energy, and the Geo-environment https://doi.org/10.1061/9780784480144.065.

Conferences

AAPG **2019-** Annual convention & exhibition. Poster and presentation sessions. May 2019. *San Antonio, Texas.*

DGMK/ÖGEW-Frühjahrstagung, Fachbereich Aufsuchung und Gewinnung. April **2017**, *Celle - Germany*

International Symposium on Life-Cycle Civil Engineering IALCCE2014. November **2014**, *Tokyo - Japan.*

XIV Colombian Geotechnical Congress. October **2014**, *Bogotá – Colombia.*